Solidification Behaviour of Fe-rich Intermetallic Compounds in Aluminium Alloys

A thesis submitted to Brunel University for
the degree of Doctor of Philosophy

by

Yipeng Zhou

BCAST (Brunel Centre for Advanced Solidification Technology)
Brunel University, Uxbridge, UB8 3PH,
United Kingdom

February, 2018

Supervision: Professor Zhongyun Fan

Abstract

The industrial use of recycled aluminium is greatly limited by the degraded mechanical properties due to the increased impurities. Fe, one of the common impurity content in Al alloys, is difficult to eliminate once introduced into aluminium during primary production or recycling processes. Due to the low solid solubility of Fe in Al, the formation of Fe-rich intermetallic compounds (Fe-IMCs) is inevitable, which is one of the main causes for the deterioration of mechanical properties in various cast Al alloys. In order to obtain desirable mechanical properties of recycled Al alloys, modification and refinement of the Fe-IMCs are urgently required as the compact and refined morphologies of such intermetallics are generally non detrimental to Al alloy's performance. However, manipulating the solidification behaviour of the Fe-IMCs phases, including nucleation and growth, is very challenging because of the inherently more difficult heterogeneous nucleation of the Fe-IMCs compared with that of a pure metal or a solid solution; and the strong growth anisotropy. Limited understanding on mechanisms of nucleation and growth of the multicomponent Fe-IMCs is available in the literature.

The aim of this study is to gain a deeper understanding on the heterogeneous nucleation and growth behaviour of Fe-IMCs in various Al alloys. The nucleation and growth of both primary and eutectic Fe-IMCs have been investigated during various solidification conditions including a number of different cooling rates and casting temperatures. Based on the experimental results of the solidification of several ternary and quaternary alloys, effect of Mg on the solidification behaviour of Fe-IMCs was investigated. Further the surface modified TiB_2 particles were used to enhance the heterogeneous nucleation of Fe-IMCs in order to refine the Fe-IMCs particles.

The dominant Fe-IMC in Al-5Mg-2Si-1.2Fe-0.7Mn alloy is identified, using transmission electron microscopy (TEM), as α-AlFeMnSi with a body centred cubic (BCC) lattice structure and lattice parameter of 1.256nm. In the current alloy system, the nucleation of primary α-AlFeMnSi occur at lower cooling rate (≤0.8K/s) when required nucleation undercooling is reached, as the slower cooling rate allows longer diffusion time for the solute to form a stable nucleation embryo. When casting with

20K superheat, the size of primary α-AlFeMnSi increases gradually from 24.5±3.1μm (870K/s) to 251.3±75.3μm (0.02K/s) and the size of α-AlFeMnSi eutectic increased gradually from 102.0μm (870K/s) to 623.3μm (0.02K/s). The Fe and Mn concentration in α-AlFeMnSi appears to reduce with the increased cooling rate due to the relatively insufficient solute supply when solute concentration is low (1.2wt.% Fe and 0.7wt.% Mn). Microstructure observation reveals that the {011} plane, especially on <111> orientation, is the preferred growth orientation of BCC primary α-AlFeMnSi, resulting in rhombic dodecahedral in 3D. The eutectic α-AlFeMnSi, prefers to initiate on the primary α-AlFeMnSi. In addition to the substantial nucleation undercooling, the research revealed that the nucleation of primary α-AlFeMnSi also rely on the local solute concentration and the solute diffusion. Compared with α-Al, the growth of α-AlFeMnSi is less sensitive to the cooling rate changes due to the complexities in multi-components interaction and different diffusion efficiency of different elements.

The addition of Mg to Al-1.2Fe-0.7Mn and Al-2Si-1.2Fe-0.7Mn alloys was found to lead to a morphology change of Fe-IMCs. $Al_6(Fe,Mn)$, the predominant Fe-IMC in the Al-1.2Fe-0.7Mn-*x*Mg alloy, changed from needle morphology to interconnected lamellar morphology when Mg composition increased from 0.004wt.% to 6.04wt%. A Mg-rich layer at about 5-20nm in thickness was commonly observed on the Fe-IMC/α-Al interface in the alloys with Mg content. The eutectic lamellar spacing for $Al_6(Fe,Mn)$ increases from 1.8±0.3μm to 4.5±0.8μm when Mg content increased from 0.004wt.% to 6.04wt.%. In the case of α-$Al_{12}(Fe,Mn)_3Si$, the predominant Fe-IMC in Al-2Si-1.2Fe-0.7Mn-*y*Mg alloys, its lamellar spacing of the eutectic increased from 1.4±0.3μm to 3.25±0.8μm when Mg increased from 0.04wt.% to 5.41wt.%. Owing to the strong anisotropy of the Fe-IMC crystals, the segregation of solute Mg on preferred growth orientation is higher, causing greater growth restriction on this orientation. Consequently, the growth velocity on other orientations becomes relatively more significant.

To optimise the morphology of Fe-IMCs in Al alloys, a novel Al-Ti-B(Fe) grain refiner for Fe-IMCs has been developed to enhance the heterogeneous nucleation of Fe-IMCs. The addition of the novel grain refiner to an Al-5Mg-2Si-1.2Fe-0.7Mn alloy under controlled solidification condition results in a considerable refinement of the primary Fe-IMCs from 251.3±75.3μm to 110.9±45.5μm and from 127.3±36.2μm

to 76.5±18.2μm at cooling rates of 0.02K/s and 0.15K/s, respectively. TEM investigations on the refiner reveal a Fe-rich adsorption monolayer in a zigzag fashion on the prismatic planes on the boride particles. This surface modification is beneficial for the heterogeneous nucleation of the Fe-IMCs. Further investigation of the Al alloy with this grain refiner addition revealed that there existed specific orientation relationships (ORs) between TiB_2 and Fe-IMCs: $(001)[020]_{Al_{13}Fe_4}$ // $(11\text{-}20)[10\text{-}10]_{TiB_2}$, and $(001)[120]_{Al_{13}Fe_4} \angle 6.05^\circ$ $(11\text{-}20)[10\text{-}11]_{TiB_2}$; $(0\text{-}11)[100]_{\alpha\text{-}AlFeMnSi}$ // $(0001)[\text{-}2110]_{TiB_2}$, and $(0\text{-}11)[111]_{\alpha\text{-}AlFeMnSi}$ $\angle 4.5^\circ$ $(0001)[10\text{-}10]_{TiB_2}$. The Fe adsorption on substrate particle, the observed ORs between TiB_2 and Fe-IMCs, and the refinement of primary α-AlFeMnSi with the addition of modified TiB_2 provide evidence of structure templating and composition templating required by heterogeneous nucleation of Fe-IMCs.

This research has delivered contribution to the understanding and new approach for optimizing the morphology of Fe-IMCs in the Fe-containing Al alloys. Using the slow cooling rates (≤0.15K/s), the formation compact primary α-AlFeMnSi can be considerably encouraged. With a lower casting temperature, the size and volume fraction of large Chinese-script α-AlFeMnSi can be significantly reduced. With addition of reasonable Mg content the morphology of Fe-IMC can be modified. Particularly, with the addition of the Al-Ti-B(Fe) grain refiner in well-controlled condition, the primary α-AlFeMnSi can be significantly refined. Thus, by implementing these approaches, the optimized Fe-IMC morphology in the microstructure of Fe-containing Al alloy is able to offer promising mechanical performance.

Acknowledgements

I would like to sincerely thank Professor Zhongyun Fan for offering me the opportunity to pursue my PhD in BCAST, Brunel University London for the last four years. His support and guidance from the first day of the PhD journey to the completion of the project have given me a great lesson not only on research but also on the value of life.

I wish to show my sincere appreciation to Dr Yun Wang who has been incredibly patient and supportive to me. Without his help on the advanced electron microscopy and academic writing, this thesis wouldn’t have been possible. I am very grateful to Dr Zhongping Que for her practical advice and valuable guidance throughout the project.

I would like to show my gratitude to Dr Feng Wang for his constructive discussion, Dr Xinliang Yang for his generous help on electron microscopes and Dr Chamini Mendis for her valuable advice on thesis. I wish to thank all the colleagues who have supported my research especially: Dr Bo Jiang, Dr Li Zhou, Dr Wenchao Yang, Dr Shouxun Ji, Professor Hari Babu Nadendla, Dr Hailin Li, Dr Yijie Zhang, Dr Hu-Tian Li and Dr Yan Huang.

I would like to thank Dr Ashley Howkins, Dr Lorna Anguilano, and Mrs Nita Verma for their kind support on electron microscopic analysis. I wish to thank Mr Steve Cook, Mr Matthew Ralph, Mr Carmelo Nunez, Mr Peter Lloyd, Ms Stephanie Kennedy, Mr Graham Mitchell and Mrs Samantha Melvin for their excellent technical support.

Finally, I am indebted to my dearest friend, Denisa, for her support and encouragement throughout my PhD study. I owe my deepest gratitude to my mother and father, who provided me with their unconditional love and support over the course of my study.

Publication List

Z.P. Que, Y. Wang, **Y.P. Zhou**, L. Liu, Z. Fan, (2015) Effect of Al-5Ti-1B grain refiner addition on the formation of intermetallic compounds in Al-Mg-Si-Mn-Fe alloys, Materials Science Forum Vols. 828-829 (2015) pp 53-57.

Z.P. Que, **Y.P. Zhou**, Y. Wang, Z. Fan, (2015) Effect of MgO on phase selection in Al–Mg–Si–Fe–Mn alloys, Trans. Indian Institute of Metals, 2015, vol 68, issue 6, pp. 1167-1172.

Y. Zhou, Z.P. Que, Y. Wang, Z. Fan, (2016) Effect of Mg content on Fe-rich intermetallic compound in Al-Fe-Mn alloys. Proceedings of the 15th International Conference on Aluminium Alloys, Chongqing, China, June 2016.

Z.P. Que, **Y.P. Zhou**, Y. Wang, Z. Fan, (2017) Composition templating for heterogeneous nucleation of intermetallic compounds. Proceedings of the 6th Decennial International Conference on Solidification Processing, Old Windsor, UK, July 2017.

Y. Zhou, Y. Wang, Z.P. Que, Z. Fan, The role of TiB_2 particle on the nucleation of primary α-AlFeMnSi in Al-Mg-Si-Fe-Mn alloy. (To be submitted to *J. Alloys. Compd.*)

Y. Zhou, Y. Wang, Z.P. Que, Z. Fan, Effect of Mg content on the morphology of Al_6(Fe,Mn) in Al-Fe-Mn alloys. (To be submitted to *Mater. Charact.*)

Y. Zhou, F. Wang, Y. Wang, Z. Fan, A crystallography study of nucleation of primary α-AlFeMnSi in Al alloy with TiB_2 inoculation. (To be submitted to *J. Alloys. Compd.*)

Nomenclature

A list of symbols is given with a brief description

Symbol	**Definition and Units**
α-Al	α-Aluminium phase
C_L, C_S	Solute content in the liquid and the solid, respectively
C_V	Heat capacity of the melt (J/(m$^{3\cdot}$K))
C_0	Chemical composition (wt.%)
D	Diffusion coefficient (m^2/s)
$\overline{D}$	Mean grain size (μm)
d	Diameter of nucleation substrate (m)
f	Calculated lattice misfit (%)
f_S	Solid volume fraction
f_L	Liquid volume fraction
$\Delta\mathrm{G}$	Gibbs free energy change (J/mol; J/m^3)
ΔG^*	Gibbs free energy change per mole (J/mol; J/m^3)
ΔG^*_{hom}	Gibbs free energy change for homogeneous nucleation (J/mol; J/m^3)
ΔG^*_{het}	Gibbs free energy change for heterogeneous nucleation (J/mol; J/m^3)
ΔG_v	Volumetric free energy change between solid liquid phases at the sample temperature (J/mol; J/m^3)
ΔH	Volumetric entropy change for phase transformation (J/mol; J/m^3)
K	Alloy dependent constant
k	Equilibrium solute distribution coefficient
k_B	Boltzmann’s constant
L	Liquid melt
L_1	Liquid melt before the binary eutectic transformation
L'	Liquid melt before $Al_{13}Fe_4$

L''	Liquid melt before Al_8Fe_2Si
L_2	Liquid melt before the ternary eutectic transformation
L_V	Latent heat of fusion (J/mol; J/m^3)
m	Slope of liquidus line (K/wt.%)
N	Nucleating substrates
ρ	Number density of particles
Q	Growth restriction factor
R_A	Area Ratio (%)
r	Nucleus radius (μm)
r_c	Critical nucleus radius (μm)
ΔS_V	Volumetric entropy of fusion (J/mol; J/m^3)
$S(\theta)$	A factor in terms of the wetting angle (°)
$\dot{T}$	Cooling rate (K/s)
ΔT	Undercooling (°C)
ΔT_c	Critical undercooling in epitaxial nucleation model (°C)
ΔT_M	Maximum nucleation undercooling (°C)
ΔT_N	Heterogeneous nucleation undercooling (°C)
ΔT_{fg}	Undercooling required for achieving the state of free growth (°C)
T_{Eu}	Primary eutectic temperature (°C)
T_L	Liquidus temperature
T_G	Growth temperature (°C)
T_N	Nucleation starting temperature (°C)
T_R	Recalescence starting temperature (°C)
λ_2	Secondary dendrite arm spacing (μm)
λ_{Eu}	Eutectic lamellar spacing (μm)
λ_a	Minimum eutectic lamellar spacing (μm)
λ_M	Maximum eutectic lamellar spacing (μm)

V	Vector; or growth rate (specified in content)
ε	Ratio of α-/β- phase width (J/mol; J/m^3)
γ_s	Specific surface energy (J/mol; J/m^3)
γ_{lv}	Interfacial energy between liquid and vapour phases (J/mol; J/m^3)
γ_{sl}	Interfacial energy between solid and liquid phases (J/mol; J/m^3)
γ_{sv}	Interfacial energy between solid and vapour phases (J/mol; J/m^3)
Z	Half thickness of the Cu wedge mould
$\lvert df_s/dT \rvert$	Slope of the solid fraction versus temperature curve
Γ	Gibbs-Thomson parameter (K/m)
θ	Wetting angle; or angle at three phase junction (specified in content)
$\emptyset$	Parameter of interface position; or diameter (specified in content)

Abbreviations

CALPHAD	CALculation of PHAse Diagram
CA	Cooling in Air
CF	Cooling in Furnace
DE	Deep Etching
Fe-IMC	Fe-rich Intermetallic Compound
GRF	Growth Restriction Factor
HAADF	High Angle Annular Dark Field
MQ	Steel mould Melt Quench
MTB	Modified TiB$_2$ particles
PS	Pseudomorphic Solid
SDAS	Secondary Dendrite Arm Spacing
TP-1	Standard Test Procedure for aluminium alloy grain refiners
TQ	(Quartz) Tube water Quench

Table of Contents

List of Tables and Figures

Chapter 2

Chapter 3

Chapter 4

Chapter 5

Chapter 6

Chapter 1 Introduction

1.1 Background

Recycling of Al alloys is a preferable way to produce aluminium compared with production from raw materials duo to its low energy consumption and low greenhouse gas emission (Kvackaj and Bidulsky, 2011; Green, 2007). The purification process from bauxite to the aluminium is a very sophisticated and energy consuming process. Recycling requires only 5% of the energy consumption required for aluminium production from the raw material (Green, 2007). Considering Al alloys' good weight/strength/cost ratio, it is becoming more dominant in metallic applications, which in return will significantly stimulate the demand of recycling aluminium and developing recycled aluminium.

Using recycled aluminium is very challenging due to the excessive amount of impurities including Fe, Si, Mn etc. Fe and Si, are accumulative elements in Al alloy and can never be completely removed once introduced during primary Al alloy production and the recycling process. Due to the low solubility of Fe (0.05wt.%) in Al (Phillips, 1959), it is inevitable that the Fe-IMCs form, which has become the main cause of deterioration of the mechanical properties of cast Al alloys (Mondolfo, 2013). As a brittle, large and strong compound, Fe-IMC can easily cause shrinkage (Taylor, 2012), porosity (Taylor, 2012), ductility reduction (Ji *et al.*, 2013), strength reduction (Wang, Makhlouf and Apelian, 1995), scattered mechanical properties (Wang, Makhlouf and Apelian, 1995), and reduction of fatigue life (Nyahumwa, Green and Campbell, 1998). Although adding grain refiner is an effective approach to increase the mechanical properties of Al alloy, a slight increase of Fe concentration can harm the mechanical properties of the final casting drastically.

Significant amount work has been done to eliminate the negative effect of Fe in Al alloys. There have been two main approaches. The first is modifying the solidification process of Fe-IMC, including nucleation enhancement (Que *et al.*, 2017; Khalifa *et al.*, 2005) and morphology modification (Mondolfo, 2013; Zhang *et al.*, 2012). The other is de-ironing including gravity segregation (Cao, Saunders and Campbell, 2004; Cao and Campbell, 2000), filtration (de Moraes *et al.*, 2006) and

EM separation etc. (Makarov, Apelian and Ludwig, 1998). However, the latter approach may only reduce Fe concentration to a certain level and normally requires very delicate procedures.

Thus, enhancing the heterogeneous nucleation and modifying the growth behaviour of Fe-IMCs have become fundamentally important. Few effective methods can be put forward to reduce the size of Fe-IMCs. There has been a significant amount of effort dedicated to advancing understanding of heterogeneous nucleation through both theoretical and experimental approaches. The heterogeneous nucleation theories including classic nucleation theory (Turnbull, 1953), Maxwell-Hellawell (M-H) model (Maxwell and Hellawell, 1975) and free growth model (Greer *et al.*, 2000) appears not to be effective at predicting the nucleation behaviour of Fe-IMCs. In recent years, the pre-nucleation theory (Men and Fan, 2014) has broadened our understanding of the nucleation process, which describes the pronounced atomic ordering in the liquid at the substrate/liquid interface (SuLI). Therefore, the lattice misfit may be manipulated with interracial segregation at the SuLI during the pre-nucleation stage, which can either promote or impede heterogeneous nucleation (Fan *et al.*, 2015). Both primary and eutectic Fe-IMCs, like every other anisotropic crystal, exhibit a coarse faceted morphology (Terzi *et al.*, 2010; Dinnis, Taylor and Dahle, 2005). Binary Al-Fe IMCs generally exhibit needle-like or long rod-like morphology and β-AlFeSi exhibits coarse plate-like morphology. The primary α-AlFeMnSi has a compact polyhedral morphology (Gao *et al.*, 2013) when the iron equivalent value (IEV) is relatively low (Cao, Saunders and Campbell, 2004), and has the most compact morphology among all the Fe-IMCs. Therefore, along with Mg and Si, Mn is also introduced to the alloy to achieve an optimised morphology of Fe-IMCs.

The heterogeneous nucleation of Fe-IMCs is much more complicated than that of pure liquid/solid solution, as it requires the creation of not only a simple crystal structure but a super-structure involving two or more elements. As suggested by Men and Fan (Men and Fan, 2014), a substrate with reasonable lattice mismatching with the nucleating phase requires structure templating for heterogeneous nucleation. Que and co-workers (Que *et al.*, 2017) suggested that for the phases with large barrier to nucleation the composition templating is significantly beneficial as the case with the heterogeneous nucleation of Fe-IMCs.

1.2 Research Objectives

The major objectives of this study are:

- Understand the heterogeneous nucleation behaviour of Fe-IMC in Al alloys
- Investigate the effect of casting conditions on the solidification behaviour of Fe-IMC
- Study the role of solute segregation on the growth of anisotropic Fe-IMC crystal
- Develop a novel grain refiner to enhance the heterogeneous nucleation of Fe-IMC
- Understand the mechanism of enhanced heterogeneous nucleation of Fe-IMC through solute element on the substrate

1.3 Outline of Thesis

After a sincere acknowledgement and an introduction of the research background, previous literature is reviewed in Chapter 2 with a detailed overview of the previous theoretical studies on the solidification behaviour, which include the classical nucleation theories, the study of potency and efficiency of nucleation substrates, the role of solute on the crystal growth, facet growth, including primary crystal and irregular eutectic crystals, and stability of the ceramic particles in Al-Ti-B alloy. Also in Chapter 2, the existing Fe-IMCs are summarized, and solidification behaviour of Fe-IMCs in Al alloys from previous research is reviewed. Chapter 3 describes the experimental procedures and characterisation techniques in details. In Chapter 4, the result of the solidification behaviour of α-AlFeMnSi and $Al_6(Fe,Mn)$ in Al-5Mg-2Si-1.2Fe-0.7Mn-2Si alloy are presented with microstructure observation of various casting conditions, thermal analysis and phase identification and these result are discussed. In Chapter 5, the effect of the addition of novel grain refiner Al-Ti-B(Fe) in the Al-5Mg-2Si-1.2Fe-0.7Mn alloy are presented, including the Fe adsorption, orientation relationships between Fe-IMCs and TiB_2 and the role of composition templating. Chapter 6 offers the effect of Mg content on the solidification behaviour of Fe-IMCs including thermal analysis, microstructure observation of alloys with different Mg contents and the quantification of α-Al and Fe-IMCs at different Mg composition. The main conclusions and suggestions for future work are listed in Chapter 7 and Chapter 8, respectively.

Chapter 2 Literature Review

2.1. Theoretical Studies of Solidification Behaviour

2.1.1. Classic Nucleation Theory

The classical nucleation theory is based on a statistical analysis of the formation of atom cluster (or spherical caps in the case of heterogeneous nucleation) with a critical radius R_c and relates to a wetting angle θ between the substrate and the nucleating solid, which is thermodynamically activated and a stochastic process (Kurz and Fisher, 1986; Kelton and Greer, 2010; Dantzig and Rappaz, 2009; Porter, Easterling and Sherif, 2009; Volmer and Weber, 1926). There are two types of nucleation: homogeneous nucleation where the new phase is formed in a uniform manner and heterogeneous nucleation where the nucleation occurs on an existing substrate. For homogeneous nucleation, the wetting angle is considered to be π since there is no substrate for wetting. The Gibbs free energy change, ΔG, associated with the process of heterogeneous nucleation is equal to the sum of the surface excess free energy ΔG_S change, and the volume excess free energy change ΔG_V. Thus, the Gibb free energy changes can be expressed as (Porter, Easterling and Sherif, 2009),

$$\Delta G = \left(-\tfrac{4}{3}\pi {R_c}^3 \Delta G_v + 4\pi {R_c}^2 \gamma_{sl}\right) S(\theta) \tag{2.1}$$

$$S(\theta) = (2+\cos\theta)(1-\cos\theta)^2/4 \tag{2.2}$$

where γ_{si} is the solid-liquid interfacial energy and *S(θ)* is the factor regarding the wetting angle θ.

2.1.1.1. Homogeneous Nucleation

When solid forms within its own melt without the assistance of a foreign material, it should nucleate homogeneously (Flemings, 1974). Nucleation in this way requires a large driving force because of the relatively large contribution of surface energy to the total free energy on very small substrate. For homogeneous nucleation, since the wetting angle is considered as π, *S(θ)* = 1. Equation 2.1 becomes,

$$\mathit{\Delta} G = -\tfrac{4}{3}\pi {R_c}^3 \mathit{\Delta} G_v + 4\pi {R_c}^2 \gamma_{sl} \tag{2.3}$$

Gibbs free energy change per unit volume can be given approximately as (Porter, Easterling and Sherif, 2009),

$$\mathit{\Delta} G_v \cong \left(L_v \frac{\Delta T}{T_m} \right) \tag{2.4}$$

where L_V is the latent heat of fusion per unit volume. Since the interfacial energy increases as R^2 whereas the volume free energy change only increases as R^3, the creation of small substrate of solid always leads to free energy increase. This increase maintains the liquid phase in a metastable state almost indefinitely at a given under cooling. Since $dG=0$ when *the* $R=R_c$, the critical nucleus is effectively in an unstable equilibrium state with the surrounding liquid as illustrated in **Fig. 2.1**.

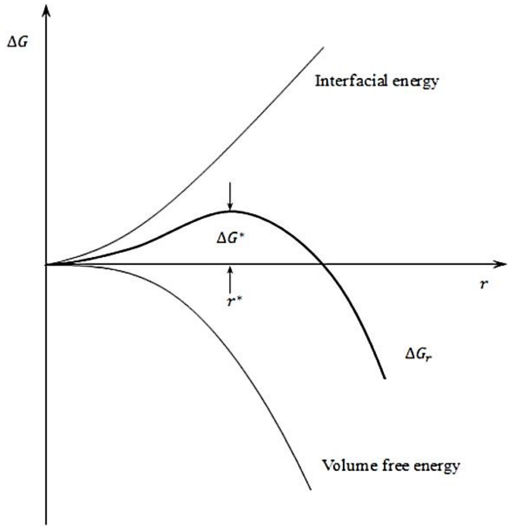

Figure 2.1 The free energy change associated with homogeneous nucleation of a sphere of radius *r* (Porter, Easterling and Sherif, 2009).

Therefore, the critical free energy barrier for the radius r^* of a stable spherical particle which is just stable at an undercooling ΔT is given by

$$r^* = \left(\frac{2\gamma_{sl}}{\mathit{\Delta} G_V} \right) \cong \frac{2\gamma_{sl} T_m}{L_V \mathit{\Delta} T} \tag{2.5}$$

$$\mathit{\Delta} G^* = \left(\frac{16\pi \gamma_{sl}^3 T_m^2}{3 L_V^2} \right) \frac{1}{\mathit{\Delta} T^2} \tag{2.6}$$

From the equations (2.3) and (2.4), it shows that both the critical radius R_c and the activation free energy ΔG^* decrease as temperature T_m decreases (ΔT increases). Physically, this means that with a lowering of temperature at temperatures below the equilibrium solidification temperature T_m, nucleation occurs more readily. The homogeneous nucleation rate is given (Dantzig and Rappaz, 2009):

$$\Delta N_{hom} = f_0 C_0 exp(\frac{\Delta G_{hom}}{kT}) \tag{2.7}$$

where f_0 is a complex function that is dependent on the vibration frequency of the atoms, the activation energy for diffusion in the liquid and the surface area of the critical nucleus. C_0 is the atoms per unit volume contained in the liquid.

2.1.1.2. Heterogeneous Nucleation

Although the level of undercooling for homogeneous nucleation might be significant, in practical situations this is often in the order of several degrees Celsius. The reason is that the activation energy for nucleation (ΔG^*) is lowered when nucleus forms on the pre-existing surface or interfaces. In another word, it is easier for nucleation to happen at these surfaces and interfaces than at other regions. Again, this type of nucleation is defined as heterogeneous nucleation. The energetic expression of heterogeneous nucleation is shown in Equation 2.1 and 2.2. The relationship between the nucleation barriers of homogeneous nucleation and heterogeneous nucleation is given (Porter, Easterling and Sherif, 2009),

$$\Delta G^*_{het} = \Delta G^*_{hom} \, S(\theta) \tag{2.8}$$

The wetting angle for heterogeneous nucleation is illustrated in **Fig. 2.2**. Thus, the energy barrier for heterogeneous nucleation is much smaller than that of homogeneous nucleation. Significant reductions are also obtained for higher values of θ. Thus, the equation 2.7 for heterogeneous nucleation is expressed as,

$$\Delta N_{het} = f_0 C_0 exp(\frac{\Delta G_{het}}{kT}) \tag{2.9}$$

where f_1 is a frequency factor similar to f_0 in equation 2.7 and C_1 is the number of atoms in contact with heterogeneous nucleation site per unit volume of liquid.

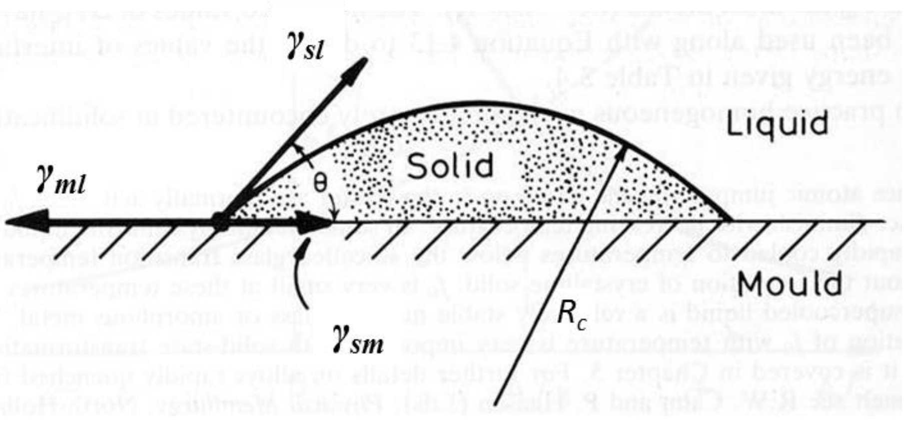

Figure 2.2 Schematic illustration of heterogeneous nucleation of a spherical cap on a flat surface or interface of the substrate, where θ is the wetting angle of the solid on the substrate, γ_{sl}, γ_{ml} and γ_{sm} are the interfacial energies of liquid/solid, mould/liquid, and solid/mould, respectively (Turnbull, 1953).

2.1.2 Potency of Nucleation Substrates

Nucleation potency, by definition, is the effectiveness of a substrate at facilitating nucleation. It is inversely related to the undercooling that is required for nucleation (ΔT_n) (Bramfitt, 1970). However, there are inherent issues with the classical nucleation theory, particularly the difficulties in the measurement of nucleation effectiveness, i.e. θ and ΔG^*, as the wetting angle cannot be observed and the interfacial energy is composed of several contributory factors (Qian, 2007; Bramfitt, 1970; Walton, 1962). Thus, it is hard to determine whether a particle can be an effective nucleus for a given phase. For the purpose of resolving this problem, the lattice misfit between substrate and nucleating phase has been used to determine the potency of the substrate (Baker and Cahn, 1971; Turnbull, 1953). This is based on the basic understanding that low values of wetting angle usually lead to low-energy interface between the substrate and the solidifying species, which should in turn be favoured by good lattice matching between the substrate and solid (Porter, Easterling and Sherif, 2009). Therefore, the lattice misfit is commonly accepted as a critical value to determine the potency of potential nucleation substrates (Fan, 2013; Zhang and Kelly, 2005a; Maxwell and Hellawell, 1975a; Turnbull, 1953). The theoretically lattice misfit, or misfit, is defined as,

$$f = \frac{|d_n - d_{sub}|}{d_n} \times 100\% \tag{2.10}$$

where d_n and d_{sub} are the atomic spacing along a specific direction on the matching planes of the nucleated phase and the nucleation substrate, respectively. The lattice spacing of these two phases is mainly dependent on the crystal structure. The lattice structure of this interface is shown schematically in **Fig. 2.3**. The interface region can be explained by a simple dislocation model that compensates for the lattice strain in the nucleated phase for the nucleation misfits up to 20% (Bramfitt, 1970).

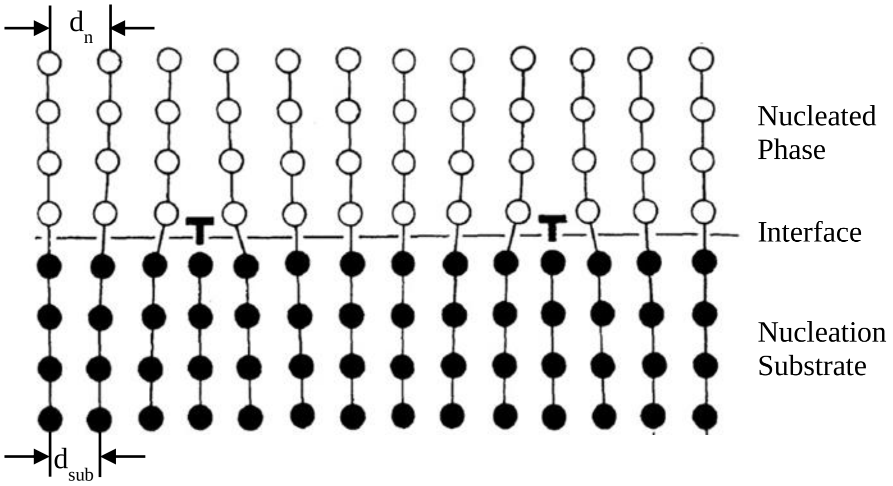

Figure 2.3 Schematic illustration of nucleated phase, substrate, interface and the atom spacing of (d_n) nucleated phase and (d_{sub}) nucleation substrate (Porter, Easterling and Sherif, 2009).

Wetting as a mechanism for nucleation has long been assumed in the condensation of vapour on wetted insoluble particles (Bykov and Zeng, 2002; Kuni *et al.*, 1996), where the nucleus is often considered to be a uniform liquid film. The nucleus is treated differently according to the thickness of the liquid film. It is proposed that the consideration should include an additional term to indicate the interactions of surface forces between the nucleation substrate and nucleating phase when the nucleating phase's film is thin (Kuni *et al.*, 1996). However this additional term can be taken to be negligible when the film thickness increases. Further, Maxwell and Hellawell (Maxwell and Hellawell, 1975a; Maxwell and Hellawell, 1975b) proposed a mechanism (the M-H model) that combines the spherical-cap model with wetting for grain formation on the faceted intermetallic compound particles. They believe that after the formation of a sphere-cap nucleus on a flat surface, it efficiently envelopes and wet the particle leading to small undercooling which implies a very small wetting angle. Thus, the nucleus spherical envelope of the nucleus radius is taken to be approximately equal to the dimensions of IMCs. This has been supported by many subsequent research. However, Yang's observation for the formation of thin metal (sodium) films by condensation of the sodium vapour on different substrates suggests that the calculated critical nucleus size from the experimental data is approximately the size of a unit cell of sodium (Yang *et al.*, 1954). Walton reassessed that for nucleus of this magnitude the uncertainties associated with the spherical-cap model

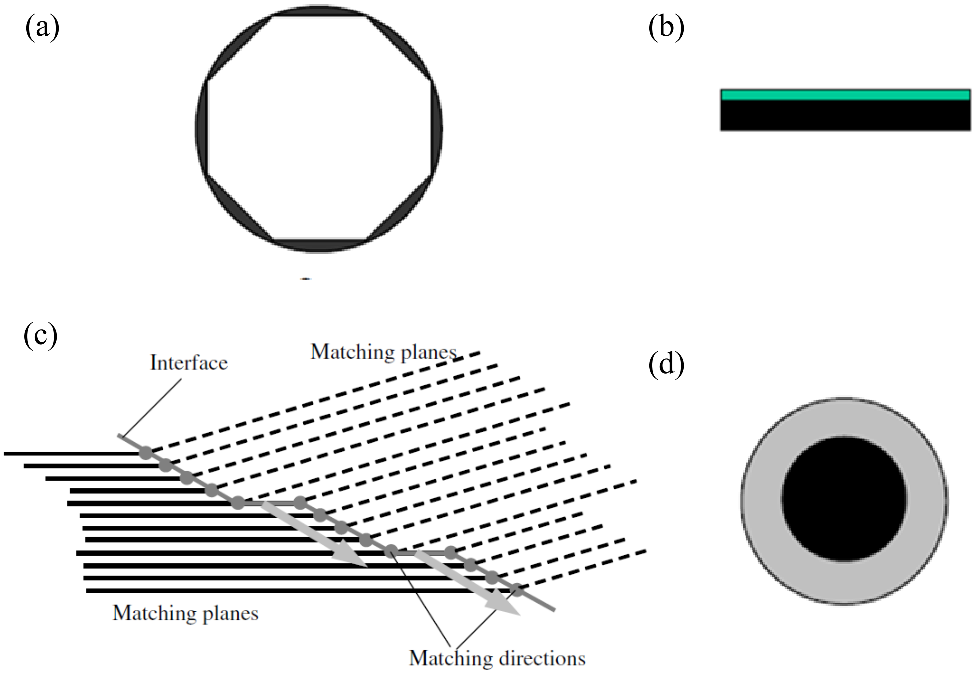

Figure 2.4 Various models proposed for heterogeneous nucleation on substrates of different potency and geometries: (a) a schematic of the M–H model drawn according to Maxwell and Hellawell's description (Maxwell and Hellawell, 1975a) where sufficient wetting (θ) implies small undercooling; (b) the adsorption model described by Cantor and Kim, where the heterogeneous nucleation takes place by dynamic atom-by-atom adsorption at the catalyst surface, which reduces the interfacial energy between substrate and nucleation phase (Cantor, 2003; Kim and Cantor, 1994); (c) Edge-to-Edge model (E2EM) described by Zhang that describes the lattice matching of the nucleation phase and substrate suggesting the capability of nucleation orientation relationship prediction (Zhang and Kelly, 2005a). (d) liquid film/drop formation on a solid wettable spherical particle in a super-cooled liquid metal (Qian, 2007), where interface adsorption of nucleating metal occurs at a critical undercooling with a thin layer of atoms enveloping the substrate.

whereas the concept of surface energy become so large that the critical nucleus approaches atomic dimensions or is actually planar, and therefore the concept of θ is no longer applicable (Walton, 1962). As shown in **Fig. 2.4**, even with the difficulties in assessing the wetting angle, some well acknowledged nucleation theories are summarized including the M-H model (Maxwell and Hellawell, 1975a), Cantor's description of adsorption (Cantor, 2003), Edge-to-edge model (E2EM) (Zhang and Kelly, 2005a; Zhang and Kelly, 2005b) and Qian's description of the potent spherical nucleation (Qian, 2007). Thus, if substrate particles can achieve good wetting, the nucleation barrier is significantly reduced, which implies good nucleation potency. Adsorption on the wetted substrate is considered to be another important factor affecting substrate particle nucleation potency. In metallic systems, minor elements additions significantly affect the nucleation and change the nucleation undercooling. Ge addition increases the lattice mismatch for the nucleation of Al-Pb and Al-Cd suggesting that the catalysis is dominated by a chemical rather than a structural compatibility (Turnbull and Vonnegut, 1952), which was further investigated by Cantor and co-workers (Zhang and Cantor, 1990; Ho and Cantor, 1992) that the Ge increases the nucleation undercooling for Cd and Pb droplet by increasing lattice misfit. Cantor and Ho later observed that the undercooling for the solidification of Si reduced dramatically by Al doped with trace P and Na due to the formation of AlP later on Al/Si interface. The mismatch between this adsorption layer and the nucleating phase was then proposed to be the dominant factor for the effectiveness of solute adsorption on the nucleation catalysis (Schumacher and McKay, 2003; Bunn *et al.*, 1999; Schumacher and Greer, 1997; Schumacher and Greer, 1994). More recently, Fan and co-workers (Fan, 2013; Fan *et al.*, 2015) proposed a model concerning both lattice mismatching and the effect of elemental adoption on the wetted substrate for heterogeneous nucleation. In their model a pseudomorphous solid layer with critical thickness h_c forms on surface of substrate (see **Fig.2.5**). The value of h_c depended on structure templating, which describes the lattice misfit between solid and substrate, and composition templating, which describes the γ_{sl} energy reduction by elemental adsorption on the substrate. Soon after, they directly observed the adsorption of Ti monolayer with an Al_3Ti structure on (112) plane on the nucleation catalyst (TiB_2 (0001) plane) in Al alloy (Fan *et al.*, 2015).

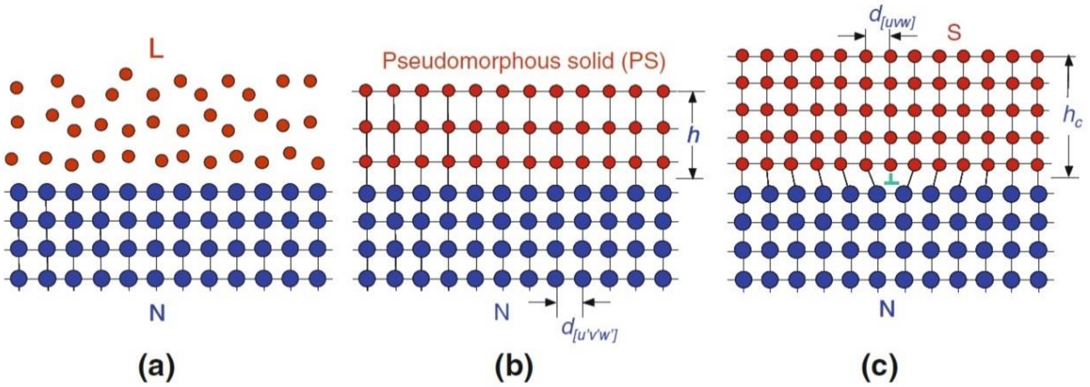

Figure 2.5 Schematic illustration of the epitaxial model for heterogeneous nucleation of a solid phase (S) on a potent nucleating substrate (N) from a liquid phase (L) under $\Delta T > \Delta T_c$: (a) liquid and substrate interface before the growth of the PS layer (h=0); (b) the initial formation of pseudomorphic solid (PS) with a coherent PS/N interface; and (c) completion of the epitaxial nucleation at a critical thickness (h_c) by creation of misfit dislocation at the S/N interface to change the PS layer into the solid and to convert the coherent PS/N interface to a semicoherent S/N interface (Fan, 2013).

In the above mentioned theories, the lattice misfit was used to assess the potency of nucleation substrate. Due to the difficulty in manipulating or determining wetting angle and interfacial energy between the substrate and nucleation phase, the lattice misfit is much more applicable for the assessment. Therefore, the lattice misfit can be used to evaluate the possibility of a certain type of particle can be the nucleation substrate for a given phase.

2.1.3 Efficiency of Nucleation Substrate

In describing grain refinement, “potency” and “efficiency” have been frequently used in the research in a way that create much confusion. Hence, it is necessary to offer more specific definitions for the nucleation potency, grain initiation efficiency and effective grain refinement.

Grain initiation efficiency is defined as the fraction of the substrate that participates in grain initiation out of the total number of available substrate in the liquid during the entire solidification process (Fan, 2013). It is clear from this definition that grain initiation efficiency is a function of the specific physical characteristics of both the nucleating particles and solidification conditions, such as the number density, grain size and the size distribution of the nucleating particles as well as the cooling rate. For a given nucleating substrate, the nucleation potency is fixed but the grain initiation efficiency can be changed by modifying the physical characteristics of the nucleating particles and/or changing the solidification conditions (Fan, 2013; Greer *et al.*, 2000; Maxwell and Hellawell, 1975a). Effectiveness of inoculation with potent spherical substrates depends on both the particle size and the undercooling of liquid metal during solidification (Qian, 2007). For a given size of potent spherical substrate, a critical nucleation undercooling is still required regardless of the contact angle. Barrierless nucleation is possible only when the particle size approaches infinity under complete wetting conditions (Fan, 2013; Greer *et al.*, 2000; Maxwell and Hellawell, 1975a).

Turnbull described nucleation rate which is defined as the ratio between the density of clusters of radius R_c in equilibrium with the liquid and the density of atoms in the liquid. The heterogeneous nucleation rate (I^{heter}) is given

$$I^{heter} = v_0 p_c n_c \exp[-\frac{16\pi}{3}\frac{\gamma_{sl}^3}{(\rho\Delta s_f \Delta T)^2 k_B T} f(\theta)] \tag{2.11}$$

where v_0 is the atomic vibration frequency, p_c is the probability of capturing an atom at the surface and n_c is the density of embryos that reach the critical radius for heterogeneous nucleation. Therefore the Time-Temperature-Transformation (TTT) curve at difference wetting angle can be given in **Fig. 2.6**.

Nucleation undercooling is another important factor that affect the nucleation. Maxwell and Hellawell (Maxwell and Hellawell, 1975a) suggested that the final grain size is the result of competition between heterogeneous nucleation and growth in the melt. In the way, the nucleation rate will become negligible when the temperature increases due to the latent heat evolved during the growth of the nucleated crystals when recalescence appears, or when the nucleation sites are exhausted. Even though this model only applies to a single nucleation substrate size, it points to the final conditions of nucleation as shown in **Fig. 2.7**.

After the nucleation, the growth of nucleated grain dominates the grain refinement. Greer and co-workers (Quested and Greer, 2005; Quested and Greer, 2004; Greer, 2003; Greer *et al.*, 2000) developed the free growth model, which suggests that a new

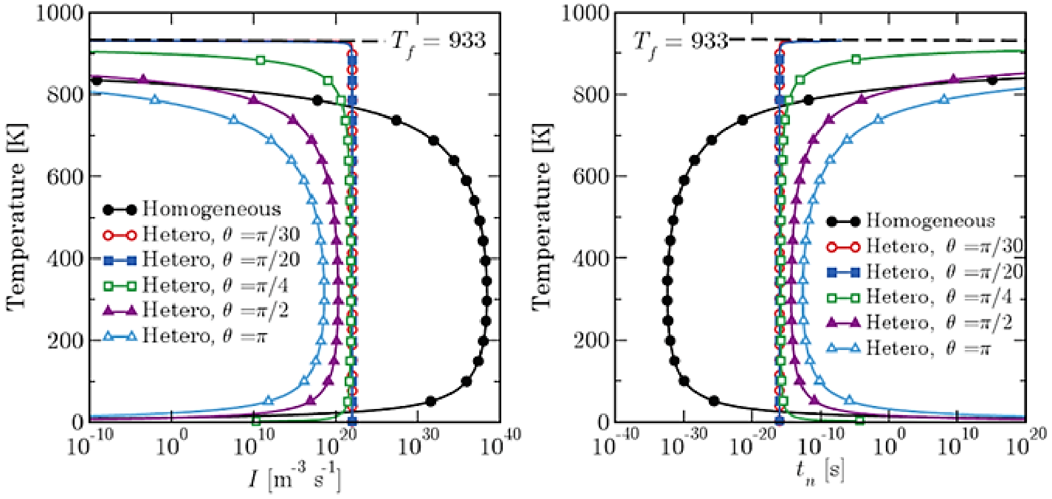

(a) The heterogeneous nucleation rate

(b) The TTT curve

Figure 2.6 The formation of critical nuclei for the heterogeneous nucleation as a function of the absolute temperature for various values of the contact angle θ. The time t_n is defined as the time to form one nucleus per cm^3 (Dantzig and Rappaz, 2009).

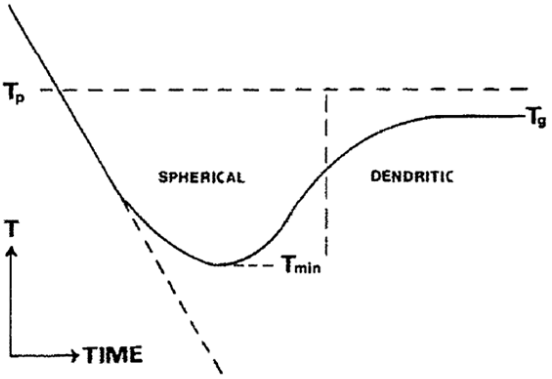

Figure 2.7 Schematic illustration of the cooling curve. The initial slope is the cooling rate, where the equilibrium transformation temperature T_p, the minimum temperature before recalescence T_{min}, and the growth temperature after recalescence T_g (Maxwell and Hellawell, 1975a).

phase should start free growth immediately on a given substrate at a required undercooling that is inversely proportional to the diameter of the substrate. This model provides that the grain initiation is not time-dependent and not stochastic, compared with the previous models, and the nucleation substrates are of multiple sizes rather than a single size as described previously by Maxwell and Hellawell. This model revealed that the largest particles in the melt start to grow first as soon as the required undercooling is reached, followed by the next largest particles as the undercooling increases. The grain size is limited by the recalescence that causes temperature rise, and no further initiation of free growth occurring afterwards. The required undercooling, ΔT_{fg}, for the free growth for a given substrate is essentially dependent on the diameter of the substrates. The undercooling is given by Greer (Greer *et al.*, 2000) as

$$\Delta T_{fg} = \left(\frac{4\gamma_{sl}}{\Delta S_v d}\right) \tag{2.12}$$

where γ_{sl} is the solid-liquid interfacial energy, ΔS_v is the entropy of fusion per unit volume, and d is the diameter of nucleation substrate. In this model, the size distribution of nucleation substrates is important, and is fitted by Quested and Greer (Quested and Greer, 2004) using a log-normal function. The fitted and measured size distribution of substrate TiB_2 in the free growth model is shown in **Fig. 2.8**.

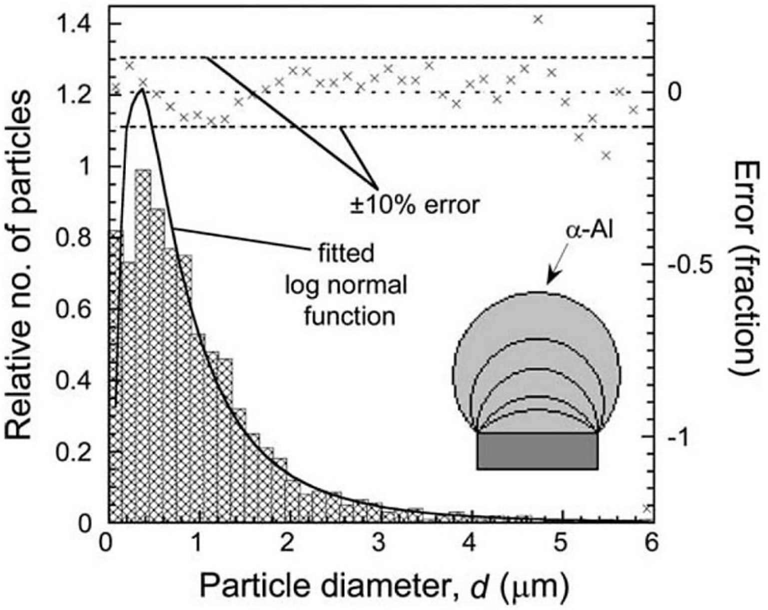

Figure 2.8 Measured size distribution of substrate TiB_2 particles in a commercial Al–5Ti–1B refiner (shaded bars) shown with log-normal fit (solid line). The error in the integrated population of particles greater than a given size (*d*) is found to be <10% over most of the range (Quested and Greer, 2004).

Turnbull’s investigation (Turnbull, 1953), suggests that higher undercooling and nucleation time might increase the nucleation rate; therefore the nucleation event could be a progressive process. With this established, Maxwell and Hellawell applied the classic nucleation theory to calculate the number of heterogeneous nucleation events in an isothermal melt at given critical nucleation embryo size. The M-H model suggested that further heterogeneous nucleation would not occur when the melt temperature increased through recalescence or heterogeneous nucleation substrate is consumed (Maxwell and Hellawell, 1975a). Based on their model, Greer (Greer *et al.*, 2000) developed the free growth model considering grain initiation on potent nucleation substrates. Unlike the time and stochastic dependent nucleation in M-H model, free growth model proposed that the nucleation is dependent on the undercooling and potent nucleation substrate size, suggesting that largest nucleating undercooling requires smallest substrate size. The substrate size distribution and the undercooling decide the number of nuclei that can free grow, and therefore the final structure can be determined.

2.1.4 The Role of Solute on Crystal Growth

Solidification is essentially an atomic movement and rearrangement process controlled by diffusion. In case a dilute alloy that has a composition of C_0. The phase diagram (**Fig. 2.9**) of the alloy has been perfected by assuming solid line and liquid line are straight. Thus, the partition coefficient k can be given (Porter, Easterling and Sherif, 2009) by

$$k = \frac{C_S}{C_L} \tag{2.13}$$

and the volume fraction of the solid can be given,

$$f_s = \frac{C_L - C_0}{C_L - C_S} \tag{2.14}$$

where the solute composition in solid and liquid are C_S and C_L, respectively.

Presume steady-state solidification at a planar interface as shown in **Fig. 2.10** has a constant interface advancing speed, v_p, in a constant temperature gradient, $G>0$. As a result of changing solute concentration at the growth front, the correspondent equilibrium transformation temperature is adjusted. The concentration profile for steady-state diffusion in an ideal system moving with the interface at a speed of $v*$ can be given according Fick’s second law (Dantzig and Rappaz, 2009; Fick, 1855) as

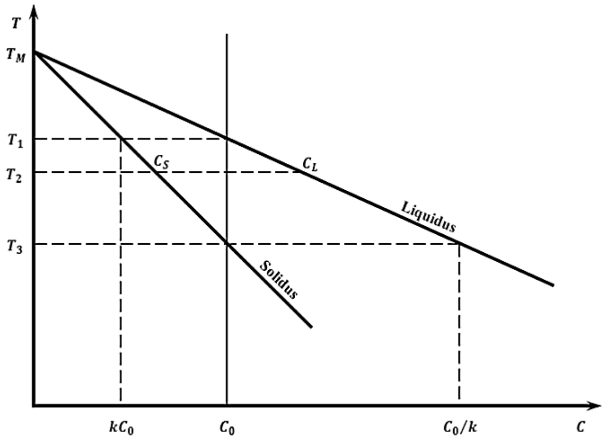

Figure 2.9 A hypothetical phase diagram. $k=C_S/S_L$ is constant (Kurz and Fisher, 1986).

$$D_l \frac{d^2 C_l}{dz^2} + v \frac{dC_l}{dz} = 0 \tag{2.15}$$

where C_l is the liquid composition, D_l is the solute diffusion coefficient in liquid and z is the distance in liquid from the S/L interface. After an initial transient, the alloy system reached a steady-state where the composition of liquid can be given as

$$C_l = C_0[1 + \frac{1-k_0}{k_0} \exp(\frac{v_p z}{D_l})] \tag{2.16}$$

where and C_0 is the nominal alloy composition. As the solidification processes, the undercooling at growth front contains two parts when the thermal undercooling is negligible (Kurz and Fisher, 1986), which can be expressed as

$$\Delta T = \Delta T_c + \Delta T_r \tag{2.17}$$

where ΔT_c is the undercooling caused by solute piling up at the growth front and ΔT_r is the curvature undercooling cause by interface shape. As shown in **Fig. 2.10**, when the actual temperature in liquid (T_l) ahead of the growth interface is below the local equilibrium transformation temperature (T_s), the growth interface will be unstable. Thus, the area where ΔT_c>0 is defined as constitutional-supercooled region (**Fig.**

2.10). Constitutional supercooled region during solidification, in the early research, is described with constitutional-supercooling parameter P (Tarshis, Walker and Rutter,

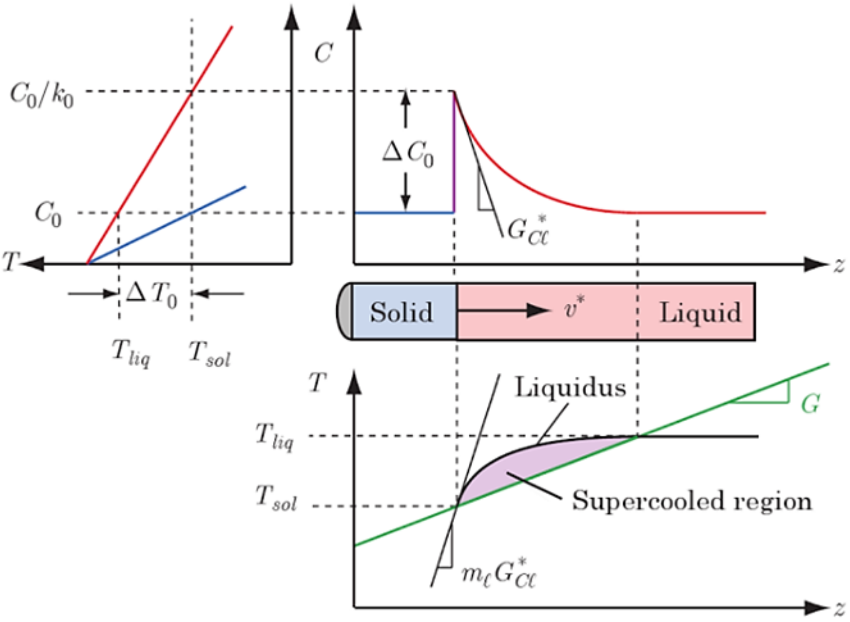

Figure 2.10 A schematic illustration of the constitutional supercooling (Tiller *et al.*, 1953) and interface stability at the growth front for binary alloy under steady-state diffusion controlled solidification at constant velocity (Kurz and Fisher, 1986; Rappaz and Thevoz, 1987) as revised by Dantzig and Rappaz (Dantzig and Rappaz, 2009).

1971), which gives

$$P = \frac{m(k-1)C_0}{k} \tag{2.18}$$

where m is the idealized liquids slope, k is the equilibrium partition coefficient. Without the consideration of solute interactions, for a multi-components system the constitutional-supercooling parameter was estimated by simply summing the P value for individual elements (Spittle and Sadli, 1995).

The M-H model considered the growth restriction of spherical crystal caused by the solute partitioning in diffusion controlled solidification (Maxwell and Hellawell, 1975a). Johnsson (Johnsson, 1995) described this effect as the growth restriction factor,

$$Q = m(k-1)C_0 \tag{2.19}$$

which was designated as Q by Greer and Easton and StJohn. In dilute multi component systems, where the solute diffusivities are considered essentially the same, additive the Q value appears good agreement with experimental observations (Greer *et al.*, 2000; Spittle and Sadli, 1995). Easton and StJohn proposed that the growth restriction allows more nucleating substrates to become active for heterogeneous nucleation before recalescence (Easton and StJohn, 1999; Easton and Stjohn, 1999). Their analysis showed that grain size is closely related to the growth restriction factor (Easton and StJohn, 2001). Further development in this direction resulted a better analytic approach to explain the solute effect (Qian *et al.*, 2010; Easton and StJohn, 2005) and the more recent postulation of the interdependence theory by StJohn and co-workers (StJohn *et al.*, 2011). Quested summarized the effect of inoculant size distribution and Q value to predict the final microstructure for Al alloys (Quested and Greer, 2004; Quested, 2004).

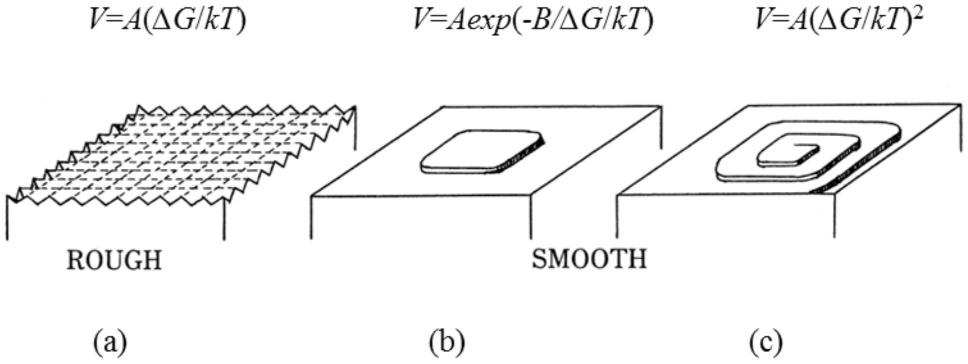

Figure 2.11 Interface structures and three types of growth mechanism. A and B are material dependent constant (Sunagawa, 1999).

2.1.5 Facet Crystal Growth

Fundamentally, facet crystal growth is a type of growth with relatively stronger growth anisotropy depending on the type of crystal structure (Sunagawa, 1999). Depending on the type of interface, generally three types of growth mechanisms can be presented, lateral growth (**Fig. 2.11a**), surface nucleation (**Fig. 2.11b**) and spiral growth (**Fig. 2.11c**). The growth rate (V) is determined by the type of interface, the growth mechanism and the driving force. Later, Sunawaga summarised the relationship between growth rate and the driving force as shown in **Fig. 2.12** (Sunagawa, 1990), suggesting that a rough surface requires larger driving force for the same growth velocity.

In most metallic systems, where interface attachment kinetic is negligible, the growth along preferable crystallographic orientation is understood to be initiated by the system to minimize the area of the surfaces with high surface energy (Dantzig and Rappaz, 2009). Although the growth mechanisms are essentially the same, growth directions of anisotropic crystal is more restricted compared with isotropic crystal. In order further understand the growth anisotropy, Bravais (Bravais, 1866) derived an empirical rule that crystal faces parallel to the net planes with higher reticular density (close-packed planes) develop faster on actual crystal than those with lower reticular densities. Consequently, as the anisotropy of the soli-liquid interface energy γ_{sl} increases, assuming that all other quantities remain the same, the dendrite will exhibit a sharper tip. When the anisotropy in γ_{sl}, is large enough, the dendrites exhibit a faceted morphology. The actual surface energy in an anisotropic crystal is given in the form,

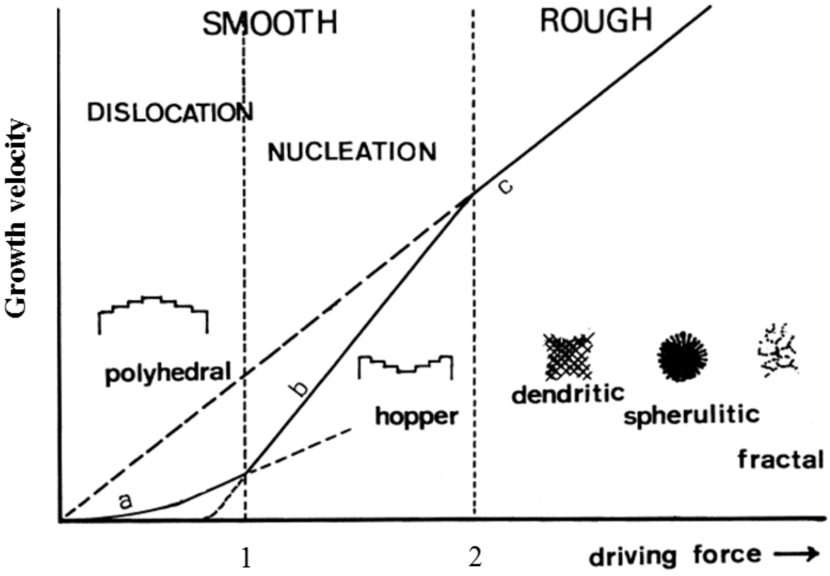

Figure 2.12 Schematic diagram showing the relations of crystal morphology, growth velocity and growth driving force (Sunagawa, 1990).

$$\gamma_{sl} = \gamma_{sl}[1 + \varepsilon_n(\cos(n\varphi)] \quad (2.20)$$

where φ is the azimuthal angle measured from a reference direction, ε_n refers to the strength of the anisotropy and n is the degree of symmetry. Basing on this understanding, the surface morphology can be reconstructed with Wulff construction principles (**Fig. 2.13)** using different level of anisotropy (Dantzig and Rappaz, 2009).

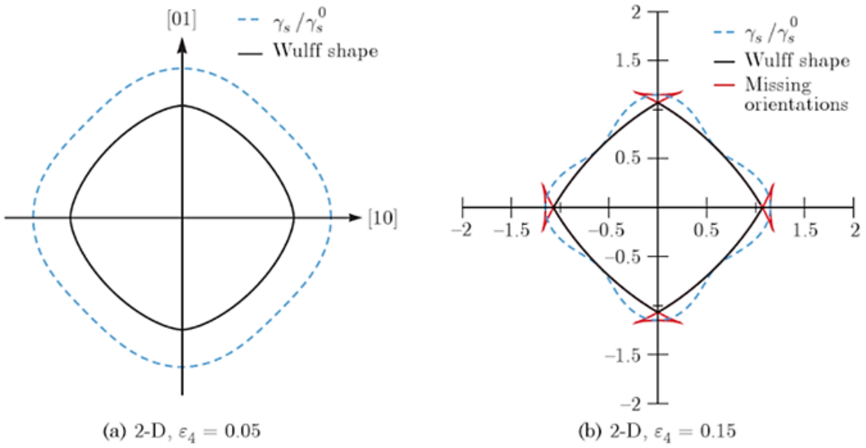

Figure 2.13 The equilibrium shape of fourfold symmetric 2-D crystal (a) ε=0.05 and (b) ε =0.15. The Wulff shap has been drawn inside of γ_{sl} for clarity (Dantzig and Rappaz, 2009).

2.1.6 Irregular Eutectic

When one of the two phases is faceted, the eutectic becomes irregular as the faceted phase is able to grow only along well-defined planes or/and directions (Dantzig and Rappaz, 2009). One faceted phase tends to grow along well-defined directions with the help of defects such as twins or screw dislocations. Therefore, the resultant eutectic structure is very complex and irregular, giving rise to an irregular eutectic morphology. A Schematic illustration of regular eutectic and irregular eutectic is shown in **Fig. 2.14**. The irregular eutectic can also develop instabilities along the edges of lamellae causing coarsening including remelting and ripping. A few defect-assisted mechanisms for the growth of irregular eutectic is explained in **Fig. 2.15**, such as the (0001) graphite flake developing a spiral defect along [10-10] direction (**Fig. 2.15a**) and twins-like flakes with a typical spacing of approximately 0.4-1μm under conventional casting (**Fig. 2.15b**). Other mechanisms are also observed where

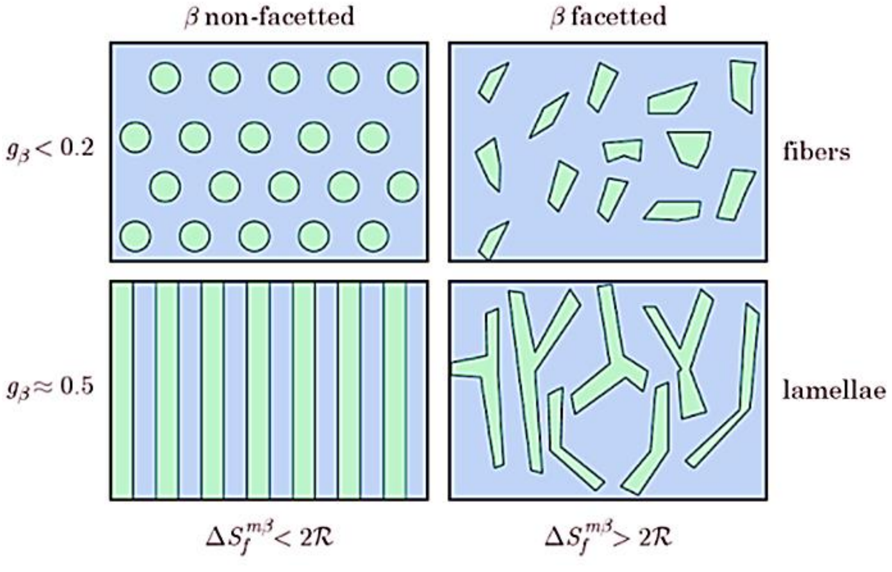

Figure 2.14 Eutectic interface morphologies that can be obtained when the α-phase is no-faceted and the β-phase is either non-faceted (left) or faceted (right). The eutectic is growing in a thermal gradient perpendicular to the page.

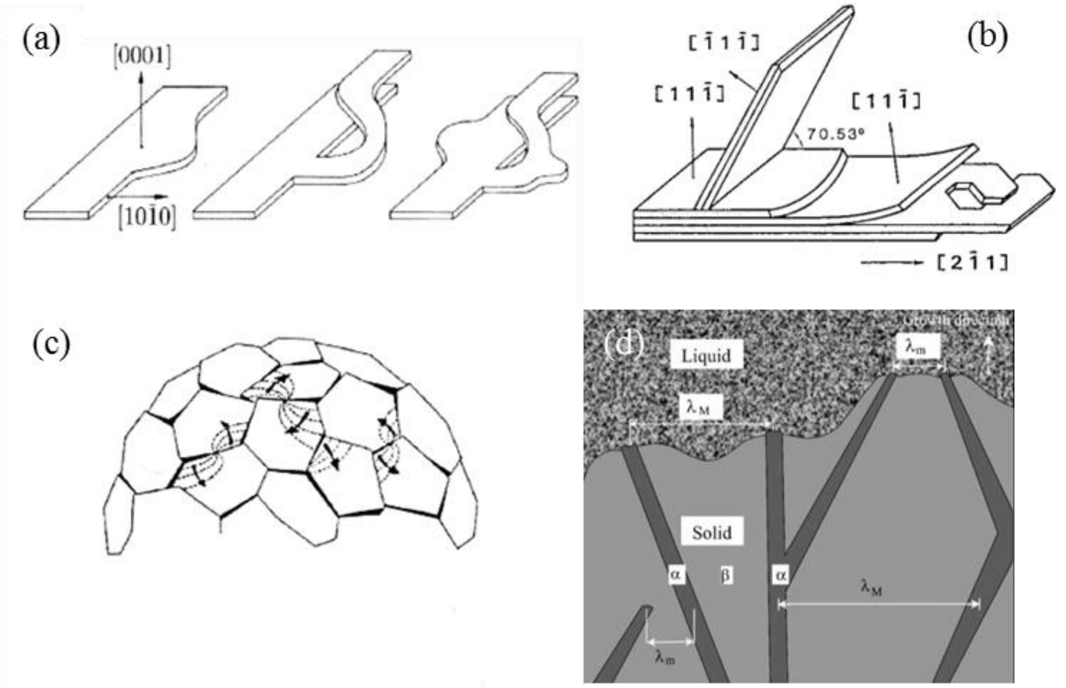

Figure 2.15 Possible irregular eutectic growth branching mechanism: (a) a rotational binary defect along [10-10] for Fe-C system (Minkoff, 1983); (b) twin formation in Al-Si (Lu and Hellawell, 1995); (c) screw dislocation growth mechanism for Ce-C nodular cast Fe (Double and Hellawell, 1995); and (d) schematic idealized irregular eutectic growth (Fisher and Kurz, 1980).

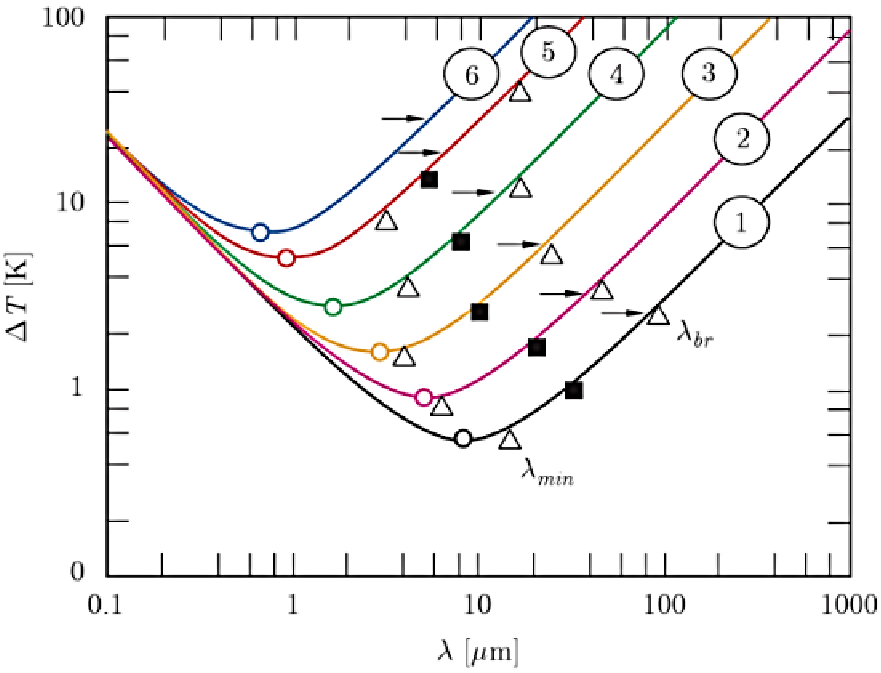

Figure 2.16 Minimum and maximum eutectic lamellar spacings (hollowed triangles) as well as average measured spacings (solid triangles)in Fe-C irregular eutectics under different growth conditions: (1) G=65K/cm, *v*=0.14μm/s, (2) G=69K/cm, *v*=1.11μm/s (3) G=72K/cm, *v*=3.47μm/s, (4) G=70K/cm, *v*=10.69μm/s (5) G=71K/cm, *v*=435.2μm/s. The measured undercooling is indicated by a solid arrow after (Jones and Kurz, 1981).

the faceted lamellar phase leading the eutectic morphology with the non-faceted phase surrounding them (**Fig. 2.15d**). Although these distributed flakes appears fairly randomly, they are interconnected in 3D and can usually be tracked back to a shared nucleation centre. The growth mechanisms of the faceted phase dominate the growth process in the irregular eutectics.

Fisher and Kurz (Fisher and Kurz, 1980) summarized that the faceted phase leads the eutectic reaction and is constrained to develop along the preferred crystallographic planes or orientations (**Fig. 2.15d**). As shown in **Fig. 2.16**, the relationship between the growth undercooling and irregular eutectic lamellar spacing are given (Dantzig and Rappaz, 2009):

$$\Delta T\bar{\lambda} = A_R(1 + \emptyset^2) \tag{2.21a}$$

$$\bar{\lambda}^2 v = \emptyset^2 \frac{A_R}{A_C} D_l \tag{2.21b}$$

where A_R and A_C are growth constant for eutectic and $\emptyset$ is the parameter that describes interface position.

2.2 Solidification Behaviour of Fe-rich Intermetallic Compounds

Fe is highly associated with the deterioration of the mechanical properties of Al alloys. It is a common impurity and unavoidably picked up during the fabrication and recycling process of Al alloys (Green, 2007). Due to the low solubility of Fe ranging from 0.052wt.% to 0.8wt.% (Phillips, 1959), the inevitable formation of the Fe-IMCs has become the main reason for deterioration of the mechanical properties of cast Al alloys (Mondolfo, 2013). There are two main approaches to eliminate the detrimental effect of Fe content in Al alloys. The first approach is the modification including nucleation enhancement (Que *et al.*, 2017; Khalifa *et al.*, 2005) and morphology modification etc. (Mondolfo, 2013; Zhang *et al.*, 2012). The second approach is the de-ironing which involves physical separation, such as gravity segregation filtration (de Moraes *et al.*, 2006) and EM separation etc. (Makarov, Apelian and Ludwig, 1998).

2.2.1 Fe-rich Intermetallic Compounds in Al Alloys.

In Al alloys, there is a range of Fe-IMCs including binary Al-Fe, ternary Al-Fe-Si and Al-Mn-Si and quaternary Al-Fe-Mn-Si intermetallic compounds etc. Binary Fe-IMCs have some variants including $Al_{13}Fe_4$ (Al_3Fe), Al_mFe ($x \approx 4.0$-4.4), Al_xFe ($x=4.5$-5.0) and Al_6Fe ($Al_6(Fe,Mn)$) (Allen *et al.*, 1998; Skjerpe, 1987; Couture, 1981); ternary Fe-IMCs have some variants including β-Al_5FeSi, α_h-Al_8Fe_2Si, γ-Al_3FeSi and δ-Al_4FeSi_2, α_c-AlMnSi (Khalifa, Samuel and Gruzleski, 2003; Stefaniay, Griger and Turmezey, 1987; Rivlin and Raynor, 1981); quaternary Fe-IMCs have some variants including α-AlFeMnSi ($Al_{12}(Fe,Mn)_3Si$ or $Al_{15}(Fe,Mn)_3Si_2$), α-Al (Fe,Mn,Cr)Si and π-$Al_8FeMg_3Si_6$ (Cao and Campbell, 2004; Davignon *et al.*, 1996; Narayanan, Samuel and Gruzleski, 1994; Barlock and Mondolfo, 1975). The crystal structure of commonly observed Fe-IMCs is given in **Table 2.1**.

Table 2.1 Common Fe-rich intermetallic compounds in Al alloy

Fe-IMC	**Bravais Lattice**	**Lattice parameters**	**Reference**
$Al_{13}Fe_4$, **Al_3Fe**	Monoclinic, C-centred monoclinic	a=1.549nm b=0.808nm c=1.248nm b=107.75˚	(Allen *et al.*, 1998; Skjerpe, 1987; Black, 1955)(Allen *et al.*, 1998; Skjerpe, 1987; Black, 1955)
Al_6Fe	Orthorhombic, C-centred orthorhombic	a=0.649nm b=0.744nm c=0.879nm	(Young and Clyne, 1981; Hughes and Jones, 1976; Jones, 1969)
Al_mFe	Body-centred tetragonal	a=0.884nm b=c=2.16nm	(Skjerpe, 1988; Skjerpe, 1987; Young and Clyne, 1981)
β-Al_5FeSi	Monoclinic	a=0.612nm b=0.612nm c=4.150nm β=91.0˚	(Rømming, Hansen and Gjønnes, 1994; Skjerpe, 1987; Rivlin and Raynor, 1981)
α_h-Al_8Fe_2Si	Hexagonal	a=1.23nm c=2.62nm	(Stefaniay, Griger and Turmezey, 1987; Munson, 1967; Sun and Mondolfo, 1967)
α_c-AlMnSi	Primitive cubic	a=1.268nm	(Kim *et al.*, 2006; Cooper and Robinson, 1966)
α_c-AlFeSi	Body-centred cubic, Primitive cubic	a=1.256nm a=12.56nm	(Kral, 2005; Stefaniay, Griger and Turmezey, 1987; Cooper, 1967; Munson, 1967)
γ-Al_3FeSi	C-centred monoclinic	a= 1.780nm b=1.025nm c=0.890 β=132.0˚	(Skjerpe, 1987; Munson, 1967)
δ-Al_4FeSi_2	Tetragonal	a=0.614nm b=0.948nm	(Rivlin and Raynor, 1981; Phragmén, 1950)
α-Al(FeMn)Si, **α-Al(FeMnCr)Si**	Body-centred cubic, Primitive cubic	a=1.256nm a=1.256nm	(Hwang, Doty and Kaufman, 2008; Kim *et al.*, 2006; Kral, 2005; Donnadieu, Lapasset and Sanders, 1994)
π-$Al_8FeMg_3Si_6$	Hexagonal	a=0.664nm c=0.794nm	(Kuijpers *et al.*, 2005; Foss *et al.*, 2003; Sha *et al.*, 2001)

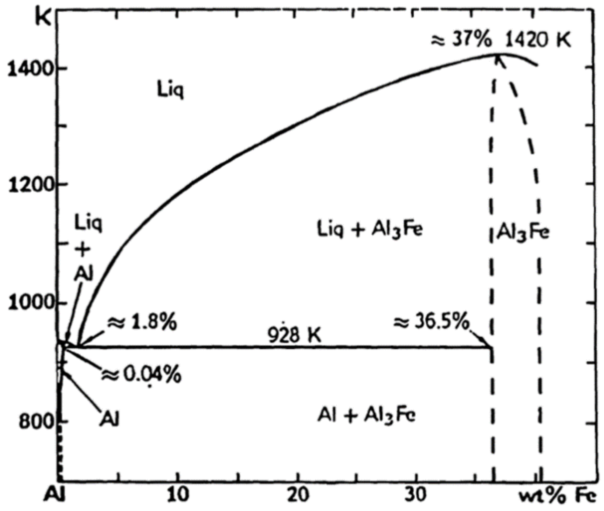

Figure 2.17 Al corner of equilibrium Al-Fe binary phase diagram (Allen *et al.*, 1998).

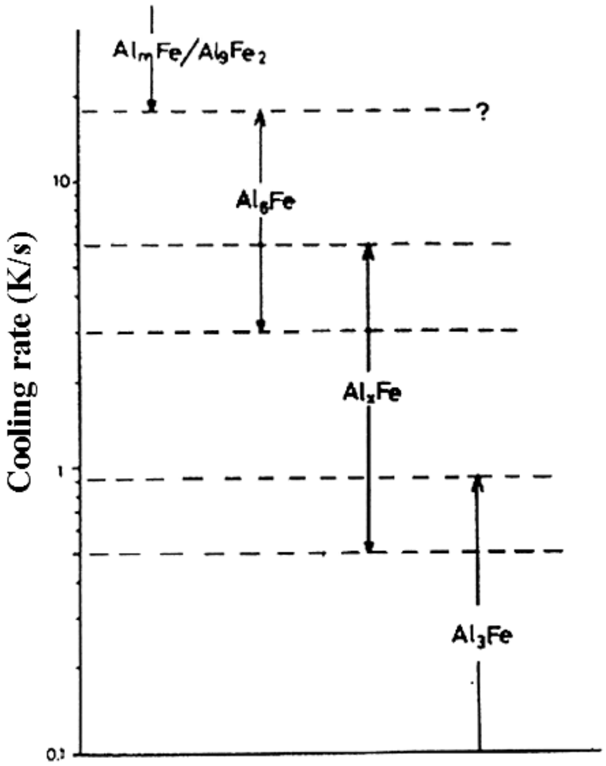

Figure 2.18 Effect of cooling rate on formation of Al-Fe eutectic in Al-Fe alloys (Young and Clyne, 1981).

2.2.1.1 Binary Compounds

Binary Fe-IMCs mainly consist of Al and Fe, and some found to contain trace Si contents (Mondolfo, 2013). The maximum equilibrium solid solubility of Si in Al is higher at ~1.6wt.% (Murray and McAlister, 1984), and low levels (~0.1-0.2 wt.%) of Si is readily accommodated by dissolution in the Al matrix and in the Al-Fe.

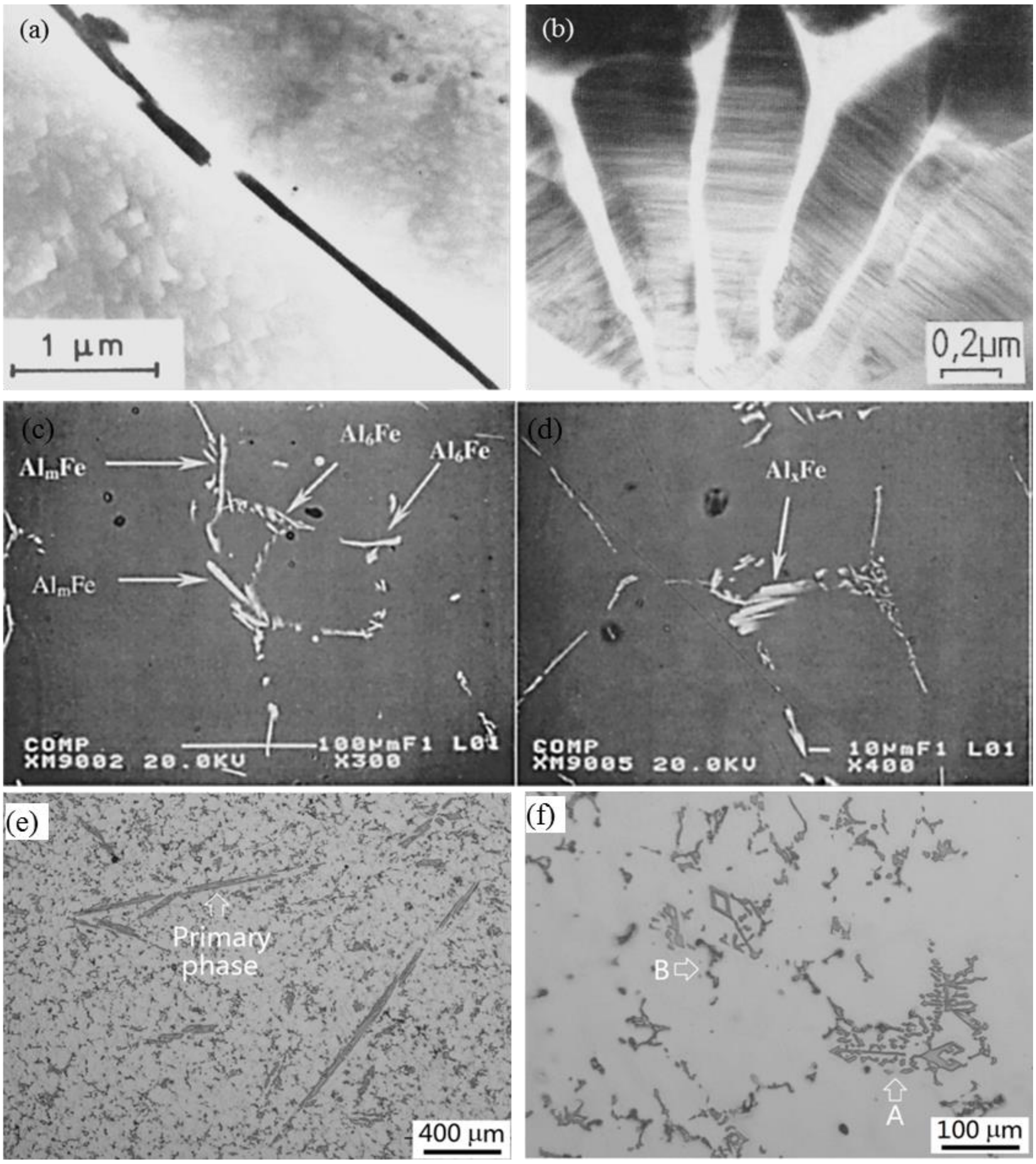

Figure 2.19 Morphologies of binary Al-Fe intermetallic compounds including (a) $Al_{13}Fe_4$ at grain boundaries in cast ingot (Skjerpe, 1987), (b) branched dendritic $Al_{13}Fe_4$ particle (Kim and Cantor, 1994), (c) Al_mFe ($m \approx 4.0$-4.4) eutectic (Khalifa, Samuel and Gruzleski, 2003); (d) Al_xFe ($x \approx 4.5$-5.0) under cooling rate of 0.15K/s (Khalifa, Samuel and Gruzleski, 2003); (e) rod-like primary $Al_6(Fe,Mn)$ and (f) duplex (marked “A”) primary/eutectic $Al_6(Fe,Mn)$ (Liu *et al.*, 2016).

Consequently, the phase contents of cast Al-Fe and Al-Fe-Si alloys with low Si concentration (≤0.1wt.%) are similar, although in the latter case the so called "binary" Fe aluminides often contain dissolved Si (Allen *et al.*, 1998). As shown in Al-Fe binary phase diagram (**Fig. 2.17**), $Al_{13}Fe_4$, also designated as Al_3Fe, is the first intermetallic phase to form on solidification of dilute Al-Fe alloys.

The fully eutectic microstructures could be attained in rapidly cooled alloys with Fe content in excess of that of the equilibrium eutectic, 1.8wt.% (**Fig. 2.17**). The transformation of binary Fe-IMCs is dependent mainly on the cooling rate (**Fig. 2.18**) when there is no additional nucleation substrate (Young and Clyne, 1981). Under non-equilibrium solidification conditions a range of thermodynamically metastable Al_6Fe eutectic phases that have smaller undercooling for the nucleation and growth than α-Al/$Al_{13}Fe_4$ forms (Skjerpe, 1987). Moreover, the typical microstructure, precipitate morphologies and Fe content of Al_6Fe and $Al_{13}Fe_4$ are very similar (**Fig. 2.10**). Al_6Fe is also an important phase in Mn-containing alloys. Al_6Mn and Al_6Fe are isomorphs, and consequently Mn can substitute freely for Fe in the Al_6Fe lattice to become more stable by lowering its energy. This raises the thermodynamic stability of the Al_6Fe phase in Mn containing Al alloys. This type of compound is often denoted as $Al_6(Fe,Mn)$ (Alexander and Greer, 2004; Couture, 1981). The morphologies of binary Al-Fe IMCs in hypereutectic and hypoeutectic alloy are shown in **Fig. 2.19a-d** and **Fig. 2.19e-f**, respectively.

2.2.1.2 Ternary Compounds

Three ternary phases form under equilibrium solidification conditions in dilute Al-Fe-Si alloys with sufficiently high Si content (>0.1wt.% Si in ≤0.2wt.% Fe containing alloys, and >0.2wt.% Si in ≤0.3-0.4wt.% Fe containing alloys). **Fig. 2.20** shows the liquidus projection and associated equilibrium solidification reactions in the Al corner of the Al-Fe-Si ternary phase diagram.

The chemical compositions of common ternary Fe-IMCs are shown in **Fig. 2.21**. The three equilibrium ternary phases are produced by one of the two ternary peritectic reactions followed by a ternary eutectic reaction are (Allen *et al.*, 1998):

R1: Liquid + $Al_{13}Fe_4 \rightarrow Al + Al_8Fe_2Si$ (also denoted as the α phase);

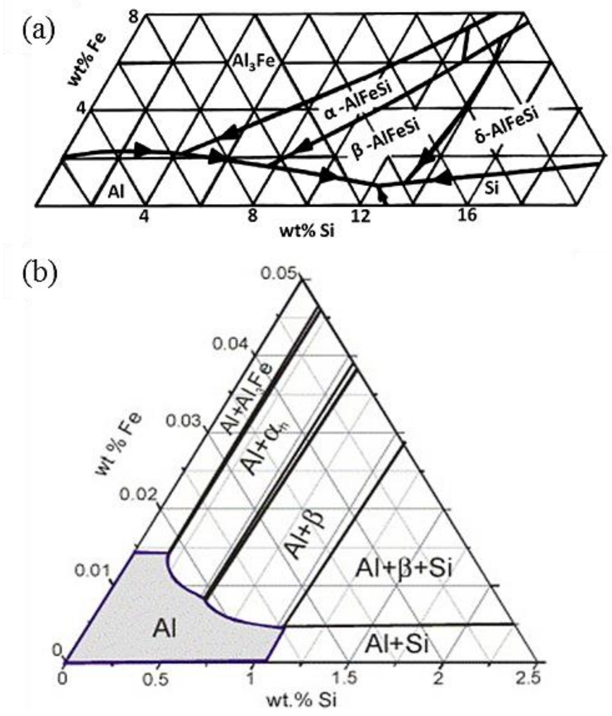

Figure 2.20 (a) Liquid projection of Al corner of the Al–Fe–Si phase diagram showing Al solidification path (Skjerpe, 1987); (b) Al corner of the calculated Al–Fe–Si phase diagram at the isotherm of 540˚C (Kuijpers *et al.*, 2005).

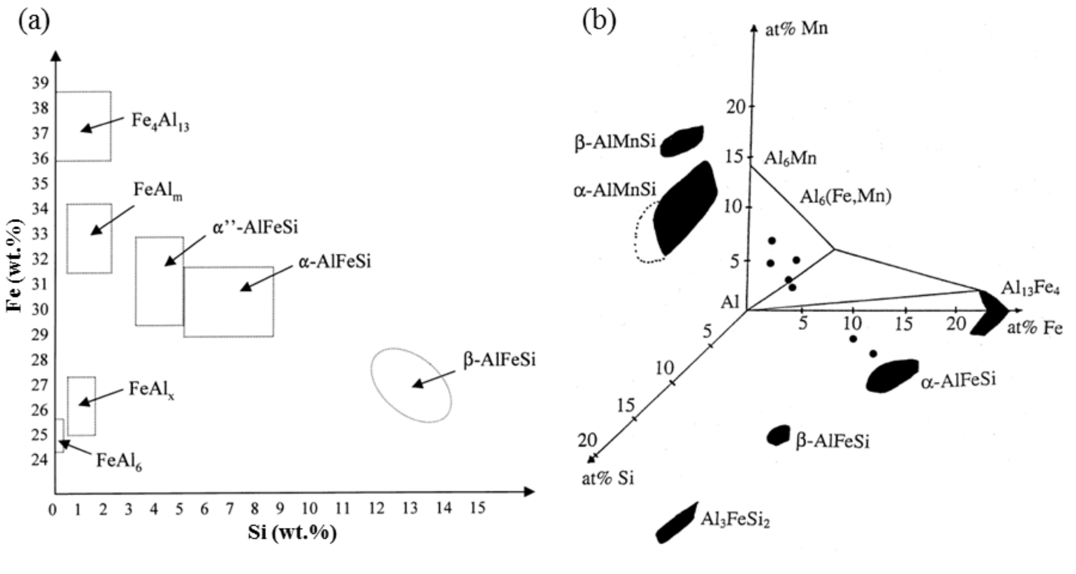

Figure 2.21 Phase maps of (a) Al-Fe-Si system (Langsrud, 1990) and (b) Al-Fe-Mn-Si system (Davignon *et al.*, 1996).

R2: Liquid + Al_8Fe_2Si → Al + Al_5FeSi (also denoted as the β phase); and/or

R3: Liquid → Al + Si + Al_5FeSi

The α-AlFeSi is identified most commonly as α_h-Al_8Fe_2Si (Munson, 1967), α_c-$Al_{12}Fe_3Si_2$ (Mondolfo, 2013), α_c-$Al_{15}Fe_3Si_2$ (Crepeau, 1995) or generally α-AlFeSi (Liu and Dunlop, 1986). There is a contradiction about the structure of the α-phase. Skjerpe showed the α-phase is body-centred cubic and Cooper described it as $Al_{19}Fe_4MnSi_2$, with the space group Im3, and a= 1.256nm (Stefaniay, Griger and Turmezey, 1987; Cooper, 1967). Kral demonstrated subsequently it to be $Al_{19}(FeMn)_5Si_2$ with space group Im-3 and a=1.256nm (Kral, 2005; Kral, McIntyre and Smillie, 2004). However in some other work, the structure of the α-phase was reported as hexagonal which is denoted as α_h (Mondolfo, 2013; Barlock and Mondolfo, 1975). The α-phase has a compact morphology such as Chinese-script structure (shown in **Fig. 2.22a**, **c** and **d**).

The platelet β-AlFeSi is usually identified as β-Al_5FeSi (Rivlin and Raynor, 1981), $Al_9Fe_2Si_2$ (Ferdian *et al.*, 2015) or generally β-AlFeSi (Rømming, Hansen and Gjønnes, 1994). There is also conflicting views on the structure of β-phase which is accepted to be monoclinic by many researchers (Mondolfo, 2013; Murali, Raman and Murthy, 1995). Murali and co-workers showed that β-Al_5FeSi is monoclinic with lattice parameters of a=0.5792nm, b=1.227nm, c=4.313nm, and β=98.93° (Murali, Raman and Murthy, 1995). However, Carpenter claimed that β-phase was B-face centred orthorhombic with a=0.6184nm, b=0.6250nm, and c=2.069nm (Carpenter and Le Page, 1993). Zheng and co-workers observed that the β-phase was orthorhombic with a=0.618nm, b=0.620nm, and c=2.08nm (Zheng, Vincent and Steeds, 2000). Kral claimed the β-phase was consistent with tetragonal $Al_3(Fe,Mn)Si_2$ with space group I4mcm, a=0.607nm and c=0.950nm (Kral, McIntyre and Smillie, 2004).

Among all these ternary Fe-IMCs, β-AlFeSi is thought to be the most detrimental to the properties of Al alloys, and significant efforts have been devoted to avoid the formation of β-AlFeSi. β-AlFeSi has undesirable platelet morphology as shown in **Fig. 2.22b, e-f**, is brittle in nature and generally act as a stress concentrator and point of weak coherence (Taylor, 2012; Lu and Dahle, 2005). Usually, higher Fe content

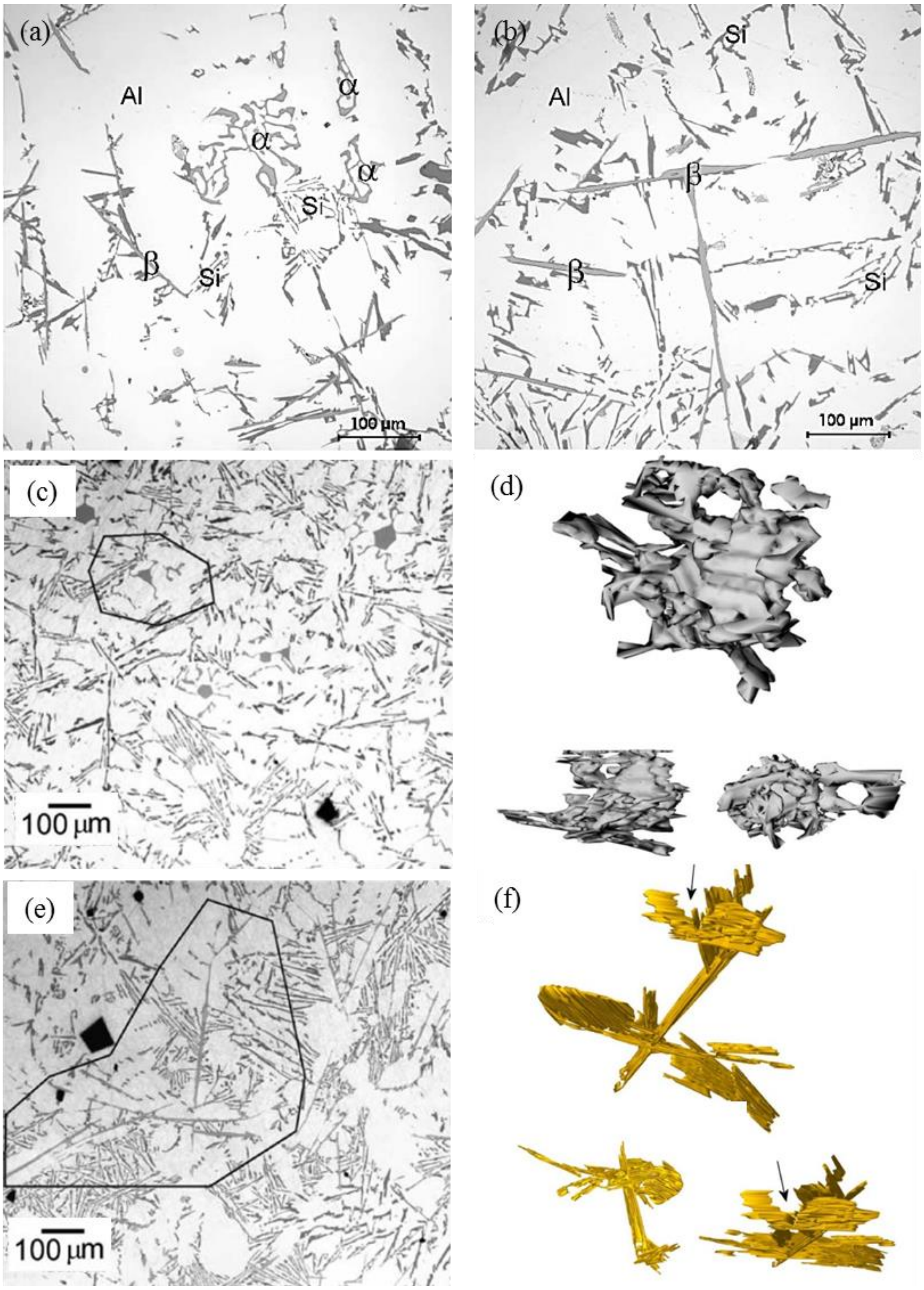

Figure 2.22 Micrographs showing (a) typical Chinese-script morphology of α-$Al_{15}(FeMn)_3Si_2$ phase (Lu and Dahle, 2005), (b) typical plate-like morphology of β-Al_5FeSi (Lu and Dahle, 2005), (c) primary/eutectic structure of α-AlFeSi (outlined area), (d) 3D morphology of α-AlFeSi shown for three orientations from the corresponding area in (c) (Dinnis, Taylor and Dahle, 2005), (e) β-AlFeSi (outlined area), (f) 3D morphology of α-AlFeSi shown in three orientations from the corresponding area in (e) (Dinnis, Taylor and Dahle, 2005).

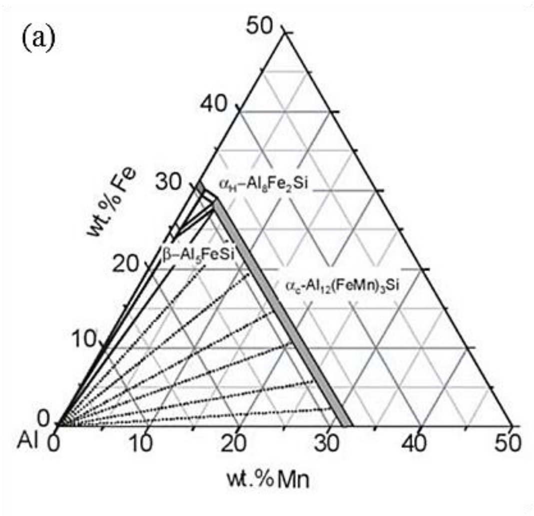

Figure 2.23 (a) Projections of the Al–Fe–Mn–0.5Si phase diagram onto the Al–Mn–Fe plane and (b) Al corner of the Al-Fe-Mn-0.5Si phase diagram at the isothermal of 540˚C (Kuijpers *et al.*, 2005).

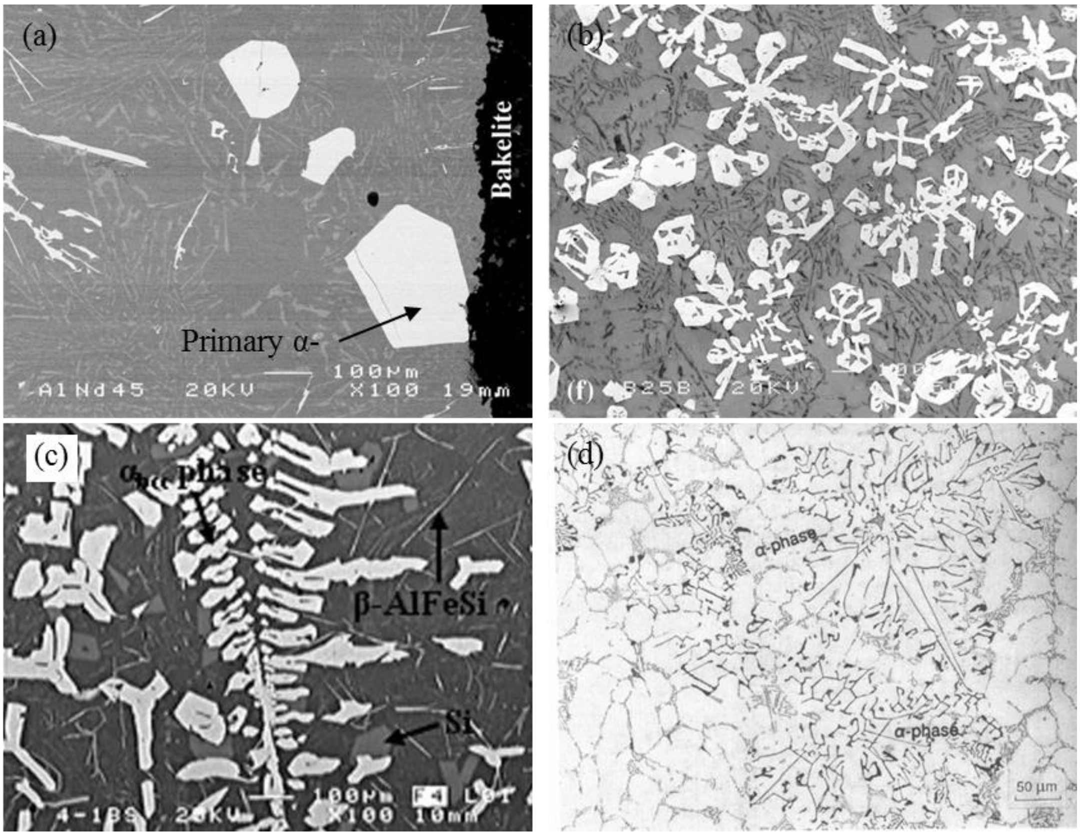

Figure 2.24 The Morphologies of α-AlFeMnSi: (a) polyhedral (Cao, Saunders and Campbell, 2004) (b) cross-like (Cao, Saunders and Campbell, 2004), (c) dendritic (Gao *et al.*, 2013; Orozco-González *et al.*, 2011) and (d) Chinese-script (Tash *et al.*, 2007; Narayanan, Samuel and Gruzleski, 1994).

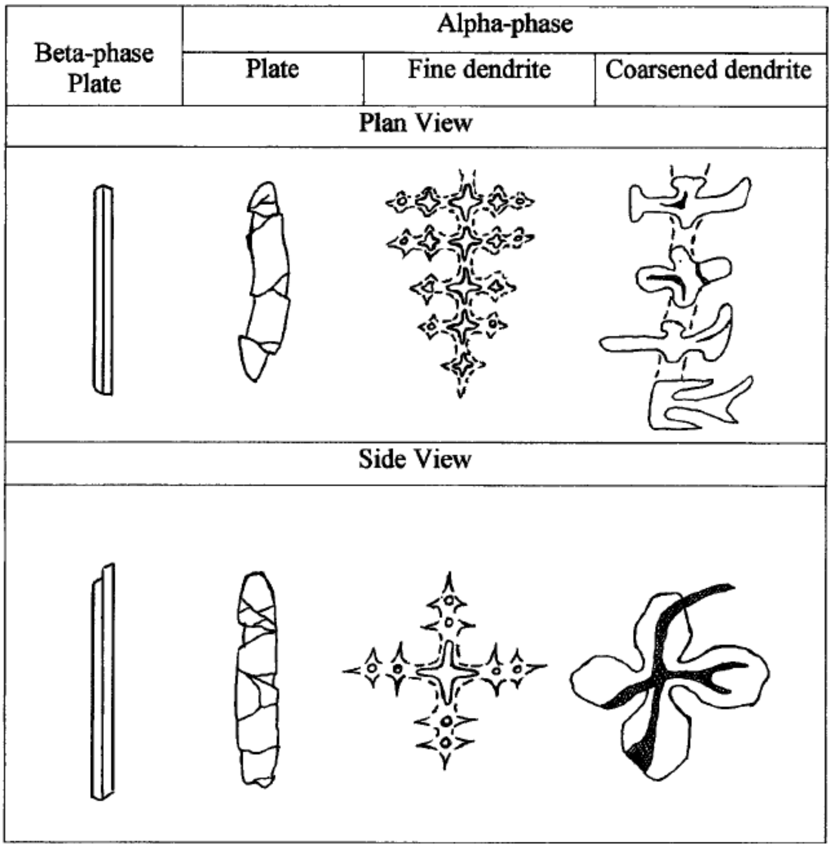

Figure 2.25 A summary of the morphologies of β- and α- Fe-IMCs when viewed in 2D sections from the longitudinal (plane view) and cross orientations (side view) (Shabestari *et al.*, 2002).

and slow cooling rate result in increasing the size of β- platelets (Tang and Sritharan, 1998).

The domination of β-AlFeSi platelet results in severe loss of strength and ductility in Al-Si cast alloys. It is noted that α- and β- Fe-IMCs may not exhibit the dendrite or platelet shape, respectively; and thus difficult to be identified by their morphology, especially when the alloys are at eutectic composition or are modified through Na or Sr additions (Fatahalla, Hafiz and Abdulkhalek, 1999).

2.2.1.3 Quaternary Compounds

As shown in **Fig. 2.23**, when Fe content in the Al-Si alloy system is above 0.15wt.%, plate-like β-Al_5FeSi is likely to form. Mn is commonly introduced to the alloy system to supress the formation of β-Al_5FeSi (Rana, Purohit and Das, 2012; Zhang *et al.*, 2012). The equilibrium phase diagram in **Fig. 2.23** shows the possible phase transformations to α-AlFeMnSi. In previous research, Mn was used as a positive modifier to suppress the formation of the coarse primary β-phase and promote the formation of less harmful α-phase in Al alloys (Ji *et al.*, 2013b; Tash *et al.*, 2007; Shabestari and Shahri, 2004). The result achieved by Abedi and co-workers shows that the volume fraction of different kinds of frequently α-phase (polyhedral, star-like and Chinese script) in specimens with various Mn:Fe ratios (Abedi and Emamy, 2010). α-AlFeMnSi was observed with different morphologies including polyhedral (**Fig. 2.24a**), cross-like (**Fig. 2.24b**), dendritic (**Fig. 2.24c**) and Chinese-script (**Fig. 2.24d**). Shabestari proposed a 3D morphology of β-AlFeSi and α-AlFeMnSi (**Fig. 2.25**) to explain differences observed in 2D observations (Shabestari *et al.*, 2002), suggesting that sectioning orientation of a integrate Fe-IMC particle is the main cause for the morphology variation by 2D observation.

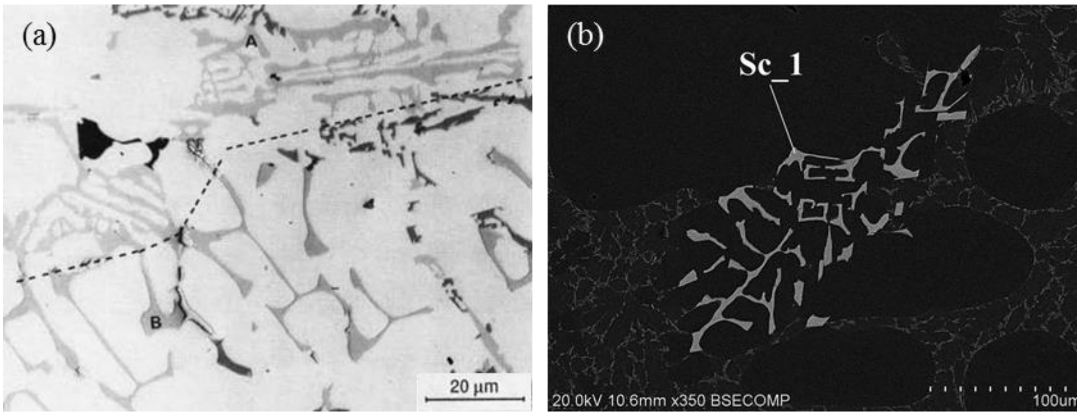

Figure 2.26 (a) Transformation of β-Al_5FeSi needles into π-$Al_8FeMg_3Si_6$ Chinese script (marked A) in A319.1 alloy containing 0.5wt% Mg with the dash lie separating π-$Al_8FeMg_3Si_6$ and α-AlFeMnSi (marked B)(Samuel and Samuel, 1997); (b) the morphology of Sc_1 (Sc rich intermetallic compound) (Chanyathunyaroj *et al.*, 2017).

Mg, Sc and Cr are often introduced to Al cast alloys to improve the mechanical properties, which changes the nucleation and growth behaviour of α-AlFeMnSi in Al alloys (Patakham and Limmaneevichitr, 2014; Shabestari, Keshavarz and Hejazi, 2009; Shabestari *et al.*, 2002; Shabestari *et al.*, 2002; Wang and Davidson, 2001; Samuel *et al.*, 1998; Samuel and Samuel, 1997; Narayanan, Samuel and Gruzleski, 1994). The Mg, Sc and Cr addition can result in the formation of π-$Al_8FeMg_3Si_6$ (**Fig. 2.26a**), a Sc-rich intermetallic compound (**Fig. 2.26b**) and α-Al(Fe,Mn,Cr)Si (almost identical morphology with α-AlFeMnSi), respectively. π-$Al_8FeMg_3Si_6$ and Sc-rich intermetallic compounds are equilibrium phases when there is minor amount of quaternary element (<0.5wt.%) in the alloy. Although, the increase in Mg is very likely to result in the formation of Mg_2Si depending on the alloy system (Salleh, Omar and Syarif, 2015; Samuel *et al.*, 1998). Cr is one of the Fe equivalent elements along with Mn (Kaye and Street, 2016; Cao and Campbell, 2000). Using the iron equivalent value (IEV) function (Kaye and Street, 2016): Fe + 2Mn + 3Cr (in wt.%), the amount of α- Fe-IMCs and the gravity segregation of primary α- Fe-IMCs can be estimated (Cao, Saunders and Campbell, 2004; Cao and Campbell, 2000).

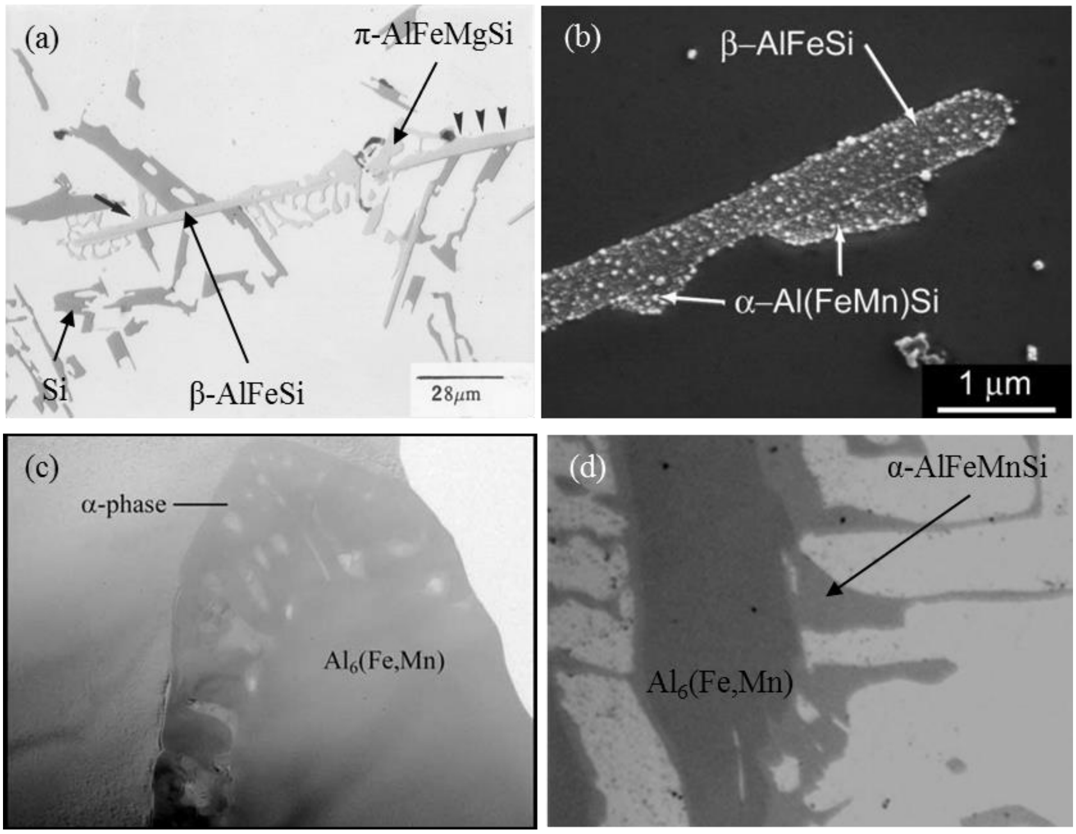

Figure 2.27 Micrograph of (a) β-Al_5FeSi to π-$Al_8FeMg_3Si_6$ transformation (Samuel *et al.*, 1998), (b) β-Al_5FeSi to α-AlFeMnSi transformation (Kuijpers *et al.*, 2003), (c) Al_6(Fe,Mn) to α-AlFeMnSi eutectoid transformation (Alexander and Greer, 2002) and (d) Al_6(Fe,Mn) to α-AlFeMnSi peritectic transformation (Warmuzek, Rabczak and Sieniawski, 2005).

2.2.2. Nucleation for Fe-rich Intermetallic Compounds.

Nucleation of Fe-IMCs is reported on two types of substrates. One is the existing phases including α-Al (Puncreobutr *et al.*, 2014) and Fe-IMCs (Kuijpers *et al.*, 2003; Alexander and Greer, 2002; Samuel *et al.*, 1998). The other is inclusions or in-situ particles (Terzi *et al.*, 2010; Miller, Lu and Dahle, 2006; Cao and Campbell, 2003; Allen *et al.*, 1999; Allen *et al.*, 1998; Narayanan, Samuel and Gruzleski, 1994). As shown in **Fig. 2.27**, Commonly observed Fe-IMC to Fe-IMC transformations are summarized as follow: β-Al_5FeSi → π-$Al_8FeMg_3Si_6$ (Samuel *et al.*, 1998), β-Al_5FeSi → α-AlFeMnSi (Kuijpers *et al.*, 2003) and Al_6(Fe,Mn) → α-AlFeMnSi (Warmuzek, Rabczak and Sieniawski, 2005; Alexander and Greer, 2002). Recently, X-ray based techniques are used to investigate Fe-IMCs including nucleation mechanism and morphology evolution (Puncreobutr *et al.*, 2014; Terzi *et al.*, 2010). As shown in **Fig. 2.28**, with the exception of self-nucleation (on existing Fe-IMCs) the β-Al_5FeSi was observed to initiate on the α-Al dendrite by Puncreobutr (Puncreobutr *et al.*, 2014).

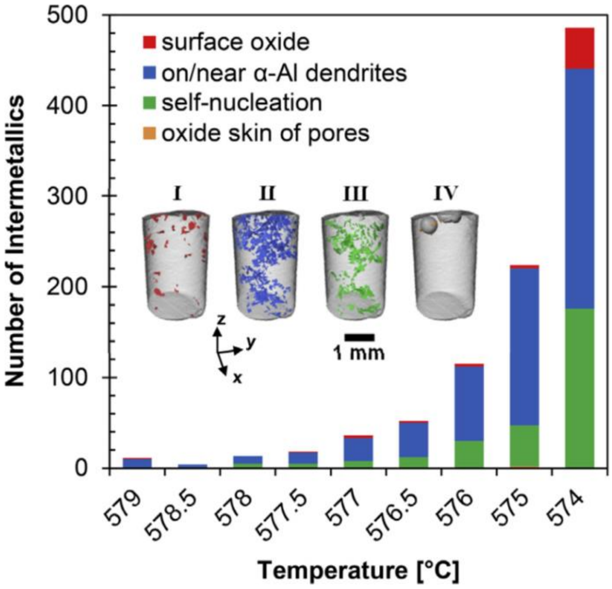

Figure 2.28 Quantified β-intermetallic compound nucleation rates, as classified by the four types of nucleation sites. Insets "I–IV" illustrate intermetallic compounds that were nucleated on the surface oxide, on/near the α-Al dendrites, on existing intermetallic compounds (self-nucleation) and on the oxide skin of pores, respectively. Note that each intermetallic compound is rendered as it first appeared in the specimen (Puncreobutr *et al.*, 2014).

The inclusion particles, such as oxides (Puncreobutr *et al.*, 2014; Miller, Lu and Dahle, 2006; Cao and Campbell, 2003) and TiB_2 (Khalifa *et al.*, 2005; Allen *et al.*, 1999; Allen *et al.*, 1998), are reported to encourage the nucleation of Fe-IMCs. To enhance a heterogeneous nucleation event, the substrate is required to be wetted and potent (good misfit/ lattice mismatching). The crystal structure of some aluminium or magnesium oxides is described in **Table 2.2**. Some oxides including MgO, γ-Al_2O_3

and $MgAl_2O_4$ have a relatively small lattice misfit with α-AlFeMnSi and easily can form and wet in Al alloys. Observation and analysis of the crack-like defects (**Fig. 2.29a**, **c** and **d**) within these Fe-IMCs was confirmed. This shows that physical

Table 2.2 Crystal structures of some aluminium or magnesium oxides (Cao and Campbell, 2003).

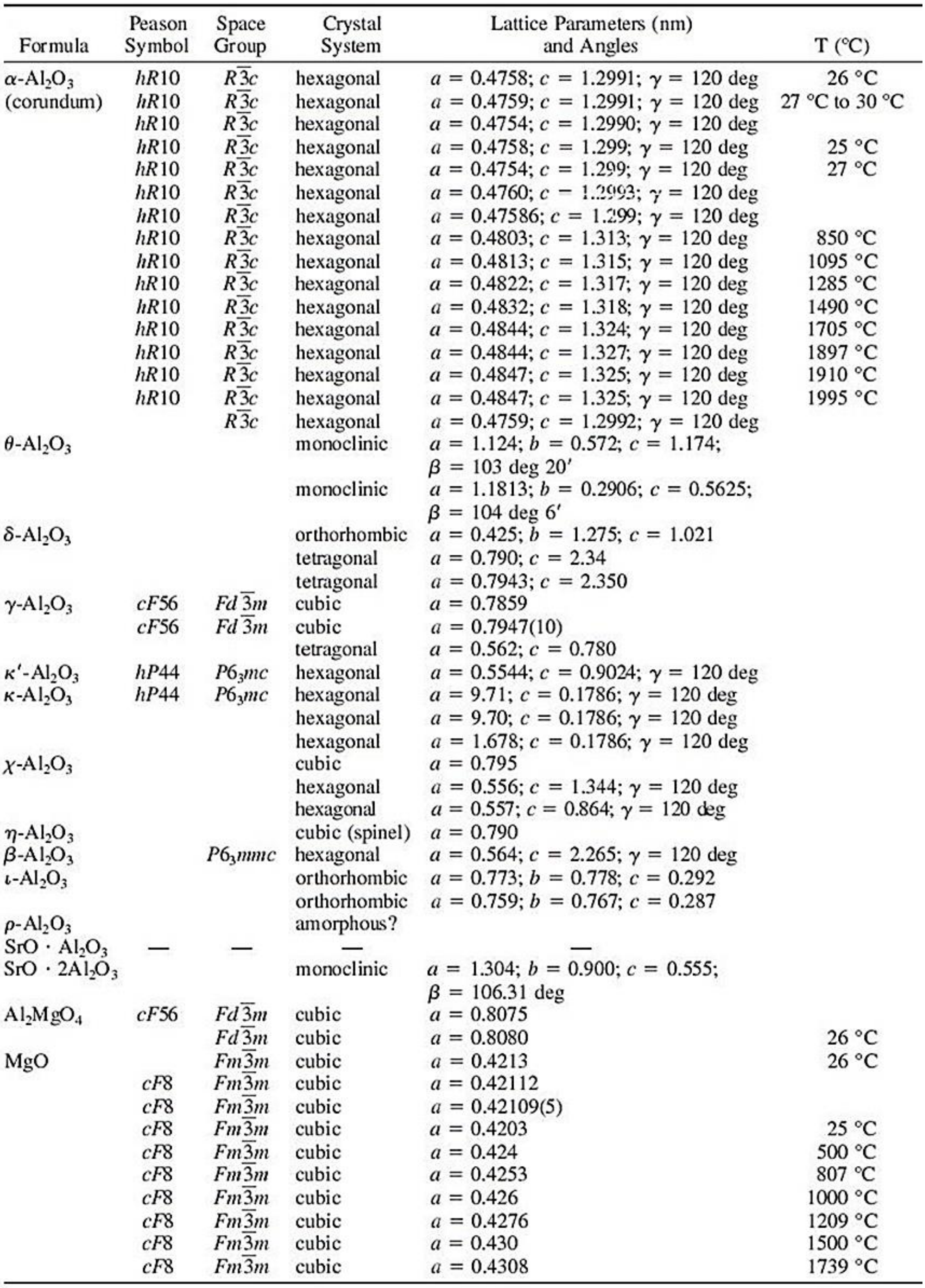

Formula	Peason Symbol	Space Group	Crystal System	Lattice Parameters (nm) and Angles	T (°C)
α-Al_2O_3	$hR10$	$R\bar{3}c$	hexagonal	$a = 0.4758$; $c = 1.2991$; $\gamma = 120$ deg	26 °C
(corundum)	$hR10$	$R\bar{3}c$	hexagonal	$a = 0.4759$; $c = 1.2991$; $\gamma = 120$ deg	27 °C to 30 °C
	$hR10$	$R\bar{3}c$	hexagonal	$a = 0.4754$; $c = 1.2990$; $\gamma = 120$ deg	
	$hR10$	$R\bar{3}c$	hexagonal	$a = 0.4758$; $c = 1.299$; $\gamma = 120$ deg	25 °C
	$hR10$	$R\bar{3}c$	hexagonal	$a = 0.4754$; $c = 1.299$; $\gamma = 120$ deg	27 °C
	$hR10$	$R\bar{3}c$	hexagonal	$a = 0.4760$; $c = 1.2993$; $\gamma = 120$ deg	
	$hR10$	$R\bar{3}c$	hexagonal	$a = 0.47586$; $c = 1.299$; $\gamma = 120$ deg	
	$hR10$	$R\bar{3}c$	hexagonal	$a = 0.4803$; $c = 1.313$; $\gamma = 120$ deg	850 °C
	$hR10$	$R\bar{3}c$	hexagonal	$a = 0.4813$; $c = 1.315$; $\gamma = 120$ deg	1095 °C
	$hR10$	$R\bar{3}c$	hexagonal	$a = 0.4822$; $c = 1.317$; $\gamma = 120$ deg	1285 °C
	$hR10$	$R\bar{3}c$	hexagonal	$a = 0.4832$; $c = 1.318$; $\gamma = 120$ deg	1490 °C
	$hR10$	$R\bar{3}c$	hexagonal	$a = 0.4844$; $c = 1.324$; $\gamma = 120$ deg	1705 °C
	$hR10$	$R\bar{3}c$	hexagonal	$a = 0.4844$; $c = 1.327$; $\gamma = 120$ deg	1897 °C
	$hR10$	$R\bar{3}c$	hexagonal	$a = 0.4847$; $c = 1.325$; $\gamma = 120$ deg	1910 °C
	$hR10$	$R\bar{3}c$	hexagonal	$a = 0.4847$; $c = 1.325$; $\gamma = 120$ deg	1995 °C
		$R\bar{3}c$	hexagonal	$a = 0.4759$; $c = 1.2992$; $\gamma = 120$ deg	
θ-Al_2O_3			monoclinic	$a = 1.124$; $b = 0.572$; $c = 1.174$; $\beta = 103$ deg 20′	
			monoclinic	$a = 1.1813$; $b = 0.2906$; $c = 0.5625$; $\beta = 104$ deg 6′	
δ-Al_2O_3			orthorhombic	$a = 0.425$; $b = 1.275$; $c = 1.021$	
			tetragonal	$a = 0.790$; $c = 2.34$	
			tetragonal	$a = 0.7943$; $c = 2.350$	
γ-Al_2O_3	$cF56$	$Fd\bar{3}m$	cubic	$a = 0.7859$	
	$cF56$	$Fd\bar{3}m$	cubic	$a = 0.7947(10)$	
			tetragonal	$a = 0.562$; $c = 0.780$	
κ'-Al_2O_3	$hP44$	$P6_3mc$	hexagonal	$a = 0.5544$; $c = 0.9024$; $\gamma = 120$ deg	
κ-Al_2O_3	$hP44$	$P6_3mc$	hexagonal	$a = 9.71$; $c = 0.1786$; $\gamma = 120$ deg	
			hexagonal	$a = 9.70$; $c = 0.1786$; $\gamma = 120$ deg	
			hexagonal	$a = 1.678$; $c = 0.1786$; $\gamma = 120$ deg	
χ-Al_2O_3			cubic	$a = 0.795$	
			hexagonal	$a = 0.556$; $c = 1.344$; $\gamma = 120$ deg	
			hexagonal	$a = 0.557$; $c = 0.864$; $\gamma = 120$ deg	
η-Al_2O_3			cubic (spinel)	$a = 0.790$	
β-Al_2O_3		$P6_3mmc$	hexagonal	$a = 0.564$; $c = 2.265$; $\gamma = 120$ deg	
ι-Al_2O_3			orthorhombic	$a = 0.773$; $b = 0.778$; $c = 0.292$	
			orthorhombic	$a = 0.759$; $b = 0.767$; $c = 0.287$	
ρ-Al_2O_3			amorphous?		
$SrO \cdot Al_2O_3$	—	—	—	—	
$SrO \cdot 2Al_2O_3$			monoclinic	$a = 1.304$; $b = 0.900$; $c = 0.555$; $\beta = 106.31$ deg	
Al_2MgO_4	$cF56$	$Fd\bar{3}m$	cubic	$a = 0.8075$	
		$Fd\bar{3}m$	cubic	$a = 0.8080$	26 °C
MgO		$Fm\bar{3}m$	cubic	$a = 0.4213$	26 °C
	$cF8$	$Fm\bar{3}m$	cubic	$a = 0.42112$	
	$cF8$	$Fm\bar{3}m$	cubic	$a = 0.42109(5)$	
	$cF8$	$Fm\bar{3}m$	cubic	$a = 0.4203$	25 °C
	$cF8$	$Fm\bar{3}m$	cubic	$a = 0.424$	500 °C
	$cF8$	$Fm\bar{3}m$	cubic	$a = 0.4253$	807 °C
	$cF8$	$Fm\bar{3}m$	cubic	$a = 0.426$	1000 °C
	$cF8$	$Fm\bar{3}m$	cubic	$a = 0.4276$	1209 °C
	$cF8$	$Fm\bar{3}m$	cubic	$a = 0.430$	1500 °C
	$cF8$	$Fm\bar{3}m$	cubic	$a = 0.4308$	1739 °C

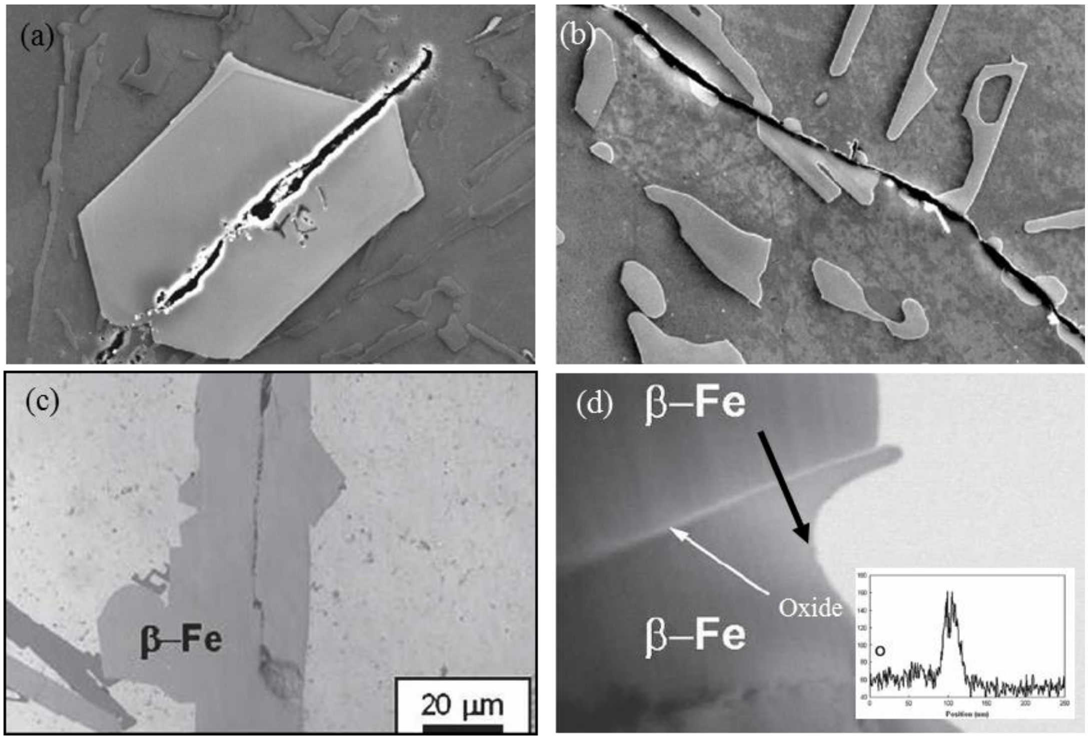

Figure 2.29 Micrographs showing (a) oxide double-film within the primary α-AlFeMnSi (Cao and Campbell, 2003), (b) crack penetrate through eutectic α-AlFeMnSi/α-Al (Cao and Campbell, 2003), (c) crack penetrate through primary β-Al_5FeSi (Miller, Lu and Dahle, 2006) and (d) oxide layer within β-Al_5FeSi inserted with EDS peaks of oxygen corresponding to dark arrowed region (Miller, Lu and Dahle, 2006).

association of the Fe-IMCs with these solid oxides (**Fig. 2.29b**) that either formed in-situ or added is in accordance with the mechanism that Fe-IMCs nucleate upon the wetted sides of double oxide films (Miller, Lu and Dahle, 2006; Cao and Campbell, 2003). In Kalifa’s study, a series of ceramic particles with good lattice mismatching with α-AlFeMnSi was introduced into Al-Fe-Si alloys (Khalifa *et al.*, 2005) which shows that increased cooling rate can generally facilitates the nucleation of Fe-IMCs on the surface of different inclusions and inclusions are more likely to be located next to the Fe-IMCs when there is a good lattice matching.Allen et al. reported (Allen *et al.*, 1999) that minor vanadium (≥500ppm) addition and/or Al-Ti-B grain refiner (≥800ppm) addition can significantly change the solidification behaviour of binary Al-Fe IMCs and enhance the nucleation of metastable Al_mFe without changing alloy composition or casting approach. Khalifa (Khalifa *et al.*, 2005) also reported the nucleation enhancement of Fe-IMCs by synthetic TiB_2 particle addition.

The nature of TiB_2 particles under different processes is summarized below. There are two common methods used to produce in- situ TiB_2, which are salts reaction (K_2TiF_6 + KBF_4) (Han, Liu and Bian, 2002; Wood, Davies and Kellie, 1993) and

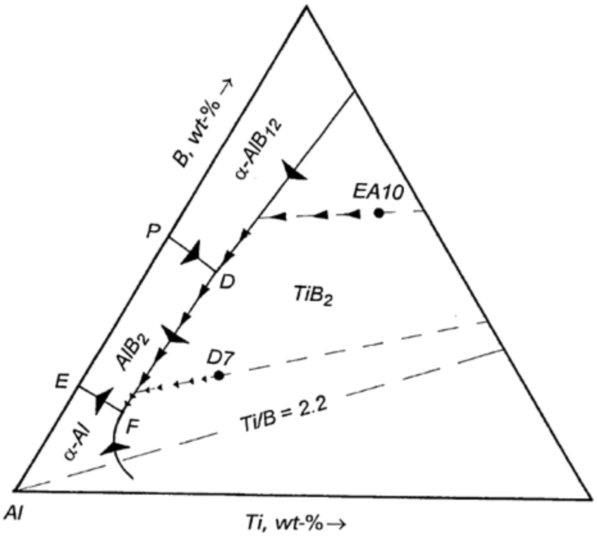

Figure 2.30 Liquid projection of in aluminium corner of Al-Ti-B ternary phase diagram. Largest arrows indicate directions of decreasing temperature. Al corner is in exaggerated form for clarity (Zupanič, Spaić and Križman, 1998b).

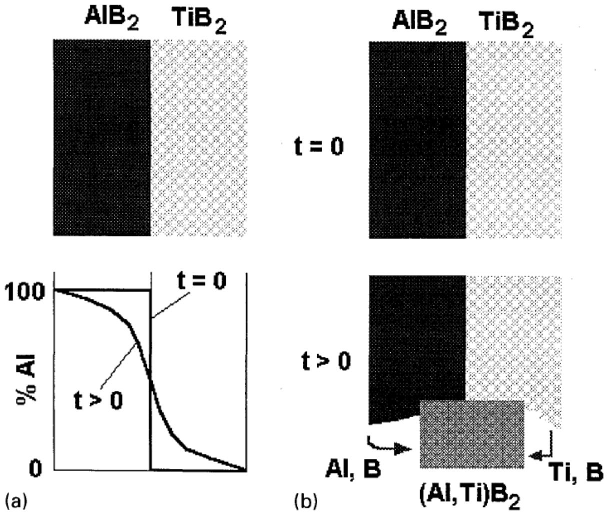

Figure 2.31 Possible mechanisms form transformation of apparently pure AlB_2 and TiB_2 to mixed $(Al,Ti)B_2$: (a) inter-diffusion of Al and Ti on cationic lattice sites in $(Al,Ti)B_2$; (b) formation of equilibrium $(Al,Ti)B_2$ and dissolution of apparently pure AlB_2 and TiB_2. (Zupanič, Spaić and Križman, 1998a)

reaction with molten master alloys (Al-Ti + Al-B) (Emamy, Mahta and Rasizadeh, 2006; Tee, Lu and Lai, 1999). As shown in **Fig. 2.30**, the ternary phase diagram equilibrium phase diagram of Al-Ti-B is described by Zupanic (Zupanič, Spaić and Križman, 1998b). In this work, the latter approach was employed using a chemical composition on the boron rich side of stoichiometric TiB_2 (i.e. with a Ti/B weight ratio < 2.2) to prevent the adsorption of free Ti atoms to TiB_2. Regardless of the production method, although TiB_2 is a thermodynamically stable phase there is a debate whether AlB_2 and TiB_2 exist as two separate phases or as a continuous solid solution, $(Al,Ti)B_2$, when there is excess B (Fjellstedt, Jarfors and Svendsen, 1999; Zupanič, Spaić and Križman, 1998a; Arnberg, Backerud and Klang, 1982; Cornish, 1975; Maxwell and Hellawell, 1975b; Backerud, 1971). Cornish and Backerud (Cornish, 1975; Backerud, 1971) have identified that Al and Ti atoms can replace each other to form $(Al,Ti)B_2$. However, Maxwell and Zupanic (Zupanič, Spaić and Križman, 1998a) reported that the large particles and particles heat treated for a long time tend to forward to stoichiometric AlB_2 and TiB_2 composition. The possible transformation mechanism associated these compounds' reaction is suggested by Zupanic as shown in **Fig. 2.31**. An update by Fan and co-workers suggested that alloying elements addition promotes thermodynamic stability of TiB_2 in Al-Ti-B-"X" system by affecting their activity coefficients (Fan, Yang and Zhang, 2005), which is adopted in this investigation to increase the stability of reaction product for Al-Ti-B(Fe) master alloys.

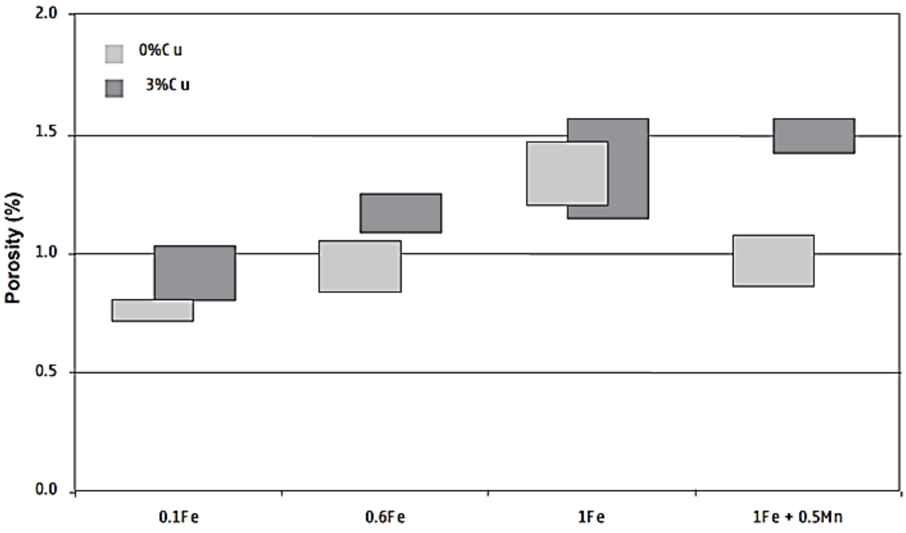

Figure 2.32 The porosity in cast Al-9Si cast alloy with and without 3.0wt% Cu as a function of Fe concentration (Dinnis, Taylor and Dahle, 2006).

2.2.3 Influence of Fe-IMCs on Mechanical Property of Al Alloys.

It is inevitable that secondary Al alloys contain a considerable amount of Fe (Mondolfo, 2013). In casting alloys, a reasonable amount of Fe is added to prevent die soldering (Han and Viswanathan, 2003). However, Fe leads to shrinkage porosity (Taylor, 2012), ductility reduction (Ji *et al.*, 2013b), scattered mechanical properties (Cao and Campbell, 2003) and potential fatigue life (Nyahumwa, Green and Campbell, 1998).

Introduction of Fe is very effective at increasing the total porosity and shrinkage defects as suggested by Dinnis and co-workers (Dinnis, Taylor and Dahle, 2006) and Taylor (Taylor, 2012). As shown in **Fig. 2.32**, the Fe concentration leads to a cumulative increase in porosity level in cast alloys regardless of the presence of Cu. Mn alone in the absence of Fe does not appear to reduce these defects, even although the α-AlFeMnSi is still dominant. The addition of Mn to an alloy with a given amount of Fe can considerably reduce the porosity due to the transformation of β-Al_5FeSi to α-AlFeMnSi (Dinnis, Taylor and Dahle, 2005).

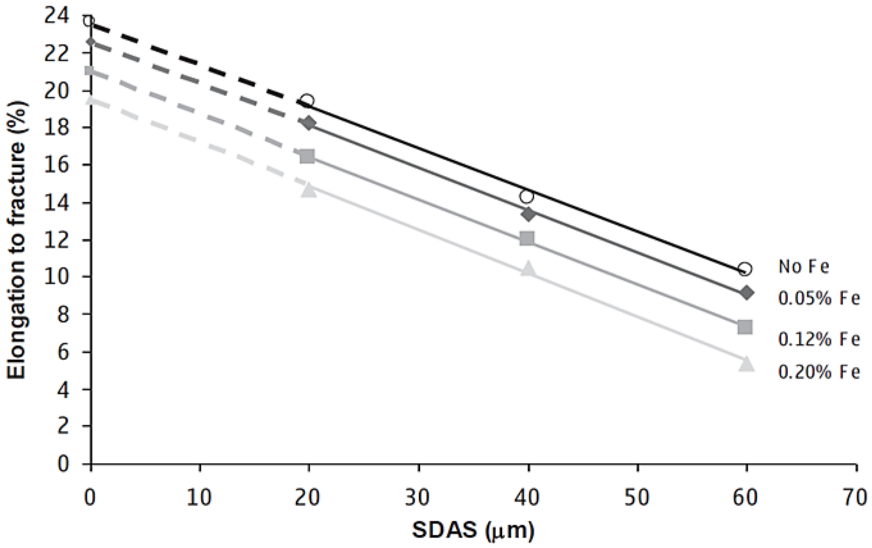

Figure 2.33 Maximum ductility (best elongation-to-fracture) as a function of SDAS for various Fe contents (Taylor, 2012).

As shown in **Fig. 2.33**, Fe induction and SDAS considerably decrease the elongation in a given Al alloy. The different points of fracture occur because of the combined effects of several variables including casting defects (e.g. oxides and porosity), cooling rate (secondary dendrite arm spacing) and Fe content. In high pressure die casting, Fe content is reported to considerable reduce the ductility of Al-Mg-Si alloys (Ji *et al.*, 2013b). Meanwhile, Mn appears to have little effect on the ductility of the alloys.

The reliability issues caused by Fe content has also been reported in some research. Campbell and Nayahumwa reported that the defect created by Fe-IMCs can also cause fatigue and tensile test property scattering (Cao and Campbell, 2003; Nyahumwa, Green and Campbell, 1998). **Fig. 2.34** shows that melt filtration can significantly increase the fatigue life of Al cast alloys. Similar to oxide defects, the cracking of Fe-IMCs is conventionally attributed to their brittle nature and coarse morphology. Even though, some compact Fe-IMCs can be strong, the cracks which are often observed travelling through the Fe-IMCs may actually be travelling along the non-bonded oxide interlayer.

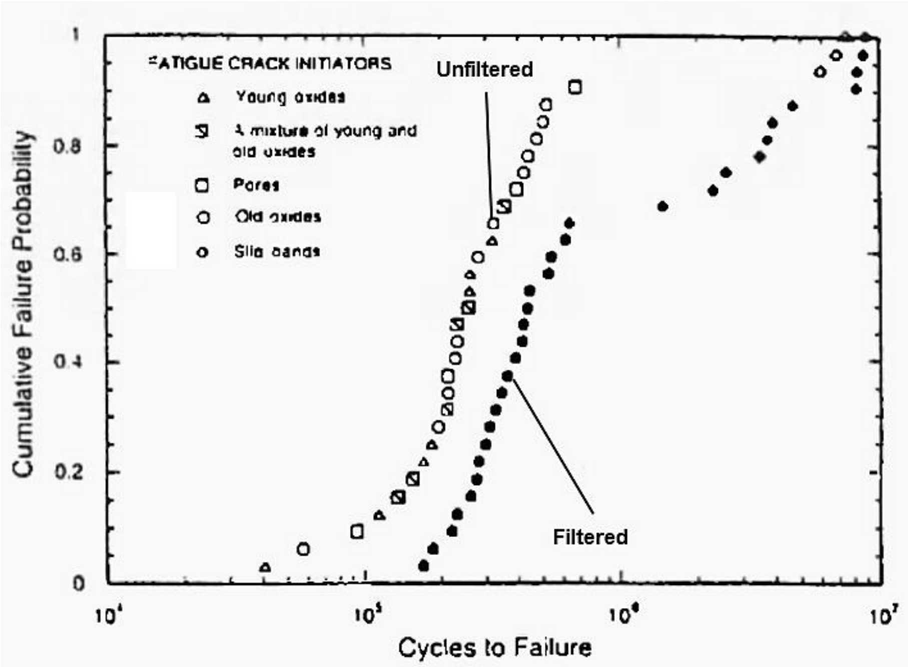

Figure 2.34 The fatigue lives for filtered and unfiltered cast Al alloy with and without filtration (Nyahumwa, Green and Campbell, 1998).

2.3 Summary

In this chapter, previous experimental and theoretical investigations on nucleation, role of solute and crystal growth of facet phases have been reviewed in section 2.1 and solidification behaviours of Fe-IMCs have been reviewed in section 2.2. This research is dedicated to gain further understanding on the solidification behaviour of Fe-IMC based on previous understanding of solidification in simpler systems. The nucleation and crystal growth will be the two fundamental objectives of this study.

The theoretical research on nucleation has been continued for many years. The classic nucleation theory is the first theory that attempted to find what act as a nucleation substrate and how nucleation occurs (Turnbull, 1953). The classic nucleation theory is fundamentally correct but hard to apply in many cases as the parameters and interaction of particles around the nuclei are difficult to determine experimentally. For common casting processes, Cantor suggested that solidification always occurs with heterogeneous nucleation as it is not possible to remove all the impurities from the parent liquid (Cantor, 2003). TiB_2 is considered to be the nuclei in Mg free alloys as the grain sizes of the alloys with and without TiB_2 addition can differ greatly. A reasonable conclusion for this phenomenon is that the potency of the particles can be one of the critical factors to determine whether they can nucleate the solid. The substrate with smaller lattice misfit is considered to be more potent than the ones with a large misfit, which determines whether a substrate can act as heterogeneous nucleation site (Maxwell and Hellawell, 1975a). The misfit has been calculated in many ways: Turnbull and Vonnegut used the lattice parameters of both phases (Turnbull and Vonnegut, 1952) and Bramfitt used three random directions of two faces and the arithmetic mean value of the three pairs of different directions and taken the angles between each pair under consideration (Bramfitt, 1970). Fan and co-workers considered only the close packed faces of the nucleation phase and potential nucleation substrates (Fan, 2013). However, using misfit as the only criterion to evaluate nucleation potency is still very confined at explaining the significant improvement on the grain refinement of α-Al by on the TiB_2 particles with trace free Ti addition very well (Fan *et al.*, 2015). One reasonable conclusion is that despite the good lattice matching between substrate and the nucleation phase, the elemental adsorption can significantly affect the heterogeneous nucleation event by reducing nucleation barrier and/or decreasing lattice misfit (Fan, 2013). Furthermore, the efficiency has been considered as another determining factor for grain refinement. Larger nucleation substrate requires small undercooling for start of free growth (Greer *et al.*, 2000). Consequently, a higher substrate number density should be able to contribute to a finer grain structure.

Crystal growth is fundamentally a diffusion controlled process. The solute concentration and elemental diffusion is very crucial for crystal growth (Dantzig and Rappaz, 2009). The constitutional undercooling caused by solute segregation at the S/L interface is one of the dominant factors for the crystal growth. There have been different parameters to assess this, such as constitutional-supercooling parameter P (Tarshis, Walker and Rutter, 1971) and growth restriction factor Q (Johnsson, 1995). The evaluation growth restriction for multi-component system is simply adding the P or Q value for each element. For the crystals with great growth anisotropy the necessary growth driving force is dependent on growth direction (Dantzig and Rappaz, 2009). These phases are highly likely to exhibit faceted structure during their growth (Sunagawa, 1990), such as Si and Fe-IMCs. Faceted phase tends to grow along well-defined directions with the help from twins and/or screw dislocations. Therefore, the resultant eutectic structure is very complex and irregular, giving the rise to an irregular eutectic morphology.

The nucleation models used for of pure elements can be used for the nucleation analysis for Fe-IMCs. Considering the complexity of Fe-IMC’s in terms of crystal structure and chemical components, the nucleation enhancement of Fe-IMC may not completely follow the principles nucleation based on pure metals. The adsorption mechanism proposed by Cantor (Cantor, 2003), Fan (Fan *et al.*, 2015) and co-workers provided a new insight into the heterogeneous nucleation of complex phases, such as intermetallics. It has been widely acknowledged that generally Fe-IMC has a unit cell of more than 100 atoms and strong anisotropy. The further theoretical understanding on the growth of Fe-IMCs must take these factors into consideration.

Chapter 3 Experimental Procedure

In this chapter, the casting methods and processing procedures used in this investigation will be described. In order to facilitate the metallurgical observation, a few sample preparation methods were employed in this study, and their processes will be illustrated. Characterization and quantification techniques used in the present study will also be introduced in this chapter.

3.1 Material Preparation

The Al alloys investigated in the present study are Al-Fe-Mn alloys and Al-Si-Fe-Mn alloys and super ductile Al-Mg-Si-Fe-Mn alloy (Ji *et al.*, 2012). For the purpose of investigating the solidification of Fe-IMCs, the alloys are chosen because of their sufficient amount of Fe and Mn content and previous research (Ji *et al.*, 2012). Various concentrations of Mg and Si are introduced to study their effect on the solidification behaviour of Fe-IMCs. The intention of choosing each alloy composition point will be further explained in each chapter. These specific alloys were made from commercially pure Al (*Norton Aluminium Ltd*, Staffordshire, UK) and commercially pure Mg (*Magnesium Elektron Ltd*, Manchester, UK) and master alloys from other sources. The compositions of commercially pure metals used in this study are shown in **Table 3.1**. The as-received compositions of the commercial master alloys are shown in **Table 3.2**.

Table 3.1 Chemical composition of pure metals

Materials	Elements (wt.%)								
	Al	Mg	Si	Fe	Mn	Cu	Zn	Ti	Others
Pure Al	**99.85**	0.003	0.04	0.08	0.0008	0.0069	0.0018	0.0055	<0.001
Pure Mg	0.04	**99.99**	0.013	0.002	0.02	0.001	-	-	<0.001

For the preparation of nominal Al-1.2Fe-0.7Mn-*x*Mg, Al-2Si-1.2Fe-0.7Mn-*y*Mg and Al-5Mg-2Si-1.2Fe-0.7Mn alloys, the electric resistance furnace (*Carbolite*, *Hope*, *UK*), was used for melting and cooling if not specified. Pure Al was molton at 750˚C and master alloys were added one by one before at least 1 hour of holding. Pure Mg was added 30 minutes before casting to reduce the oxidation. Composition measurement of these alloys was performed by *Foundry-Master Pro* (*Oxford Instruments*) as shown in **Fig. 3.1a**. For chemical composition analysis, a cast sample with minimum surface size 20 cm^2 was produced by pouring stirred melt into a steel

Table 3.2 Chemical composition of master alloys.

Materials	**Elements (wt.%)**							
	Al	**B**	**Mg**	**Si**	**Fe**	**Mn**	**Cu**	**Ti**
Al-50Si	Bal.	-	<0.02	50	0.6	0.12	0.03	0.02
Al-20Mn	Bal.	-	0.01	0.09	0.27	18.2	0.02	0.02
Al-38Fe	Bal.	-	<0.02	0.05	38	<0.02	<0.02	<0.02
Al-5B	Bal.	5.44	-	0.09	0.17	<0.02	<0.02	<0.02
Al-10Ti	Bal.	-	0.01	0.11	0.29	-	-	9.3

Figure 3.1 Photos of (a) floor standing metal analyser *Foundry-Master Pro, Oxford Instruments* and (b) mould used for the chemical composition test sample.

mould (shown in **Fig. 3.1b**). Before running the composition analysis, the cast sample was ground with SiC 800 grit paper to produce a flat surface and dried in an air stream after washing with ethanol. The chemical compositions of the alloys acquired by this method will be presented **Table 3.3**.

The preparation of Al-5Ti-2.5B(Fe) (nominal) master alloy was conducted at 900˚C in an electric resistance furnace. For producing 1kg of Al-5Ti-2.5B(Fe) master alloy, firstly 500g Al-10Ti master alloy and 40g pure Al was heated to 900˚C followed by the addition of 460g of Al-5.44B master alloy once the alloy was molten. The melt was then held at 900˚C for 8 hours, and the sludge was removed from the top of the

Table 3.3 Chemical composition of the alloys characterized with Foundry Master using composition test sample.

Alloys	**Elements (wt.%)**					
	Al	**Mg**	**Si**	**Fe**	**Mn**	**Others**
Al-5Mg-2Si-1.2Fe-0.7Mn	Bal.	5.26±0.42	2.14±0.23	1.22±0.08	0.71±0.05	≤0.1
Al-1.2Fe-0.7Mn-*x*Mg	Bal.	0.003	0.04±0.01	1.26±0.02	0.73±0.03	≤0.17
	Bal.	1.31±0.02	0.03±0.01	1.25±0.05	0.67±0.01	≤0.12
	Bal.	3.22±0.05	0.04±0.01	1.23±0.12	0.64±0.02	≤0.17
	Bal.	6.07±0.13	0.04±0.01	1.18±0.03	0.67±0.12	≤0.14
Al-2Si-1.2Fe-0.7Mn-*y*Mg	Bal.	0.01	2.19±0.08	1.20±0.04	0.66±0.02	≤0.04
	Bal.	1.26±0.02	2.24±0.14	1.21±0.06	0.67±0.01	≤0.02
	Bal.	3.05±0.20	2.22±0.09	1.25±0.06	0.65±0.02	≤0.03
	Bal.	5.41±0.35	2.11±0.06	1.26±0.10	0.68±0.03	≤0.14

melt before adding 13g Al-3.8Fe master alloy to the liquid melt. After a further 8 hours of holding at 900˚C and mechanical stirring every hour, the melt was cast in 60*60*200 mm steel mould with Ø10*200 mm cylinder mould cavity to allow a rapid cooling to achieve homogenised particle distribution. However, due to the sensitivity limit, *Foundry-Master Pro* was unable to characterize the final chemical composition of Al-5Ti-2.5B(0.5Fe) master alloy.

3.2 Casting Procedures

In this section, the casting procedures for the investigation are described. The TP-1 mould was adopted to investigate the effect of solute concentration and casting temperature at a cooling rate of 3.5K/s. Various casting approaches such as, Cu wedge mould casting, cooling in furnace (CF) and melt quenching with water (MQ), were used to understand the solidification path and the effect of cooling rate on the solidification behaviour of Fe-IMC in various alloys.

3.2.1 TP-1 Standard Casting

In order to achieve a consistent and moderate cooling rate for the experiments, TP-1 standard mould was used (Aluminium Association, 1987). The mould wall was cooled in water bath with a constant flow rate of 3.9 litres per minute (**Fig. 3.2a**),

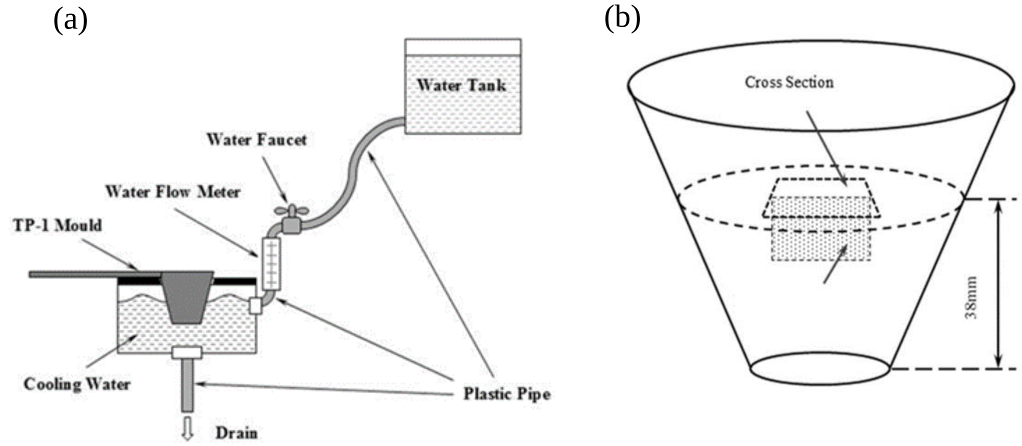

Figure 3.2 Schematic illustration of (a) TP-1 casting (Aluminium Association, 1987), (b) TP-1 sample. The specimens for metallography and characterization were taken from arrow indicated position.

providing a constant 3.5K/s cooling rate at the cross section 38 mm from the bottom of the TP-1 sample (Aluminium Association, 1987). Metallography observation of TP-1 sample was taken place on the cross section 38 mm from the bottom and the vertical section from the centre of the sample if specified (**Fig. 3.2b**). For the investigation of the effect of casting temperature on the formation of α-AlFeMnSi at a cooling rate of 3.5K/s, an experiment with multi-temperature casting was employed. The processing route shown in **Fig. 3.3** illustrates two processing stages: cooling in air and TP-1 casting. The air cooling started from 750˚C and finished at TP-1 casting temperature. Designated TP-1 casting temperature ranged from 50˚C above primary phase formation temperature to eutectic temperature according to the alloy phase diagram, are 720, 700, 680, 670, 660, 650, 640, 630, 620ºC.

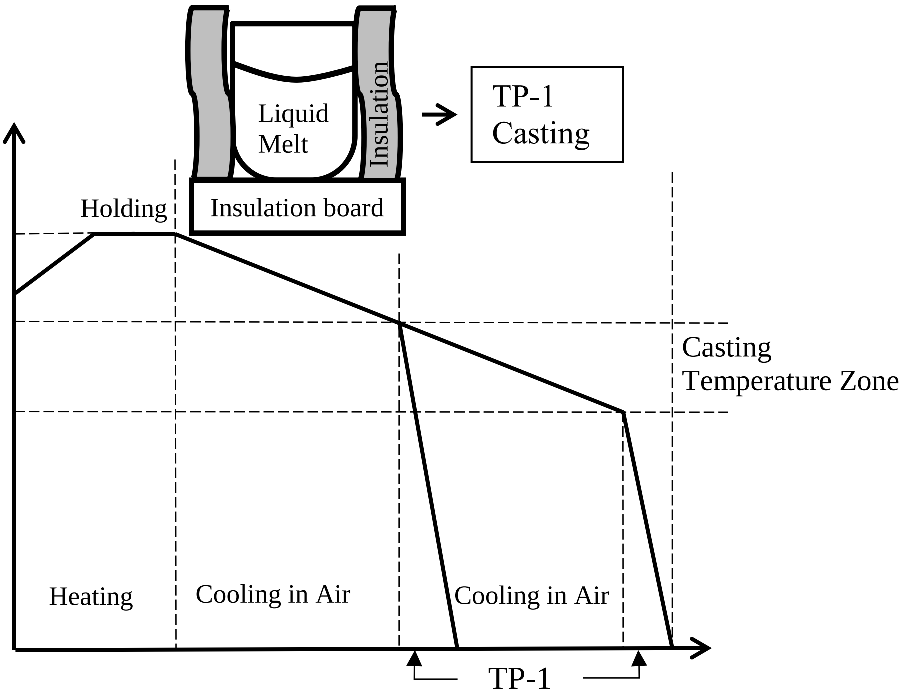

Figure 3.3 The processing route of TP-1 casting experiment at various casting temperature which ranges from 620˚C to 680˚C.

3.2.2 Furnace Cooling

Furnace cooling (CF) was conducted simply by placing melt in a preheated furnace at a given temperature depending on the alloy, and allowed to solidify while it was in the cooling furnace. Although the heat release rate of the furnace is dependent on the isolation of the furnace, the cooling rate of such experiments cooling from 720˚C to

620˚C was 0.02±0.005K/s (sensitivity limit of the K-type thermocouples). It should be noted that when temperature difference between furnace and environment become small the cooling rate will decrease along with the rate of heat release. Given that the solidification of the target alloy finishes at around 580˚C, the cooling rate variation was considered negligible for the CF sample analysis.

3.2.3 Cu Wedge Mould

As shown in **Fig. 3.4**, the Cu wedge mould was used to study the effect of cooling rate on the morphology of α-AlFeMnSi due to the cooling rate range that it is available with a wedge mould (Kotadia, 2010; Pryds and Huang, 2000). The cooling rate was determined using an empirical relationship between the cooling rate ($\dot{T}$ K/s) and half thickness of mould wall (Z mm). This relationship is proposed by Pryds and co-workers (Pryds and Huang, 2000):

$$\dot{T} = \frac{926\ (K \bullet mm^2/s)}{Z^{1.8}} \tag{3.1}$$

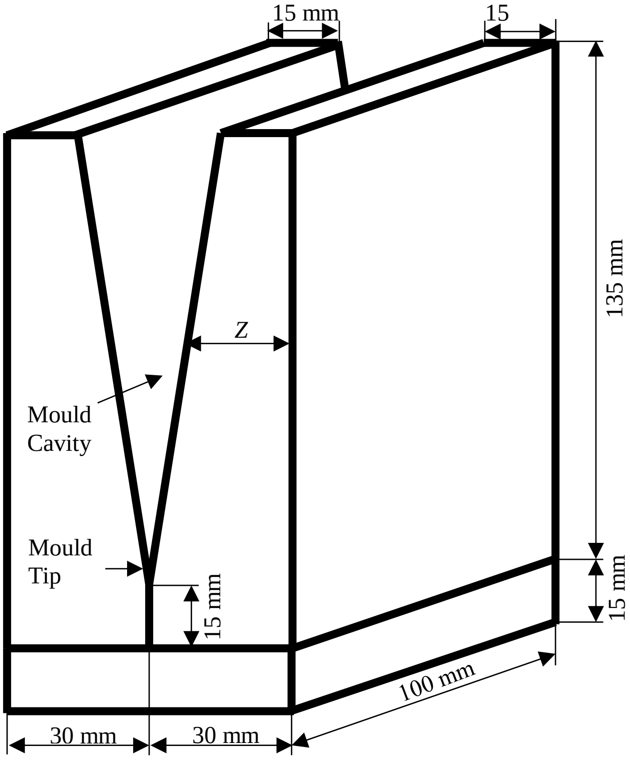

Figure 3.4 Schematic illustration of the Cu wedge mould showing mould cavity, half thickness of mould wall (Z) and mould dimensions.

The relationship between the half thickness of mould cavity and height was calculated with the measured thickness/height ratio. Basing on this equation, the cooling rate at 10 mm, 40 mm, 70 mm and 100 mm from tip of the mould are approximately 871K/s,72K/s, 26.2K/s and 13.8K/s, respectively. These cooling rates have been experimentally measured by placing thermocouples at the thin areas of wedge mould, which show comparable result.

3.2.4 Steel Mould Melt Quench

Water quench is commonly used to obtain a constant high cooling rate due to the high heat capacity of water (4.184 J/g•K) and good thermal conductivity of steel (32.6 W/(m·K) at 1000K). The steel mould melt quench (MQ) was employed here to achieve freezing which means a cooling rate surge during solidification when the melt was transferred to water bath. Thus, the solidification sequence can be investigated through microstructure observation. This method was also used with the assistance of a thin wall steel mould (**Fig. 3.5**) to study the nucleation behaviour at a higher cooling rate which, was experimentally measured to be 50±10K/s.

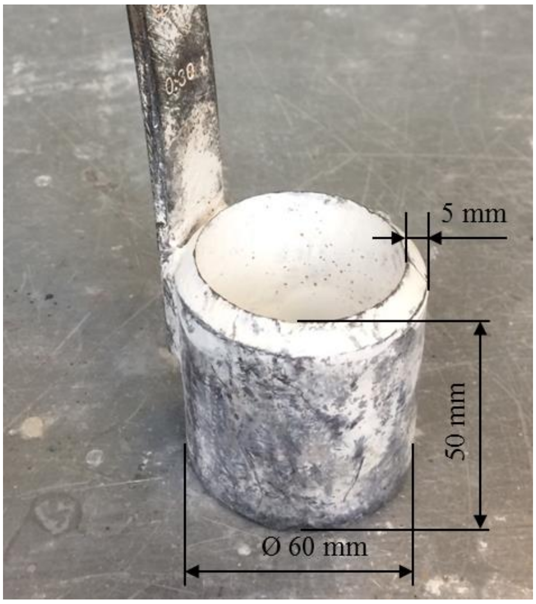

Figure 3.5 Photo of steel mould coated to boron nitride used for melt quench (MQ) and cooling rate measurement, showing the dimensions of the mould.

The steel mould is used for the melt quenching experiment and cooling curve measurement (see section 3.4.7). For melt quenching experiment, the processing route is relatively simple. The melt is held in a graphite crucible at 750˚C and then divided into several the steel moulds (**Fig. 3.5**) that is preheated to 750˚C in an electric resistance furnace. The steel mould will be placed back in the furnace for slow cooling and submerged in room temperature water for melt quenching when the selected quenching temperatures are reached. The temperatures selected are 620˚C, 600˚C and 579˚C based on the phase transformation temperatures of the alloy system. Metallurgical observation was made at the cross section 10mm from the bottom of the steel mould.

3.2.5 Quart Tube Melt Quench (TQ)

This casting approach is designed to have a reliable the control of casting temperature. Induction furnace (*Meltech Ltd*, *Suffolk*, *UK*) shown in **Fig. 3.6**, was employed for this experiment (MelTech, 2017), in order to obtain homogenised particle and temperature distributions during the solidification process as well as a

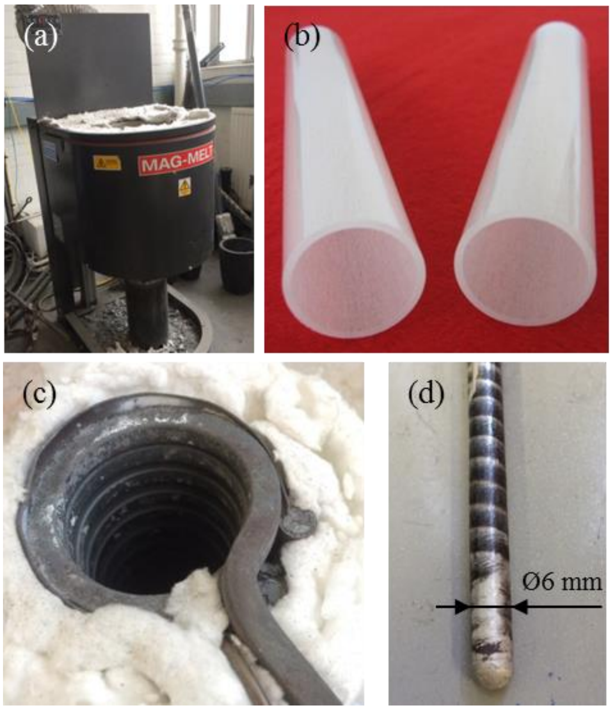

Figure 3.6 Photos showing (a) MelTech induction furnace which is currently in working position, (b) Ø8mm translucent quartz tube, (c) Ø40mm resistant heater and (d) water quenched sample with a diameter of Ø6 mm by quartz tube.

sustained cooling rate which is measured to be 0.15±0.02K/s. A quartz tube with 5±0.5mm inner diameter and 8±0.5mm outer diameter was used in this experiment for transferring the melt from crucible in induction furnace to water. The measurement of the cooling rate of water was not straight forward due to the variation in sample diameters. However, because of the cross-section (Ø5±0.5mm) of the quenched sample, the entire sample was considered to be solidified immediately once submerged in water.

The processing route of this casting approach includes two stages: cooling in induction furnace and melt quenching, labelled as Stage 1 and Stage 2 in **Fig 3.7**, respectively. A mass of 2kg of Al-5Mg-2Si-1.2Fe-0.7Mn alloy was molten in induction furnace (**see Fig. 3.6a**) after 15 minutes of heating, and holding at 750ºC for 5 minutes (lower power output) until the temperature stabilised. Melt temperature was then decreased by reducing the power output of the induction furnace. During this stage the melt temperature was monitored with K-type thermocouples which

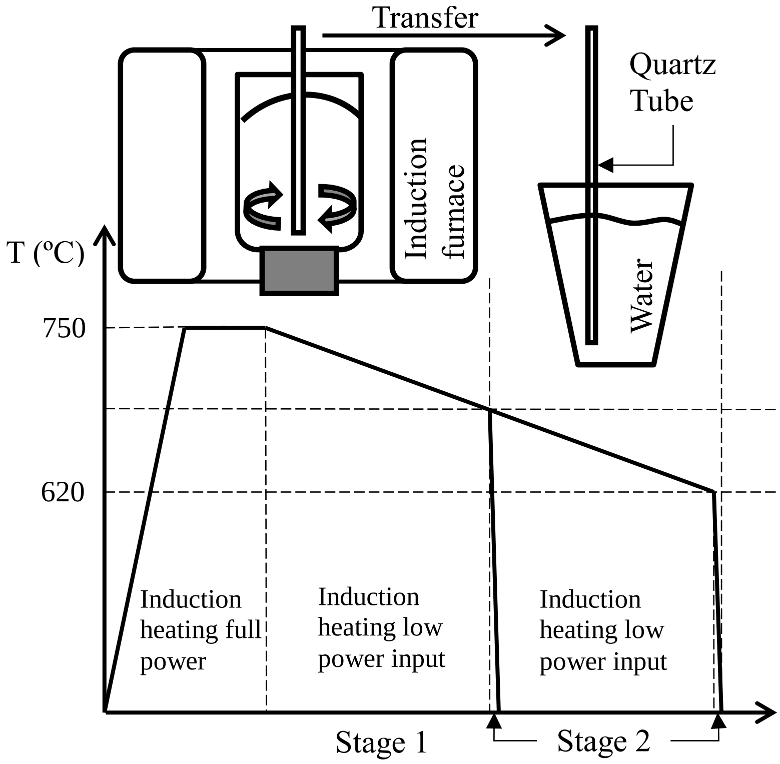

Figure 3.7 Schematic illustration of processing route of quart tube water quench experiment which includes mainly two stages which are slow cooling (Stage 1) and Quench in Water (Stage 2).

showed a cooling rate of 0.2K/s. The quartz tube (**Fig. 3.6b)**, connected to a syringe and preheated to 750ºC with an electric resistance heater (shown in **Fig 3.6c**), was used for transferring melt from crucible to water bucket. In Stage 2, a small amount of melt (4-7g) was draw with the preheated quartz tube from crucible and then the withdrawn melt was dropped into water with drawn melt. Thus, Ø5mm quenched rod samples (see **Fig. 3.6d**) were produced. Designated melting quenching temperatures ranging from 20K above primary phase formation temperature to the eutectic temperature according to the phase diagram of Al-5Mg-2Si-1.2Fe-0.7Mn alloy, were 675, 670, 665, 660, 655, 650, 645, 640, 635, 630, 625 and 620ºC. Due to the very fine morphology of quenched liquid, it can be easily distinguished from slowly

Table 3.4 The metallographic sample preparation route I for hard materials.

	Surface	**Abrasive**	**Force**	**Time (mm:ss)**	**Rotation speed (rpm)**		**Rotation Direction (Base/Head)**
					Base	**Head**	
1	CarbiMet	P320 SiC	25 N	Until Flat	300	50	> >
2	CarbiMet	P800 SiC	25 N	3:00	150	50	> <
3	CarbiMet	P2500 SiC	25 N	3:00	150	50	> <
4	CarbiMet	P4000 SiC	25 N	2:00	150	50	> <
5	MD-Mol	0.04μm SiO_2 OP-S	25 N	5:00	150	50	> <
* All consumables are provided by *Buehler, Coventry, U.K.*, except OP-S which is from *Struers Ltd., Catcliffe Rotherham, U.K.*							

cooled liquid. The solidification behaviour of the phases formed in temperature range of 680ºC to 620ºC, which in this alloy is primary α-AlFeMnSi, should exhibit a much coarser morphology.

3.3 Sample Preparation

3.3.1 Grinding and Polishing

The preparation route I was used for metallographic preparation of hard materials, such as most of quinary Al-Mg-Si-Fe-Mn and quaternary Al-Mg-Fe-Mn alloy samples, the wedge samples (from Cu wedge mould) and water quenched samples. Metallography samples were collected from various areas of the as-cast ingot depending on the observation needs. They were sectioned off from as-cast sample with AbrasiMet™ 250 (*Buehler, Coventry, UK*) from as-cast ingot, and it was then mounted with CitoPress mounting press (*Struers Ltd., Catcliffe Rotherham, UK*) into

Table 3.5 The metallographic sample preparation route II for soft materials.

	Surface	**Abrasive**	**Force**	**Time (mm:ss)**	**Rotation speed (rpm)**		**Rotation Direction (Base/Head)**
					Base	**Head**	
1	CarbiMet	P320 SiC	25 N	Until Flat	300	50	> >
2	TexMet P	9μm diamond	15 N	5:00	150	50	> <
3	TexMet P	3μm diamond	15 N	5:00	150	50	> >
4	MD-Mol	0.04μm SiO_2 OP-S	15 N	12:00	150	50	> <

* All consumables are provided by *Buehler, Coventry, U.K.*, except OP-S which is from *Struers Ltd., Catcliffe Rotherham, U.K.*

Ø30mm by 15±10mm cylindrical sample using Bakelite resin (*MetPrep, Coventry, UK*). The samples were then ready for grinding and polishing, and the preparation route is illustrated in **Table 3.4**.

Preparation route II was used for metallographic preparation of relatively soft materials, such as CF quinary Al-Mg-Si-Fe-Mn alloys, CF quaternary Al-Mg-Fe-Mn alloys, quaternary Al-Si-Fe-Mn alloys, ternary Al-Fe-Mn alloys and DSC samples. The cutting method and mounting method were identical to preparation route I. However, this route has different grinding and polishing procedures as shown in **Table 3.5**.

3.3.2 Anodising

Anodising was used to obtain coloured image for grain size analysis and grain boundary observation. As-cast samples prepared with standard mechanical polishing procedures was etched in Barker's reagent (5ml HBF4 (48%) + 200ml water (Vander-Voort, 2015)) for 90-120 seconds under a constant voltage of 20V at room temperature (Weidmann and Guesnier, 2016; Cerri and Evangelista, 1999), where the etching current pass through sample which is dependent on surface area of the sample. Schematic illustration of anodising station is shown in **Fig. 3.8**.

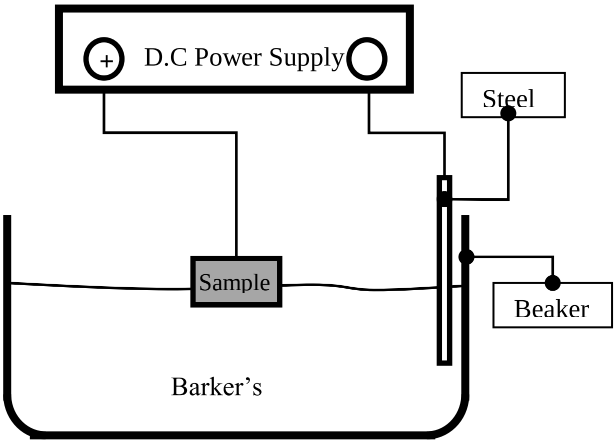

Figure 3.8 Schematic illustration of constant voltage Al alloy anodising station that with a sample in electrolyte solution.

3.3.3 Electropolishing for EBSD Samples

An Electropolishing station was set up as illustrated in **Fig 3.9**. The DC power supply worked as a constant voltage and stable current source providing 12V during the electropolishing. The current through the sample is dependent on specific specimen and surface area exposed to the solution. For Al-5Mg-2Si-1.2Fe-0.7Mn alloy, the current was stable at 0.8A when surface area is around 2.28cm^2. Electropolishing was done with a constantly stirred the 20% HNO_3 ethanol based solution at 243K for 20 seconds, followed by rinsing in pure ethanol and drying in a warm air stream. Due to the unstable nature of the electrolyte for this process, the risk assessment of the electropolishing procedure including electrolyte preparation and disposal was conducted. The solution was maintained under -10ºC and disposed after being neutralised with Sodium carbonate.

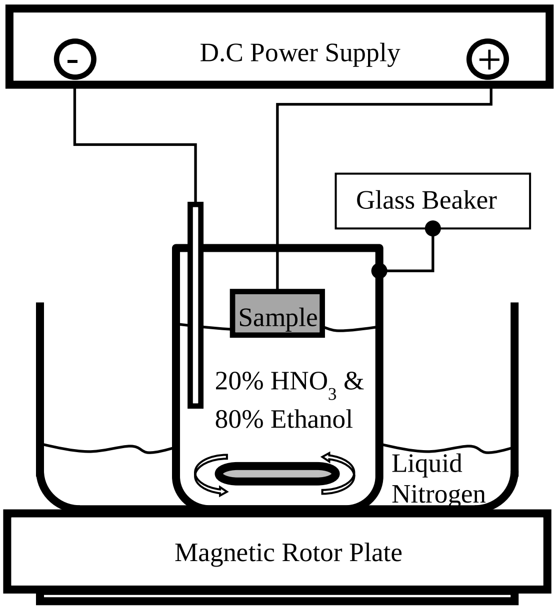

Figure 3.9 Schematic illustration of electropolishing station for Al alloy with a sample in electrolyte solution.

3.3.4 Deep-etching

Fe-IMCs, exhibiting faceted morphology, are strongly anisotropic along different crystal orientations, which makes it difficult to describe its morphology through 2D observation. Therefore, the 3 dimensional morphologies of Fe-IMCs were revealed via deep-etching (DE). As can be seen from the schematic illustration in **Fig. 3.10a**, sample was firstly submerged in 15% HCl aqueous solution in a thoroughly cleaned beaker and then after a sufficient amount of time Fe-IMC will be exposed due to the lower chemical affinity of Fe-IMC to HCl compared with Al. The sample was then carefully taken out from the solution and cleaned with ethanol before drying in hot air stream.

For the extraction of Fe-IMC particle, the same mechanism as for the separation of Al and Fe-IMC was used, as shown in **Fig. 3.10b**. After an adequate amount of reaction time, a small amount of HCl aqueous solution at the bottom of the beaker containing separated Fe-IMC particles were taken out and poured onto filter paper and washed in an ethanol bath. Once the particles were clean, they were transferred to a hot plate for drying to prevent any oxidization.

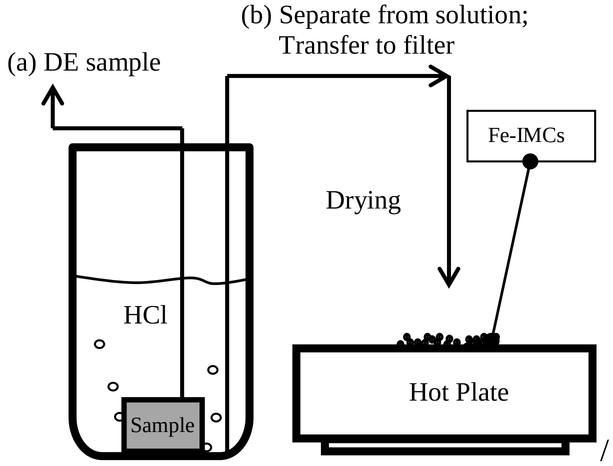

Figure 3.10 Schematic illustration of deep-etching procedure (a) for deep-etching and (b) extraction of Fe-IMC particles.

3.3.5 TEM Specimen Preparation

The specimen were ground to 40-60μm in thickness with P4000 SiC paper after cutting into round Ø3mm thin disc with disc punch. Then the TEM disc sample was further thinned using Ion thinning method on Precision Ion Polishing System (PIPS) model 691 (*Gatan, Inc., Pleasanton, CA, US*) at 5keV double ion beam at 5˚ incident beam angle for 3-4 hours until the thin disc pierced and further 20 minutes at 5˚

incident angle under the same voltage. Thus, the sample is sufficiently thin for TEM characterization.

3.4 Characterisation

3.4.1 Optical Microscopy

The optical microscope (OM) shown in **Fig. 3.11a** for microstructural observation and quantitative metallography is a Zeiss Optical Axio Microscope A1 (*ZEISS Group., Oberkochen, Germany*) equipped with Zeiss AxioCam ICc3 digital camera (ZEISS Inc, 2017). Polarized light images are widely used for Al grain size measurement as the grains in different crystal orientation will reflect light to different directions resulting in grains with different colours when reflected light passes through objective lenses (Vander-Voort, 2015; Smallman, 1985). Thus, the grain size measurement was performed on polarized micrographs and analysed with AxioVision 4.8 (ZEISS Inc, 2017). Metallographic sections for optical microscopy and scanning electron microscopy were prepared using metallographic procedures described in section 3.3.1 and 3.3.2.

3.4.2 Scanning Electron Microscopy

Scanning electron microscopy (SEM) was carried out using a Zeiss Supra 35 microscope (**see Fig. 3.11b**) (*ZEISS Group., Oberkochen, Germany*) equipped with an EDAX energy Dispersive X-Ray Spectroscopy (EDS) and EDAX Electron Backscattered Diffraction (EBSD) detectors (**Fig. 3.11c)**, operated at an accelerating voltages ranging from 5 or 20kV. Several different signals are produced due to the interaction between the beam and the sample. These signals provide the user with detailed information on the differences among the average atomic number the various phases within the sample, structure and elemental content (Goodhew, Humphreys and Beanland, 2000). The SEM used in this study imaging modes include secondary electron imaging, back scattered electron (BSE) imaging, and EDS.

3.4.3 Electron Backscattered Diffraction

The as-cast samples were prepared using metallographic procedures described in section 3.31 before electro-polishing at 12V for 20s as described in section 3.3.3. EBSD analysis was performed on the Zeiss Supra 35VP fitted with high sensitivity DigiView camera (*EDAX Inc., NJ, U.S.*) as shown in **Fig. 3.11c** with EDAX TEAM 4.3 system (EDAX, 2017). Both EDAX TEAM 4.3 and OIM 7.3 were used for EBSD data analysis. For the EBSD acquisition in this study, the accelerating voltage, working distance and condenser aperture used were 20kV, 10mm and 120μm, respectively, in high current mode. The step size was between 0.2μm and 1μm depending on the size of the area analysed.

Crystallographic data for Kikuchi pattern indexing was from the Inorganic Crystal Structure Database (ICSD) and are listed in following chapters. The Kikuchi pattern of α-AlFeMnSi indexing was performed manually in EDAX TEAM 4.3 (EDAX, 2017), as the low confident index (CI) value caused by very close asymmetric double bands in the Kikuchi pattern of α-AlFeMnSi from its pseudo-symmetry (Hwang, Doty and Kaufman, 2008).

3.4.4 Transmission Electron Microscopy

A JEOL 2100 field emission gun transmission electron microscope (FEG TEM), as shown in **Fig 3.11d,** was used for the characterization at an accelerating voltage of 200 kV. A double tilt sample (*JEOL Ltd., Tokyo, Japan*) was used in this TEM for the acquisition of bright field (BF) images, selected area electron diffraction (SAED) patterns, high resolution (HR) images and TEM/EDS spot analyses.

Titan ChemiSTEM, a new design of spherical aberration corrected microscope which is fitted with FEI's ultra-high brightness field emission gun (X-FEG) which provides probe size of less than 0.1nm and optimised for atomic resolution chemical analysis using four energy dispersive X-ray spectroscopy (HR-EDS) detector incorporated into the pole piece of the objective lens, was employed for atomic resolution observation (The University of Manchester, 2016). High-angle annular dark-field imaging (HADDF) and HR-EDS mapping were performed the on TiB_2 and Fe-IMC interface at a voltage of 200kV. Dr Yun Wang, a senior research fellow at Brunel University London, is greatly acknowledged for the operation and his guidance with this device.

Experimentally obtained SAED patterns were measured with GMS 3 (*Gatan, Inc., Pleasanton, CA, U.S.*). The SAED patterns were indexed with crystallographic data reported in Inorganic Crystal Structure Database (ICSD) by Royal Society of Chemistry (RSC).

3.4.5 X-ray Diffraction

Crystallographic characterization of intermetallic compounds was performed with Bruker D8 Advance X-ray diffraction (XRD) diffractometers (**Fig. 3.11f**). XRD analysis was performed on 2-5g extracted intermetallic compounds to get diffraction peaks. The acquisition time, step size, and the 2θ angle range for powder diffraction pattern were chosen as 1s, 0.02˚ and 20-100˚, respectively.

3.4.6 Differential Scanning Calorimetry

In this investigation, the differential scanning calorimetry (DSC) was performed with on a Netzsch STA 409 PC Luxx (**Fig. 3.11f**) to characterise the phase transformation temperature using TP-1 sample prepared at various casting temperatures. The specimens with a mass ranging from 8mg to 194mg were taken from the centre of the cross-section 38mm from the bottom of TP-1 samples (**Fig. 3.2b**) for DSC analysis. The program parameters were set as: heating: 10K/min to 750˚C; isothermal: 10 minutes at 750˚C; cooling: 0.6K/min, 3K/min, 6K/min, or 10K/min to room temperature. Each test was recycled for 3 times for a more reliable result.

3.4.7 Cooling Curve Measurement

For the ceramic mould (CM) cooling curve measurement, the alloy was molten at 750˚C in a graphite crucible and poured into a cylindrical ceramic mould that was preheated to 410˚C. The cylindrical ceramic mould was covered with 13mm thermal isolation, and the whole cooling curve measurement equipment was surrounded with N17 isolation boards so that the effect of environment changes can be minimized. The temperature was measured with two sets of exposed wire thermocouples and the data was recorded with *NI SCC-68* at a frequency of 100Hz and analysed with

Measurement & Automation Explorer (National Instruments). The thermocouple 1 was located at the centre of the ceramic crucible 40mm away from the bottom and

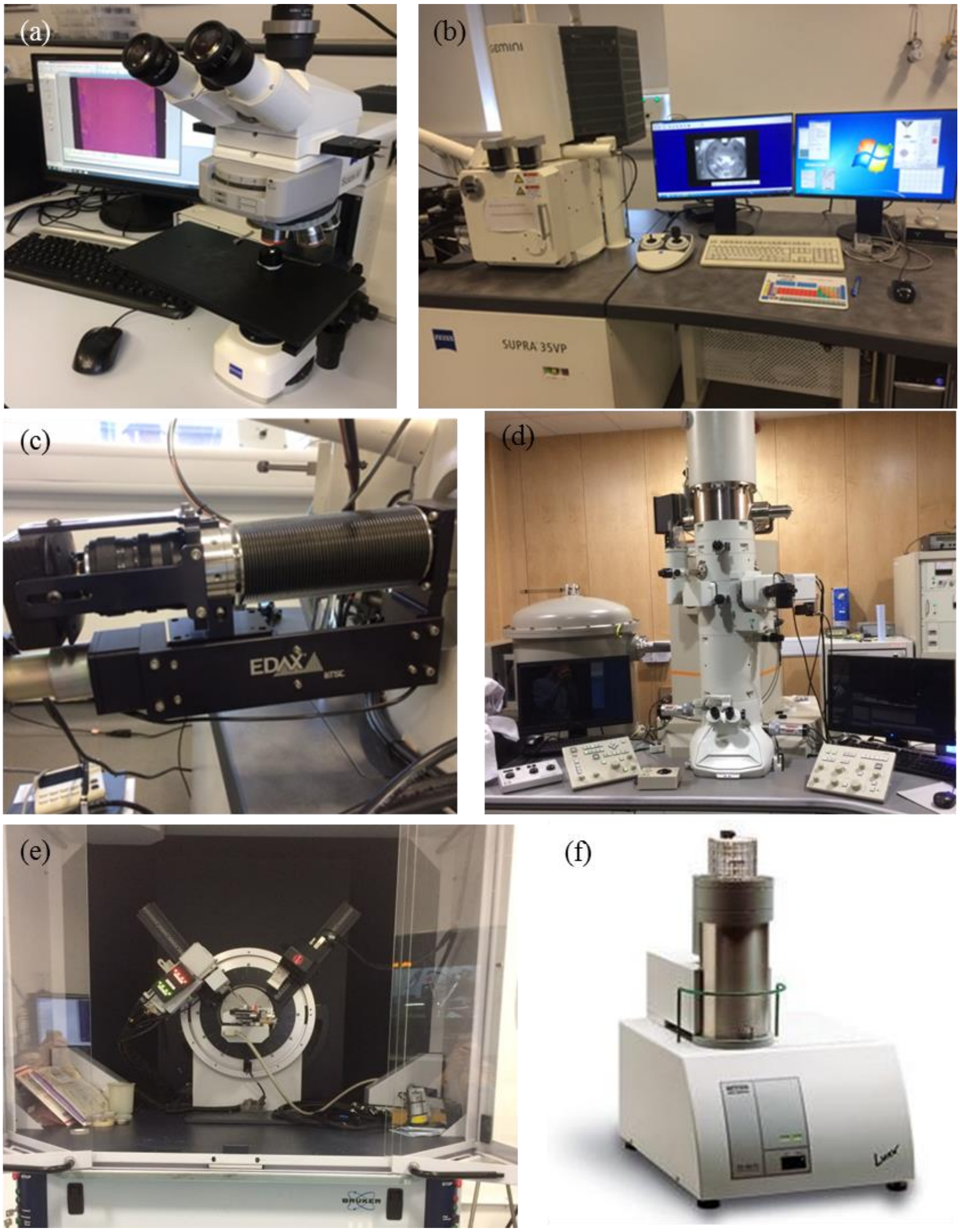

Figure 3.11 Images of facilities used in this study: (a) Zeiss Optical Axio Microscope A1 equipped with AxioCam ICc 3 camera; (b) Zeiss Supra 35VP field emission gun Scanning Electron Microscope; (c) EDAX TSL EBSD camera; (d) Transmission electron microscope type JEOL 2100; (e) Bruker D8 Advance X-Ray Diffraction equipment; (f) DSC type Netzsch STA 409 PC *Luxx*.

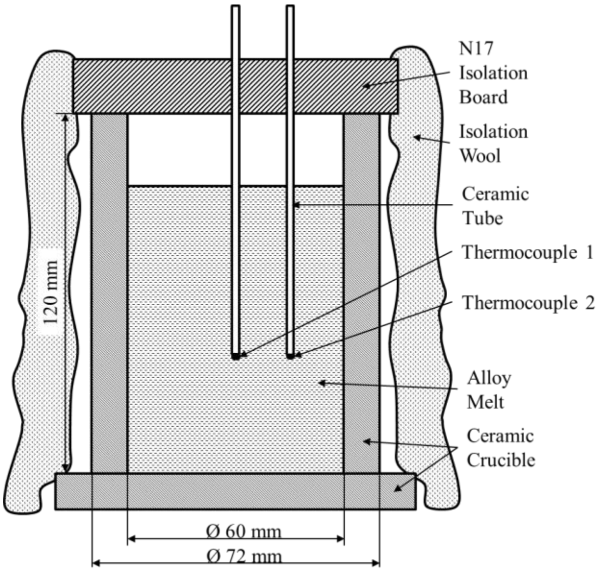

Figure 3.12 Schematic illustration of cooling curve measurement equipment.

thermocouple 2 was about 15mm away from thermocouple 1. A schematic illustration of the setup is shown in **Fig. 3.12.**

For the melt quench (MQ) cooling curve measurement, the alloy was molten and hold at 750˚C before pouring into the steel mould. The thermal couples fixed on an isolation board was inserted into the centre of the melt (about 15mm from bottom) once the melt was poured into the steel crucible (**Fig. 3.5**). The crucible was dipped in water at two temperatures, 720˚or 680˚C, monitored with identical recording parameters as the ceramic mould (CM) cooling curve measurement.

3.5. Quantification

3.5.1 Grain Size Measurement

The grain size of α-Al grain by TP-1 casting was determined on polarized light image by Carl Zeiss AxioScope A1 of anodized samples taken from the standard observation area (**Fig. 3.2b**). The quantification was performed according to ASTM E112 standard test procedures using general intercept procedures:

$$\bar{l} = \frac{1}{N_l} = \frac{L_T}{G} \tag{3.2}$$

where $\bar{l}$ is the mean intercept length, G is the grain boundary intersection count and L_T is the total length of the test line. Grain boundary intersection count (GBIC) method (**Fig. 3.13**), that the number of times one test line cuts across, or is tangent to, grain boundaries (triple point intersections are considered as 1.5 intersections), was used in this research to determine the G value. At least 20 interception lines covering 50% of grains in metallurgical observation area of TP-1 sample were examined for each data point.

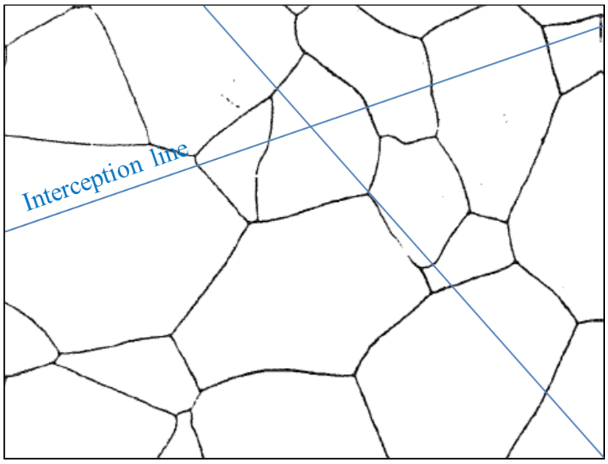

Figure 3.13 Illustration of grain boundary intersection count (GBIC) measurement.

3.5.2 Secondary Dendrite Arm Spacing Measurement

Secondary dendrite arm spacing (SDAS) measurement was conducted on polarized OM images from anodized TP-1 sample using linear intercept method via AxioVision software (Vandersluis and Ravindran, 2017). A example is demonstrated in **Fig 3.14**, which uses the following equation for SDAS (λ_2) calculation:

$$\lambda_2^i = L/(n\text{-}1) \tag{3.3}$$

where L is the length of interception line and n is the number of secondary arms counted along on side of the primary arm; thus, the mean λ_2 can be acquired using the individual SDAS (λ_2^i). At least 100 sets of λ_2^i values were obtained for each data point. Since L is specifically measured on the counted dendrite arms, dendrite asymmetry does not influence this method. Therefore, the side of primary arms chosen for the measurement does not affect the final outcome.

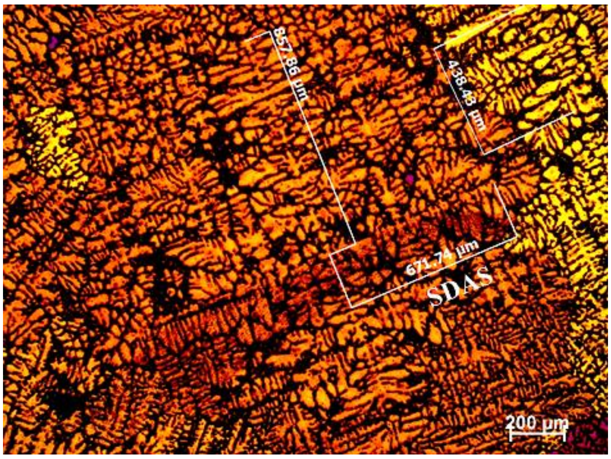

Figure 3.14 Demonstration of linear intercept method for SDAS measurement.

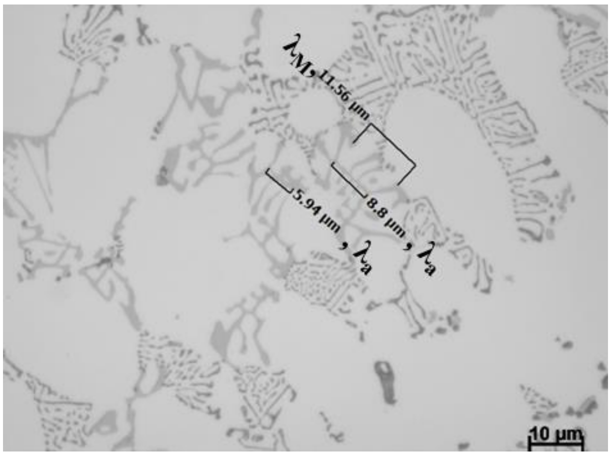

Figure 3.15 Illustration of liner intercept method for minimum eutectic lamellar spacing (λ_a) and maximum eutectic lamellar spacing (λ_M) measurement.

3.5.3 Eutectic Lamellar Spacing Measurement

This measurement was very similar approach to SDAS measurement, using linear intercept equation:

$$\lambda_{EU}^{i} = L/(n\text{-}1) \tag{3.4}$$

The λ_{EU} can then be acquired by calculating the mean value of all induvial lamellar eutectic lamellar spacing (λ_{EU}^{i}). At least 120 sets of λ_{EU}^{i} values were measured for each data point. An illustration of the measurement is shown in **Fig. 3.15** showing the difference between the minimum eutectic lamellar spacing (λ_a) and the maximum eutectic lamellar spacing (λ_M).

3.5.4 Particle Size Measurement

The particle size of both primary and eutectic Fe-IMCs were obtained by measuring the diameter of individual Fe-IMC. As shown in **Fig. 3.16**, the individual particle size was acquired by simply measuring the maximum diameter since the maximum diameter of Fe-IMC is commonly described as Fe-IMC particle size in literatures (Terzi *et al.*, 2010; Dinnis, Taylor and Dahle, 2005). At least 200 primary/eutectic Fe-IMC particles were processed for each sample.

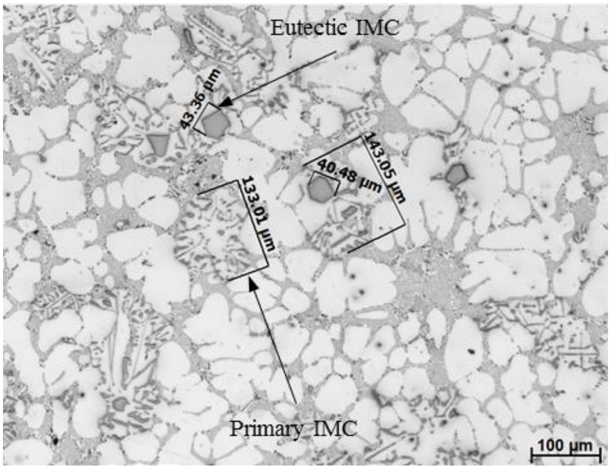

Figure 3.16 Illustration of the particle size measurement of Fe-IMCs by AxioVision.

3.5.5 Volume Fraction Measurement

The volume fraction measurement of Fe-IMCs was conducted on backscattered electron SEM images. ImageJ was used to classify the grey contrast of Fe-IMC particle and other phases so that the area fraction of grey contrast of Fe-IMC gives the area fraction of Fe-IMC in the image. With the random distribution of the phases/particles, the area fraction is equal to the volume fraction in 3D (Underwood, 1969). At least 20 images with magnification of x500 were processed for each data point.

Chapter 4 Solidification of Fe-rich Intermetallic Compounds in Al-5Mg-2Si-1.2Fe-0.7Mn Alloy

The objective of this chapter is to investigate the solidification behaviour of Fe-IMCs in Al-5Mg-2Si-1.2Fe-0.7Mn alloy along with the effect of cooling rates and casting temperatures. In this study various casting methods was used, such as TP-1, Cu wedge mould, cooling in furnace (CF), cooling in air (CA) etc. This study includes results from thermodynamic calculations, cooling curve measurement, optical microscopy, scanning electron microscopy, transmission electron microscopy, X-Ray diffractometer and differential scanning calorimetry. The solidification sequence of this alloy, formation temperatures of Fe-IMCs, effect of cooling rate and casting temperature on different Fe-IMCs are discussed.

4.1 Solidification Behaviour

4.1.1 Phase Diagram Calculation

CALculation of PHAse Diagram (CALPHAD) method was applied here to predict the equilibrium phase diagram and phase fraction of Al-5Mg-2Si-1.2Fe-0.7Mn alloy with solidification under Scheil rule. The cross section of calculated equilibrium phase diagram of Al-5Mg-2Si-0.7Mn-*x*Fe is predicted with Pandat^{TM} 8.2 (CompuTherm LLC) using PanAl2013 database and presented in **Fig. 4.1**. When Fe concentration in the alloy is at 1.2wt.% and solidified under equilibrium condition, the solidification of the primary α-AlFeMnSi commences at liquidus temperature of 670.4˚C, and then followed by the formation of eutectic α-AlFeMnSi/α-Al at 620.5˚C and Mg_2Si/α-Al/$Al_{13}Fe_4$ at 584.2˚C. After that, small amount of $Al_{13}Fe_4$ and $Al_6(Fe,Mn)$ forms. The solidification of current alloys is expected to occur under non-equilibrium condition during casting due to the difference in kinetics, which will be discussed later in this chapter. During the calculation, impurity elements such as Ti and Cu were not considered as the concentration sum of these elements is low enough (<0.1wt.%) to be taken to be negligible.

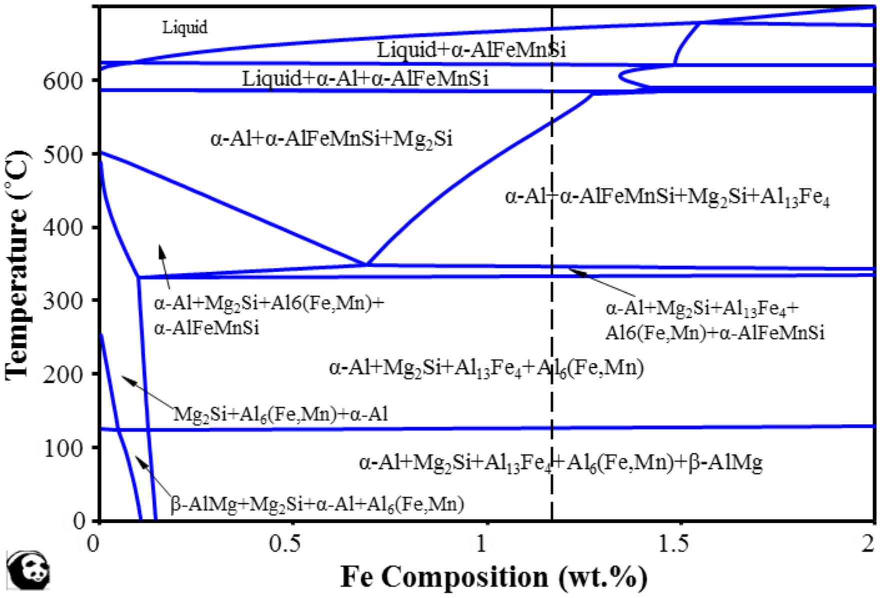

Figure 4.1 Cross section of equilibrium phase diagram of Al-5Mg-2Si-0.7Mn-*x*Fe using Pandat^{TM} 8.2. Dash line marks Fe composition at 1.2 wt.%

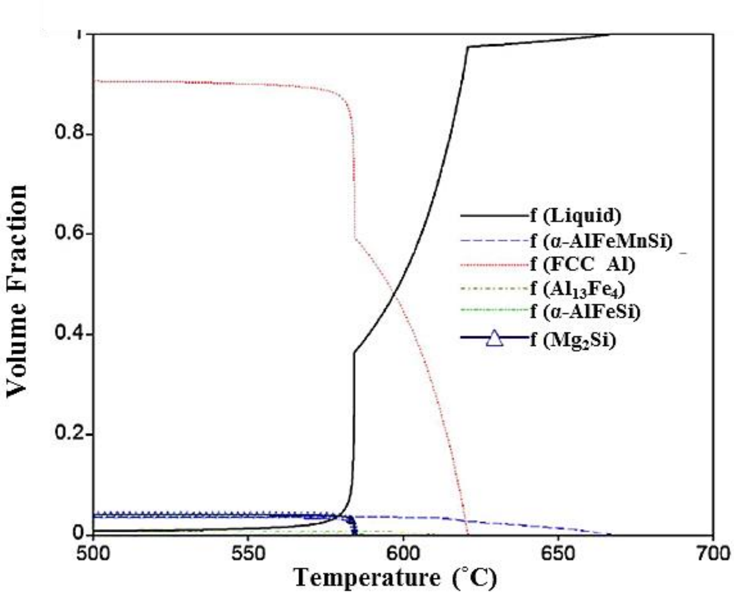

Figure 4.2 The liquid fraction of Al-5Mg-2Si-1.2Fe-0.7Mn alloy as a function of temperature during solidification calculated with Pandat^{TM} 8.2 under Scheil rule.

The phase volume fractions of Al-5Mg-2Si-1.2Fe-0.7Mn alloy as a function of temperature during solidification is shown in **Fig. 4.2**. The solidification temperature of binary eutectic α-AlFeMnSi/α-Al is not consistent and decrease as solidification continues. Meanwhile, the solidification temperature of the following ternary eutectic

Mg_2Si/α-Al/Fe-IMC is consistent as the solidification continues. The calculated volume fraction of each phase in non-equilibrium conditions is shown in **Table 4.1**. When the solidification process finished, the solid consists of 89.6% of α-Al, 3.49% of α-AlFeMnSi, 3.9% of Mg_2Si, 0.9% of $Al_{13}Fe_4$ and 0.38% of Al_8Fe_2Si by volume. More specifically, the volume fractions of the primary and eutectic α-AlFeMnSi are 2.7% and 0.79% of, respectively.

Table 4.1 The solid volume fraction of each phase at different solidification stages calculated with Pandat^{TM} 8.2.

No.	**Transformation**	**Temperature (°C)**	**Volume fraction**
1	L → α-AlFeMnSi	670.4	α-AlFeMnSi: 2.7vol.%
2	L → α-Al + α-AlFeMnSi	620.5	α-AlFeMnSi: 0.39vol.%; α-Al: 14.7%
3	L → α-Al + α-AlFeMnSi + $Al_{13}Fe_4$	615.7	α-AlFeMnSi: 0.4vol.%; α-Al: 38.4vol.%; $Al_{13}Fe_4$: 0.8vol.%.
4	L → α-Al + Al_8Fe_2Si	591.2	α-Al: 5.5vol.%; Al_8Fe_2Si: 0.15vol.%
5	L → α-Al + Mg_2Si + Al_8Fe_2Si + $Al_{13}Fe_4$	584.2	α-Al: 31vol.%; $Al_{13}Fe_4$: 0.1vol.%; Al_8Fe_2Si: 0.23vol.%; Mg_2Si: 3.9vol.%.

4.1.2 Microstructure

4.1.2.1 Primary α-AlFeMnSi

The microstructure of Al-5Mg-2Si-1.2Fe-0.7Mn alloy achieved with TP-1 casting 650˚C is shown in **Fig. 4.3a**. The primary α-AlFeMnSi generally exhibits polyhedral morphology located in the centre of a eutectic α-AlFeMnSi/α-Al grain. 3D morphology of primary α-AlFeMnSi is revealed by deep-etching (**Fig. 4.3a**) showing dominantly rhombic dodecahedron morphology, indicating strong anisotropy of primary α-AlFeMnSi particle. However, the presence of the particles of these morphologies is closely dependent on casting conditions despite CALPHD prediction that α-AlFeMnSi is a thermodynamically stable phase in Al-5Mg-2Si-1.2Fe-0.7Mn.

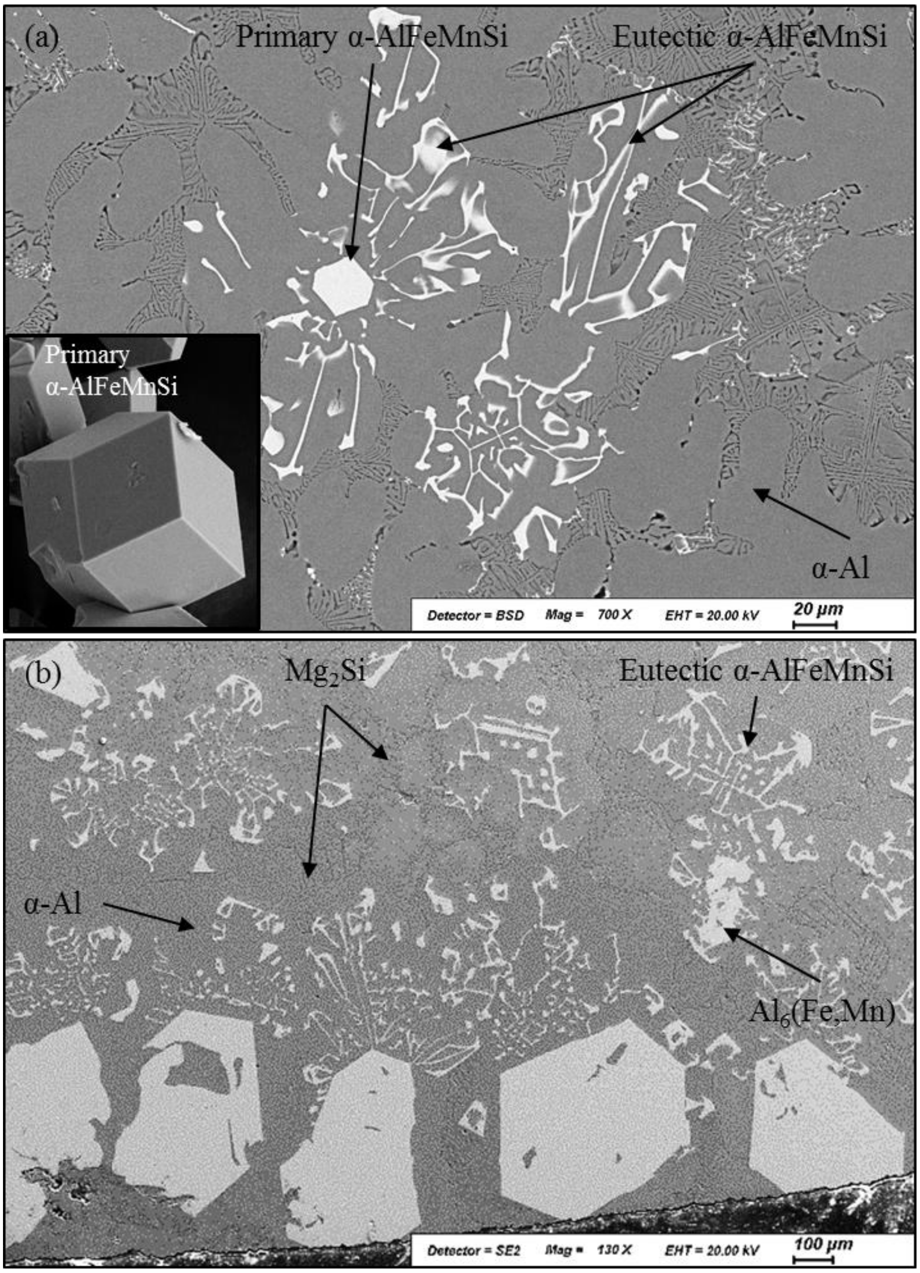

Figure 4.3 SEM micrographs (a) Al-5Mg-2Si-1.2Fe-0.7Mn alloy by TP-1 casting inserted with 3D morphology of primary α-AlFeMnSi and (b) cooling in furnace, showing the primary α-AlFeMnSi, Al_6(Fe,Mn), eutectic α-AlFeMnSi, α-Al and eutectic Mg_2Si. The phase identification is given with SEM/EDS.

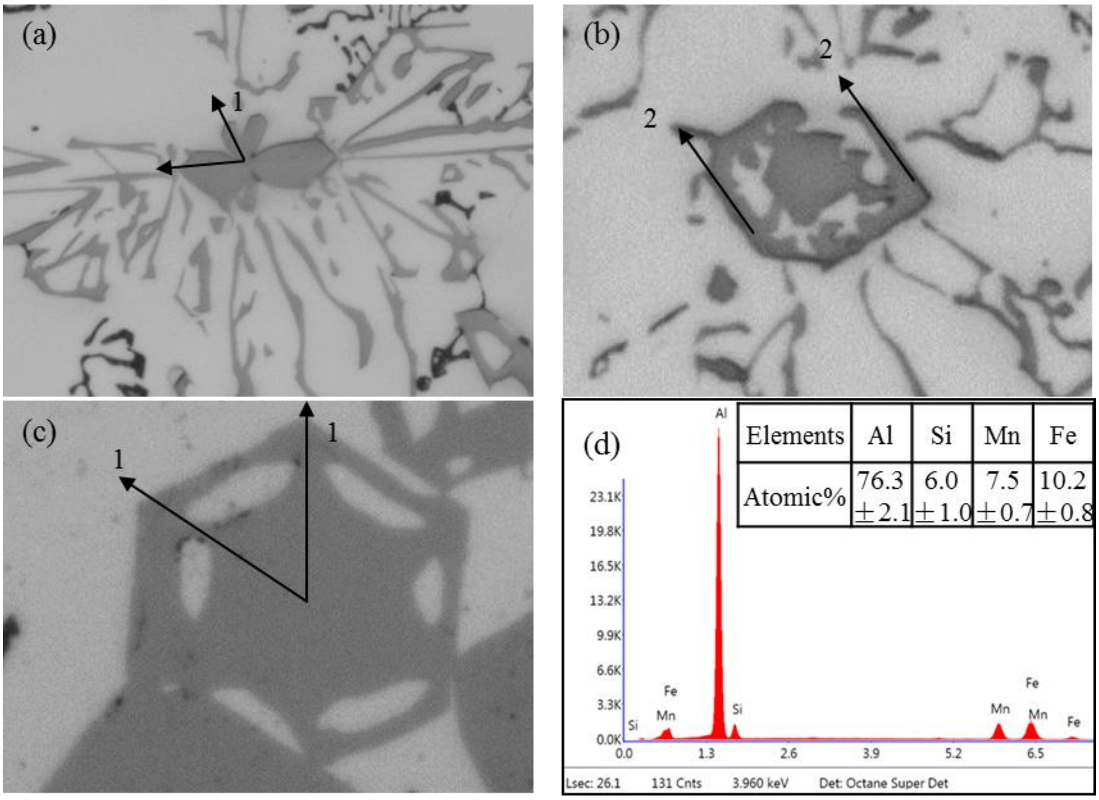

Figure 4.4 Optical micrographs showing (a – c) the morphology of primary α-AlFeMnSi; (d) the EDS results taken from several primary particles (attached table showing the average chemical composition). Arrows marked as 1 and 2 indicates the primary and secondary branches, respectively.

Further, as shown win **Fig 4.3b,** in furnace cooling condition the primary α-AlFeMnSi maintains the polyhedral morphology but coarser than that of TP-1 casting. There are some variations in the morphology of the primary Fe-IMC phase in TP-1 samples, as shown in **Fig. 4.4**. The primary Fe-IMCs have coarse star-like (**Fig. 4.4a**), hollowed polyhedral (**Fig. 4.4b**, **c**) and compact polyhedral morphologies (**Fig. 4.4d**). Despite the variation in morphology, these α-AlFeMnSi particles show almost identical chemical composition ($Al_{12}(Fe,Mn)_3Si$) with SEM/EDS analysis. This suggests that the morphology variation is due to random sectioning orientation. For instance, the compact polyhedral morphology of α-AlFeMnSi may be caused by random sectioning of the complex particles or a specific orientation sectioning of the developing particles. Further, the morphology variation reveals that the growth of primary α-AlFeMnSi has number of stages: initiation (**Fig. 4.4a**), hollowed polyhedron (**Fig. 4.4b** and **Fig. 4.4c**) and compact polyhedron (**Fig. 4.3a**). During the initial stage of the growth of primary α-AlFeMnSi, there are] a few symmetrical hillocks on the particle (indicated with arrows marked as “1” in **Fig 4.4a**). At the later growth stage, secondary growth orientation (see arrow “2” in **Fig 4.4b**) starts to develop as well as the primary growth orientation. In the end, when growth completed the hollows are filled during the isotropic growth, showing a compact polyhedral morphology.

The growth of anisotropic primary α-AlFeMnSi was further investigated with Al-6Si-5Fe-4Mn alloy due to the higher volume fraction of primary α-AlFeMnSi obtained in this alloy. As shown in **Fig. 4.5**, two typical types of polyhedral primary α-AlFeMnSi that was observed which share the similar morphological characteristics with primary α-AlFeMnSi in Al-5Mg-2Si-1.2Fe-0.7Mn. As shown in **Fig 4.5a**, the primary branches (indicated with solid arrows) have approximately 60˚ angle to each other, exhibiting a hexagonal morphology. Meanwhile, the primary branches in α-AlFeMnSi particle shown in **Fig. 4.5b** has 90˚ angle to each other, resulting in a square morphology for the primary α-AlFeMnSi particle. The facet morphology are generally cause by growth anisotropy (Dantzig and Rappaz, 2009). Given the BCC structure of primary α-AlFeMnSi and some description on the growth of bulk primary α-AlFeMnSi (Sunagawa, 1999 2009; Gao, 2013)., the preferred growth orientation of primary α-AlFeMnSi can be proposed basing on the observation of the OM images (**Fig. 4.5**).

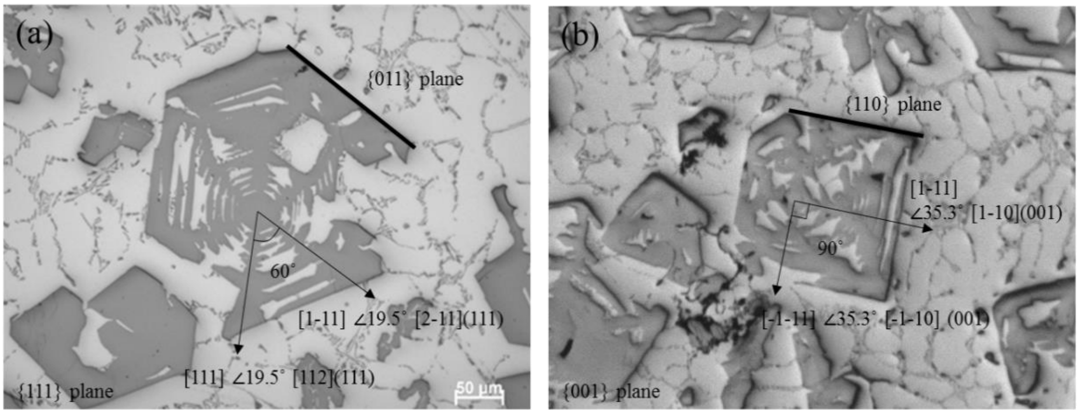

Figure 4.5 Morphologies of growing primary α-AlFeMnSi particles (a) on {111} plane and (b) on {001} plane before completing into compact polyhedral structure in Al-6Si-5Fe-4Mn alloy by TP-1 casting. The arrows indicate secondary arm orientations whose angles to the observation plane were shown. Solid lines indicate the intersection of exposed plane and observation plane.

4.1.2.2 Eutectic α-AlFeMnSi

The microstructure of Al-5Mg-2Si-1.2Fe-0.7Mn alloy shown in **Fig. 4.3** and **Fig. 4.7**, has the binary eutectic α-AlFeMnSi/α-Al which exhibits Chinese-script morphology. This type of eutectic is often described as irregular or anomalous eutectic (Porter, Easterling and Sherif, 2009; Flemings, 1974). 3D morphology of the eutectic α-AlFeMnSi was revealed by deep-etching, as shown in **Fig. 4.6b** and **Fig. 4.6c**. It isseen that the α-AlFeMnSi eutectic exhibits a branched structure where branch tips (region within solid-line circle in **Fig. 4.6c**) tend to be coarser compared with the branch joint (region within dash-line circle in **Fig. 4.6c**). Although the coarsening of α-AlFeMnSi branch tip is relatively more significant compared with the cases with Al-Al_6Fe and Sn-Cu eutectic system (Allen *et al.*, 1998; Elliott, 2013), the tip coarsening phenomenon has been addressed as common eutectic solidification behaviour in other alloy systems (Kurz and Fisher, 1986). As shown in **Fig 4.3** and **Fig. 4.7** there are physical connections between eutectic α-AlFeMnSi and primary α-AlFeMnSi observed in microstructure; and these connections are mostly located at the corner/edge of the primary α-AlFeMnSi polyhedrons. The physical relationship between primary α-AlFeMnSi, eutectic α-AlFeMnSi and the surrounding α-Al has been revealed by polarized light using OM (**Fig. 4.7**), showing both primary and eutectic α-AlFeMnSi (dark areas) are contained within the same α-Al grain (area with the same colour) which also compresses a considerable volume of α-Al which does not have any typical eutectic structure. Furthermore, a large amount of α-Al is observed in microstructure without any α-AlFeMnSi or other Fe-IMCs. This gives an ideal of the severity of the drift in the α-AlFeMnSi/α-Al eutectic reaction from the couple growth regular eutectics and an insight of the solidification process of eutectic α-AlFeMnSi which will be discussed later. Given these points, the eutectic α-AlFeMnSi/α-Al in Al-5Mg-2Si-1.2Fe-0.7Mn alloy can be described as divorced (irregular) eutectic.

4.1.2.3 Eutectic Mg_2Si

Eutectic Mg_2Si, as shown in **Fig. 4.8**, exhibits irregular eutectic morphology with very fine lamellar spacing (not quantified here), located between α-Al dendrite arms and α-Al grain boundaries. The composition of the Mg_2Si phase was confirmed with EDS as shown in **Table 4.2**. There are two type of Mg_2Si eutectic observed in the microstructure of Al-5Mg-2Si-1.2Fe-0.7Mn by TP-1 casting. With the assistance of SEM/EDS mapping and microstructure observation, the first one have a binary Mg_2Si/α-Al structure, whereas the other one appears to be ternary Mg_2Si/α-Al/Fe-IMC. Interestingly, the binary Mg_2Si eutectic often contains a polyhedral Mg_2Si core

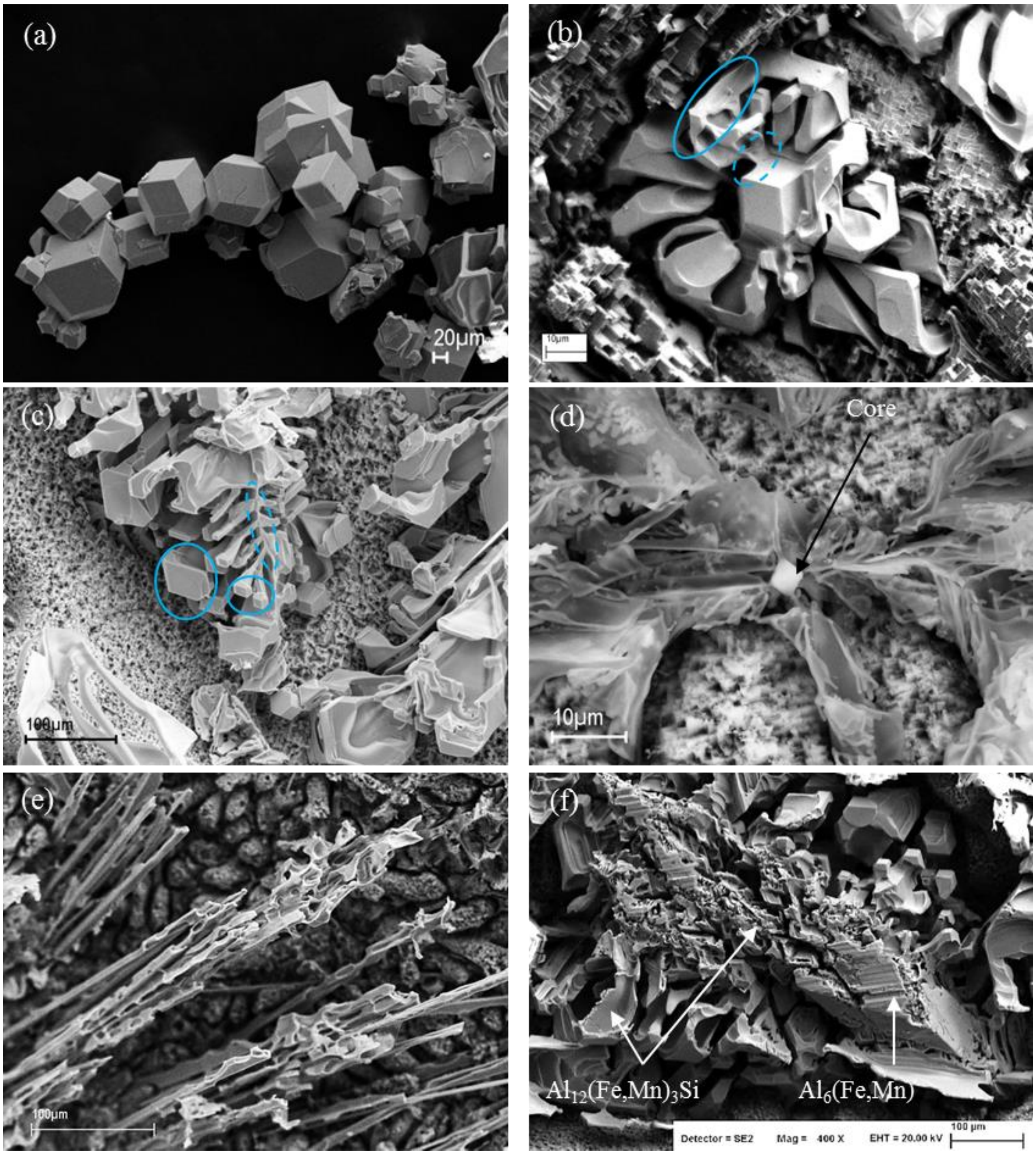

Figure 4.6 SEM micrographs showing the 3 dimensional (3D) morphologies of (a) primary α-AlFeMnSi, (b) primary α-AlFeMnSi and its attached eutectic α-AlFeMnSi, (c) eutectic α-AlFeMnSi branches and (d) eutectic Mg_2Si with a octahedral compact core, (e) $Al_6(Fe,Mn)$ rods and (f) transverse section of $Al_6(Fe,Mn)$/α-AlFeMnSi duplex particle that were obtained in Al-5Mg-2Si-1.2Fe-0.7Mn alloy by 15wt.% HCl etching.

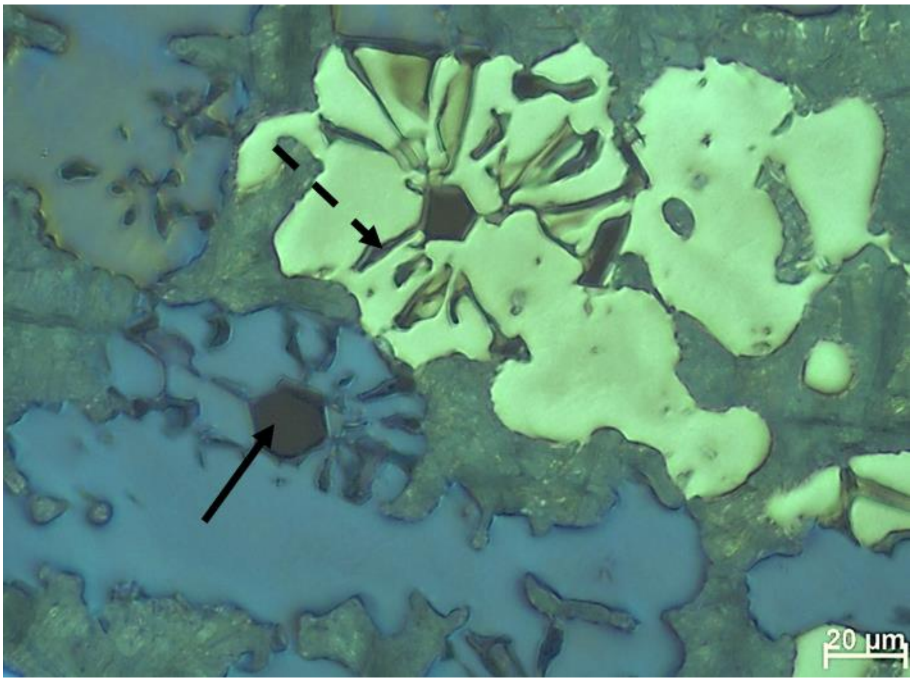

Figure 4.7 OM polarized light image showing the microstructure of α-AlFeMnSi/α-Al eutectic grain in Al-5Mg-2Si-1.2Fe-0.7Mn alloy etched Barker's regent. The solid arrow indicates the primary α-AlFeMnSi whilst dash line arrow indicates the branch of eutectic α-AlFeMnSi.

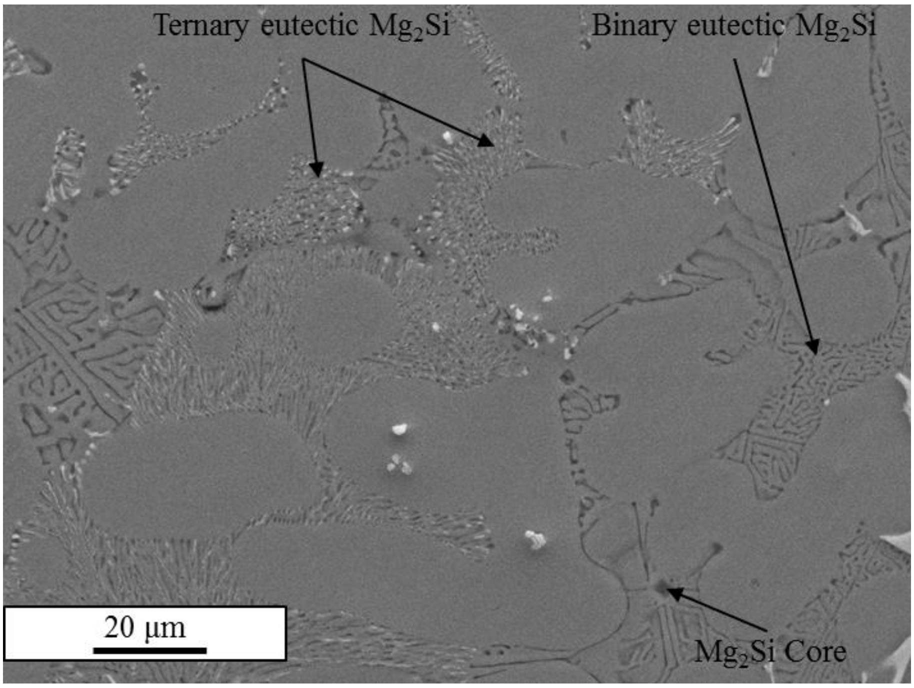

Figure 4.8 SEM image showing the morphologies of few types of Mg_2Si in Al-5Mg-2Si-1.2Fe-0.7Mn alloy by TP-1 casting including polyhedral Mg_2Si core, binary eutectic Mg_2Si/α-Al eutectic and ternary eutectic Fe-IMC/Mg_2Si/α-Al.

in the centre of the eutectic (**Fig. 4.6** and **Fig 4.8** indicated with solid arrow), which is normally identified as primary Mg_2Si (Li, Liu and Wu, 2008; Ji *et al.*, 2013a). This means that at the early stages of the formation of Mg_2Si the local microsegregation of Mg and Si in the remaining liquid is adequate enough to exceed the eutectic point, 13.9wt.% in Al-Mg_2Si system.

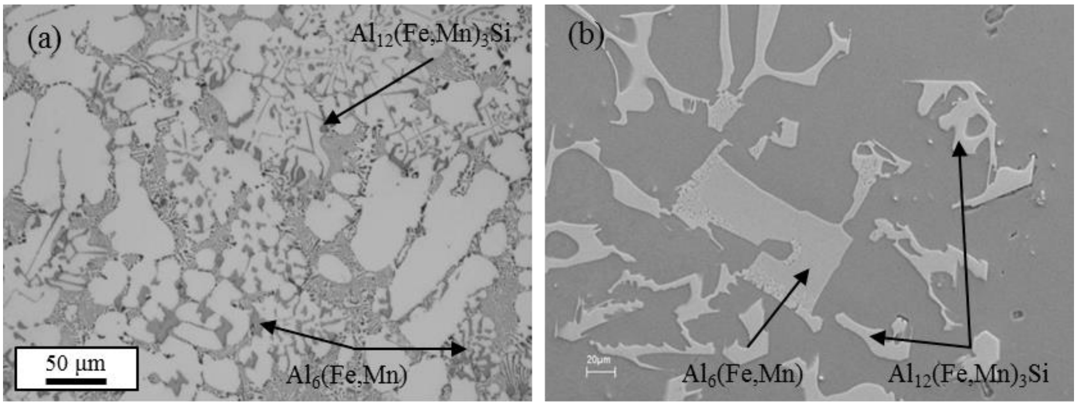

Figure 4.9 Micrographs of Al-5Mg-2Si-1.2Fe-0.7Mn alloy showing (a) the morphology of Al_6(Fe,Mn) in TP-1 casting and (b) the morphology of Al_6(Fe,Mn)/α-AlFeMnSi duplex particle in CF condition (identified with SEM/EDS).

4.1.2.4 Primary and Eutectic Al_6(Fe,Mn)

As shown in **Fig. 4.9a**, there are small amount of Al_6(Fe,Mn) clusters, confirmed with SEM/EDS, were observed in the microstructure of Al-5Mg-2Si-1.2Fe-0.7Mn alloy in TP-1 castings. It exhibits a hollowed parallelogrammatic morphology in 2D observation; and the 3D structure has been revealed in **Fig. 4.6e** showing a rod-like morphology. However, unlike the single phase Al_6(Fe,Mn) particle in TP-1 condition, the Al_6(Fe,Mn) exists in a form of Al_6(Fe,Mn)/α-AlFeMnSi duplex particles (**Fig. 4.9b**) in CF condition (0.02K/s). All such particles have a transition region which consists of α-Al regions and α-AlFeMnSi network between the coarse and compact Al_6(Fe,Mn) and α-AlFeMnSi branches. 3D observation, shown in **Fig. 4.6f**, illustrate that the Al_6(Fe,Mn) has branched columnar morphology with faceted surface and the transition region observed combined with α-AlFeMnSi branches.

4.1.3. Solidification Sequence

In this section, the phase transformation during solidification of the alloys is characterized with DSC and cooling curve measurements are presented. The two methods provided the direct observation of the phase transformation temperature and nucleation temperature of Al-5Mg-2Si-1.2Fe-0.7Mn alloy at various cooling rate. The difference between simulated ideal solidification and experimental solidification will be discussed.

4.1.3.1 DSC Curves

The samples for DSC measurement were taken from the centre of TP-1 sample cast at 650˚C. There was a sufficient amount of primary α-AlFeMnSi (3.1% according to quantification shown later) before DSC characterization that was confirmed with OM. As shown in **Fig. 4.10**, three heat flow peaks have been detected commencing at 639.0±3.4˚C, 619.5±2.1˚C and 586.0±1.7˚C, respectively, indicating the starting temperature of the phase transformations. However, there are a few minor turbulences at 614.0-610.0˚C, 608.0-605.5˚C and 590.0-586.5˚C on the cooling curves. These turbulences are most likely associated with experimental noises instead of phase transformation. Finding the liquidus temperature for a multi-component alloy system has always been difficult using DSC as the melting in the multi-component alloy system is a highly reversible transformation. Nonetheless, in this experiment the actual liquidus has been considered as the end point of the heat flow difference, which in this sample was 665.0˚C.

4.1.3.2 Cooling Curves

The cooling curve measurement was carried out with liquid metal in two containers which are ceramic mould wrapped with thermal wools and steel mould for melt quench with water (see section 3.4.7). Thermal data were monitored with two thermocouples located at the centre (T1) and 8mm from T1 horizontally (T2), respectively. As shown in **Fig. 4.11**, the cooling curves and their first derivatives recorded by two thermocouples during the solidification of Al-5Mg-2Si-1.2Fe-0.7Mn alloy in ceramic mould are almost overlapped. Thus, these results are reliable. The cooling curve and its first derivative of T2 was shifted 30s to the right along the *x*-axis for the convenience of the observation. In order to observe the transformation

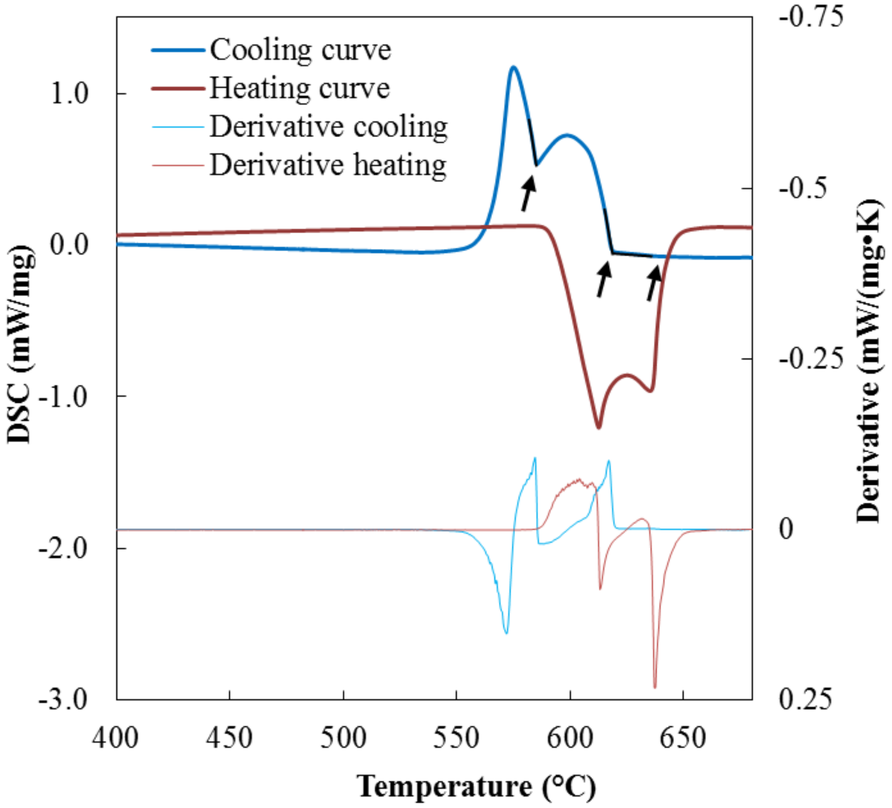

Figure 4.10 DSC analyses showing the heating and cooling curves as a function of temperature of large mass cylindrical sample (180±20mg) taken from Al-5Mg-2Si-1.2Fe-0.7Mn alloy cast withTP-1 at 650˚C; calculated first derivative of DSC heating and cooling curves as a function of temperature. Solid arrows indicate the three major heat flow changing points are at 639.0±3.4˚C, 619.5±2.1˚C and 586.0±1.7˚C, respectively.

with lower amount of latent heat released, cooling curve was also measured at a higher cooling rate experiment. As shown in **Fig. 4.12**, two cooling curves were measured from water quench experiments and their first derivatives show that the heat releasing temperatures of the system are very similar. Hence these two sets of cooling curves are considered to be reliable. The recalescence and growth temperatures for binary eutectic transformation for T1 are indicated with arrows and marked as T_R and T_G, respectively. The first and second major eutectic transformation points are indicated by arrows and marked on the derivative curve of T1 as T_{Eu1} and T_{Eu2}, respectively. For ceramic mould cooling curve measurement (0.18±0.01K/s), the data measured is selected from 680˚C where the system is isothermal. Before solidification starts, the melt cooling rate stabilized at around 0.18±0.01K/s (First derivative in **Fig. 4.11**).

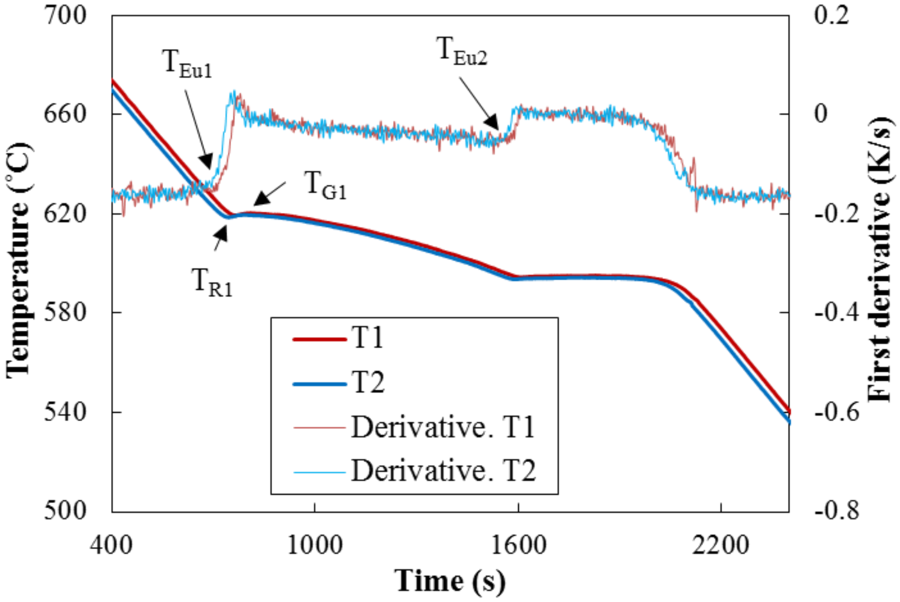

Figure 4.11 Two sets of measured cooling curves and its first derivatives of Al-5Mg-2Si-1.2Fe-0.7Mn alloy cast at 730˚C into a ceramic crucible covered with 13mm thermal insulation. T1 is right in the centre of the mould, both horizontally and vertically. T2 is vertically in the centre of the mould, horizontally 8mm away from the centre. The recalescence and growth temperatures for binary eutectic transformation for T1 are indicated with arrows and marked as T_R and T_G, respectively. The first and second major eutectic transformation points are indicated by arrows and marked on the derivative curve of T1 as T_{Eu1} and T_{Eu2}, respectively.

There is no recalesence observed until 620.4±0.2˚C. Two major growth temperatures (T_G), which can be considered as the subtraction of a small growth undercooling from the phase transformation temperature, are 620.4±0.2˚C and 594.0±0.1˚C, respectively. Since the growth undercooling (ΔT_G) is relatively small for phase transformations, it can be considered that the growth temperature is approximately equals to the equilibrium phase formation temperature. The maximum nucleation undercooling (ΔT_M) during solidification is defined to be the temperature difference between growth temperature (T_G) and recalescence starting temperature (T_R). As shown in **Fig. 4.11**, the transformation temperature ranges of the binary and ternary eutectic transformations in this cooling curve measurement are about 1.1K and 0.7K, respectively.

As shown with CALPHAD approach prediction (see **Table 4.1** in section 4.1.1), ideally large volume fraction (60.34%) of solid should solidify continuously within the temperature range 620.5˚C to 584.2˚C, and 35.23% of solid should be solidifies below

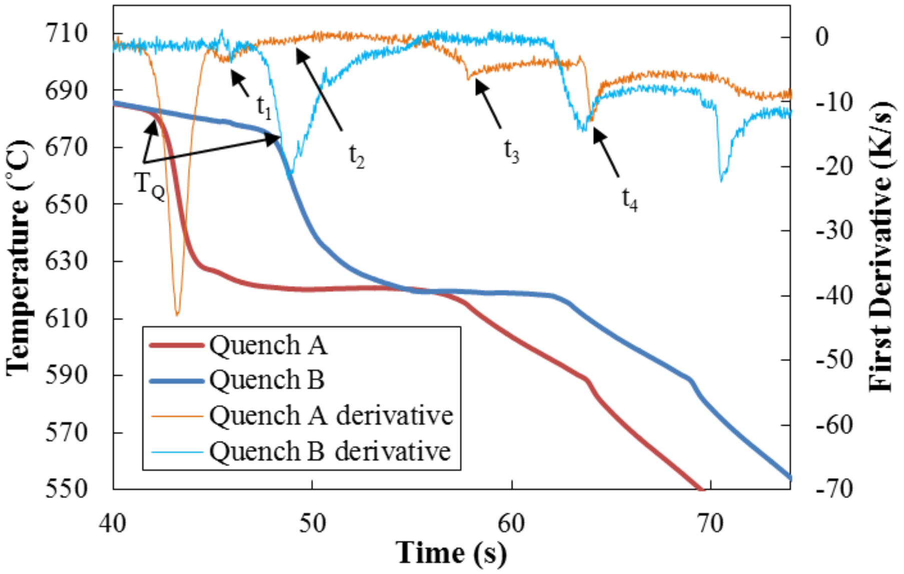

Figure 4.12 Two sets of measured cooling curves and their first derivatives for Al-5Mg-2Si-1.2Fe-0.7Mn alloy quenched into water from 680±3˚C in the steel mould by water. T_Q indicates the quenching temperature. On Quench A derivative curve t_1, t_2, t_3 and t_4 points where the cooling rate increased, represent the first, the second, the third and the fourth phase transformation points, respectively.

584.2˚C till the end of the solidification. The 620.5˚C is considered as binary eutectic (α-AlFeMnSi/α-Al) formation temperature. Although calculated ternary eutectic (Mg_2Si/α-Al/Fe-IMC) transformation temperature is 584.0˚C, the measured ternary eutectic transformation temperature appears to be 594.0±0.1˚C from the experimental cooling curve. When the alloy system is complex, actual solidification process may deviate significantly from the CALPHAD approach prediction due to the complexity in atomic interaction when the system is complex and the non-equilibrium solidification condition.

For steel mould cooling curve measurement (45±15K/s), the alloy was molten at 750˚C and held for an hour before pouring into an ø40x50mm steel mould (**Fig. 3.5**).

Two thermocouples were inserted into the melt once melt was transferred into the steel mould (see section 3.4.7). Prior to quenching, the cooling rate shown in **Fig. 4.12** stabilized at around 0.15K/s. However, the recalescence temperature was unable to be identified as the system heat releasing was significantly larger than the latent heat releasing from the melt. Therefore, the first derivatives increasing points of the cooling curves, which can be considered as recalescence starting points, are marked in **Fig 4.12** as t_1, t_2, t_3 and t_4, are 624.1±2.2˚C, 618.9±0.6˚C, 614.7±2.1˚C and 585.7±2.3˚C, respectively. The maximum nucleation undercooling ΔT_N for binary eutectic transformation in steel mould experiment (45±15K/s) is hard to describe using the principle for determining T_G and T_R with previous case, as the heat extraction is too rapid for recalescence. Thus, the ΔT_N for primary transformation and eutectic transformations cannot be concluded from the experimental result as the recalescence for these two transformations was not observed owing to the large transformation temperature range for primary α-AlFeMnSi (50K), α-AlFeMnSi eutectic (35K) and Mg_2Si eutectic (40K) as suggested by equilibrium phase diagram (**Table 4.1**).

4.2 Phase Identification

For any new alloy system and casting conditions, it is crucial to confirm the thermodynamically predicted phases with experimental analyses. For this purposes, two casting methods, TP-1 and CF, were adopted for microstructure observation and phase identification. Characterization techniques, including OM, SEM and TEM, were used for microstructure observation. Chemical composition and crystal structure of the phases were determined with SEM/EDS, XRD and SAED. The average compositions and their error associate for existing phases in Al-5Mg-2Si-1.2Fe-0.7Mn alloy are shown in **Table 4.2**. EDS analysis is considered reliable as the chemical compositions remained within errors. The morphologies of solidified phases were presented in section 4.1.2. Generally any identical phase should have the same chemical composition and growth habit; hence in this study, the phases are classified using chemical compositions and observed morphologies. Polyhedral/Chinese-script Fe-IMCs, hollowed-rod/skeleton-like Fe-IMCs, star-like Fe-IMC and the lamellar irregular eutectic, have the stoichiometry of

Table 4.2 Chemical composition of the major phases in Al-5Mg-2Si-1.2Fe-0.7Mn alloy at two cooling rate, 3.5K/s (TP-1) and 0.02K/s (CF).

Sample	**Phase Morphology**	**Elements (at.%)**					**Stoichiometry**
		Al	**Mg**	**Fe**	**Mn**	**Si**	
TP-1	Polyhedral	Bal.	-	10.2±1.0	7.1±0.7	6.0±0.8	$Al_{12}(Fe,Mn)_3Si$
	Chinese-Script	Bal.	-	10.8±1.7	5.5±2.2	5.8±1.0	$Al_{12}(Fe,Mn)_3Si$
	Hallowed Rod	Bal.	-	9.4±0.4	4.6±0.3	-	$Al_6(Fe,Mn)$
	Skeleton	Bal.	-	10.6±2.4	4.7±2.1	-	$Al_6(Fe,Mn)$
	Star-like	Bal.	-	16.4±1.4	5.6±0.7	2.0±0.4	$Al_{38}(Fe,Mn)_{11}Si$
	Lamellar Eutectic	-	66.6±3	-	-	33.4±3	Mg_2Si
	Matrix	Bal.	3.6±0.6	-	-	-	-
CF	Polyhedral	Bal.	-	10.7±1.1	7.5±0.8	5.8±0.9	$Al_{12}(Fe,Mn)_3Si$
	Chinese -Script	Bal.	-	11.6±1.3	6.0±1.4	5.9±1.5	$Al_{12}(Fe,Mn)_3Si$
	Hallowed Rod	Bal.	-	9.3±0.3	5.0±1.0	-	$Al_6(Fe,Mn)$
	Lamellar Eutectic	-	63.3±5	-	-	36.7±4.1	Mg_2Si
	Matrix	Bal.	3.3±0.2	-	-	-	-

$Al_{12}(Fe,Mn)_3Si$, $Al_6(Fe,Mn)$, $Al_{38}(Fe,Mn)_{11}Si$ and Mg_2Si, respectively. However, the skeleton-like Fe-IMC and star-like Fe-IMC were not observed in the sample by CF conditions as neither microstructure observation nor EDS analysis can detect the existence these two phases. EDS spectrum from α-Al in TP-1 shows that there is about 3.3at.% of Mg in the solid solution distributed uniformly in the matrix. Interestingly, there was a macro segregation of Mg in CF samples where the Mg concentration was around 4.4at.% at the bottom of the sample where the primary α-

AlFeMnSi sediment locate and 3.0at.% in other areas where $Al_6(Fe,Mn)/\alpha$-AlFeMnSi duplex particle exists.

4.2.1 Chemical Composition

α-AlFeMnSi particles have a very similar stoichiometry to that of $Al_{12}(Fe,Mn)_3Si$, but there were some compositional variations with different casting conditions. The average composition and the composition fluctuation are sown in **Table 4.2**. As shown in **Fig. 4.13**, the concentrations of Fe in primary and eutectic α-AlFeMnSi are higher at a cooling rate of 0.02K/s compared with 3.5K/s, by 0.5at.% and 0.8at.%, respectively. Same applies to Mn concentration in primary and eutectic α-AlFeMnSi which are both higher at a cooling rate of 0.02K/s compared with 3.5K/s by 0.4at.% and 0.7at.%, respectively. In addition, there is generally more Fe in eutectic particles, but the Mn content in eutectic particles was up to 2.2at.% less than the primary particles. In the meantime, Si concentration and (Fe+Mn)/Si ratio showed little change when cooling rate changes at 5.8at.% and 2.9at.%, respectively.

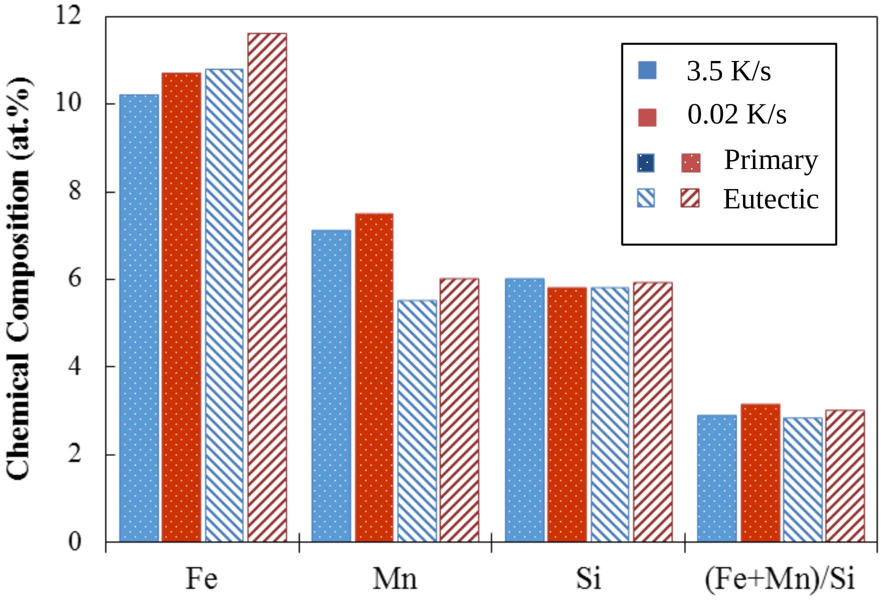

Figure 4.13 Comparison of the chemical composition variation of primary and eutectic α-AlFeMnSi solidified at cooling rates of 0.02K/s (CF) and 3.5K/s (TP-1) using values from **Table 4.2**.

SEM/EDS mapping was performed to understand the distribution of elements areas containing Fe-IMCs including eutectic α-AlFeMnSi, eutectic Mg_2Si//α-Al/Fe-IMC and Al_6(Fe,Mn) particles. For α-AlFeMnSi/α-Al eutectic, the elemental distribution of Mg, Si and Fe around eutectic α-AlFeMnSi area is shown in **Fig 4.14**. It is seen that the distribution of Si and Fe are consistent on all the α-AlFeMnSi branches. Additionally, Mg is adequately contained in α-Al matrix and Mg_2Si phase but barely detected on α-AlFeMnSi branches.

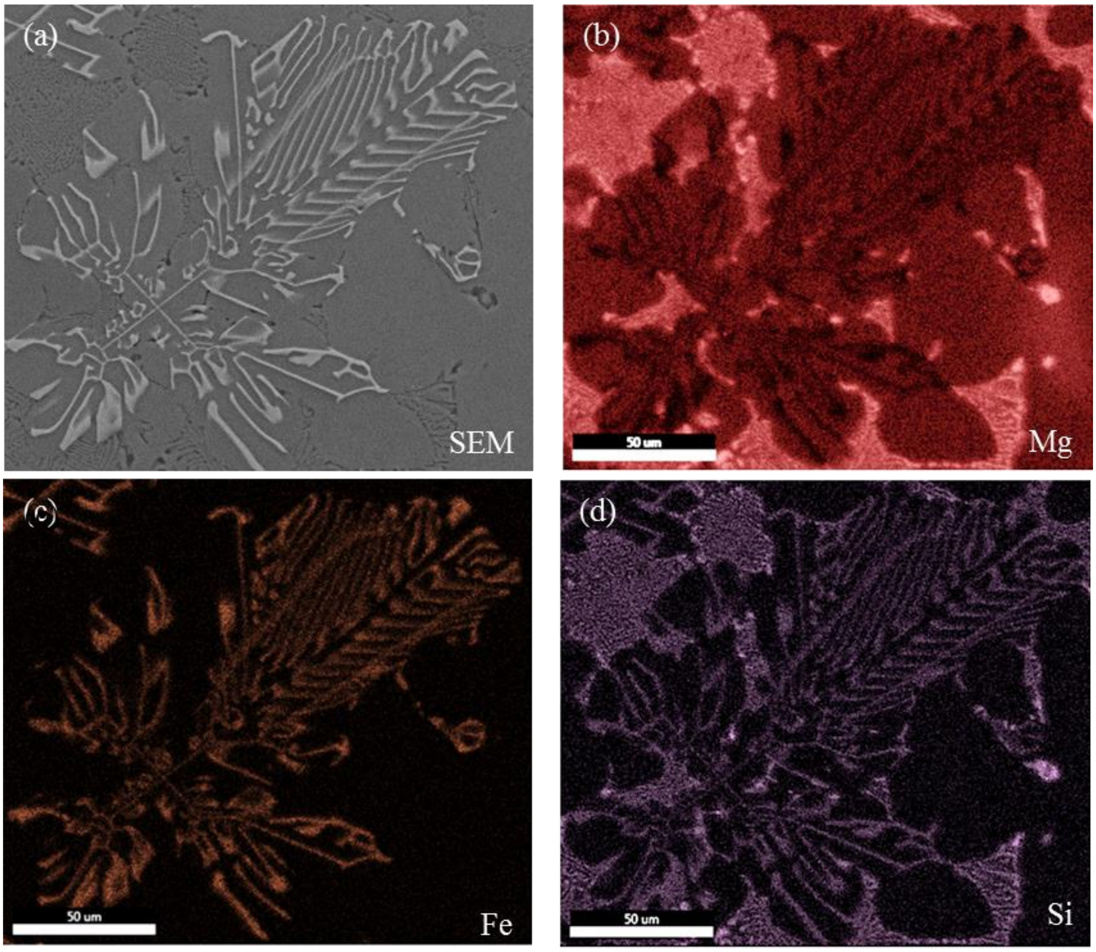

Figure 4.14 SEM micrograph showing (a) the morphology of binary eutectic α-AlFeMnSi/α-Al grain in Al-5Mg-2Si-1.2Fe-0.7Mn alloy; SEM/EDS mapping showing the elemental distribution of (b) Mg, (c) Si and (d) Fe corresponding to (a). Fe distribution in (d) is coherent with the morphology of the grey phase in (a). The quantitative chemical composition of eutectic α-AlFeMnSi is presented in **Table 4.2**.

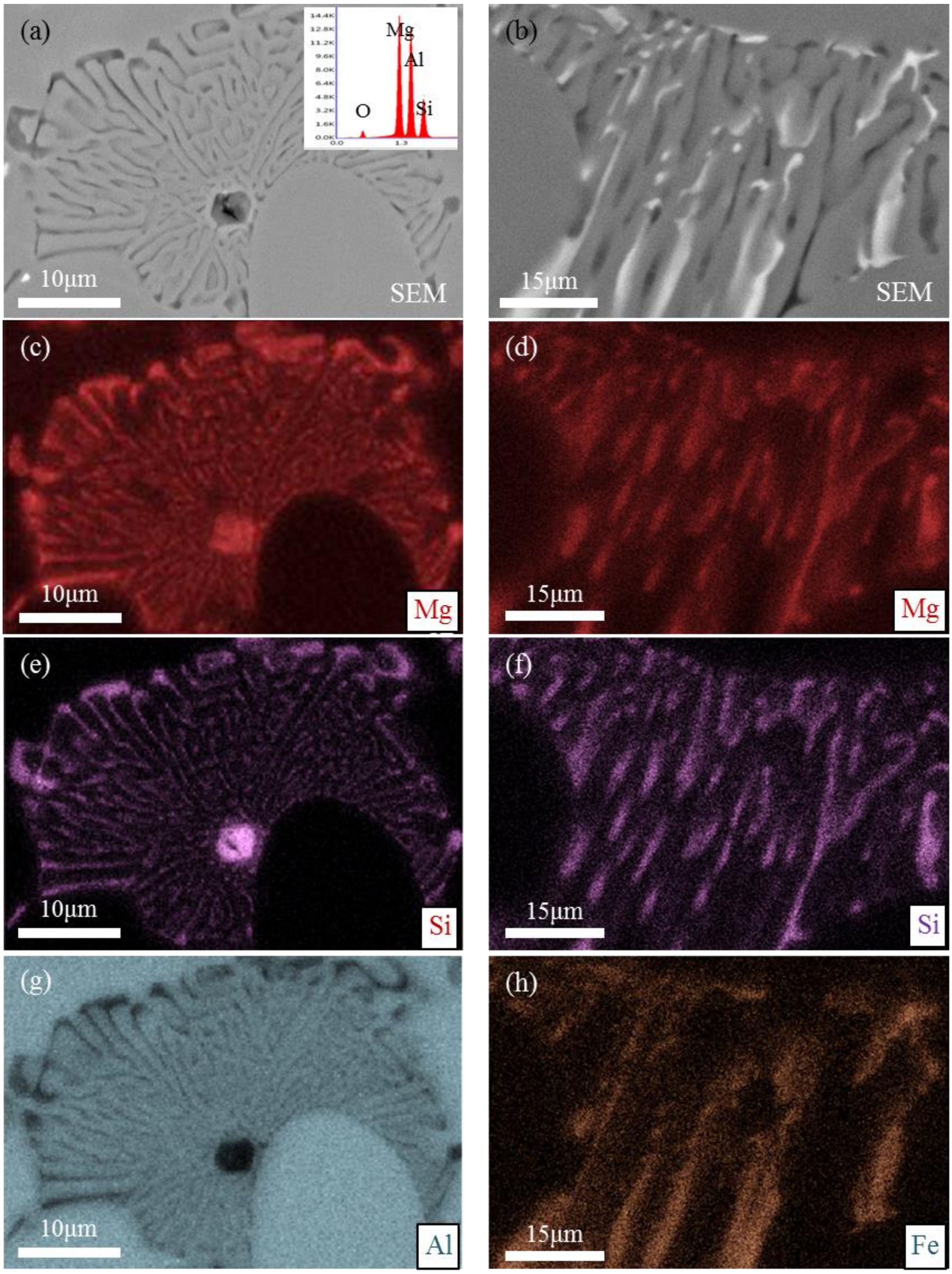

Figure 4.15 SEM micrographs showing the morphology of (a) binary Mg_2Si/α-Al eutectic and (inserted with SEM/EDS spectrum on the core area of Mg_2Si) (b) ternary Mg_2Si/α-Al/Al_6(Fe,Mn) eutectic (Mg_2Si in dark grey, Al in light grey and α-AlFeMnSi in white); SEM/EDS mapping showing the elemental distributions of (c) Mg, (e) Si and (g) Al in binary Mg_2Si/α-Al eutectic, and (d) Mg, (f) Si and (h) Fe in ternary Mg_2Si/α-Al/Fe-IMC eutectic corresponding to (a) The quantitative chemical composition of Mg_2Si will be presented in **Table 4.3**.

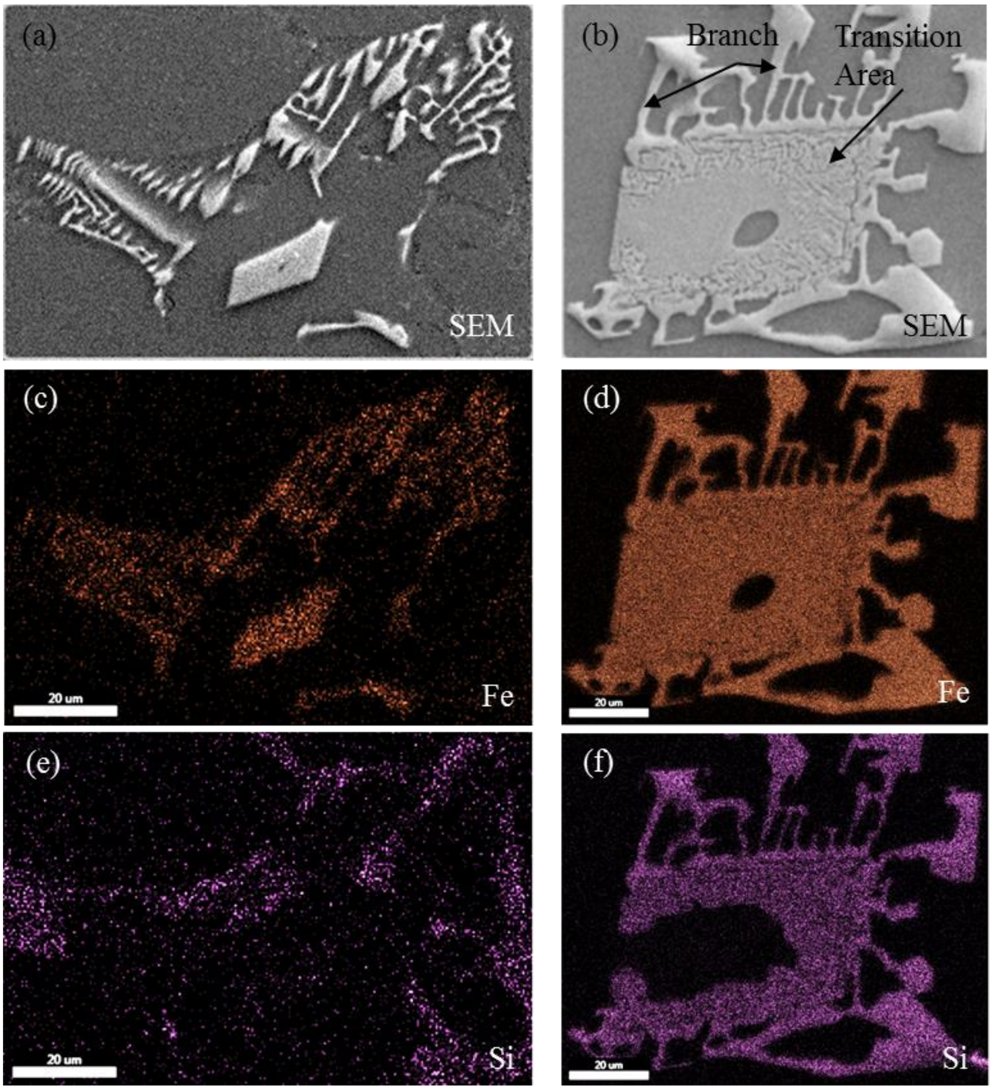

Figure 4.16 SEM micrographs showing (a) the morphology of Al_6(Fe,Mn) particle, (b) the morphology of duplex Al_6(Fe,Mn)/α-AlFeMnSi particle, (b) Fe distribution corresponding to (a), (d) Fe distribution corresponding to (b), (e) Si distribution corresponding to (a) and (f) Si distribution corresponding to (b). Transition area is indicated with solid arrow in (b). The quantitative chemical composition of duplex particle will be presented in **Table 4.3**.

As described previously there are two types of Mg_2Si which are Mg_2Si/α-Al eutectic with a compact core and ternary Mg_2Si/α-Al/Fe-IMC eutectic, which are characterised by SEM/EDS point analysis as shown in **Table 4.2**. Their elemental distributions are characterized and shown in **Fig 4.15**. The Mg and Si distribution have been consistent with dark areas in morphology image (**Fig. 4.15a** and **Fig. 4.15b**). As shown in **Fig. 4.15g**, Al was minimal in the polyhedral core area of eutectic Mg_2Si and Fe content was not detected in this eutectic region. Moreover, as shown in **Fig. 4.15h**, Fe distribution in ternary Mg_2Si eutectic region and did not overlap with Si or Mg, indicating a concentration of Al and Fe elements on Fe-IMC between eutectic α-Al and Mg_2Si lamellae.

The Al_6(Fe,Mn) particles, as demonstrated previously in section 4.1.2, occurs in different forms including Al_6(Fe,Mn) particles and branched Al_6(Fe,Mn)/α-AlFeMnSi duplex particles. As shown in **Fig. 4.16**, their elemental distribution maps indicate the regions and the interfaces of Al_6(Fe,Mn) and α-AlFeMnSi on this two types of Al_6(Fe,Mn). **Fig. 4.16c** and **Fig. 4.16e** show that the distributions of Fe and Si were completely independent and no Si was found in Al_6(Fe,Mn) phase. As shown in **Fig. 4.16d** and **Fig. 4.16f**, the distributions of Fe and Si overlap on branches and transition regions, but Si is not detected in the parallelogram particle within the transition regions. Meanwhile, in the transition region of the duplex particle, the spots in the gap of α-AlFeMnSi network were confirmed to be Al, Mg rich. The SEM/EDS point analysis performed on both branch area and transition region shows a stoichiometry of $Al_{12}(Fe,Mn)_3Si$.

4.2.2 Crystal Structure

TEM SAED and XRD were used to identify the crystal structure of α-AlFeMnSi in TP-1 and CF for Al-5Mg-2Si-1.2Fe-0.7Mn alloy. The bright field images of primary (**Fig. 4.17a**) and eutectic (**Fig. 4.17b**) Fe-IMC and SAED patterns of primary (**Fig. 4.17c**) and eutectic (**Fig. 4.17d**) Fe-IMC were obtained from Al-5Mg-2Si-1.2Fe-0.7Mn alloy using TEM. Both polyhedral and Chinese-script $Al_{12}(Fe,Mn)_3Si$ have lattice parameters consistent with a body-centred cubic, space group Im-3 and lattice parameter of 1.256nm (see **Fig. 4.18**) α-AlFeMnSi phase identified by Cooper (Cooper, 1967). The α-AlFeMnSi in CF condition usually shows a coarse polyhedral morphology (**Fig. 4.3b**) and settles at the bottom of sample along with the attached Chinese-script α-AlFeMnSi (**Fig. 4.3b**). For its crystallographic characterization, a slice of material (3mm thickness) was taken from the bottom of CF sample for Fe-IMC particle extraction using methodology introduced in section 3.3.4. Once the Fe-IMCs extracted from the material, the Fe-IMC particle powder (average particles size of 251.3±75.3μm) was characterized with XRD. As shown in **Table 4.4**, the experimentally measured data shows very good matching with the standard crystal

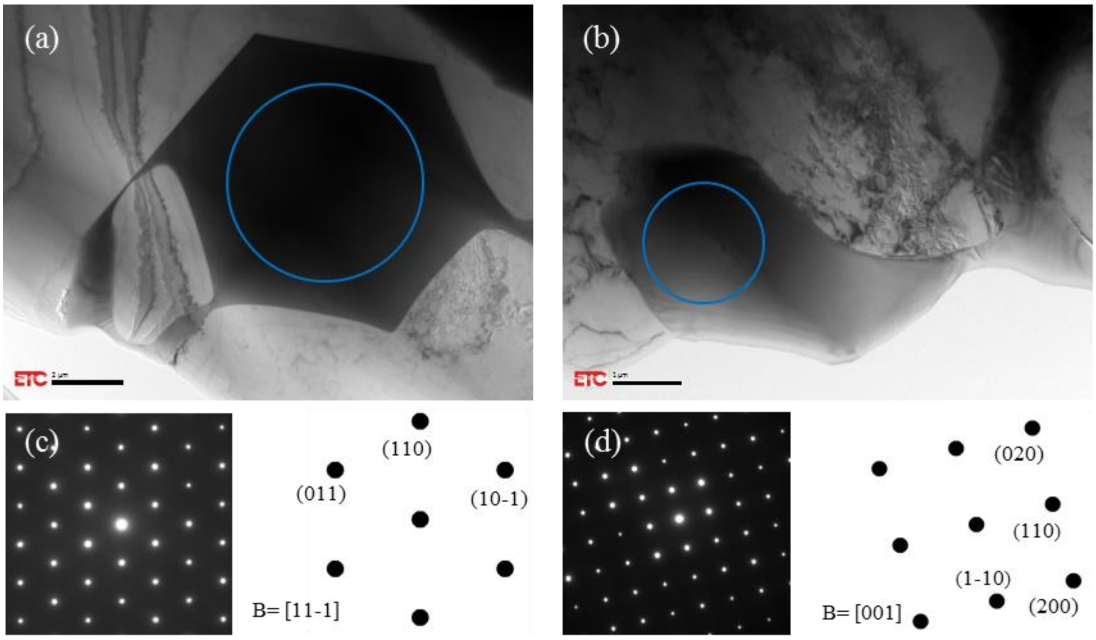

Figure 4.17 TEM bright field images showing the morphology of (a) polyhedral and tip of (b) Chinese-script Fe-IMC when the incident electron beam is parallel to [11-1] and [001], respectively; Selected Area Electron Diffraction (SAED) pattern taken from the blue circled area in (c) polyhedral Fe-IMC and (d) Chinese-script Fe-IMC. The schematic illustrations of diffraction pattern indexing are shown next to the SAED patterns respectively.

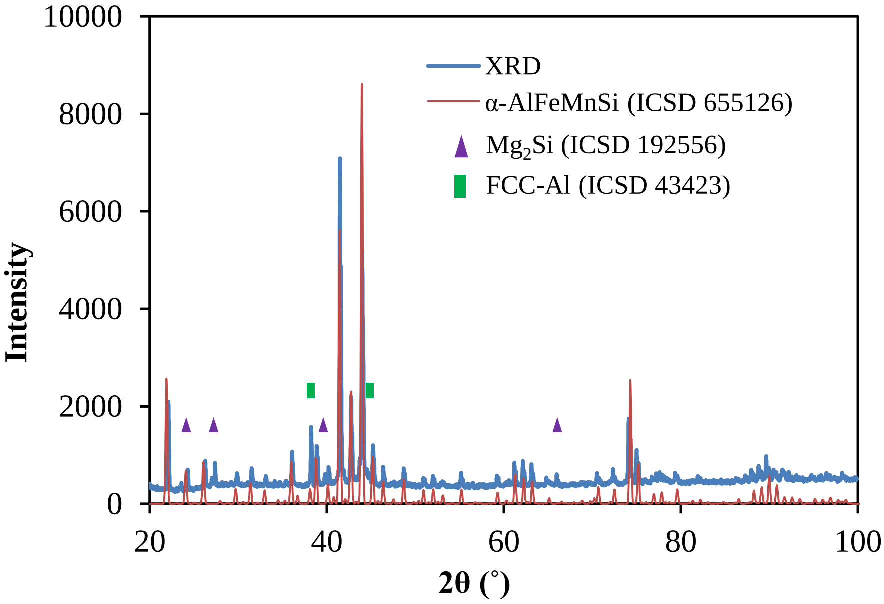

Figure 4.18 Comparison of experimental XRD result of exacted α-AlFeMnSi particles and standard α-AlFeMnSi crystallography information provided by ICSD.

information of BCC α-$Al_{19}Fe_4MnSi_2$ (Cooper, 1967), No.655126 in Inorganic Crystal Structure Database (ICSD).

Thus, we can conclude that the polyhedral and Chinese-script Fe-IMC in Al-5Mg-2Si-1.2Fe-0.7Mn alloy both share BCC, space group Im-3, a=1.256nm crystal structure with a stoichiometry of $Al_{12}(Fe,Mn)_3Si$. This phase is designated in present study as α-AlFeMnSi.

4.3 Effect of the Casting Temperature and the Cooling Rate on Phase Formation and Microstructure

These experiments look at the role of casting temperature or cooling rate on the microstructural revolution to understand the solidification behaviour of α-AlFeMnSi in Al-5Mg-2Si-1.2Fe-0.7Mn alloy. The thermocouple monitoring during experiments have suggested that the cooling rate during CF was 0.02K/s, CA was 0.8K/s and TP-1 water bath was (3.5K/s). Thus, in various casting temperature experiment, pouring the melt into TP-1 mould at different temperature is fundamentally equivalent to changing the cooling rate from 0.8K/s to 3.5K/s at different temperatures. The cooling rate experiment is focused on microstructure evolution and phase transformation at a constant cooling rate. This investigation has been focusing on the microstructure evolution when casting temperature varies (section 3.2.1). Finally, water quench experiment at various temperature is designed to observe the phase transformation of $Al_6(Fe,Mn)$-to-α-AlFeMnSi (section 3.2.4). The relevant quantification results will be presented in this section.

4.3.1 Casting Temperature

Eight pouring temperatures to TP-1 mould was selected ranging from a maximum of 50K superheat (liquidus at 670°C) to eutectic temperature, which are 720°C, 700°C, 680°C, 670°C, 660°C, 650°C, 640°C, 630°C and 620°C. Before casting into TP-1 mould, the melt is cooled in CA condition with gentle stirring until the pouring temperature is achieved. The microstructures of each sample are presented in **Fig. 4.19**. When cast with 30K and 10K superheat (**Fig. 4.19a** and **Fig. 4.19b**), there is no primary (polyhedral) α-AlFeMnSi observed in microstructure, and Fe-IMCs exists predominately eutectic α-AlFeMnSi (Chinese-script) located mainly between dendrite of primary α-Al grains. As the casting temperature decreases (**Fig. 4.19c**, **Fig. 4.19d** and **Fig. 4.19e**) a noticeable amount of primary α-AlFeMnSi particles which are commonly attached to the Chinese-script α-AlFeMnSi form. For those α-AlFeMnSi grains contained within α-Al grains, meanwhile some eutectics sit at the inter-dendritic regions of primary α-Al grains. As shown in **Fig. 4.19f**, **Fig. 4.19g** and **Fig. 4.19h**, a sufficient amount of primary α-AlFeMnSi located in α-Al dendrites form when the casting temperatures further decreases (640°C or lower). Meanwhile, the branches of eutectic α-AlFeMnSi become much less leading to a smaller eutectic size in 2D observation. The location of the eutectic α-AlFeMnSi is mainly related to the position of primary α-AlFeMnSi as they commonly have a primary α-AlFeMnSi "core". As shown in **Fig. 4.19**, the solidification of α-AlFeMnSi is significantly affected with changing the TP-1 casting temperature. The eutectic α-AlFeMnSi dominant microstructure evolved to a primary and eutectic α-AlFeMnSi mixed microstructure as temperature decreased. The micrographs at the same magnification were taken from similar regions for metallographic observation for the quantification of volume fraction and size distribution of α-AlFeMnSi. The volume fraction evolution of primary and eutectic α-AlFeMnSi (**Fig. 4.20**) shows three distinct regions where the volume fraction changes. During first stage the volume fraction of primary α-AlFeMnSi increased moderately from casting between 680˚C and 660˚C. The primary α-AlFeMnSi first emerged in the microstructure in sample cast at 680˚C casting sample with a volume fraction around 0.2±0.1vol.%, and increased slowly to 0.5±0.2vol.% until casting at 660˚C. However, during the second stage volume fraction of primary α-AlFeMnSi increased rapidly to 3.2±0.3% when cast at 650˚C, and followed by a minor increase to 3.6±0.5±% until casting at 630˚C.

During the last stage, the volume fraction of primary α-AlFeMnSi decreased rapidly to 0.66% when cast at the eutectic temperature, 620˚C. Meanwhile, the eutectic α-AlFeMnSi was also affected by the casting temperatures. As shown in Fig. 4.20, the volume fraction of eutectic α-AlFeMnSi remained at 6.5±0.4vol.% at casting temperatures above 660˚C and decreased to 3.4±0.3vol.% when casting at 650˚C which is followed by a considerable decrease to 3.1±0.3vol% at 620˚C. The overall volume fraction of α-AlFeMnSi remained at 6.5±0.5% from 720˚C to 630˚C, and

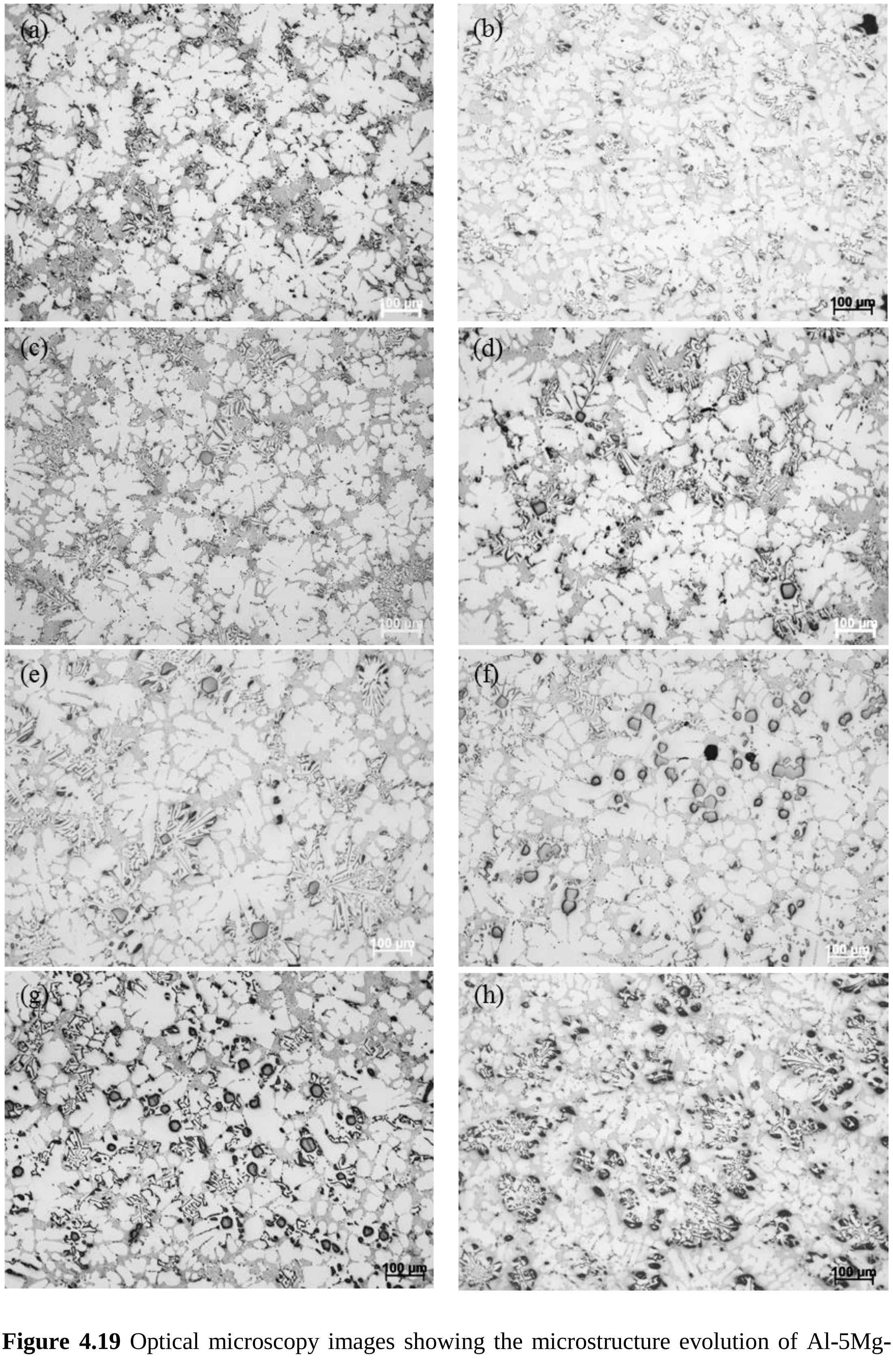

Figure 4.19 Optical microscopy images showing the microstructure evolution of Al-5Mg-2Si-1.2Fe-0.7Mn alloy at various TP-1 pouring temperature: (a) 700°C, (b) 680°C, (c) 670°C, (d) 660°C, (e) 650°C, (f) 640°C, (g) 630°C and (h) 620°C. Observation was carried out from the similar place of TP-1 sample which has a cooling rate of 3.5K/s.

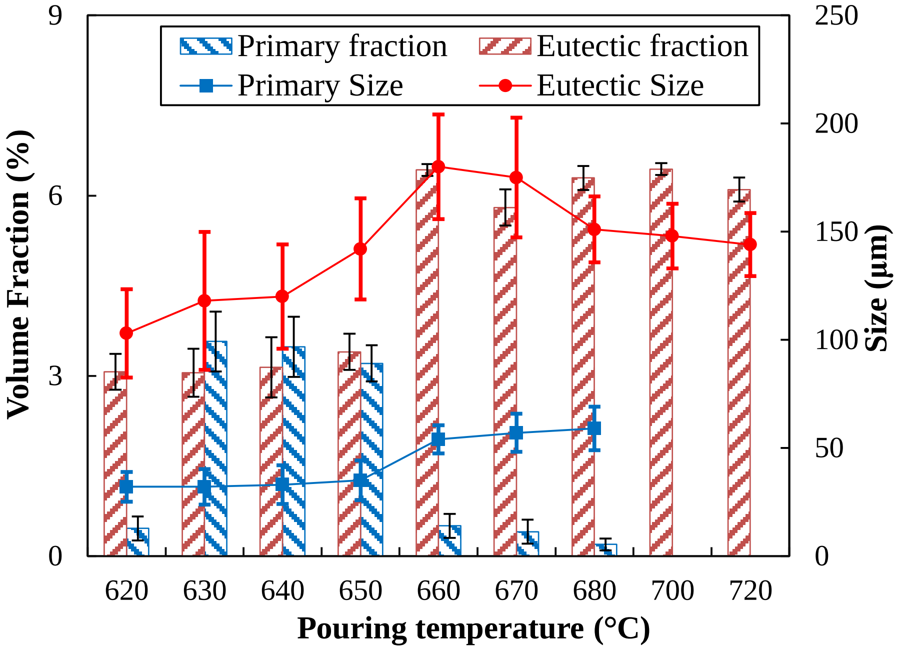

Figure 4.20 Volume fraction (Bars) and colony size (Markers) of primary α-AlFeMnSi (blue) and eutectic α-AlFeMnSi (red) in Al-5Mg-2Si-1.2Fe-0.7Mn by TP-1 casting as a function temperature. The bars with red dot filling and blue strap line filling represent volume fraction of eutectic and primary α-AlFeMnSi, respectively; Red line and blue line refers to the grain size of eutectic and primary α-AlFeMnSi, respectively.

decreased sharply at 620˚C mainly due to the volume fraction decrease in the primary α-AlFeMnSi. **Fig. 4.20** shows that the particle size of primary α-AlFeMnSi is also affected when casting temperature changes, and shows a moderately decreasing trend from 52.6±5.0μm to 35.0±9.6μm when pouring temperature decreased from 680˚C to 620˚C. In another word, the size of primary α-AlFeMnSi was not affected greatly by the volume fraction change. Meanwhile, the size of eutectic α-AlFeMnSi grain is obviously dependent on the casting temperature. It was approximately 165.1±24.4μm when there was no primary α-AlFeMnSi observed and then increased to approximately 175.5±32.5μm when a moderate amount of primary α-AlFeMnSi forms. A significant decrease in eutectic α-AlFeMnSi to 120.9±30μm when there is large amount primary α-AlFeMnSi (casting at 650˚C or below).

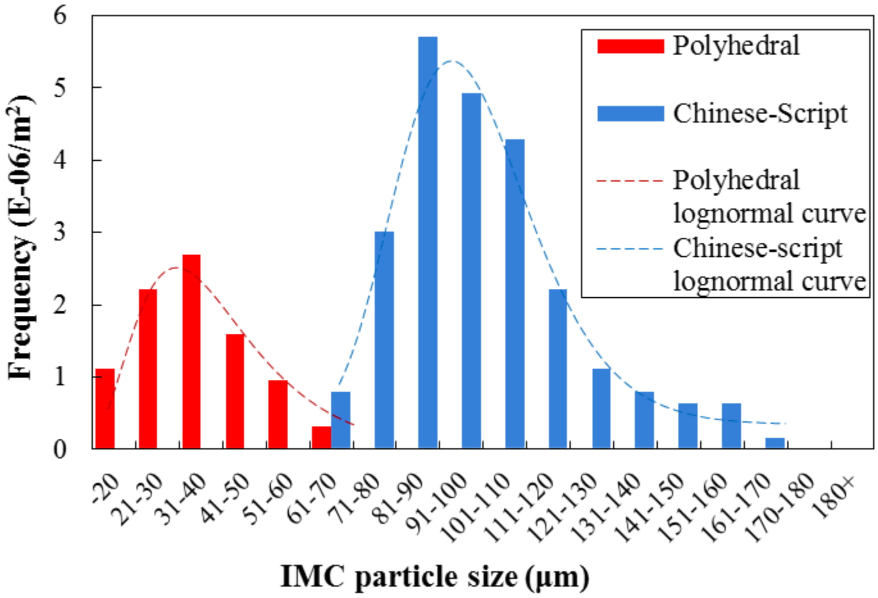

Figure 4.21 The size distribution of α-AlFeMnSi particles in TP-1 cast at 650˚C. The lognormal curves are fitted on the frequency bars.

The particle size distribution of primary and eutectic α-AlFeMnSi was quantified to reveal the relationship between the two morphologies. The quantification was performed on the same micrographs used for volume fraction analysis. As shown in **Fig. 4.21**, in Al-5Mg-2Si-1.2Fe-0.7Mn alloy cast with TP-1 at 650˚C the mean primary α-AlFeMnSi particle size is about 35.0±9.6µm which nearly 4 times smaller than the eutectic colony size (120.9±30.8µm). The eutectic colonies were more frequent than primary α-AlFeMnSi. The 3D morphology of eutectic α-AlFeMnSi (**Fig. 4.6c**) allows one colony to look as two separate grains in 2D observation depending on the section plane, but this was not the case with for primary α-AlFeMnSi due to the compact morphology (**Fig. 4.6a**). The α-AlFeMnSi colony size can be significantly reduced when the formation of primary α-AlFeMnSi is encouraged.

4.3.2 Cooling Rate

The Cu wedge mould schematically explained in section 3.2.3 is used here to get various cooling rates for the solidification process. The microstructure and Fe-IMC's morphology in Cu wedge mould sample will be compared with TP-1 and CF samples with the same casting temperatures above liquidus (similar superheating). Three casting superheats including 50K, 30K and 10K were used initially, but primary α-AlFeMnSi particles were only observed in the sample superheated by 10K. The primary α-AlFeMnSi is supressed at all the cooling rates but the CF (0.02K/s) or CA (0.8K/s) when casting with 50K superheat or higher. Therefore, the microstructure of the 10K superheat samples was compared with the TP-1 and CF samples with the same superheat. As shown in **Fig. 4.22**, the dominant Fe-IMC are polyhedral (categorized as primary α-AlFeMnSi) and Chinese-script (categorized as eutectic α-AlFeMnSi) Fe-IMCs regardless of the cooling rate, and minor amount of parallelogrammatic Al_6(Fe,Mn) can be found with SEM/EDS at almost all the cooling rates, except for CF sample which has a significant amount of Al_6(Fe,Mn) between α-Al grains and some primary α-AlFeMnSi segregated to the bottom of the crucible. In the Cu wedge mould, the impact of cooling rate can be dominantly reflected with the Al dendrite spacing and eutectic α-AlFeMnSi branch spacing. **Fig. 4.22** shows that the decrease in cooling rate leads to an appreciable increase in both the dendrite of α-Al and the colony size of α-AlFeMnSi. The primary α-AlFeMnSi is observed to be embedded within α-Al dendrites at all examined cooling rates but not in CF condition (0.02K/s) due to the extremely coarse morphology of α-Al and α-AlFeMnSi.

The quantification of α-AlFeMnSi at various cooling rates is performed by measuring the grain diameter using same optical micrographs used for the metallurgical observation. The average grain size of primary and eutectic α-AlFeMnSi as a function of cooling rate is presented in **Fig 4.23**, showing the mean diameter of at least 50 grains for each point. The size of primary α-AlFeMnSi changes minimally and remains at around 24.5±1.1μm when the cooling rate is between 870K/s and 13.8K/s, which increased to 52.6±5.0μm when the cooling rate was 3.5K/s and followed by a significant increase to 251.3±75.3μm at 0.02K/s. The eutectic α-AlFeMnSi colony size change shows a slightly different trend from the primary α-AlFeMnSi; it increases gradually from 102.0±12.1μm at 870K/s to 122.5±17.1μm, 125.4±20.5μm and 145.6±13.7μm at cooling rates of 71.8K/s, 26K/s and 13.8K/s, respectively. When the cooling rate was 3.5K/s, the size of eutectic α-AlFeMnSi grains reached 213.7μm, and followed by a considerable increase to 623.3±157μm at 0.02K/s. The area ratio (R_A), for the amount of primary and eutectic α-AlFeMnSi grains, is calculated by dividing the total grain area of primary α-

AlFeMnSi by total grain area of α-AlFeMnSi/α-Al eutectic. The area ratio was around 2.2±0.4% at 870K/s and 71.8K/s, which increased to 3.0±0.2% at 26.2K/s and followed by a rise to 3.8±0.4% at 13.8K/s. The area ratio in CF sample was not taken into calculation as there was a significant amount of $Al_6(Fe,Mn)$ that consumed Fe and Mn atoms that could be used for the formation of α-AlFeMnSi.

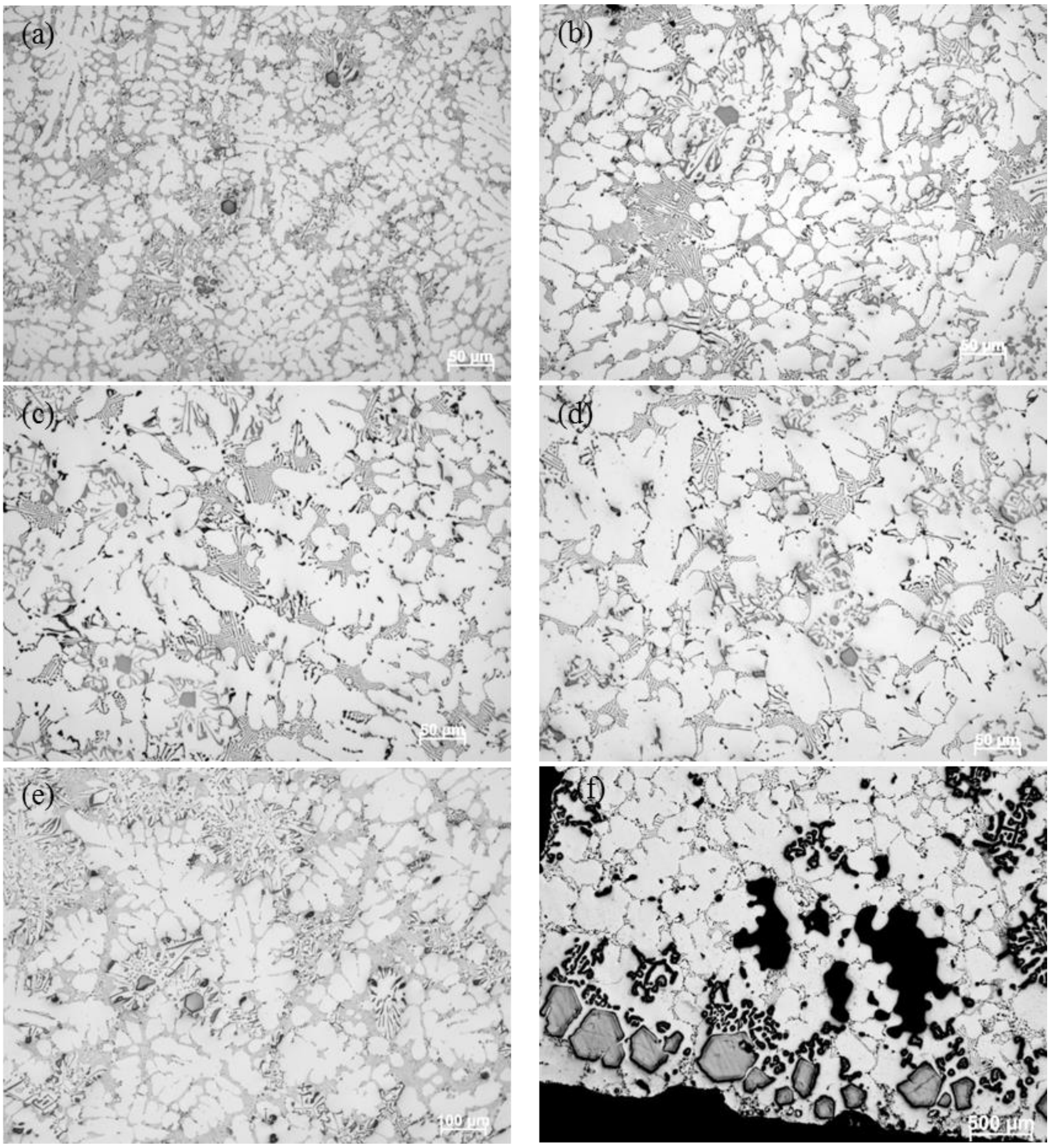

Figure 4.22 Optical micrographs showing the microstructure of Al-5Mg-2Si-1.2Fe-0.7Mn at different height of Cu wedge mould (a) 10mm from tip, (b) 40mm from tip, (c) 70mm from tip and (d) 100mm from tip, (e) in TP-1 sample and (f) at the bottom of CF sample. All the samples are cast at 10K superheat.

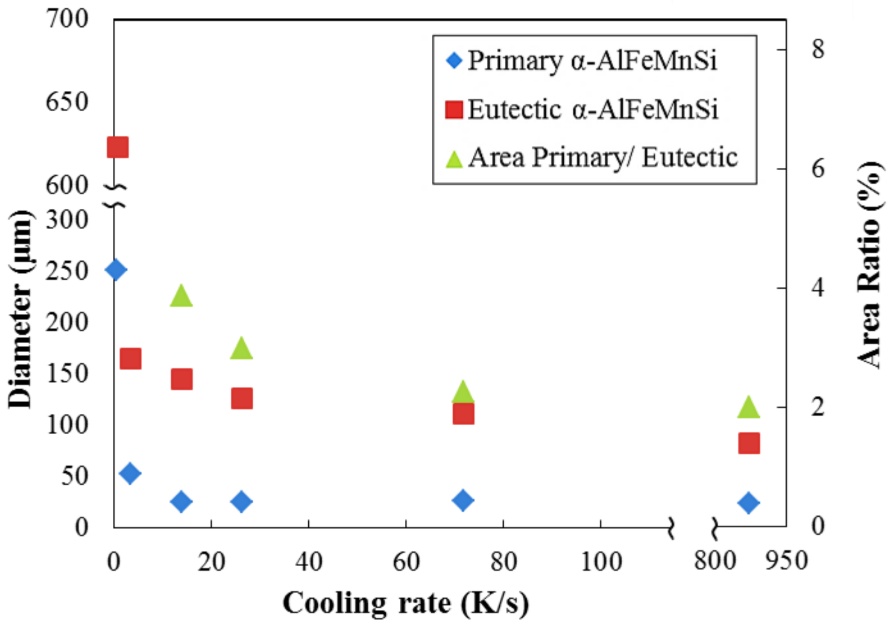

Figure 4.23 Particle size of α-AlFeMnSi in Al-5Mg-2Si-1.2Fe-0.7Mn alloy at different cooling rate cast with 10K superheat. The data of six cooling rates from left of the figure to the right were collected from (1) CF sample (0.02K/s), (2) TP-1 sample (3.5K/s), wedge sample (3) 100mm to tip (13.8K/s), (4) 70mm to tip (26.2K/s), (5) 40mm to tip (71.8K/s) and (6) 10mm to tip (871.2K/s), respectively. The Area Ratio was calculated with measured the diameters using the equation $R_a = \{[\pi*(d_{PFe\text{-}IMC}/2)^2]*\rho_{PFe\text{-}IMC}/[\pi*(d_{EuFe\text{-}IMC}/2)^2*\rho_{EuFe\text{-}IMC}]\}$ *100%. Number density of particles is denoted as ρ.

Overall, the occurrence of primary α-AlFeMnSi is dependent on cooling rate and the casting temperature; the criteria for the promoting and suppressing the formation of primary α-AlFeMnSi is shown in **Fig. 4.24**. It shows that at cooling rates less than 3.5K/s primary α-AlFeMnSi form at all temperatures and when cooling rate is higher than 3.5K/s the formation will be supressed when casting temperatures are above 680˚C.

4.3.3 Melt Quenching at Various Temperatures

In this experiment (detailed description in section 3.2.4), CF samples along with its steel container (**Fig. 3.5**) were taken out from furnace and submerged in a water bath to quench the microstructure since the given temperature. The formation of $Al_6(Fe,Mn)$ is encouraged with CF in Al-5Mg-2Si-1.2Fe-0.7Mn, although $Al_6(Fe,Mn)$ is not thermodynamically stable in this system suing CALPHAD approach (**Fig. 4.1)**. The microstructure evolution for various quenching temperature is summarized in **Fig. 4.25**. The duplex particle has been characterized with SEM/EDS as shown **Table 4.2** and **Fig 4.16** suggesting the stoichiometry of $Al_6(Fe,Mn)$ and $Al_{12}(Fe,Mn)_3Si$ for parallelogrammatic Fe-IMC and surrounding branched Fe-IMCs, respectively.

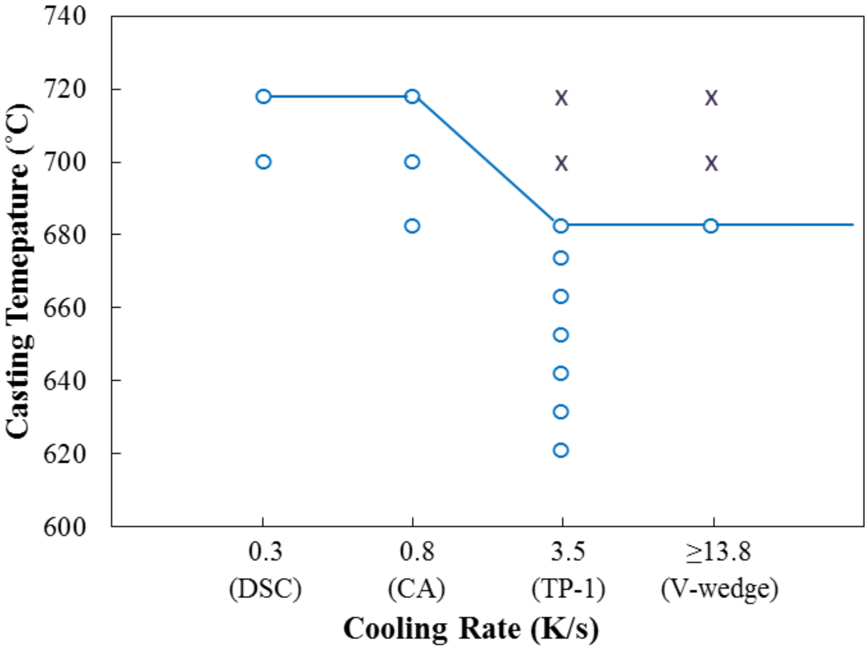

Figure 4.24 Variation of the casting temperature for the occurrence of primary α-AlFeMnSi (marked in blue circle) as a function of cooling rates. The conditions for supressing primary α-AlFeMnSi are marked with black crosses which are separated by the blue line from the formation conditions. The cooling rates from left to right of the *x*-axis are from DSC sample, CA sample, TP-1 casting and wedge mould casting, respectively.

The morphology evolution of CF sample at different quenching temperature is summarized in **Table 4.3**. The phase transformation temperature is determined by microstructure observation that if a phase transformation occurred before quenching then it will show a coarse morphology (**Fig. 4.25d**). Otherwise, it shows a very fine morphology (indicated with solid arrows in **Fig. 4.25b** and **c**). For instance, the $Al_6(Fe,Mn)$, exhibiting a parallelogrammatic morphology, at the centre of the $Al_6(Fe,Mn)$ colony is considered form before quenching at 620˚C and the fine $Al_6(Fe,Mn)$ branches are considered solidify after 620˚C. The partially coarsened

Mg_2Si/α-Al eutectic in 600˚C quenched sample suggests that the Al_6(Fe,Mn)-to-α-AlFeMnSi transformation has already started when Mg_2Si forms. Hence, phase transformations in Al-5Mg-2Si-1.2Fe-0.7Mn alloy are consistent with the prediction in section 4.1.1 that L, L + primary α-AlFeMnSi, L + primary α-AlFeMnSi + eutectic α-AlFeMnSi and L + primary α-AlFeMnSi + eutectic α-AlFeMnSi + Mg_2Si are quenched from the designated temperatures, 700˚C, 620˚C, 600˚C and 579˚C, respectively.

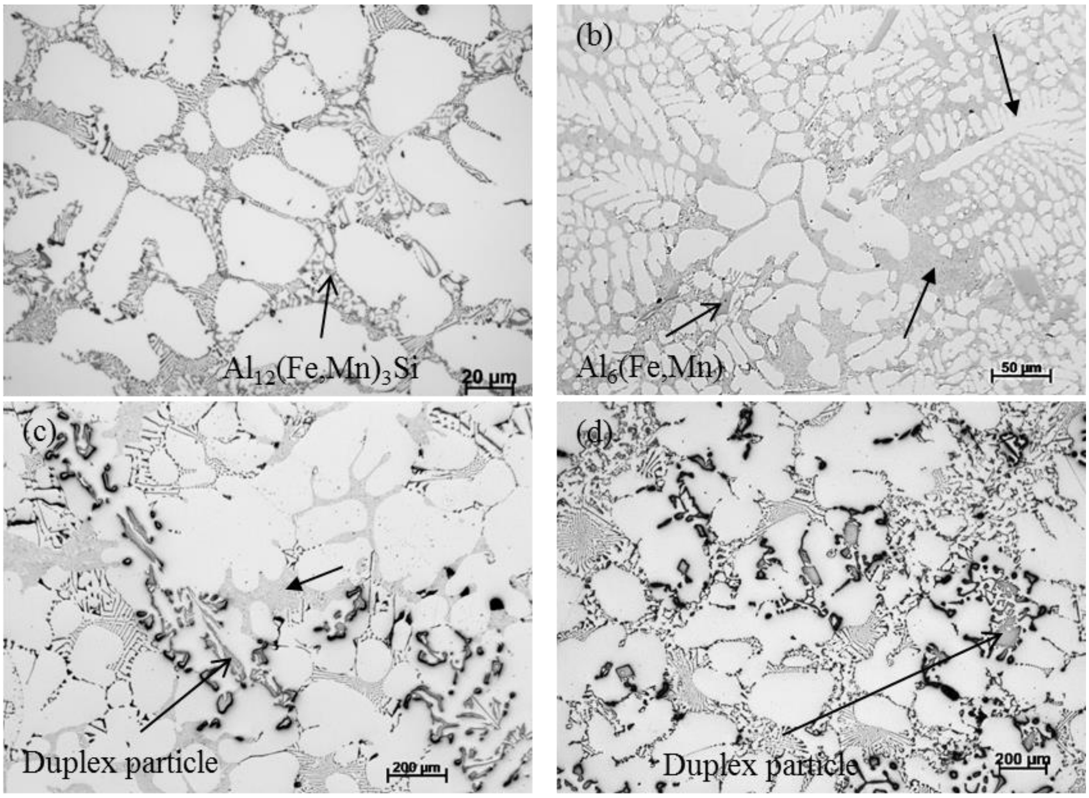

Figure 4.25 OM images showing the microstructure of Al-5Mg-2Si-1.2Fe-0.7Mn alloy water quenched by steel mould at (a) 700˚C, (b) 620˚C, (c) 600˚C and (d) 579˚C. Quenched melt is marked by solid arrow, and (a) is fully quenched. Al_6(Fe,Mn) particle and Al_6(Fe,Mn)/α-AlFeMnSi duplex particle are indicated by liner arrows.

As shown in **Fig. 4.25**, the quenching temperature leads to a dramatic change in the morphology of Al_6(Fe,Mn). When quenching from 700˚C (30K above liquidus), Al_6(Fe,Mn) is not observed and eutectic α-AlFeMnSi appeared as the predominant Fe-IMC. When quench at 620˚C and 600˚C (binary eutectic temperature), or 579˚C (ternary eutectic temperature), Al_6(Fe,Mn) particles, generally locates within α-Al

Table 4.3 Comparison of morphology for phases at different water quench temperature after CF Al-5Mg-2Si-1.2Fe-0.7Mn alloy.

Cooling method	**Holding time**	**Morphology**			
		α-Al	**Primary $Al_6(Fe,Mn)$**	**Dendritic $Al_6(Fe,Mn)$**	**Eutectic Mg_2Si**
Quench at 680˚C	0	Fine dendrite	Not observed	dot-like $Al_6(Fe,Mn)$	Fine lamellar spacing
Quench at 620˚C	50 minutes	Partially coarse dendrite	$Al_6(Fe,Mn)$	$Al_6(Fe,Mn)$	Fine lamellar spacing
Quench at 600˚C	68 minutes	Coarse dendrite	Duplex $Al_6(Fe,Mn)$ + α-AlFeMnSi	Duplex $Al_6(Fe,Mn)$ + α-AlFeMnSi	Mixed lamellar spacing
Quench at 579˚C	87 minutes	Coarse dendrite	Duplex $Al_6(Fe,Mn)$ + α-AlFeMnSi	α-AlFeMnSi	Coarse lamellar spacing
Non-quench	540 minutes	Coarse dendrite	Duplex $Al_6(Fe,Mn)$ + α-AlFeMnSi	α-AlFeMnSi	Coarse lamellar spacing

*Samples were cooled in furnace before quenching which has a cooling rate of 0.02K/s;

**Water quenching provides a cooling rate of 50±20K/s;

***Equilibrium formation temperature of primary α-AlFeMnSi, α-Al, and Mg_2Si eutectic are 670.4˚C, 620.5˚C and 584.2˚C, respectively.

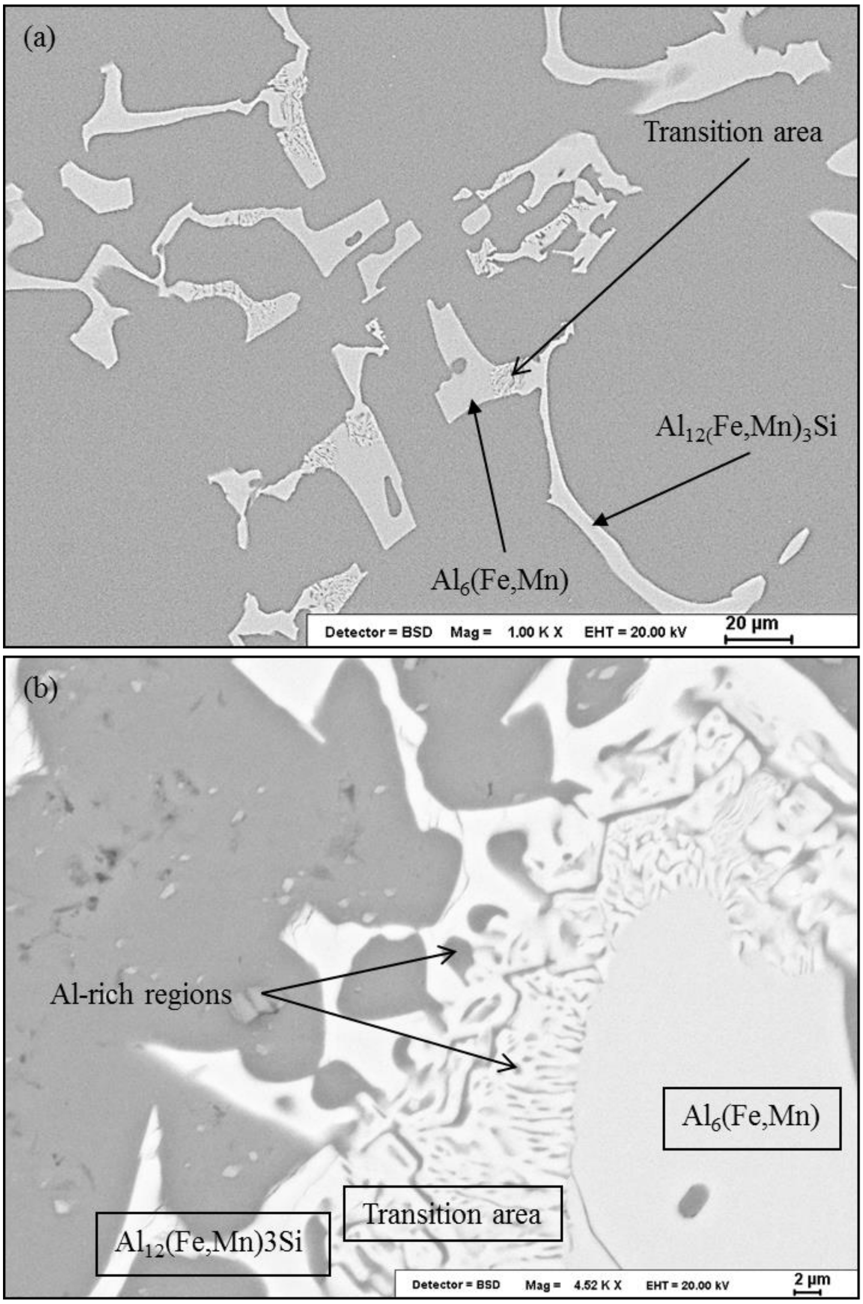

Figure 4.26 SEM micrographs showing the morphology of $Al_6(Fe,Mn)$-to-α-AlFeMnSi transition particles in Al-5Mg-2Si-1.2Fe-0.7Mn alloy produced by (a) water quench at 600˚C after CF and (b) CF (non-quenching). Al-rich regions and α-$Al_{12}(Fe,Mn)_3Si$ in transition regions are indicated with a arrows.

grains, has a hollowed parallelogrammatic morphology and sometimes with attached branches. Meanwhile, the $Al_6(Fe,Mn)$/α-AlFeMnSi duplex particles were not observed when quenching temperature reaches 620˚C and the solidification of binary eutectic has already started (**Fig. 4.25b**). As shown in **Fig. 4.25c**, the transition region depth from the edge of duplex particle to Al_6(Fe,Mn) at the centre increases when quenching from 600˚C compared with that of quenching at 620˚C. When quenching at even lower temperature (579˚C), the depth of transition region does not seem show an obvious change and there is almost no quenched melt observed. For primary α-AlFeMnSi, an identical polyhedral morphology to the samples cooling in furnace until completely solidified was observed, and the particles settled to the bottom of the mould in all three quenching temperatures (620˚C, 600˚C and 579˚C). Chinese-script α-AlFeSi were attached to primary α-AlFeMnSi at the bottom of the mould; occurred by itself at other areas; or surrounding the Al_6(Fe,Mn) particles which sometimes had physical connection to Chinese-script α-AlFeMnSi. When cooling in furnace until fully solidified (**Fig. 4.25**), the coarse rod-like Al_6(Fe,Mn) appears to be the primary Fe-IMC in this cooling rate (0.02K/s) given the morphology and large volume fraction, although an appreciable amount primary polyhedral α-AlFeMnSi segregate to the bottom of the mould. This is caused by gravity segregation and sufficient settling time for large primary α-AlFeMnSi. Then, the formation of primary Al_6(Fe,Mn) occur when the liquid composition changes because of the primary α-AlFeMnSi sedimentation.

Two typical types of particles that show phase transformations, branched particle and coarse primary particle, are discussed in in detail. **Fig. 4.26** shows that the transition can occur on both at the boundaries of coarse Al_6(Fe,Mn) particles and tip of Al_6(Fe,Mn) branches. Large number of Al-rich regions exist at the Al_6(Fe,Mn)-to-α-AlFeMnSi transition region. There Al-rich region appears to be significantly large in diameter when it is close to particle boundary compared with the ones close to Al_6(Fe,Mn). The Al-rich regions are not observed any more at the α-AlFeMnSi side of the duplex particle, showing to α-AlFeMnSi single phase area.

4.4 Discussion

4.4.1 Solidification Sequence of Al-5Mg-2Si-1.2Fe-0.7Mn Alloy

The equilibrium phase transformation temperatures of Al-5Mg-2Si-1.2Fe-0.7Mn calculated with Pandat^{TM} 8.2 and the experimental observations at different cooling rates are compared in **Table 4.4**. Based on the microstructures of the samples cast with different cooling rates (**Fig. 4.22**) and quenched with different temperature points, the solidification sequence is proposed:

$L \rightarrow$ Primary α-AlFeMnSi $+L_1$ (reaction R4.1)

$L_1 \rightarrow Al_6(Fe,Mn) + L_1'$ (R4.2)

$L_1' \rightarrow$ α-Al + α-AlFeMnSi + L_2 (R4.3)

$L_2 \rightarrow$ α-Al + $Mg_2Si + L_2'$ (R4.4)

$L_2' \rightarrow$ α-Al + $Mg_2Si + Al_6(Fe,Mn)$ (R4.5)

The cooling curve measurements revealed that the nucleation of primary α-AlFeMnSi in Al-5Mg-2Si-1.2Fe-0.7Mn alloy requires a $\Delta T \geq 20.2$˚C (**Table 4.4**) at a cooling rate (<3.5K/s), except TP-1 or Melt Quenching (MQ) which did not contain primary α-AlFeMnSi when casting with 30K superheat. The primary α-AlFeMnSi forms at cooling rates ≤0.8K/s, but the transformation starting point was not observed with thermal analyses at cooling rate of 0.02K/s. Due to the low volume fraction (2.7% at equilibrium) and large transformation temperature range (50˚C), the heat release during the solidification of primary α-AlFeMnSi may not be enough to recalescence (**Fig. 4.12**) or even to be detect by thermal analysis devices (**Fig. 4.11**). The formation $Al_6(Fe,Mn)$, which is observed in microstructure and solidifies before primary α-Al in CF melt quenching experiment (**Fig. 4.25**), was not detected with thermal analyses. Eutectic α-AlFeMnSi/α-Al has consistent transformation temperatures with CM and MQ condition (**Fig. 4.11** and **Fig. 4.12**) which are 620.4±0.2˚C and 618.9±0.6˚C, respectively, due to different cooling rates in two solidification conditions.

Table 4.4 Comparison of phase transformation temperatures in Al-5Mg-2Si-1.2Fe-0.7Mn alloy between calculation and different cooling rates.

	Phase Diagram Calculation	Measured transformation temperature (T_G)		
Transformation	Pandat^{TM} (Scheil Rule)	DSC (0.3K/s)	Cooling curve CM (0.02K/s)	Cooling curve MQ (40K/s)
L → Primary α-AlFeMnSi $+L_1$	670.4	639.0	650.2	$^{\#}$
$L_1 \rightarrow Al_6(Fe,Mn) + L_1'$	$^{\#}$	$^{\#}$	> 620.0$^{\#}$	$^{\#}$
$L_1' \rightarrow$ α-Al + α-AlFeMnSi $+ L_2$	620.7	619.5	620.4	618.9
$L_2 \rightarrow Al + Al_{15}(Fe,Mn)_3Si_2 + Al_{13}Fe_4$	615.7	-	-	-
$L_2 \rightarrow Al + Al_8Fe_2Si$	591.2	-	-	-
$L_2 \rightarrow$ α-Al $+ Mg_2Si + L_2'$	584.2	585.0	594.0	586
* “CM” refers to ceramic mould; ** “MQ” refers to melt quenching in steel mould; *** “$^{\#}$” refers to not confirmed and “-” refers to not experimentally observed.				

As shown in **Table 4.4**, the measured transformation temperature of ternary eutectic Mg_2Si/α-Al/Fe-IMC or the Mg_2Si/α-Al when cooling rate ≥3.5 is above the equilibrium transformation temperature (584.2˚C) which are 585.0˚C (DSC), 594.0±0.1˚C (CM) and 585.7±2.3˚C (MQ). This is caused by non-homogenised liquid solution and complicate solute interaction between Fe, Mn, Si and Mg, which leads the actual solidification path to shift significantly from the equilibrium phase diagram. Mg_2Si eutectics, suggested by CALPHAD approach prediction to be ternary eutectic Mg_2Si/α-Al/$Al_{13}Fe_4$, are observed in forms of polyhedral Mg_2Si/eutectic-Mg_2Si/α-Al (**Fig.4.15a**) and Mg_2Si/α-Al/Al_6(Fe,Mn) (**Fig. 4.15b**). The polyhedral core is considered to be the morphology of primary Mg_2Si (Zhang *et al.*, 2000). As the formation of primary Mg_2Si requires a concentration of 14.2wt.% (Zhang *et al.*, 2000), the existence of polyhedral Mg_2Si core suggests that the local Mg and Si segregation was very high during TP-1 and Cu wedge mould casting. Thus, the solidification sequence at Mg_2Si is proposed to be: L_2 → polyhedral Mg_2Si → binary eutectic Mg_2Si/α-Al (reaction R4.4) → ternary eutectic Mg_2Si/α-Al/Al_6(Fe,Mn) (reaction R4.5). As the reaction R4.4 decreased the Mg and Si enrichment and prompted Fe and Mn concentration, ternary eutectic reaction R4.5 eventually occurred.

4.4.2 Solidification Behaviour of Primary α-AlFeMnSi

4.4.2.1 Nucleation

The common understanding of solidification process is that the formation of a phase requires a nucleation event which is either homogeneous nucleation or heterogeneous nucleation (Kelton and Greer, 2010; Quested, 2004; Greer *et al.*, 2000; Maxwell and Hellawell, 1975a). The heterogeneous nucleation needs to overcome a significantly smaller energy barrier compared with homogeneous nucleation due to the small wetting angle with the substrate (Turnbull and Vonnegut, 1952) or good lattice mismatching (Maxwell and Hellawell, 1975a). It was proposed that in Al alloys, the in-situ oxides, such as Al_2O_3, MgO, and $MgAl_2O_4$, can act as nucleation substrate for Fe-IMCs due to the small lattice matching with α-AlFeMnSi (Miller, Lu and Dahle, 2006; Cao and Campbell, 2003). The current observation shows that the nucleation of primary α-AlFeMnSi was not noticeably encouraged after the wetting and dispersion of oxides films through intensive shearing technology described by Fan and co-workers (Men, Jiang and Fan, 2010). This suggests that good lattice mismatching between the nucleation substrate and nucleation phase is not the sole parameter for the heterogeneous nucleation of α-AlFeMnSi.

Based on the current experimental observations, the nucleation of primary α-AlFeMnSi occur when cast with a low superheat (≤10K) with TP-1 (**Fig. 4.19**) and

Cu wedge mould (**Fig. 4.22**), but it is supressed when casting with a higher superheat. As a thermodynamically stable phase suggested by Pandat^{TM} prediction, α-AlFeMnSi should form when the required nucleation undercooling is reached, unless any intermediate phase forms (Verma *et al.*, 2013; Shabestari and Malekan, 2005; Allen *et al.*, 1998). This suggests that the nucleation of primary α-AlFeMnSi is dependent not only on the undercooling but on the casting superheat. The **Fig. 4.23** shows that the size of primary α-AlFeMnSi particles rises moderately from 24.5±3.1μm at 871K/s to 52.6±5.0μm at 3.5K/s, which is not in good agreement with the literature which suggest the cooling rate significantly restricts the growth time and activates more nucleation sites, which lead to a finer morphology (Easton and StJohn, 2008; Shabestari and Malekan, 2005; Quested, 2004; Greer *et al.*, 2000; Chai, Bäackerud and Arnberg, 1995). When cooling rate is between 871K/s and 3.5K/s the nucleation and growth of existing α-AlFeMnSi particles is not affected by the cooling rate change given unchanged morphology, but determined by the cooling process before mould cooling. Thus, it can be suggested that when the solidification process has a small cooling rate (≤0.8K/s) the nucleation of primary α-AlFeMnSi is significantly dependent on cooling rate, however when the solidification process has a large cooling rate (≥3.5K/s) and a small superheat (≤10K) the nucleation of primary α-AlFeMnSi occurs before casting due to stronger non-homogeneities in liquid temperature gradient and solute concentration in liquid. Once the stable primary α-AlFeMnSi nuclei exist in the liquid, the growth can be initiated, which is largely dependent on the cooling rate considering the very large particle size under 0.02K/s.

Thus, the nucleation of primary α-AlFeMnSi is essentially determined by cooling rate instead of casting temperature. Despite the established theory that higher cooling rate can activate more nucleation sites due to the larger nucleation undercooling it creates, current experimental observation suggests that the nucleation of α-AlFeMnSi requires a low cooling rate (≤0.8K/s) when casting superheats are the same. Based on the observations above, two assumptions for the mechanism behind a lower cooling rate encouraging the nucleation instead of higher cooling rate are proposed:

The first assumption is that the formation energy barrier is the effective factor affecting the nucleation of primary α-AlFeMnSi (Gibbs free energy: ΔG). The precise values for thermodynamic parameters of multicomponent compounds such as Fe-IMCs are very difficult to obtain due to multi atom interaction. Even so, many different approaches were used to investigate the thermodynamic parameters of Fe-IMCs (Lacaze, Eleno and Sundman, 2010; Du *et al.*, 2008; Du *et al.*, 2004; Liu and Chang, 1999; Redlich and Kister, 1948). The formation ΔG has been reassessed by Lacaze (Lacaze, Eleno and Sundman, 2010) using Redlich-Kister polynomial (Lacaze, Eleno and Sundman, 2010; Redlich and Kister, 1948), which gives:

$$ {}^{0}G_{M}^{S} = x_{Al}\,{}^{0}G_{Al}^{S} + x_{Mn}\,{}^{0}G_{Mn}^{S} + x_{Si}\,{}^{0}G_{Si}^{S} + RT(x_{Al}lnx_{Al} + x_{Mn}lnx_{Mn} + x_{Al}lnx_{Si}) + x_{Al}x_{Mn}L_{Al,Mn}^{S} + x_{Al}x_{Si}L_{Al,Si}^{S} + x_{Si}x_{Mn}L_{Si,Mn}^{S} + x_{Al}x_{Mn}x_{Si}L_{Al,Mn,Si}^{S} \quad (4.1) $$

where R is the gas constant, and x_{Al}, x_{Mn} and x_{Si} are the mole fraction of Al, Mn and Si, respectively. Thus, the formation free energy is given:

$$ \Delta G = {}^{0}G_{M}^{S} - \sum x_i * {}^{0}G_{i}^{S} - \sum x_i\,{}^{0}G_{i}^{L} \quad (4.2) $$

Lacaze reassessed one α-AlFeMnSi variant $Al_{18}(Fe,Mn)_4Si_1$ and the calculated free energy change to be ΔG= -34144+17.49×T J/mol; for FCC α-Al the ΔG^*= -10711+11.47×T J/mol. Thus, we can see that the ΔG for given volume of α-AlFeMnSi is much more significant than α-Al. From this point of view, the formation energy barrier of α-AlFeMnSi is much larger than α-Al. As suggested Turnbull, the stable nucleus formation energy barrier is given (Dantzig and Rappaz, 2009):

$$ \Delta G_{n}^{het} = \frac{4\pi\gamma_{sl}R_c^2}{3} f(\theta) \quad (4.3a) $$

$$ V_s = \frac{\pi R_c^3}{3}(2 + cos\theta)(1 - cos\theta)^2 \quad (4.3b) $$

where V_S is the volume of solid, R_c is the nucleus radius and θ is the wetting angle. It is seen that when the substrate particles are the same (ideally same θ) in the liquid melt large formation ΔG^* of α-AlFeMnSi is very likely to lead to substantially large critical nuclei radius. In actual situation the solute elemental distribution is not uniform in the liquid solution; the nucleated solid therefore might not be able to reach the critical nuclei radius due to the insufficient solute atom supply which is restricted by solute density in liquid and diffusion efficiency. Thus, with higher cooling rates where the diffusion time is lower, it is more difficult for primary α-AlFeMnSi to obtain an atomic cluster that surpasses the critical nucleus' radius. In TP-1 casting experiment where the melt composition, cooling rate and the available nucleation substrate remain constant and casting temperature varies, the nucleation occurs in the castings with longer cooling time (CA condition) before pouring into TP-1 than these with a shorter cooling time (higher TP-1 casting temperature). Furthermore, the primary α-AlFeMnSi forms with TP-1 casting using a higher iron equivalent value (IEV) alloy, Al-6Si-5Fe-4Mn alloy (**Fig. 4.5**), which shows that the higher solute concentration can facilitate the nucleation of primary α-AlFeMnSi. This strongly suggests that when there is adequate amount of solute atoms the longer diffusion time is no longer needed for the nucleation of primary α-AlFeMnSi.

The second assumption is that the kinetics of the melt is a dominating factor for the nucleation of primary α-AlFeMnSi that the nucleation of primary α-AlFeMnSi requires an adequate amount of diffusion time for the critical amount of Fe, Mn and Si atoms to compose a stable nucleus with radius R_c. In a supercool liquid, a nucleus of critical R_c will grow if it manages to add one more atom. The rate at which this occurs is proportional to the atomic vibration frequency v_0 and the probability of capturing an atom at the surface, p_c. This rate of formation of heterogeneous nuclei, I^{hetro}, is given by (Dantzig and Rappaz, 2009):

$$I^{het} = v_0 p_c n_c = v_0 p_c n_l \exp\left(-\frac{16\pi}{3}\frac{\gamma_{sl}\Gamma_{sl}}{\Delta T^2 k_B T_m} f(\theta)\right) \; nucleus/m^3/s \qquad (4.4)$$

where n_l is the density of atoms in liquid n_l is the density of atoms in liquid. Thus the Time-Temperature-Transformation (TTT) curve may be determined, suggesting that the activated nuclei count can be significantly low when the cooling rate ($\Delta T/t$ in **Fig. 2.6**) is either very low or very high. In a multi component system, the p_c can be relatively lower than unary system due to the non-ideal atom interactions, and n_l can be very low compared with unary system given the α-AlFeMnSi phase's dilute component elements concentration. Based on this, the count of stable nuclei of primary α-AlFeMnSi can be restricted, especially at higher cooling rate (≥3.5K/s), due to the low solute (Fe, Mn and Si) concentration, non-ideal elements interaction and diffusion coefficients (atomic vibration frequency). Thus, the nucleation rate at cooling rates ≥3.5K/s is highly like very low which means primary α-AlFeMnSi nucleation being suppressed. The approach to enhance the heterogeneous nucleation by facilitating the capability of substrate capturing the atoms will be developed and introduced in chapter 6.

Many reports suggest that a system requires a relatively lower cooling rate to nucleate more thermodynamically stable phase due to the more significant nucleation barrier (Dutta and Rettenmayr, 2000; Allen *et al.*, 1998; Backerud, Chai and Tamminen, 1990; Adam and Hogan, 1972). This is in a good agreement with the experimental observation that primary α-AlFeMnSi prefers to nucleate during DSC (0.3K/s) (**Table 4.4**) and cooling in furnace (**Fig. 4.22f**) when the nucleation undercooling is satisfied. Thus, the longer homogenisation time allows the nucleation of more thermodynamically stable Fe-IMC, and equilibrium phase can be nucleated when the solute is sufficiently supplied. The diffusion coefficient of alloying elements in liquid Al at 650˚C is shown in **Table 4.5**. It shows that Fe ($3.6\times10^{-10}m^2/s$) has the lowest diffusion efficiency compared with Si ($5.2\times10^{-10}m^2/s$) and Mn ($6.2\times10^{-10}m^2/s$), which suggests that Fe is likely to be the dominant factor at restricting the nucleation event.

Based on the above discussions, due to large formation energy barrier (-34144+17.49×T), low element concentration and non-ideal multi component interaction, both potent nucleation substrates for smaller critical nucleus radius and sufficient diffusion time for forming nucleus cluster are the governing factors for the heterogeneous nucleation of primary α-AlFeMnSi in Al-5Mg-2Si-1.2Fe-0.7Mn alloy.

4.4.2.2 Faceted Growth

α-AlFeMnSi, as an equilibrium phase in Al-Fe-Mn-Si system (Zhang *et al.*, 2012; Ghosh, 2008), has a crystal structure of body-centred cubic (BCC) and can be altered from Im-3 to Pm-3 by increasing Mn/Fe ratio or heat treatment owing to the multi-atomic species and vacant sites in its complex structure (Kim *et al.*, 2006; Yoo *et al.*, 1999; Donnadieu, Lapasset and Sanders, 1994; Lai and Li, 1993). As shown in **Fig. 4.18**, the experimentally measured crystallographic structure fits with the BCC (Im-3) structure. Intermetallic compounds are commonly found to be anisotropic and shows faceted morphology, such as Al_3Ti, $Al_{13}Fe_4$ and β-AlFeSi et al. (Wang *et al.*, 2016; Puncreobutr *et al.*, 2014; Allen *et al.*, 1998). The crystal morphology after growth is complete is generally dependent on the crystal geometry (Donnay and Harker, 1937). A recent update by Gao (Gao *et al.*, 2013) on the growth of primary α-$Al_{15}(Fe,Mn)_3Si_2$ suggests that its morphology is largely dependent on the crystallographic features. In

Table 4.5 Thermodynamic data used in this chapter: Liquidus Slopes (m_i), Partition Coefficients (k_i) (Easton and StJohn, 2001), Pre-exponential Factor (D_0) in Al, Activation energy (Q), Diffusion Coefficients in liquid Al D_{650} at 650°C (Du *et al.*, 2003).

Element (i)		**Mg**	**Si**	**Mn**	**Fe**
m_i **(K·wt.%$^{-1}$)**		-6.2	-6.6	-1.6	-3
k_i		0.51	0.11	0.94	0.02
Solid	D_{0s} **(m^2/s)**	1.49×10^{-5}	1.38×10^{-5}	1.35×10^{-2}	3.62×10^{-1}
	Q_{s580} **(kJ·mol)**	120.5	117.6	211.5	214.5
	D_s **(m^2/s)**	4.82×10^{-16}	7.98×10^{-16}	5.22×10^{-21}	7.68×10^{-20}
Liquid	D_{0l} **(m^2/s)**	9.9×10^{-5}	1.34×10^{-7}	1.93×10^{-7}	2.34×10^{-7}
	Q **(kJ·mol)**	71.6	30	31	35
	D_{650} **(m^2/s)**	1.6×10^{-10}	5.2×10^{-10}	6.2×10^{-10}	3.6×10^{-10}
	G_C **(at.%/m)**	-6.2×10^{10}	1.4×10^{10}	1.8×10^{10}	3.2×10^{10}
* Arrhenius equation for diffusion coefficient is $D = D_0\exp[-Q/(RT)]$ (Du *et al.*, 2003; Arrhenius, 1889)					

current alloy system, a complete primary α-AlFeMnSi particle located in α-Al grain shows polyhedral morphology with 2D observation (**Fig. 4.3a** and **Fig. 4.5**) and rhombic dodecahedral morphology with 3D observation (**Fig. 4.3a** and **Fig. 4.6a**). The faceted crystal is suggested to be a common morphology for anisotropic crystal because of the low energy barrier for continuous growth compared with surface nucleation of other directions (Sunagawa, 1995).

During the growth process to a complete rhombic dodecahedron, three growth stages are proposed for the faceted growth of primary α-AlFeMnSi including initial stage, hollowed polyhedral stage and completed polyhedral stage. During the initial stage of the growth, a few hillocks would generate on the preferred growth orientations. In hollowed polyhedral stage, due to the concentration gradient caused by the consumption of the alloying elements during initial growth, secondary branches develop on primary hillocks. Following the same principle, tertiary branches develop on the secondary branches. Consequently, the solute concentration at the centre of the primary particle should be less compared with outer ring, which could lead to this hollowed polyhedral with a core morphology shown in **Fig. 4.4b** and **Fig. 4.4c.** When the solute is more abundant, this phenomenon can be more significant (see **Fig. 4.5a-b**) as the growth on preferable direction is further facilitated. Thus, it can be suggested that the primary arm orientation should be <111> where projection vectors on {111} plane should be 60˚ to each other, which agrees with the experimental observation in **Fig. 4.5a**. With this establishment, if observing the crystal from <001> direction, the projections vectors of <111> on {001} should have 90˚ angle to their neighbouring ones, which is consistent to the observation shown in **Fig. 4.5b**. Thus, the <111> is one of the preferred growth orientations. In the particles with 6-fold (**Fig. 4.5a)** and 4-fold (**Fig. 4.5b**) symmetric morphologies, the projection vectors of their secondary arm on the observation planes are both parallel to their primary arm orientations. Therefore, <111> is established as the most/ one of the preferred growth orientations, because of its relatively larger growth driving force; and the secondary arm and tertiary branches' growth orientation belong to <111> as well. Therefore, the exposed outer plane of a complete primary (see **Fig. 4.5**) is highly likely to be the {110} plane of BCC crystal, which is the highest reticular density crystal plane for BCC structure (Sunagawa, 1995; West and Fredriksson, 1985). Consequently, as shown in **Fig. 4.5a**, [112], the projection of [111] on (111) plane, has exactly 60˚ angle with [2-11] which is the projection [1-11] on (111) plane. The projection angles of <111> to <112>{111} is about 19.5˚. Meanwhile, as shown in **Fig. 4.5b** [-1-10], the projection of [-1-11] to (001) plane, has a 90˚ angle with [1-10] which is the projection [1-11] on (001) plane. The projection angles of <111> to <110>{001} is about 35.3˚. Thus, the {111} directions appear to be one of the preferred growth orientation of anisotropic primary α-AlFeMnSi crystal. On this establishment, {110} appears to be the facet planes of anisotropic primary α-AlFeMnSi crystal.

At the last growth stage, the edges of primary α-AlFeMnSi developed to have rhombic dodecahedral structure. During the growth to a complete rhombic dodecahedral primary α-AlFeMnSi, impurity elements are rejected to the surrounding melt, and enriched the region near the interface (Chernov, 1974). Additionally, the solutes become more difficult to diffuse at faceted plane of the primary particle compared with the edge and corner. Thus the driving force for growth on the edge and corner is higher, which leads to the stability of a complete rhombic dodecahedral structure. This, in return, may stop the elongation of the edge, giving rise to macro-steps growth tangentially towards the centre of the facet. If the impurity concentration is relatively low, these steps on preferred orientations will be merged at the centre. Thus, a complete rhombic dodecahedral structure is established. On the other hand, the higher concentrations of impurities at the edges to diffuse into the larger body of the melt are easier compared with the centre of the facet. As a result, it gives rise to the higher driving force for growth on the corner and edges, which contributes to the size increase of the faceted primary particles.

On the other hand, the particle size increase is also a very importantly factor to understand the growth of primary α-AlFeMnSi crystal. The growth velocity of primary α-AlFeMnSi seems not to be greatly affected by the casting temperature or cooling rate when it is above (3.5K/s). As established in previous section 4.4.2.1, the nucleation of primary α-AlFeMnSi can be trigged at lower cooling rate (≤0.8K/s) and the formation of minor amount of primary α-AlFeMnSi at low casting superheat (10K) is considered to be a product of local non-homogeneities liquid during the cooling process before casting or the heat balancing process at the beginning of the casting. This effect is reflected in **Fig. 4.20** that the average size of primary α-AlFeMnSi does not change drastically as casting temperature decreases where longer growth time is allowed and volume fraction of primary α-AlFeMnSi increases very moderately. Further, once the nucleation was trigged with enough undercooling when TP-1 casting was applied at low temperature (650˚C, 640˚C and 630˚C) the average size of primary particle is significantly reduced (see **Fig. 4.20**). With the same casting temperature as cooling rate decreases the area ratio of primary to eutectic α-AlFeMnSi (shown in **Fig. 4.23**) increase, which suggests that low cooling rate allows more primary α-AlFeMnSi nucleation site and/or more growth time. It is considered at the results of longer diffusion and growth time at lower cooling rates. Moreover, in the relatively more homogenised liquid (at a cooling rate of 0.02K/s) the primary particle can gain significant increase in size (251.3±75.3μm), but with a very low number density. This can be cause by the composition shift from nominal value after the initial nucleation and growth of primary particle further nucleation stops as the actual undercooling is not enough to activate further nucleation site of primary α-AlFeMnSi. The joining morphology of two or more polyhedral primary α-AlFeMnSi particle is considered as a result of remelting of sediment primary particle during growth as they are very close and sometime with physical contact.

It may be proposed that as a strongly anisotropic crystal primary α-AlFeMnSi's preferred growth orientations are <111> which are relatively more accelerated during growth. The consequential local solute profile change leads to the rhombic dodecahedron morphology at the end of its growth. The growth of faceted primary α-AlFeMnSi can be facilitated by sufficient amount of growth time and a more homogenised liquid.

4.4.3 Solidification Behaviour of Eutectic α-AlFeMnSi

4.4.3.1 Nucleation

In Al-5Mg-2Si-1.2Fe-0.7Mn alloy system, Chinese-script eutectic is the other form of α-AlFeMnSi observed in addition to polyhedral primary α-AlFeMnSi. Al-5Mg-2Si-1.2Fe-0.7Mn, a hypereutectic alloy (**Fig. 4.1**), should show a primary α-AlFeMnSi and eutectic α-AlFeMnSi/α-Al mixed microstructure. **Fig. 4.19a-b** shows that there is a large amount of dendritic α-Al containing α-AlFeMnSi/α-Al eutectics. When primary α-AlFeMnSi is formed microstructure, it is observed (**Fig. 4.19c-g**) that a considerable amount α-Al dendrite containing both primary and eutectic α-AlFeMnSi and α-Al grains. Porter and co-workers suggested that irregular eutectic structure can be encouraged when one of the solid phases is capable of faceting due to high melting entropy (Porter, Easterling and Sherif, 2009), which causes primary α-AlFeMnSi and eutectic α-AlFeMnSi/α-Al mixed microstructure showing a α-Al dendrite and α-AlFeMnSi/α-Al mixed microstructure due to α-AlFeMnSi's strong anisotropy. Further, the appearance of large number density of primary α-AlFeMnSi can lead to a considerably reduced colony size of eutectic α-AlFeMnSi. Conversely the eutectic α-AlFeMnSi can be increased when there is only limited amount of primary α-AlFeMnSi (**Fig. 4.20**). This strongly indicates that the presence of primary particle encourages the nucleation of eutectic α-AlFeMnSi considering the substantial size reduction with increasing primary α-AlFeMnSi.

Based on microstructure observations and previous analyses, two potential transformations mechanisms for eutectic α-AlFeMnSi are proposed: (1) the primary α-Al solidifies first providing higher solute concentration for the formation of new α-AlFeMnSi/α-Al eutectic grain (**Fig. 4.27a**); (2) eutectic α-AlFeMnSi branches solidifies first on primary α-AlFeMnSi as primary α-AlFeMnSi is an ideal nucleation substrate and followed by coupled growth of α-Al (**Fig. 4.27b**). In current experiment, it is very likely that both of the mechanisms have contributed to the final microstructure as the microstructure contains mixed morphology of the products of three formation mechanisms. Although in the case without primary α-AlFeMnSi, such as casting with superheat more than 30K (**Fig. 4.19a**), the first assumption strongly supports that the primary α-Al forms first followed by the formation of eutectic α-AlFeMnSi, as a substantial fraction of dendritic α-Al grains do not contain any eutectic structure and eutectic α-AlFeMnSi grains mainly located at the inter-dendritic regions of α-Al.

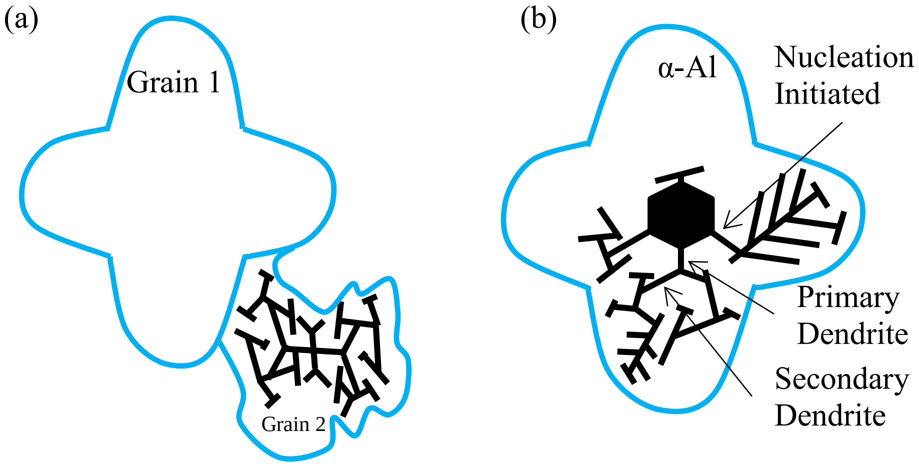

Figure 4.27 A schematic illustration of the formation mechanism of α-AlFeMnSi irregular eutectic showing that (a) Fe-IMC located at inter-dendrite area of α-Al and (b) Fe-IMC contained within α-Al grain with nucleation and eutectic growth on primary α-AlFeMnSi particle.

More importantly, the second assumption is confirmed in **Fig. 4.7** and **4.19c-g** that eutectic α-AlFeMnSi branch developed from the edges of primary α-AlFeMnSi particle followed by the formation of irregular α-AlFeMnSi/α-Al eutectic. Both of the mechanisms are believed to be dependent on the actual liquid situation that the mechanism (1) dominates the solidification with higher cooling rate and mechanism (2) dominates the solidification with the formation of primary α-AlFeMnSi. Local nucleation undercooling is the determining factor of whether α-Al or α-AlFeMnSi nucleates first for the formation of eutectic α-AlFeMnSi/α-Al.

The boundary of a Fe-IMC colony is considered as the tip of a branch in an interconnected α-AlFeMnSi eutectic network. During the formation of the eutectic Fe-IMC branches, the excess elements, such as Al and Mg, are rejected to the liquid, leading to local deviation in composition from that of the equilibrium eutectic composition. As the local impurity elements concentrations is dilute, the driving force for the α-Al increases and driving force for the growth of α-AlFeMnSi is reduced. This leads to a higher growth velocity on α-Al compared with α-AlFeMnSi. Subsequently, as the Al atoms are consumed faster than others, the growth velocity of α-Al and α-AlFeMnSi reaches a stable state. Then, this branched irregular eutectic structure forms.

4.4.3.2 Growth

The growth of eutectic α-AlFeMnSi is dependent on the type of nucleation mechanism for the formation of eutectic α-AlFeMnSi established in previous section 4.4.3.1. Based on this, we can understand the eutectic α-AlFeMnSi morphology change as the casting condition and the amount of primary α-AlFeMnSi in microstructure vary. As observed with various casting temperature experiments (**Fig. 4.19**), when the primary α-AlFeMnSi formation is encouraged, the solute elements will at first contribute to the formation of primary α-AlFeMnSi and then take part in the formation for eutectic α-AlFeMnSi/α-Al. As a result, eutectic volume fraction decreases considerably in from 6.3±0.2vol.% to 3.4±0.2vol.% (see **Fig. 4.20**) at TP-1 pouring temperatures 720-660˚C and 650-630˚C, respectively. However, if the nucleation of primary α-AlFeMnSi (reaction R4.1) is not triggered, instead of participating to the reaction R4.1, the excess Fe and Mn content will enhance the reaction for eutectic α-AlFeMnSi (R4.2) leading to an larger volume fraction of eutectic α-AlFeMnSi (6.2%±0.2vol.%). It is inevitable that the actual solidification parameters have some disagreement with that of CALPHAD approach prediction using Pandat^{TM}. The volume fraction of primary α-AlFeMnSi (3.4%±0.2vol.%) has a small deviation from the prediction value (2.7%); while the measured volume fraction of eutectic α-AlFeMnSi (3.1%±0.3vol.%) is significantly different from the prediction value (0.8%). This disagreement is caused by its 3D morphology and higher toughness of Fe-IMC compared with matrix, which can easily increase the surface area during 2D observations. The primary α-AlFeMnSi does not have a significant surface area increase due to the compact 3D morphology. The suppression of primary α-AlFeMnSi still contributed to a considerable volume fraction increase for eutectic α-AlFeMnSi as the quantification methods were kept the same. The sharp drop of primary α-AlFeMnSi volume fraction is very likely to be caused by settling effect and low fluidity as melt approaches the eutectic temperature. Therefore, a large amount of primary α-AlFeMnSi was trapped in the crucible and lead to the lower volume fraction observed when pouring at 620˚C.

In the current investigation, cooling rate is mainly causes changes in the amount of time available for the the growth, effective nucleation site density and the number density primary α-AlFeMnSi. In various cooling rate experiments where the alloy composition and superheat are kept constant, the size of α-AlFeMnSi/α-Al colonies appears to be less sensitive to the cooling rate compared with the α-Al, as the eutectic α-AlFeMnSi only increased by 43% from 102.0±12.1μm to 145.6±13.7μm as the cooling rate decreased by more than 50 times from 870K/s to 13.8K/s (**Fig. 4.23**). The slower cooling rate activate lower nucleation site number and allows more growth time for eutectic grains (Easton and StJohn, 2008; Greer *et al.*, 2000), which consequently provide more solute for each nucleated grain. For primary α-AlFeMnSi, as a potential nucleation site for eutectic α-AlFeMnSi, has a significant effect on solidification of process eutectic α-AlFeMnSi. As established previously (**Fig. 4.22** and **Fig. 4.23**), slower cooling rate allows a relatively smaller heat gradient during cooling which can be preferable to the nucleation of primary α-AlFeMnSi, which causes the size reduction of primary α-AlFeMnSi even though the cooling rate decreases. As the amount of solute in the melt is the same, lower solute content for the formation of eutectic α-AlFeMnSi is available as slower cooling rate facilitate the increase in the volume fraction of primary α-AlFeMnSi. Thus, if the solute content is constant, decreased cooling rate can increase the relative amount of primary α-AlFeMnSi than the eutectic α-AlFeMnSi. Considering the large Chinese-script morphology of the eutectic α-AlFeMnSi and compact polyhedral morphology for primary α-AlFeMnSi, the solidification of primary α-AlFeMnSi is certainly relatively more beneficial to the microstructure and the resulting properties.

4.4.4 Effects of Solute Segregation on Solidification of α-AlFeMnSi

Before analysing the micro-segregation for α-AlFeMnSi during solidification, it is very important to understand which the thermodynamically stable Fe-IMC phases are. It has been reported that the α-AlFeMnSi compounds sharing same crystal symmetry can exhibit different stoichiometry, particularly when Fe and Mn are both present (Ji *et al.*, 2013b; Crepeau, 1995; Narayanan, Samuel and Gruzleski, 1994; Gustafsson, Thorvaldsson and Dunlop, 1986). Due to their chemical similarities, Fe, as well as Cr, can replace Mn to participate in the formation of Fe-IMCs (Kim *et al.*, 2006). The Si vacancies can be taken by Al while the BCC crystal structure is maintained. Consequently, the Fe/Mn and (Fe,Mn)/Si ratio are largely dependent on solute flux during solidification, which is essentially controlled by the casting condition and alloy composition. Two often observed α-AlFeMnSi phase stoichiometry are $Al_{15}(Fe,Mn)_3Si_2$ and $Al_{12}(Fe,Mn)_3Si$, which have the ratios (Fe+Mn)/Si of 1.5 and 3, respectively. When Si concentration is higher (normally in Al-Si alloys) $Al_{15}(Fe,Mn)_3Si_2$ tends to form (Liu, Cao and Chen, 2014; Cao and Campbell, 2004), otherwise $Al_{12}(Fe,Mn)_3Si$ is the preferred stoichiometry for α-AlFeMnSi (Yang *et al.*, 2014; Ji *et al.*, 2012; Kuijpers *et al.*, 2002). Thus, the observation of $Al_{12}(Fe,Mn)_3Si$ in current alloy composition is expected. The literature reported the same crystal symmetry for $Al_{12}(Fe,Mn)_3Si$ and $Al_{15}(Fe,Mn)_3Si_2$ when Mn presents in Al-Fe-Si system, but the mechanism for this variation has not been well described. In current experiment, the stoichiometry appears to be not significantly affected by the cooling rate. Given that, in Al-Mg-Si alloys the presence of Mn content determine the crystal structure of the α-AlFeMnSi and the Fe, Mn and Si concentrations of dominant Fe-IMC's.

The element concentration of Fe-IMCs in current investigation is illustrated in **Fig 4.13** showing a considerable difference when cooling rate varies. Solute concentration variation is observed in both matrix and compounds when the cooling rate changes, which is normally regarded as microsegregation (Verma *et al.*, 2013; Dutta and Rettenmayr, 2002; Langsrud, 1990). For Fe-IMC in both Al-Fe and Al-Fe-Si systems, the morphology and the volume fraction of Fe-IMCs are altered by varying the cooling condition, where diffusion plays a crucial role in this change (Verma *et al.*, 2013; Dutta and Rettenmayr, 2002; Dutta and Rettenmayr, 2000; Allen *et al.*, 1998). In the current investigation, the concentrations of elements in the compounds varies in both primary and eutectic α-AlFeMnSi particles suggesting that the composition of Fe-IMC is constrained and form even at lower solute concentration when there is insufficient solute supply (diffusion time and solute flux). However, when the local solute composition is below the critical level for the formation of α-AlFeMnSi during non-equilibrium solidification, other metastable phases which requires lower formation energy (Khalifa, Samuel and Gruzleski, 2003), such as $Al_6(Fe,Mn)$ (see **Fig. 4.9**), form.

The solute concentration profiles in **Fig. 4.28** demonstrate the solute distribution during the growth of α-AlFeMnSi. In **Fig. 4.28** the relative solute concentration profile at the growth front of solid phase is illustrated. The distance needed to reach the chemically near-homogenised liquid is given as (Kurz and Fisher, 1986):

$$\delta_c = \frac{2D}{V} \tag{4.5}$$

where δ_c, the thickness, is defined as the equivalent boundary layers for a planer interface, D is the diffusion coefficient and V is the growth velocity. The solute concentration at the growth front is dominated by the solute concentration in the solid, solute concentration in the remaining liquid and the solute diffusivities. More importantly, the difference in diffusion rate appears to be a critical factor causing different microsegregation levels through α-AlFeMnSi phase as the Si concentration in α-AlFeMnSi does no change much while Fe and Mn concentrations varied notably with the change in cooling rate (**Table 4.2**).

Thus, the Fick's second law of diffusion is introduced here to get an insight into the significance of the impact caused the diffusion rate on the composition of Fe-IMC. It provides the reject atom flux at the cross section (A) because of the formation of the solid to be:

$$J_S = -A\left(\frac{dz'}{dt}\right) * (C_l - C_0) \tag{4.6}$$

where C_l is the solute concentration at the interface and C_0 is the alloy composition. At steady state, the resultant flux should be balanced by an equal flux from liquid, which gives:

$$G_C = -AD(\frac{dC_l}{dz}) \tag{4.7}$$

By combining **equation 4.6** and **equation 4.7**, the solute fluxing balance is given by

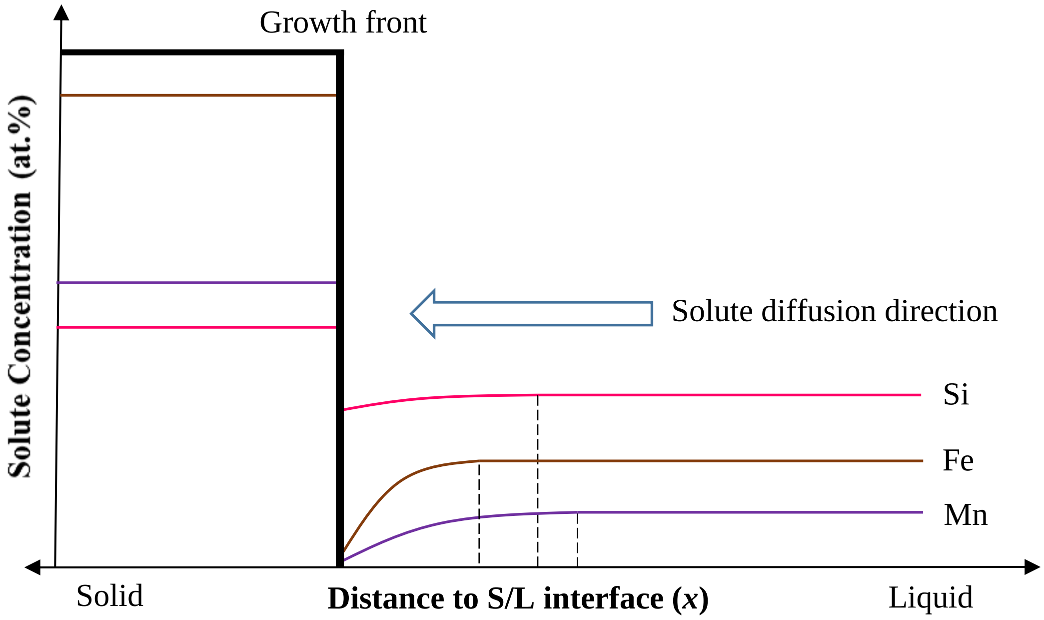

Figure 4.28 Schematic illustration of the concentration profiles for Fe, Mn and Si at the front of solid phase (α-AlFeMnSi). The concentrations of elements were marked based on the stoichiometry of the solid phase and the initial composition of the liquid. Diffusion directions in liquid and solid are indicated with hollowed arrows. The distance from the interface until chemically near-homogenised liquid labelled with dash line. Interface liquid solute profile is calculated with C_0/k (Kurz and Fisher, 1986).

Kurz and Fisher as (Kurz and Fisher, 1986):

$$G_C = \left(\frac{dC_l}{dz}\right)_{z=0} = -\left(\frac{V}{D}\right)\Delta C_0 \quad (4.8)$$

where G_C is the solute concentration gradient, V is the growth rate, D is the diffusion coefficient and ΔC_0 is defined as solute concentration difference between solute concentration in S/L interface and alloy composition. For a given growth rate (1m/s), the calculated value for steady state is shown in **Table 4.5**. The desired rate of the solute atoms traveling through the liquid to the interface area are 1.4×10^{10}, 1.8×10^{10} and 3.2×10^{10} at.%/m for Si, Mn and Fe, respectively. It suggests that at steady state the amount of Fe+Mn atoms required for the solidification of α-AlFeMnSi is 3.5 times more than that of Si. However, the diffusion of Fe and Mn in liquid Al is at the same order of magnitude with the diffusion of Si in liquid Al. Consequently, in non-equilibrium solidification, there is a severe shortage of Fe and Mn compared with Si for the formation of $Al_{12}(Fe,Mn)_3Si$; the (Fe+Mn)/Si ratio increases as the cooling rates decreases due to more sufficient diffusion time for Fe and Mn to diffuse to the S/L interface at slow cooling process. Other factors, such as competitive growth and nucleation, are negligible here as the increased cooling rate did not noticeably alter either the transformation temperature or crystal structure of Fe-IMCs.

Therefore, the stoichiometry of α-AlFeMnSi is mainly dependent on chemical composition. However, for a complicate compound α-AlFeMnSi, the segregation of elements is evidenced and depended on the elements' diffusion coefficient and solute concentration in liquid.

4.4.5 $Al_6(Fe,Mn)$ to α-AlFeMnSi Transformation

4.4.5.1 Nucleation of $Al_6(Fe,Mn)$

It is well known that the metastable phase $Al_6(Fe,Mn)$, with almost identical crystal structure to the thermodynamically stable Al_6Mn, tends to form at low Fe, Mn concentration or at higher cooling rates (Khalifa, Samuel and Gruzleski, 2003; Maggs, 1996; Narayanan, Samuel and Gruzleski, 1994; Skjerpe, 1987; Young and Clyne, 1981). CALPHAD approach prediction using Pandat^{TM} PanAl2013 database suggests that in the Al-5Mg-1.2Fe-0.7Mn-*x*Si system Al_6Mn becomes thermodynamically stable when Si concentration decreases below 1.8wt.%. Thus, with CF condition (0.02K/s) when Si is consumed by the growth of primary α-AlFeMnSi, the nucleation of Al_6Mn is very likely to take place once the nucleation undercooling is reached. Due to its long and thin morphology and reduced settling time during the solidification compared with primary α-AlFeMnSi, primary $Al_6(Fe,Mn)$ is more likely to remain in the melt, which will then allow the nucleation of $Al_6(Fe,Mn)$/α-Al on its surface.

The formation of α-AlFeMnSi on $Al_6(Fe,Mn)$ requires a nucleation event to initiate the phase transformation. Observation of the intermediate stage of this transformation was not possible, and it is very difficult to determine the point of nucleation. The **Fig. 4.26** shows that the transition regions located at both $Al_6(Fe,Mn)$ branches and parallelogrammatic primary $Al_6(Fe,Mn)$. One continuous branch can consist of several transition region (**Fig. 4.26a**), and α-AlFeMnSi branched areas are always connected to the transition region on $Al_6(Fe,Mn)$ but not

$Al_6(Fe,Mn)$ directly. Due to the limitation of 2D observation the 3D morphology could be different from the interpretation, but over 30 partially transformed particles show the same trend and should represent the 3D situation. Based on this, the nucleation of α-AlFeMnSi occurs at $Al_6(Fe,Mn)$ branches so that the transformation can develop towards $Al_6(Fe,Mn)$ grain centre, and the α-AlFeMnSi has multiple nucleation sites on $Al_6(Fe,Mn)$ to allow the presence of separate transition regions.

4.4.5.2 Eutectoid Transformation

A number of researchers have addressed this transformation as $Al_6(Fe,Mn)$-to-α-AlFeMnSi transformation, but the type of transformation proposed is different. Some suggested that in the system with a high Fe composition (above 10wt.%) the $Al_6(Fe,Mn)$-to-α-AlFeMnSi transformation is a peritectic transformation (Zhou *et al.*, 2016; Warmuzek, Rabczak and Sieniawski, 2005; Stefaniay, Griger and Turmezey, 1987), that α-AlFeMnSi form on existing $Al_6(Fe,Mn)$ particles through peritectic reaction and then become a solid-state diffusion dominated transformation when $Al_6(Fe,Mn)$ solid liquid interface disappears (Ha and Hunt, 2000; St John and Hogan, 1987). Different from peritectic reaction, Alexander and Greer suggested that $Al_6(Fe,Mn)$-to-α-AlFeMnSi transformation is a eutectoid transformation in dilute Al alloys ($C_{Fe}+C_{Mn}+C_{Si}$ less than 5wt.%) and that the reaction is dependent on homogenisation time and Si solid diffusion coefficient (Alexander and Greer, 2004; Alexander and Greer, 2002; Watanabe, Ohori and Takeuchi, 1984; Munson, 1967; Sun and Mondolfo, 1967). The reaction equation for this eutectoid transformation is given by Alexander (Alexander and Greer, 2002):

$$3Al_6(Fe,Mn) + Si \rightarrow \alpha\text{-}Al_{12}(Fe,Mn)_3Si + 6Al \qquad \text{(R4.6)}$$

The product eutectoid composes of 75% $\alpha\text{-}Al_{12}(Fe,Mn)_3Si$ and 25% α-Al volumetrically (Alexander and Greer, 2002), which is generally consistent with the microstructural observation in transition regions as it composes of Al-rich region and $\alpha\text{-}Al_{12}(Fe,Mn)_3Si$.

Microstructure of the sample quench at 620˚C (shown in **Fig. 4.26b**) show that the $Al_6(Fe,Mn)$-to-α-AlFeMnSi transformation did not initiate after the formation of $Al_6(Fe,Mn)$ and its surrounding α-Al grains. There is no liquid-$Al_6(Fe,Mn)$ interface for the peritectic transformation present here. In fact, the microstructure of the sample quenched at 600˚C (shown in **Fig. 4.26c**) reveals duplex particles appeared on both primary and dendritic Al_6(Fe,Mn) particles prior to the solidification of Mg_2Si. Thus, the Al_6(Fe,Mn)-to-α-AlFeMnSi transformation initiate between 620˚C and 600˚C when the Al_6(Fe,Mn) particles were already surrounded by α-Al. Therefore, Al_6(Fe,Mn)-to-α-AlFeMnSi transformation is considered to be a eutectoid transformation that commences between 620˚C and 600˚C. Compared with the solid state transformation, the activation energy for diffusion for peritectic transformation is much lower, Q_{Fe}= 215kJ/mol in solid, while Q_{Fe}= 35kJ/mol in liquid (**Table 4.5**). Consequently, the transition layer of peritectic transformation should easily surround the S/L interface, instead of having some separate transition regions on the solid (**Fig. 4.26**).

During the eutectoid transformation, as indicated in **Fig 4.26b**, Al atoms were rejected from Al_6(Fe,Mn) phase and therefore Al-rich region forms. After the formation of α-Al region, it will coalesce and start to *spheroidise* in order to minimize the surface area to reduce surface energy, which is a diffusion dominated process (Kamyabi-Gol and Sheikh-Amiri, 2010; Alexander and Greer, 2002). Longer diffusion times facilitate the growth of the intergranular Al-rich regions, and eventually the interface with Fe-IMC will disappear when the granular Al-rich region moves into Al matrix. The **Fig. 4.26b** shows that Al-rich regions have a very fine morphology when it is close to untransformed Al_6(Fe,Mn) and have a coarser morphology when it is close to the Al/α-AlFeMnSi interface. This is because the transition on the grain boundary initiated earlier than the centre of the particle, which should allow longer dissolution time for these fine Al-rich regions to decrease interface energy. The incomplete spheroidization of Al-rich regions is considered to be mainly caused by limited Si in solid solution.

Thus, it is proposed that the Al_6(Fe,Mn)-to-α-AlFeMnSi is a Si diffusion dominated eutectoid transformation. The formation of Al_6(Fe,Mn) is most likely caused by the reduction of solute content during the solidification of primary α-AlFeMnSi.

4.5 Summary

In this chapter, the nucleation and growth behaviour of both primary and eutectic α-AlFeMnSi in an Al-5Mg-2Si-1.2Fe-0.7Mn alloy was described in detail. The solidification sequence of this alloy was confirmed with thermal analysis and microstructure observation, which shows solidification reactions as follow: L → Primary α-AlFeMnSi + L_1 → $Al_6(Fe,Mn)$ + L_1' → α-Al + α-AlFeMnSi + L_2 → α-Al + Mg_2Si+ L_2' → α-Al + Mg_2Si + $Al_6(Fe,Mn)$. $Al_6(Fe,Mn)$, is a metastable phase in current system, and able to transform into α-AlFeMnSi at a low cooling rate (0.02K/s). The primary α-AlFeMnSi exhibits compact polyhedral morphology, and the eutectic α-AlFeMnSi exhibits Chinese-script morphology; they were both identified with TEM to correspond to a body-centred cubic (BCC) structure with a lattice parameter of 1.256nm which was consistent with the crystal structure of α-AlFeMnSi or $Al_{19}Fe_4MnSi_2$, and their stoichiometry were both measured with EDS to be $Al_{12}(Fe,Mn)_3Si$. It is unlike α-Al or α-Mg the formation of primary α-AlFeMnSi was encouraged by slower cooling rates (≤0.8K/s). When the nucleation of primary α-AlFeMnSi occurs (casting with 10K superheat), the size of primary α-AlFeMnSi increased gradually from 24.5±3.1μm over 800K/s to 52.6±5.0μm at 3.5K/s, and it then increased dramatically to 251.3±75.3μm when the cooling rate decreased to 0.02K/s. The colony size of eutectic α-AlFeMnSi/α-Al increased gradually from 102.0±12.1μm at over 800K/s to 165.1±36.4μm at 3.5K/s before an large increase to 623.3μm at 0.02K/s. EDS analysis of α-AlFeMnSi particles reveals that increasing cooling rate (0.02K/s → 3.5K/s) can lead to the decrease in the concentration of Fe+Mn in α-AlFeMnSi by 1.0at.% in average, due to the solute segregation during solidification. Microstructure observation reveals that the {011} planes, especially in <111> orientations, are the preferred growth orientations of BCC primary α-AlFeMnSi resulting in rhombic dodecahedral 3D.

The volume fraction of eutectic α-AlFeMnSi significantly reduced with the formation of primary α-AlFeMnSi, for instance, the volume fraction of eutectic α-AlFeMnSi decreased from 6.2% (TP-1 casting at 720˚C (50K superheat) to 3.0% (TP-1 casting at 630˚C) whilst the volume fraction of primary α-AlFeMnSi increased from 0vol.% to 3.6±0.7vol.%; the average colony size of eutectic α-AlFeMnSi/α-Al is decreased by 31.1% from 175.5±32.5μm to 120.9±30.8μm when a large amount of primary α-AlFeMnSi forms. Nucleation of eutectic α-AlFeMnSi initiates on the primary α-AlFeMnSi particle when primary α-AlFeMnSi presents, otherwise it nucleates after the formation of α-Al. Despite the large undercooling required for the nucleation of primary α-AlFeMnSi, more homogenised liquid and longer diffusion time are both required to achieve a stable nucleation embryo which is then able to undergo free growth. In the last chapter, a novel grain refiner will be developed to overcome this issue and enhance the nucleation of Fe-IMCs.

Chapter 5 Effect of Magnesium Addition on Fe-rich Intermetallic Compounds

Mg, as a common alloying element in many Al alloys, has a significant influence on the solidification behaviour and microstructure, including secondary phases and intermetallic compounds (Wang and Davidson, 2001; Caceres *et al.*, 1999; Samuel *et al.*, 1998; Samuel and Samuel, 1997; Joenoes and Gruzleski, 1991). This chapter focuses on the impact of Mg content on the formation, morphology and structure of microstructure of Fe-IMCs in Al-Fe-Mn and Al-Si-Fe-Mn alloys, characterised using OM, SEM and TEM. The morphology evolution, characterization and mechanism of the influence of Mg content will be presented.

5.1 Solidification microstructure of Mg-containing Al Alloys

5.1.1 Phase Diagram Calculation

The CAlPHAD approach was adopted to predict the effect of Mg content on the solidification sequence, phase transformations and phase volume fraction. It was performed with Pandat^{TM} 8.2 using thermodynamic data from PanAl2013 database.

The calculated equilibrium phase diagrams at the cross section of Al-1.2Fe-0.7Mn-*x*Mg (*x*=0-8wt.%) and Al-2Si-1.2Fe-0.7Mn-*y*Mg (*y*=0-6%) are presented in **Fig. 5.1a** and **Fig. 5.1b**, respectively. In Al-1.2Fe-0.7Mn-*x*Mg alloy, $Al_{13}Fe_4$ solidifies as the primary phase followed by the formation of $Al_{13}Fe_4$/α-Al eutectic, and a minor amount of Al_6(Fe,Mn) forms during the last stage of solidification or during solid state transformation depending on the Mg composition. However, microstructure observation (see section 5.1.2) suggests that Al_6(Fe,Mn) is the predominant Fe-IMC instead of $Al_{13}Fe_4$ in TP-1 samples. Therefore a phase diagram that suppresses the $Al_{13}Fe_4$ phase and allows Al_6(Fe,Mn) phase was calculated with Pandat^{TM} 8.2 (indicated with red dash lines in **Fig. 5.1a**); the eutectic composition of intermediate Al_6(Fe,Mn) phase is 5.25wt.% Mg, while the eutectic point is at 1.45wt.% Mg when $Al_{13}Fe_4$ is not supressed in this system. In Al-2Si-1.2Fe-0.7Mn-*y*Mg alloy (**Fig. 5.1b**), α-AlFeMnSi solidifies as primary phase followed by the formation of α-Al/α-

AlFeMnSi eutectic and a small amount of β-AlFeSi, Mg_2Si or $Al_{13}Fe_4$ forms depending on the Mg concentration during the last stages of solidification. The α-AlFeMnSi was found to be the predominant Fe-IMC in microstructure of TP-1 sample with more than 40K superheat (see section 5.1.2).

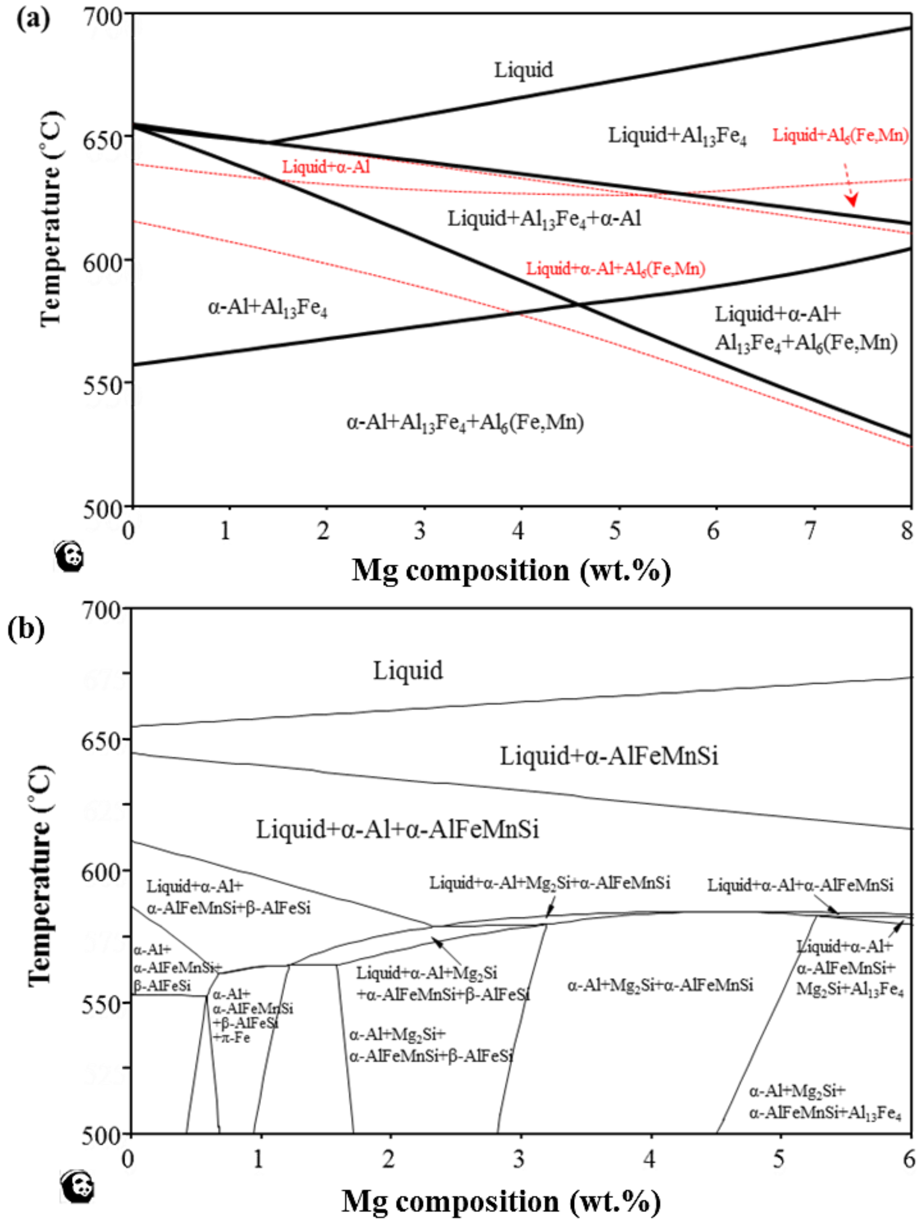

Figure 5.1 The cross section of equilibrium phase diagram for (a) Al-1.2Fe-0.7Mn-*x*Mg (red dash lines representing the diagram with α-Al and intermediate Al_6(Fe,Mn) only) and (b) Al-2Si-1.2Fe-0.7Mn-*y*Mg using Pandat^{TM} 8.2.

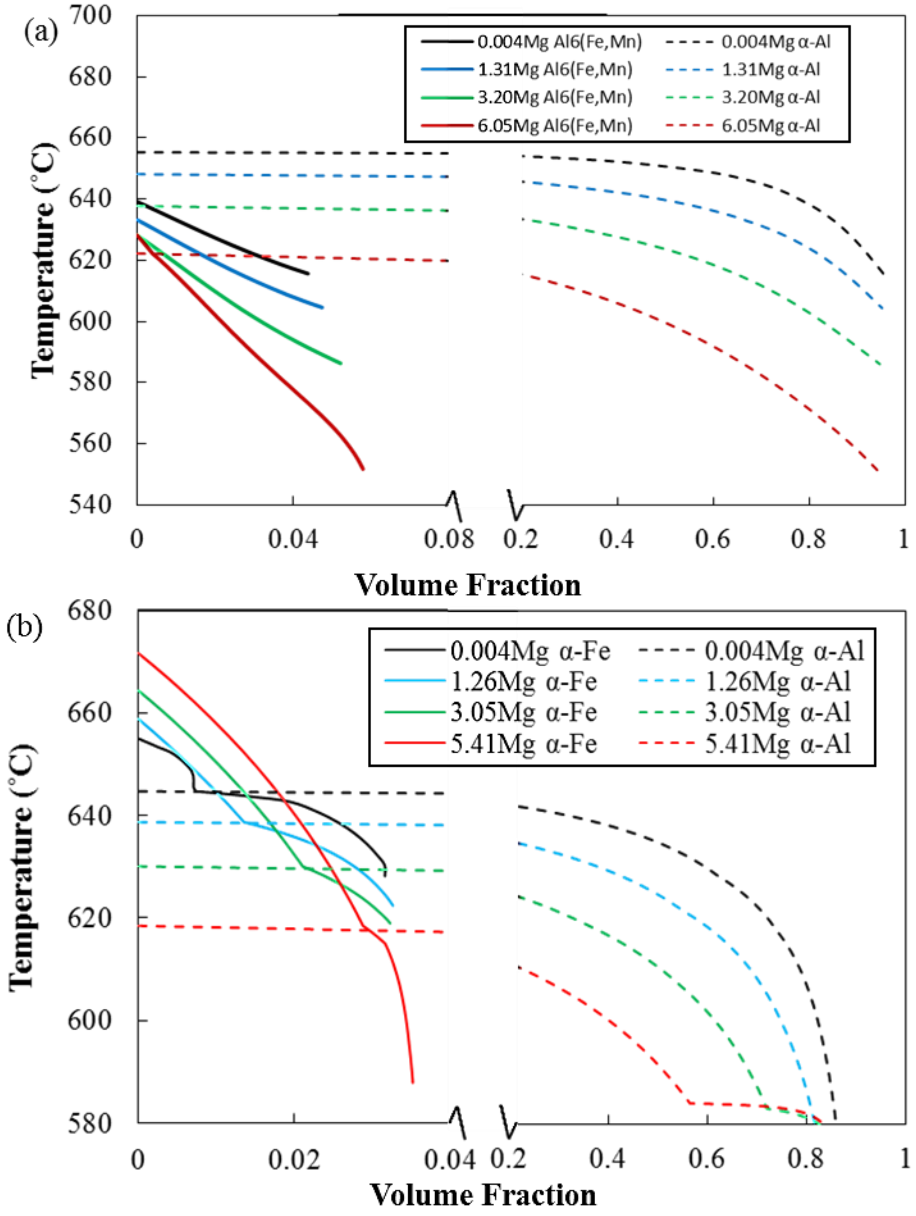

Figure 5.2 Comparison of volume fractions of Fe-IMCs and α-Al in (a) Al-1.2Fe-0.7Mn alloy with Fe-IMCs supressed to form Al_6(Fe,Mn) and (b) Al-2Si-1.2Fe-0.7Mn alloy at various Mg contents with Pandat^{TM} 8.2 under Scheil rule. α-Fe represents α-AlFeMnSi. The volume fraction of Fe-IMCs and α-Al are shown indicated with solid lines and dash lines, respectively. In Al-1.2Fe-0.7Mn alloy, Mg contents at 0.004, 1.3, 3.2 and 6.0wt.% are shown in black, blue, green and red respectively; in Al-2Si-1.2Fe-0.7Mn alloys, Mg contents at 0.01, 1.2, 3.0 and 5.4wt.% are shown in black, blue, green and red, respectively.

The comparisons of volume fractions of Fe-IMCs and α-Al at different Mg contents in both alloy systems are shown in **Fig. 5.2**. For Al-1.2Fe-0.7Mn alloy, Al_6(Fe,Mn) was the stable phase according to the equilibrium phase diagrams. **Fig. 5.2a** shows that the amount of Al_6(Fe,Mn) increased gradually from 4.4vol.% (0.004wt.% Mg) to 4.7vol.% (1.3wt.% Mg), to 5.2vol.% (3.2wt.% Mg) and finally reaches 5.8vol.% (6.0wt.% Mg), even though Mg does not participate in the formation of Al_6(Fe,Mn) or other Fe-IMCs in this system. Meanwhile, increased Mg content allows for a larger formation temperature range (**Fig. 5.2a**) which almost doubled from 39.7˚C at 0.004twt.% Mg to 76.5˚C at 6.0wt.% Mg. For Al-2Si-1.2Fe-0.7Mn alloys, there is no eutectic point for Fe-IMCs in this system range that is investigated (**Fig.5.1b**). **Fig. 5.2b** shows that the total volume fraction of Fe-IMCs were essentially unaffected by the Mg addition (from 3.16vol.% at 0.01wt.% Mg to 3.23vol.% at 5.4wt.% Mg). However, a higher Mg content allows a much larger temperature range for the primary α-AlFeMnSi transformation, which increased from 11.05˚C at 0.01wt.% Mg to 19.65˚C, 32.84˚C and then 51.57˚C at 1.3wt.%, 3.1wt.% and 5.4wt.% of Mg.

5.1.2 Microstructure Evolution with Various Mg Additions

5.1.2.1 α-Al

TP-1 was chosen in the experiment for a repeatable cooling rate which allows comparable result when Mg content in the alloys varied. Both Al-1.2Fe-0.7Mn-*x*Mg and Al-2Si-1.2Fe-0.7Mn-*y*Mg alloys were cast at 720˚C with 50–70K and 45–55K superheat (**Fig. 5.1**) for Al-1.2Fe-0.7Mn alloys and Al-2Si-1.2Fe-0.7Mn alloys, respectively.

As shown in **Fig. 5.3**, with the increased Mg content from 0.004wt.% Mg to 6.0wt.% Mg the solidification microstructure was reduced from 1336±209μm to 513±80μm and from 1233±238μm (0.01wt.% Mg) to 945±68μm (5.4wt.% Mg) in Al-Fe-Mn-*x*Mg and Al-2Si-1.2Fe-0.7Mn-*y*Mg alloys (**Fig. 5.4**), respectively. Equiaxed dendritic grains were observed on both cross and vertical sections of all four TP-1 samples with no grain refiner, except in the areas ranging 0-5mm away from mould wall. The effect of different Mg content seems to be less significant when silicon is present, as the grain size change was more significant in Al-1.2Fe-0.7Mn alloys (change of 823μm when Mg increases to 6.0 wt.%) compared with Al-2Si-1.2Fe-0.7Mn alloys (change of 270μm when Mg increases to 5.4 wt.%).

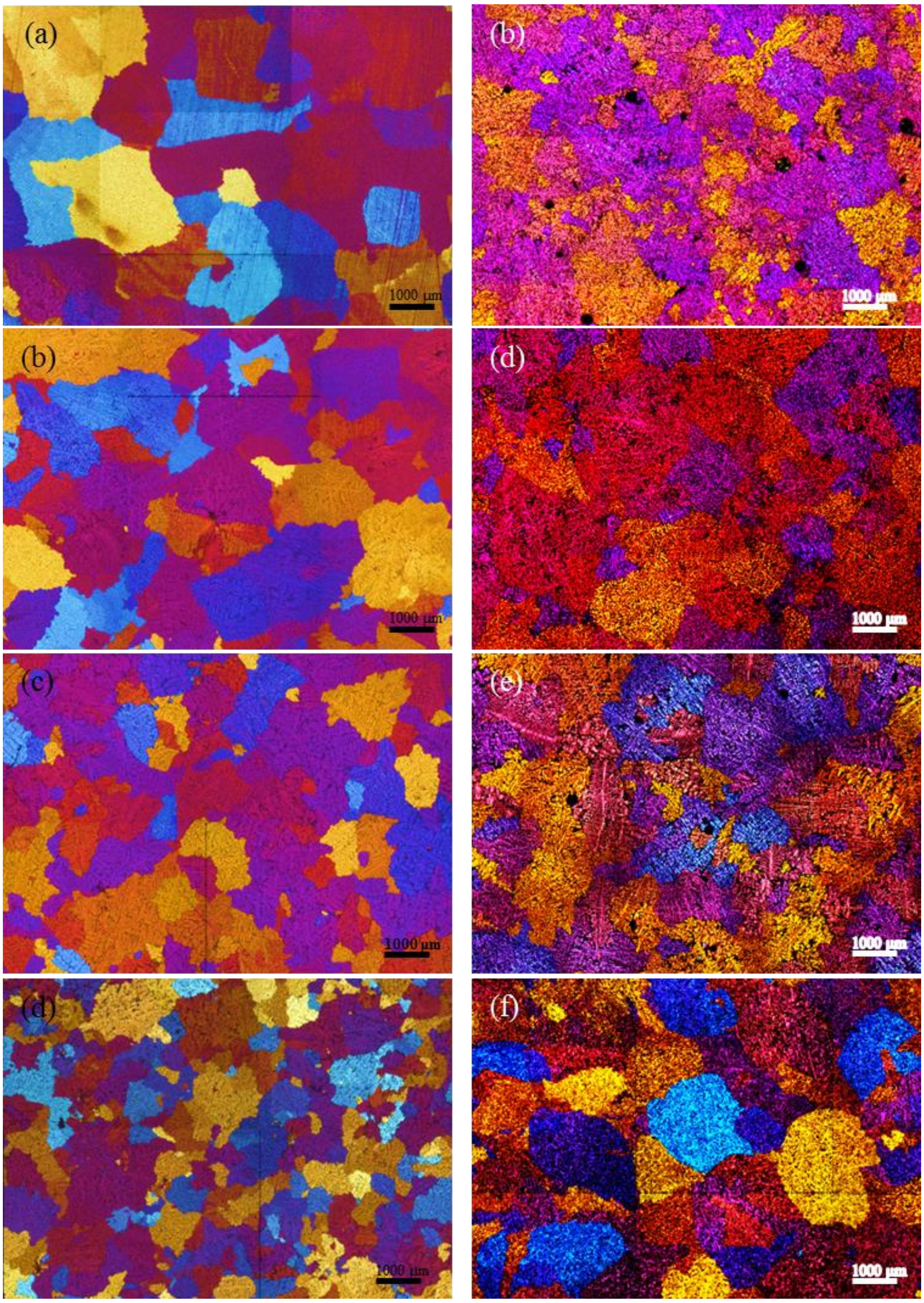

Figure 5.3 Microstructure of the cross section of TP-1 samples cast with superheat ranging 50K-70K showing the effect of Mg content on grain structure of Al-1.2Fe-0.7Mn alloy with (a) 0.004wt.%, (c) 1.3wt.%, 3.2wt.% and (e) 6.0wt.% of Mg, and Al-2Si-1.2Fe-0.7Mn alloy with (b) 0.01wt.%, (d)1.3wt.%, (f) 3.1wt.% and 5.4wt.% of Mg.

The SDAS is an important factor affecting the solidification of secondary phase (Fe-IMCs) including morphology of Fe-IMCs and Fe-IMC particle distribution in Al

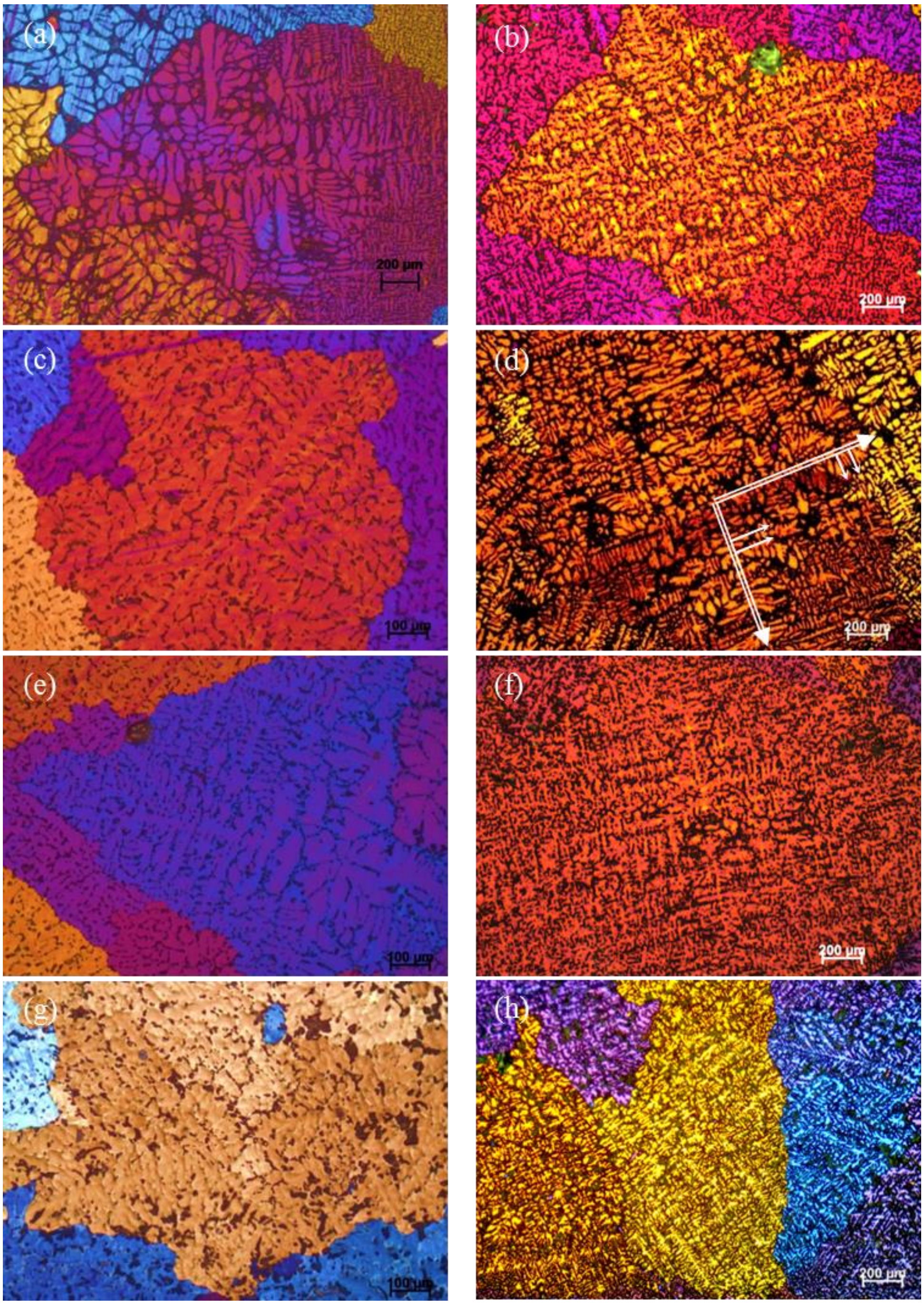

Figure 5.4 Microstructure of the cross section of TP-1 samples cast with superheat ranging 50K-70K showing the effect of Mg content on SDAS of Al-1.2Fe-0.7Mn alloy with (a) 0.004wt.%, (c) 1.3wt.%, 3.2wt.% and (e) 6.0wt.% of Mg, and Al-2Si-1.2Fe-0.7Mn alloy with (b) 0.01wt.%, (d)1.3wt.%, (f) 3.1wt.% and 5.4wt.% of Mg. Double-line arrows and single-line arrows in (d) indicate the primary dendrite arms and secondary dendrite arms, respectively.

alloys (Caceres *et al.*, 1999; Samuel and Samuel, 1995). It was taken into consideration for understanding the solidification behaviour of secondary intermetallics. The SDAS appears to be effected by Mg addition in both alloys. **Fig 5.4** shows the optical micrographs of Al-1.2Fe-0.7Mn-*x*Mg and Al-2Si-1.2Fe-0.7Mn *y*Mg alloys taken from the same area from different TP-1 samples. It shows that the secondary phases are mainly at the inter-dendritic regions, but also a considerable amount of secondary phases were observed within the grain or the dendrites. **Fig. 5.4** shows that the effect of Mg is more effective in Al-Fe-Mn alloys, leading to a more significant decrease from 41.9 in SDAS compared with that of Al-Si-Fe-Mn when Mg content increases.

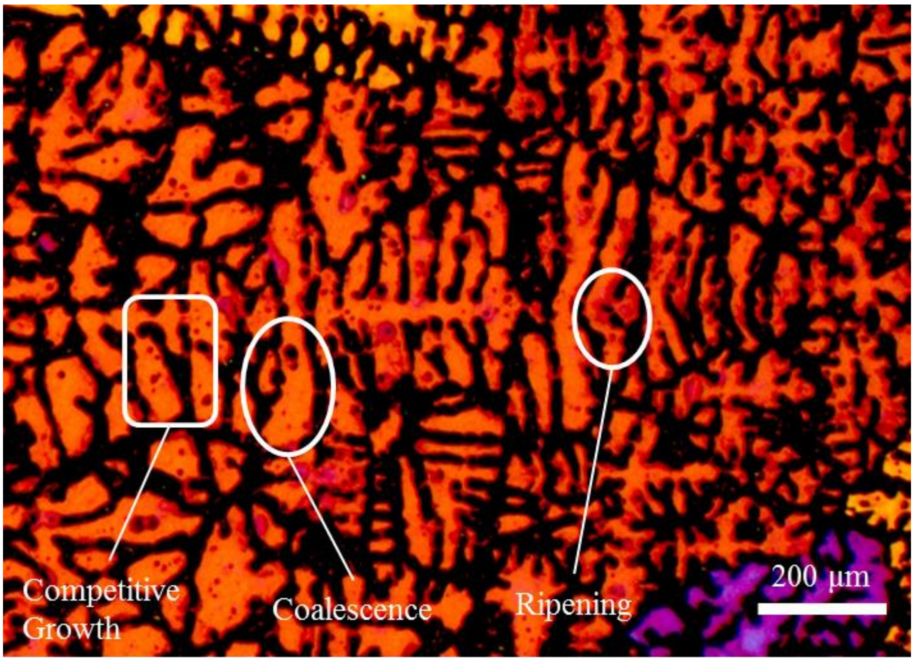

Figure 5.5 Polarized light optical micrograph of α-Al dendrites in Al-2Si-1.2Fe-0.7Mn-3.2Mg alloy showing the dendrite arms coarsening mechanisms of three potential mechanisms including competitive growth, coalescence and ripening.

During the dendritic growth of α-Al, the coarsening of dendrites arm has been observed. As shown in **Fig. 5.5**, the highlighted regions indicate the coarsening including competitive growth, coalescence and ripening (which is sometimes considered to be remelting process) (Li, Brody and Kazimirov, 2004; Diepers, Beckermann and Steinbach, 1999; Mortensen, 1991; Flemings, 1974). The dendrite coarsening was observed in various Mg contents for both Al-Fe-Mn and Al-Si-Fe-Mn alloys. It appears that the heat gradient in TP-1 casting is not relevant as the coarsening is observed on both vertical and cross sections of TP-1 sample (defined in **Section 3.2.1**).

5.1.2.2 Fe-IMCs

The microstructures of Al-1.2Fe-0.7Mn-*x*Mg alloy with various Mg contents are presented in **Fig. 5.6**. The microstructures consist of not only $Al_6(Fe,Mn)/\alpha$-Al eutectic but also significant amount of primary α-Al in all the compositions in current alloy system (eutectic point was suggested by the phase diagram in **Fig. 5.1a**). The $Al_6(Fe,Mn)$ phase in $Al_6(Fe,Mn)/\alpha$-Al eutectic exhibits a rod-like morphology when there is no Mg content (**Fig. 5.6a**), which is consistent with Hunt's observation (Hunt and Jackson, 1966). When Mg was introduced to the alloy, eutectic $Al_6(Fe,Mn)$

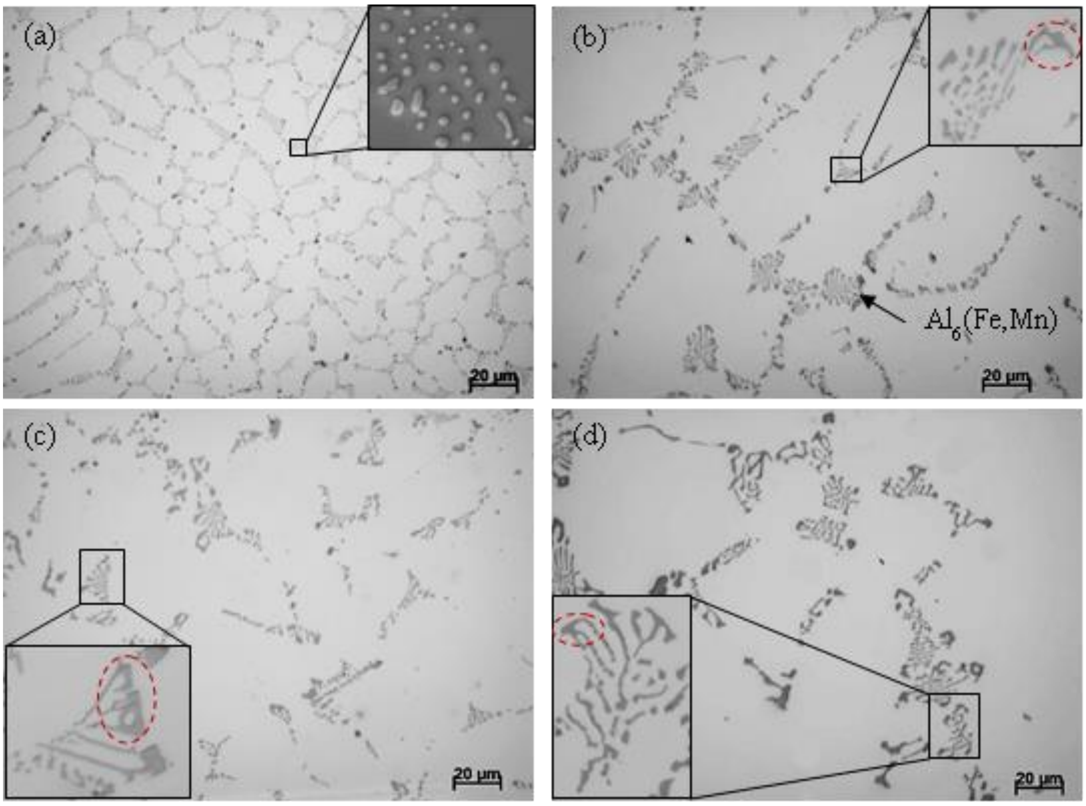

Figure 5.6 Optical microscopy images at the same magnification showing the microstructure of TP-1 sample of Al-1.2Fe-0.7Mn alloy with (a) 0.004wt.% Mg (inserted micrograph showing the morphology of Fe-IMC eutectic at higher magnification), (b) 1.3wt.% Mg, 3.2wt.% Mg and 6.0wt.% Mg addition. Dark grey phase shows a stoichiometry of $Al_6(Fe,Mn)$ examined with SEM/EDS, and the dark area is α-Al matrix. Coarsened eutectic lamellar tips are indicated with red dash circles.

with dot-like morphology (**Fig. 5.6a**) started to evolve into a lamellar morphology and build up interconnections between Al_6(Fe,Mn) eutectic lamellae (**Fig. 5.6b-c**). This phenomenon became more significant as Mg content in the alloy increases. Eventually, its transverse section exhibits a script-like morphology (**Fig. 5.6d**).

The actual morphology of Fe-IMCs can be misleading from 2D observation (Puncreobutr *et al.*, 2014; Dinnis, Taylor and Dahle, 2005; Kuijpers *et al.*, 2002); therefore 3D observation was performed with deep-etched samples. As shown in **Fig. 5.7**, the length of Al_6(Fe,Mn) is much longer in one direction, compared to its cross section (double sided arrow in **Fig. 5.7d**), and have a preferred growth orientation (single arrow in **Fig. 5.7d**). 3D observation reveals that eutectic Al_6(Fe,Mn) tends to develop from needle-like morphology (**Fig. 5.7a**) into a lamellar morphology (**Fig. 5.7b**) with Mg addition. Meanwhile, as the Mg content increases, the eutectic

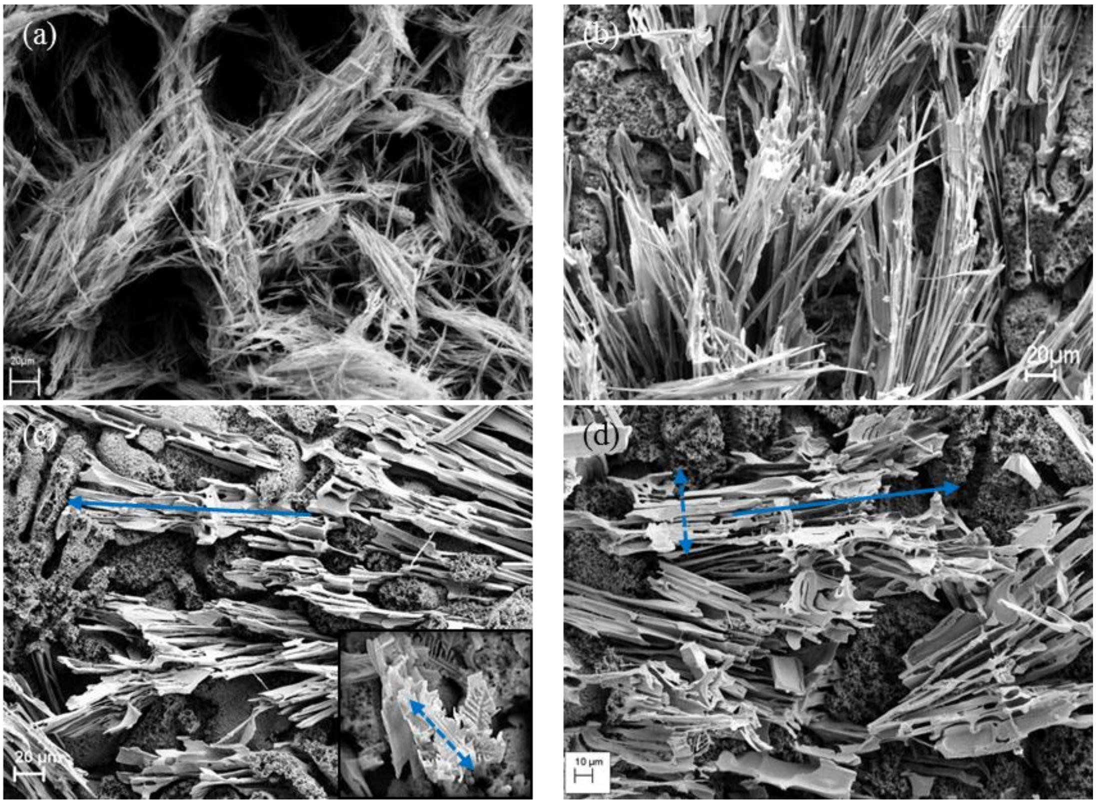

Figure 5.7 SEM micrographs showing the 3D morphology of Al_6(Fe,Mn) in deep-etched TP-1 samples of Al-1.2Fe-0.7Mn alloy with (a) 0.004wt.%, (b) 1.3wt.%, (c) 3.2wt.% (inserted micrograph showing the morphology of Al_6(Fe,Mn) from longitudinal direction of the eutectic) and (d) 6.0wt.% Mg addition. Single solid arrows indicate the preferred growth orientation, whilst the double-sided dash line arrows indicate the interconnection orientation. The observation towards preferred growth orientation is inserted in (c).

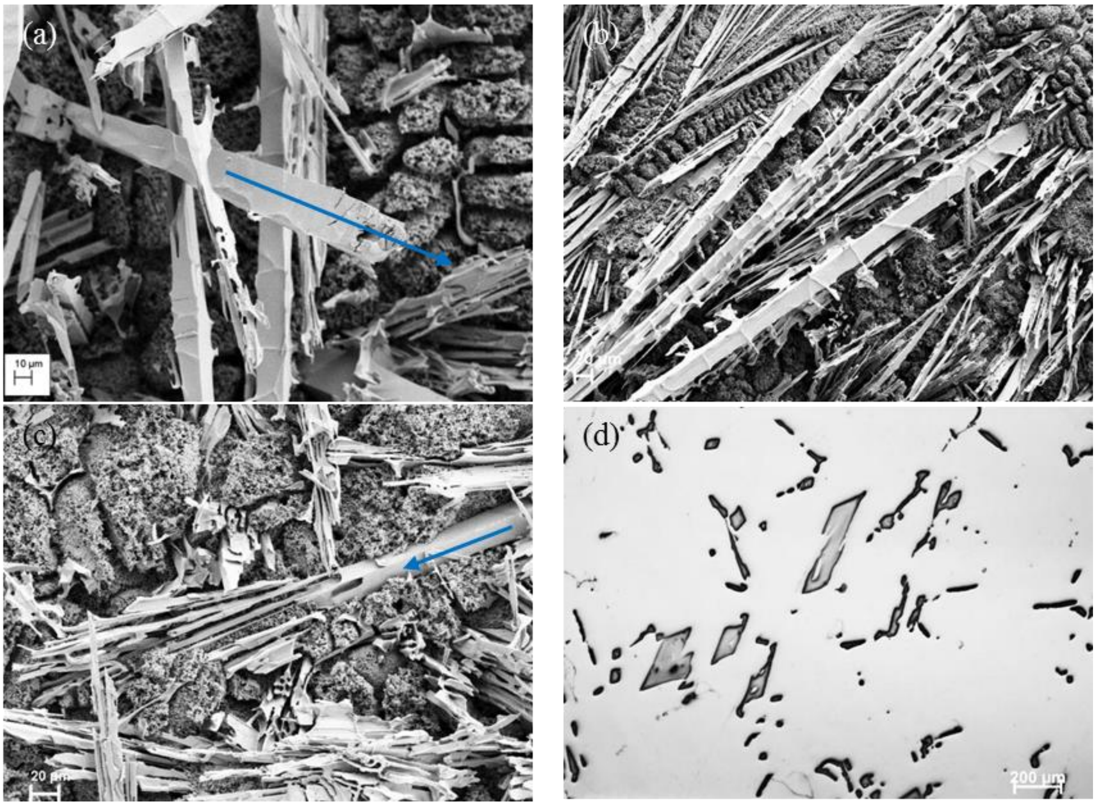

Figure 5.8 SEM micrographs showing the 3D morphology of (a) rod-like Al_6(Fe,Mn) (b) rod-like Al_6(Fe,Mn) with attached branches on cross-section and (c) rod-like Al_6(Fe,Mn) with attached branches on longitudinal direction in Al-1.2Fe-0.7Mn-3.2Mg alloy with CA (0.8K/s) condition; (d) optical micrograph showing both parallelogrammatic and branched Al_6(Fe,Mn) (characterized with SEM/EDS). Solid arrows alongside of Al_6(Fe,Mn) rod indicate its preferred growth orientation.

lamellae's growth on cross orientation (double sided arrow in **Fig. 5.7b**) was further facilitated, which lead to a well-developed lamellar interconnections observed from preferred growth orientation (**Fig. 5.7c**).

In order to have an insight into the effect of cooling rate on Al_6(Fe,Mn), the microstructure observation was performed on Al-1.2Fe-0.7Mn-3.2Mg alloy with CA condition (0.8K/s). The Al_6(Fe,Mn) particles has a hollowed rod (**Fig. 5.8a**), branched rod (**Fig. 5.8b**) and interconnected lamellar 3D morphologies (**Fig. 5.8c** and **Fig. 5.8d**). The transition from rod-like morphology to lamellar morphology is also observed in **Fig. 5.8c**. Although the alloy composition was the same, slower cooling rate (0.8K/s) encourages the formation of rod-like Al_6(Fe,Mn). For Al-2Si-

1.2Fe-0.7Mn-*y*Mg alloys, the slower cooling rates (≤0.8K/s) encourage the formation of primary α-AlFeMnSi, as demonstrated in section 4.3.2; therefore it will not be presented here.

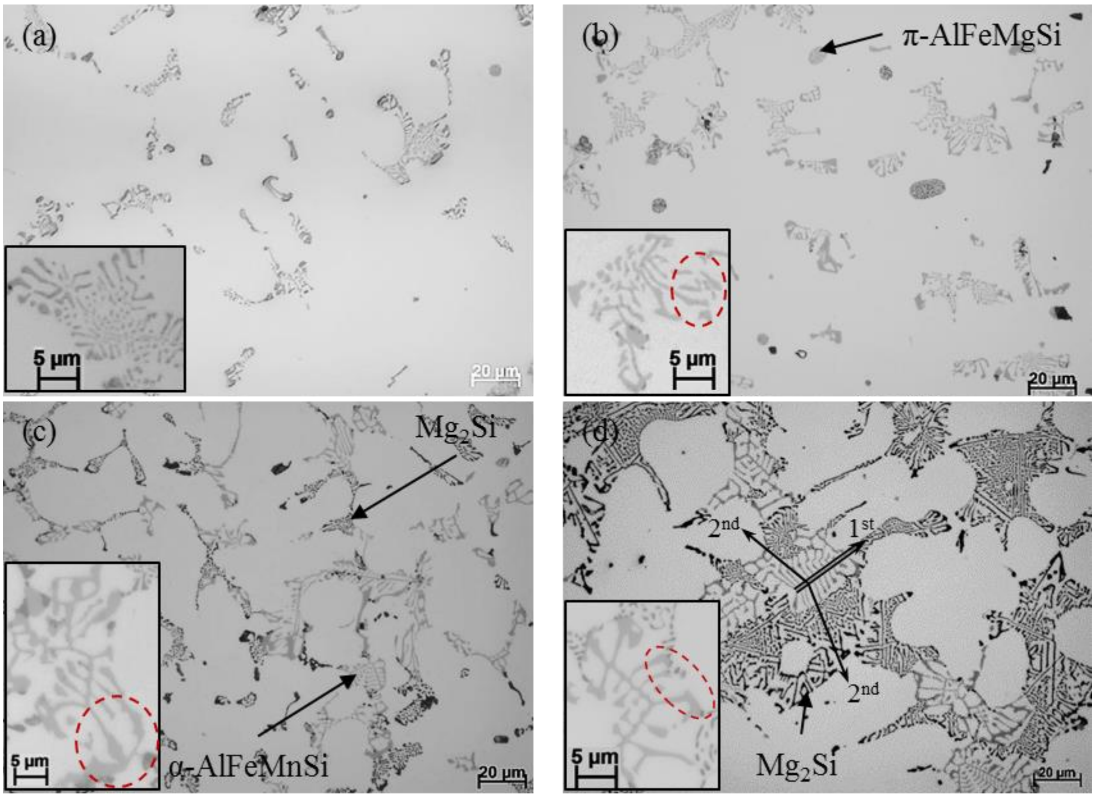

Figure 5.9 Optical microscopy images at the same magnification showing the microstructure of TP-1 sample of Al-2Si-1.2Fe-0.7Mn alloy with (a) 0.01wt.% Mg (inserted micrograph showing the morphology of Fe-IMC eutectic at higher magnification), (b) 1.3wt.% Mg, 3.1wt.% Mg and 5.4wt.% Mg addition. Light grey phase shows a stoichiometry of Al_{12}(Fe,Mn)$_3$Si examined with SEM/EDS, and the dark area is α-Al matrix. α-AlFeMnSi, Mg$_2$Si and π-AlFeMgSi phases are indicated with solid arrows respectively. Dash-line arrows 1st and 2nd indicate the primary and secondary lamellae of eutectic α-AlFeMnSi, respectively. Coarsened eutectic lamellar tips are indicated with red dash circles.

For Al-2Si-1.2Fe-0.7Mn-*y*Mg alloys, the influence of Mg content was. **Fig 5.5** shows that the microstructures have a both eutectic α-AlFeMnSi/α-Al and primary α-Al in the at various Mg contents in this alloy system, although it is the formation of primary α-Al is not suggested according to the calculated equilibrium phase diagram (**Fig. 5.1b**). Eutectic α-AlFeMnSi exhibited a mixed rods and lamellae morphology when there is minor amount (0.004wt.%) of Mg. When additional Mg of 1.26wt.%, 3.1wt.% and 5.4wt.% were introduced to the alloy, α-AlFeMnSi's individual lamella developed connections to each other and evolved to a script-like structure which often described as Chinese-script or skeleton depending on observation direction. For these Chinese-script α-AlFeMnSi eutectics, normally there is a primary lamella/branch (see 1st double-line in **Fig 5.9d** and double-line arrow in **Fig. 5.10d**) and secondary lamella/branch deviated from primary lamella/branch to other orientation (see 2nd solid-line arrow in **Fig. 5.9d** and solid-line arrow in **Fig. 5.10d**). Two examples in **Fig. 5.10d** indicates 45˚ and 90˚ angle between primary lamellae (double-line arrow) and secondary lamellae (solid-line arrow). Additionally, some Mg-containing phases, such as π-AlMgFeSi (**Fig. 5.9b**) and Mg_2Si (**Fig. 5.9c**), start to solidify as Mg content increases, in agreement with the phase diagram prediction (**Fig. 5.1b**).

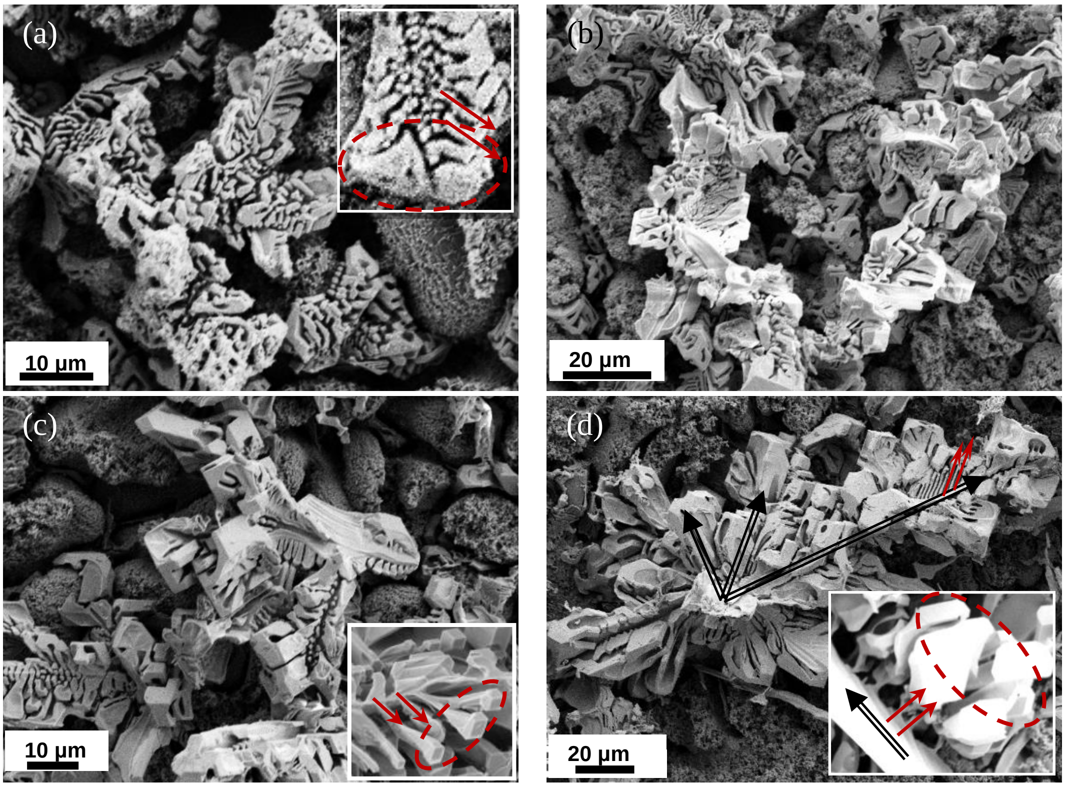

Figure 5.10 SEM micrographs showing the 3D morphology of α-AlFeMnSi in deep-etched TP-1 samples of Al-2Si-1.2Fe-0.7Mn alloy with (a) 0.01wt.%, (b) 1.3wt.%, (c) 3.1wt.% and (d) 5.4wt.% Mg addition (inserted micrograph showing the branching area). Single-line arrow and double-line arrow indicate primary and secondary lamellae, respectively.

The 3D observations of α-AlFeMnSi are shown in **Fig. 5.10**. The α-AlFeMnSi lamellae tend to grow preferably on the directions (double-line arrow in **Fig. 5.10d**), showing a strong anisotropy. The α-AlFeMnSi lamellae tend to have a coarsened tip (see red dash-line circles in **Fig. 5.10a** and **Fig. 5.10d**) which are likely to form interconnections at the coarsened areas according to observation (see red dash-line circles in **Fig. 5.9b-d**). With the increased Mg content, this coarsening effect at branch tips became more significant, and these lamellae tend to develop from mixed rod-lamellar morphology into lamellar morphology.

5.2 Phase Identification

The identification of main phases has been carried out with SEM/EDS, TEM/EDS and SAED. As shown in **Fig. 5.11**, the EDS analysis shows that only Al, Fe, Mn and a negligible amount of carbon were detected on $Al_6(Fe,Mn)$ EDS point analysis in Al-1.2Fe-0.7-3.2Mg alloy. However, Mg was sometimes detected with point analysis

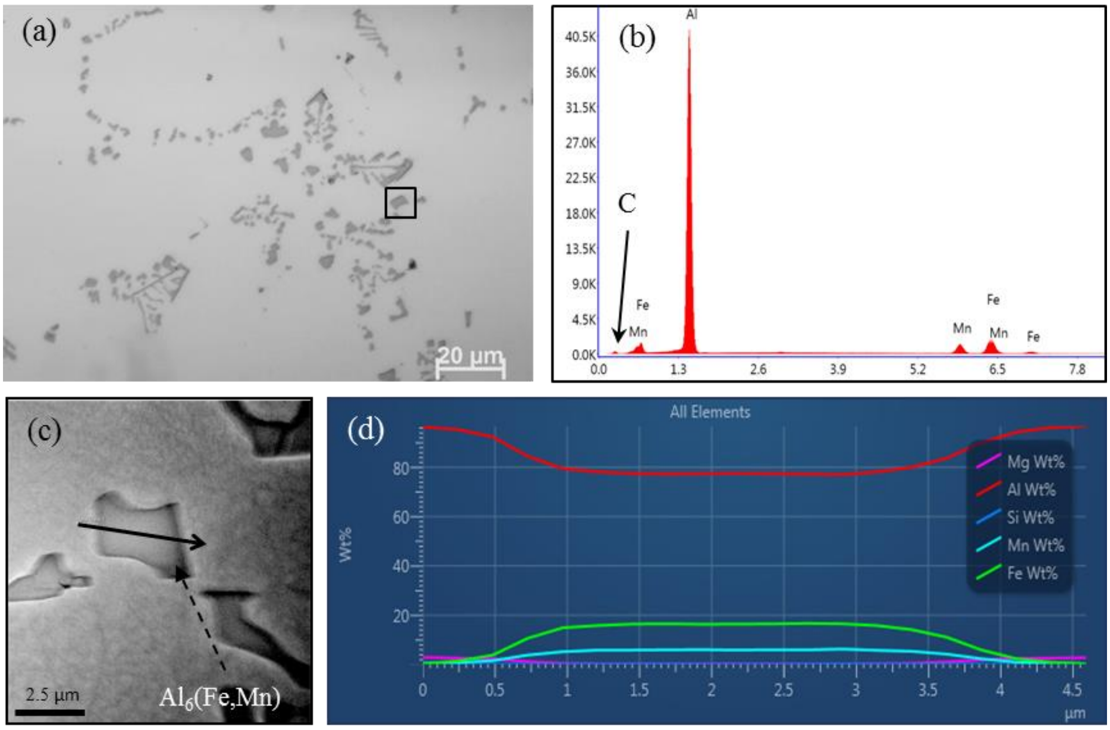

Figure 5.11 (a) Microstructure of Al-1.2-0.7Mn-3.2Mg alloy by TP-1 casting; (b) example of SEM/EDS point analysis peaks of $Al_6(Fe,Mn)$ in (a); (c) high-magnification of squared area in (a) showing the area of line scan indicated with solid arrow; (d) elements concentration peaks corresponding to the scanning line shown in (c).

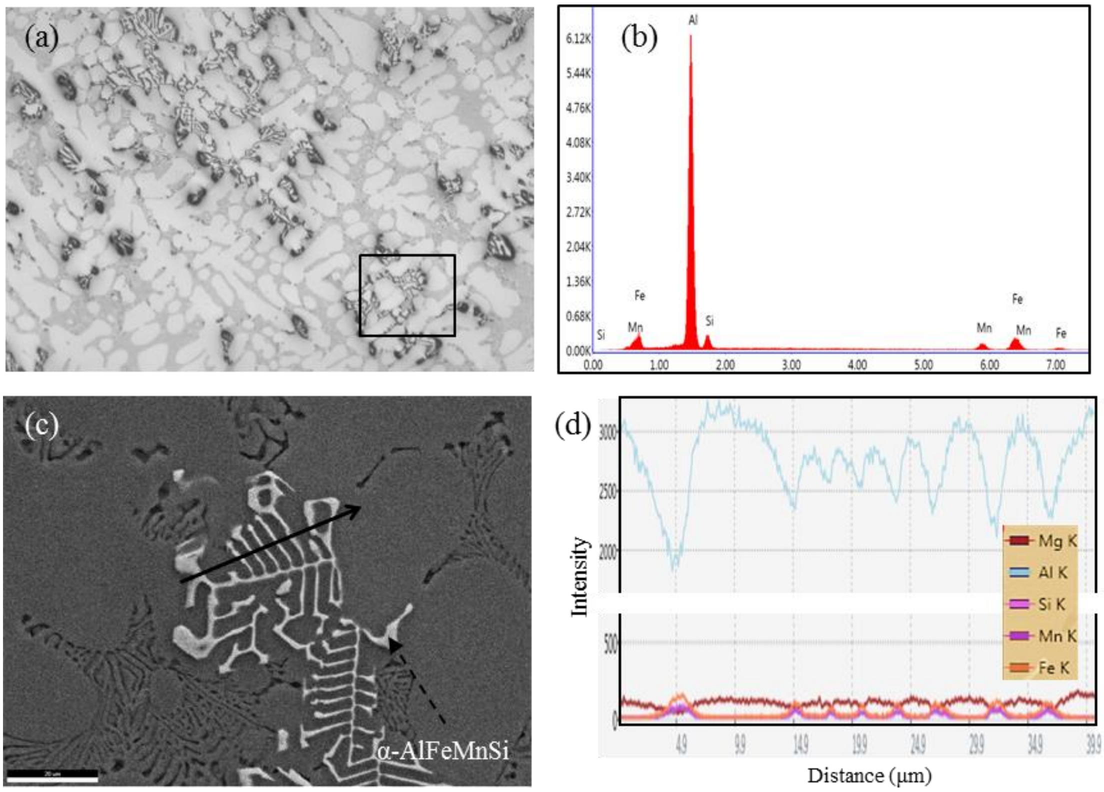

Figure 5.12 (a) Microstructure of Al-2Si-1.2-0.7Mn-3.1Mg alloy by TP-1 casting; (b) example of SEM/EDS point analysis peaks of α-AlFeMnSi in (a); (c) high-magnification of squared area in (a) showing the area of line scan indicated with solid arrow; (d) elements concentration peaks corresponding to the scanning line shown in (c).

on Al_6(Fe,Mn) particles. The EDS line scan shown in **Fig. 5.11d** suggests that the concentration of the elements change gradually and became relatively stable when the analysis area is at the centre of the compound. Al, Fe, Mn and Si were the only elements observed (**Fig. 5.12**) in α-AlFeMnSi in Al-2Si-1.2Fe-0.7Mn-3.1Mg alloy, and Mg content was sometimes detected in the EDS analysis on α-AlFeMnSi. The Mg content variation in Fe-IMC is possibly due to limited resolution or the difference between electron interaction area of secondary electron signal and EDS signal. Therefore, the EDS analysis result on the coarse eutectic lamellae was considered more reliable.

Chemical makeup of Fe-IMCs and α-Al matrix in Al-1.2Fe-0.7Mn-*x*Mg alloys and Al-2Si-1.2Fe-0.7Mn-*y*Mg alloys with various Mg contents are shown in **Table 5.1** and **Table 5.2**, respectively. The increasing Mg content did not have a significant impact on the chemical composition of $Al_6(Fe,Mn)$, and the stoichiometry formulas obtained from EDS analysis are shown in **Table 5.1**. A moderate amount of Mg was detected during EDS point analysis of Fe-IMC particles, although Mg solid solution has not been reported for $Al_6(Fe,Mn)$. For Al-2Si-1.2Fe-0.7Mn-*y*Mg alloys, EDS results in **Table 5.2** suggest a stoichiometry of $Al_{12}(Fe,Mn)_3Si$ for α-AlFeMnSi when Mg content is at higher level (5.4wt.%) (Ji *et al.*, 2013a; Sun, Kang and Koo, 2000). However, when Mg composition decreased, the stoichiometry of α-AlFeMnSi varied and became $Al_{15}(Fe,Mn)_3Si_2$; meanwhile, Mn and Fe remain at a similar level in the Fe-IMC as Mg content reduces. This stoichiometric transition is observed in Mg-free Al alloys with different Si content (Kim *et al.*, 2006; Dinnis, Taylor and Dahle, 2005; Narayanan, Samuel and Gruzleski, 1994).

Table 5.1 The chemical compositions of $Al_6(Fe,Mn)$ and matrix in Al-1.2Fe-0.7Mn alloy with various Mg contents by SEM/EDS analysis.

Areas	**Mg Content**	**Al (at.%)**	**Mg (at.%)**	**Mn (at.%)**	**Fe (at.%)**
$Al_6(Fe,Mn)$	0.004wt.%	Bal.	0	2.9±2.3	11.8±2.6
	1.3wt.%	Bal.	0.9*	2.9±1.2	12.0±2.2
	3.2wt.%	Bal.	1.2*	3.0±1.1	10.2±2.8
	6.0wt.%	Bal.	2.6*	2.6±0.8	10.9±1.1
Matrix	0.004wt.%	Bal.	0	0.1*	0.1*
	1.3wt.%	Bal.	1.1±0.6	0.3*	0.1*
	3.2wt.%	Bal.	2.8±0.8	0.1*	0.2*
	6.0wt.%	Bal	5.4±1.3	0.2*	0.1*
* Inaccurate readings with over 50% error suggested by TEAM EDS software.					

Table 5.2 The chemical compositions of α-AlFeMnSi and matrix in Al-2Si-1.2Fe-0.7Mn alloy with various Mg contents by SEM/EDS analysis.

Areas	**Mg Content**	**Al**	**Mg (at.%)**	**Si (at.%)**	**Mn (at.%)**	**Fe (at.%)**
α-AlFeMnSi	0.01wt.%	Bal.	0	9.0±3.8	4.2±1.1	12.6±2.4
	1.3wt.%	Bal.	1.01*	8.9±0.6	4.2±0.9	11.4±1.6
	3.1wt.%	Bal.	1.54*	6.8±1.8	4.1±0.4	11.9±1.3
	5.4wt.%	Bal.	1.36*	4.7±0.5	4.3±0.7	11.7±1.3
Matrix	0.01wt.%	Bal.	0	0.9*	0.1*	0.2*
	1.3wt.%	Bal.	1.30±0.6	0.9*	0.3*	0.3*
	3.1wt.%	Bal.	2.34±0.6	0.3*	0.3*	0.1*
	5.4wt.%	Bal	4.51±1.5	0.1*	0.2*	0.1*
* Inaccurate readings with over 50% error suggested by TEAM EDS software.						

In **Fig. 5.13**, TEM observation on the interface area of Fe-IMC/α-Al in Al-1.2Fe-0.7Mn-3.2Mg alloy shows the bright field (BF) image, high resolution (HR) image, SAED pattern and EDS results. In Al-1.2Fe-0.7Mn alloy with 1.3wt.% and 3.2wt.% Mg content, a bright layer (**Fig. 5.13a**) which was distinguished from Fe-IMC and matrix is often observed at interface areas of Fe-IMC/α-Al matrix. This layer has a range of thickness from 2 to 20nm according to BF image observation. HR observation of Mg-rich area is shown in **Fig. 5.13b**, showing an interface that is different from the sharp interface of faceted Fe-IMC particles. As shown in **Fig. 5.13c** the selected area electron diffraction (SAED) pattern from the centre of Fe-IMC did not suggest two set of patterns. The SAED pattern was indexed according to Al_6(Fe,Mn) with a orthorhombic structure, space group of Cmcm and lattice parameter of a=7.4986, b= 6.495, c= 8.837, α=β=90˚ and γ=107.7˚, as identified by Barlock (Barlock and Mondolfo, 1975) and further confirmed by Young (Young and Clyne, 1981;). The inserted table in **Fig. 5.13** shows the chemical compositions of Al_6(Fe,Mn)/α-Al interface area, where three separate analysis points were acquired, showing that there is no Mg detected in Al_6(Fe,Mn) particle and the α-Al matrix's Mg content is at 2.8±0.8wt.%, but the Mg content of bright layer reached 6.1±2.1wt.%.

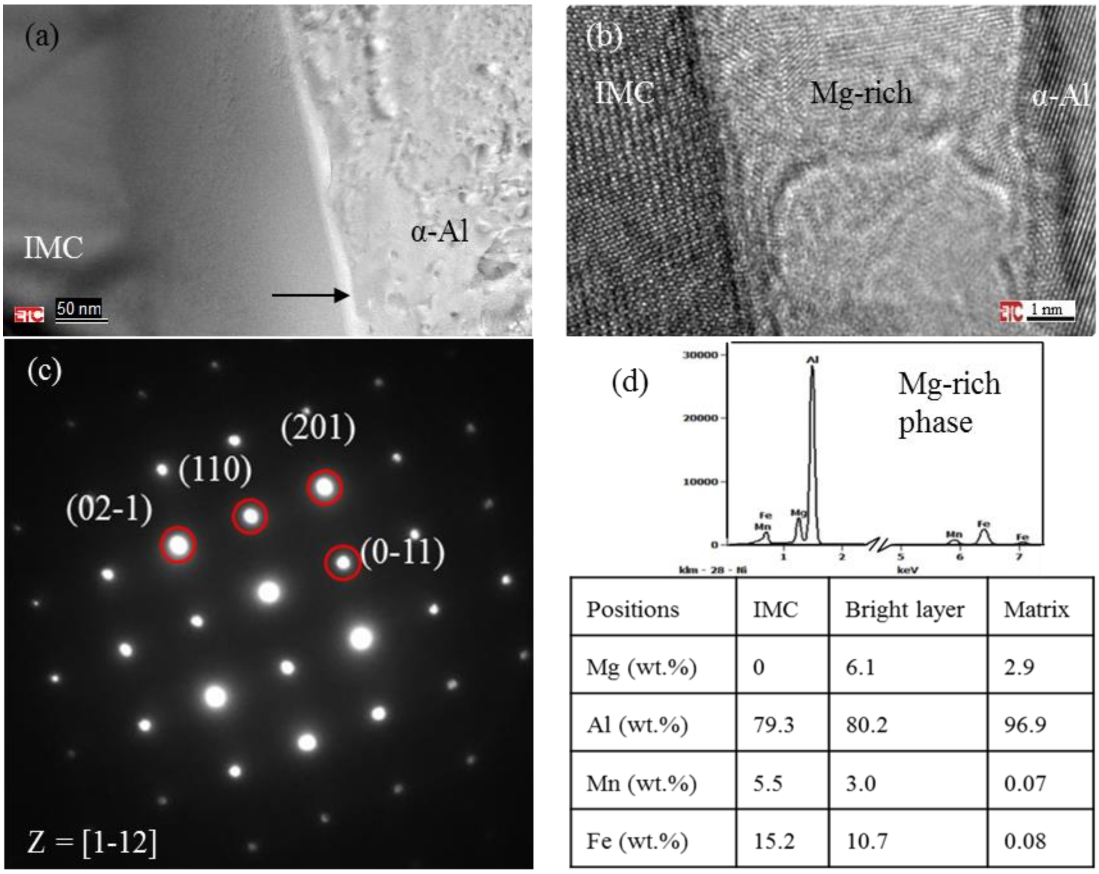

Positions	IMC	Bright layer	Matrix
Mg (wt.%)	0	6.1	2.9
Al (wt.%)	79.3	80.2	96.9
Mn (wt.%)	5.5	3.0	0.07
Fe (wt.%)	15.2	10.7	0.08

Figure 5.13 TEM images of Al-1.2Fe-0.7Mn-3.2Mg TP-1 sample showing (a) the bright field image of Al_6(Fe,Mn)/α-Al interface, (b) the high resolution image of Al_6(Fe,Mn) /Mg-rich/α-Al area, (c) the index SAED pattern of Al_6(Fe,Mn) on the zone axis of [1-12], (d) the TEM/EDS peaks of Mg-rich phase on the interface of Al_6(Fe,Mn)/α-Al indicated with arrow in (a). The inserted table showing the average value of chemical composition of Fe-IMC, Mg-rich layer and Al matrix of the interface area acquired from 6 interface areas by TEM/EDS point analysis.

5.3 Quantification with Various Mg Additions

This section will demonstrate some quantitative relations between the microstructure evolutions and Mg contents in both Al-1.2Fe-0.7Mn-*x*Mg and Al-2Si-1.2Fe-0.7Mn-*y*Mg alloys.

5.3.1 Grain size

As shown in **Fig. 5.14**, it is clear that Mg promotes grain refinement at a cooling rate of 3.5K/s. In Al-1.2Fe-0.7Mn-*x*Mg alloys, Mg addition shows a considerable effect on reducing grain size which decreased from 1336±209μm (0.004wt.% Mg) till 513±80μm (6.0wt.% Mg). Meanwhile, when 2.0wt.% Si added to Al-Fe-Mn alloy, it shows a minor grain size reduction from 1336±209 to 1233±238μm.

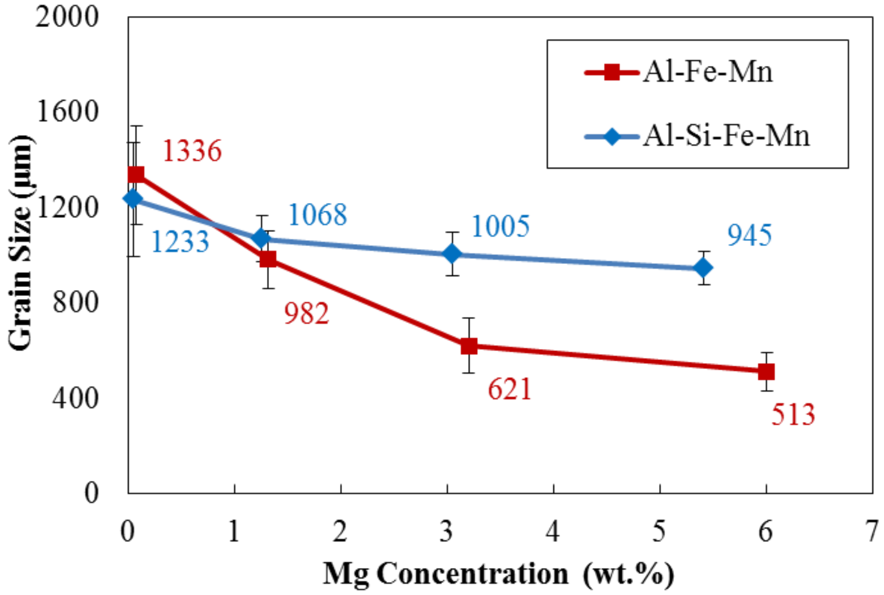

Figure 5.14 Mean grain size of α-Al in Al-1.2Fe-0.7Mn alloys (red) and Al-2Si-1.2Fe-0.7Mn alloys (blue) as a function of Mg composition. Error bars show the standard deviation of each point; and inserted numbers represent the mean value of each data point.

On the other hand, Mg in Al-2Si-1.2Fe-0.7Mn-*y*Mg alloys, showed a very small effect on the grain size, and the grain size reduced to 1068±97μm (1.3wt.% Mg) and followed by a modest decrease to 945±68μm (5.4wt.% Mg). Interestingly, the effect of Mg content on the α-Al grain size reduction is more moderate in Al-2Si-1.2Fe-0.7Mn-*y*Mg alloys compared with Al-1.2Fe-0.7Mn-*x*Mg alloys.

5.3.2 Secondary Dendrite Arm Spacing (λ_2)

Secondary Dendrite Arm Spacing (SDAS), denoted as λ_2, was taken into consideration due to its correlation with secondary phase morphology and particle distribution of secondary phases (Fe-IMCs in this study) (Sivarupan, Caceres and Taylor, 2013; Caceres *et al.*, 1999; Samuel and Samuel, 1995). The SDAS is dependent on the cooling rate and can also be controlled by alloy composition (Sivarupan, Caceres and Taylor, 2013; Dobrzański, Borek and Maniara, 2006). The SDAS is normally described by the semi-empirical relation (Samuel *et al.*, 1998; Gustafsson, Thorvaldsson and Dunlop, 1986):

$$\lambda = A\dot{T}^{n} \tag{5.1}$$

where *A* and *n* is alloy composition dependent factor (Caceres *et al.*, 1999; Young and Kerkwood, 1975) and $\dot{T}$ is cooling rate. As shown in **Fig. 5.15**, the SDAS was measured as a function of Mg composition in Al-1.2Fe-0.7Mn-*x*Mg and Al-2Si-1.2Fe-0.7Mn-*y*Mg alloys. The Mg addition decreased the SDAS of both alloys, and

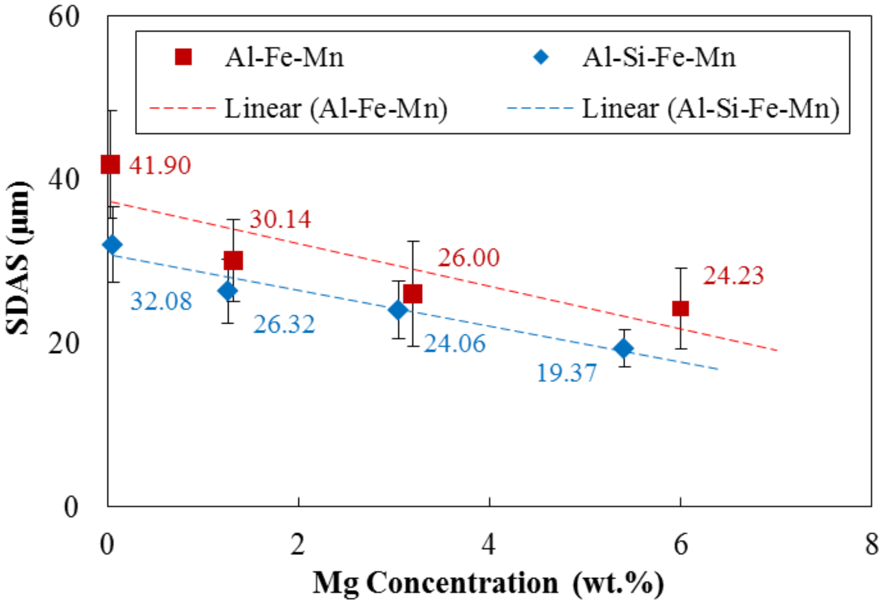

Figure 5.15 The mean SDAS of α-Al in Al-1.2Fe-0.7Mn alloy (red) and Al-2Si-1.2Fe-0.7Mn alloy (blue) as a function of Mg composition. Error bars show the standard deviation of each point; and inserted number represents the mean value of each data point.

at 2.0wt.% of Si leads to 20% decrease in SDAS of Al-1.2Fe-0.7Mn alloy. The SDAS of Al-1.2Fe-0.7Mn-*x*Mg alloys decreased quickly from 41.9±6.6μm (0.004wt.% Mg) to 30.1±5.1μm (1.3wt.% Mg), and followed by a moderate decrease to 24.2±5.4μm as Mg content rises to 6.0wt.% Mg. On the other hand, as Mg contents increases the SDAS of Al-2Si-1.2Fe-0.7Mn-*y*Mg alloys show a les significant decreasing trend, which decreased from 32.1±4.6μm with 0.01wt.% Mg addition to 19.3±2.3μm with 5.4wt.% Mg addition. `

5.3.3 Eutectic Lamellar Spacing (λ_a)

As established previously, there is a noticeable change at morphology of Fe-IMCs with the addition of Mg. Eutectic lamellar spacing (λ_{Eu}) that is also applicable for irregular eutectic (Gündüz *et al.*, 2004; Liu and Shang, 1992; Hunt and Jackson, 1966), is introduced here to demonstrate the morphology evolution as a function of Mg composition. As introduced in section 3.5.3, λ_a describes the minimum lamellar spacing and λ_M describes maximum lamellar spacing. As shown in **Fig. 5.16**, in Al-1.2Fe-0.7Mn-*x*Mg alloys, the average λ_a increased gradually from 1.3±0.3μm at

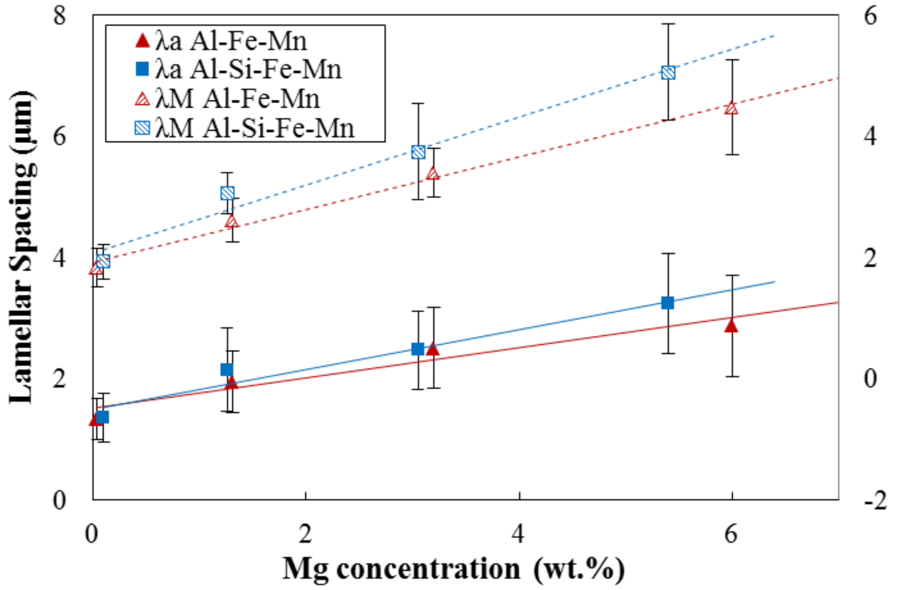

Figure 5.16 The mean Fe-IMC eutectic lamellar spacing λ_a (bottom of the branch) and λ_M (tip of branch) of Al-1.2Fe-0.7Mn alloys (red triangle) and Al-2Si-1.2Fe-0.7Mn alloys (blue cubic) as a function of Mg composition. The measurement areas are consistent with grain size measurement and SDAS measure. Linear trend lines are fitted on λ_a (solid line) and λ_M (dash line). Error bars indicate the standard deviation of the measurement points.

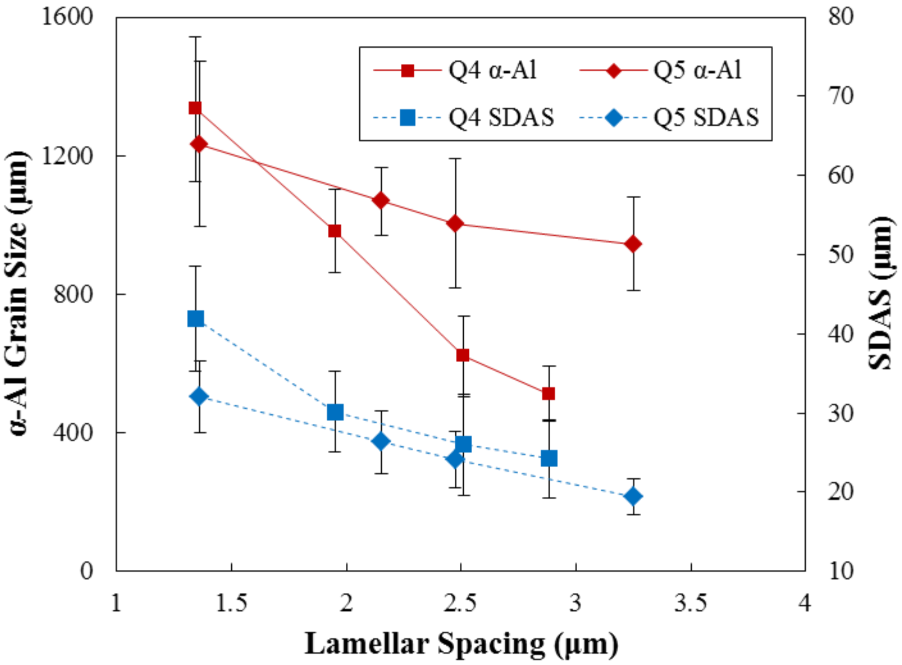

Figure 5.17 Grain size of α-Al (solid line) and SDAS of α-Al (dash line) as a function of Fe-IMC eutectic lamellar spacing (λ_a) in both Al-1.2Fe-0.7Mn-*x*Mg (Q4) (in red) and Al-2Si-1.2Fe-0.7Mn-*y*Mg (Q5) (in blue).

0.004wt.% Mg to 2.9±0.8μm at 6.0wt.% Mg; and the λ_M, which was averagely 1.41 times larger than λ_a, increased from 1.8±0.3μm at 0.004wt.% Mg to 4.5±0.8μm 6.0wt.% Mg. In the Al-2Si-1.2Fe-0.7Mn-*y*Mg alloys, the average λ_a increase continuously from 1.4±0.3μm with 0.01wt.% Mg to 3.3±0.8μm with 5.4wt.% Mg; and the λ_M, which was about 1.42 times larger than λ_a, increased from 1.9±0.3μm with 0.01wt.% Mg to 5.1±0.8μm with 5.4wt.% Mg.

The correlations of Fe-IMC's eutectic lamellar spacing to α-Al grain size and SDAS was summarized and shown in **Fig. 5.17**. The minimum lamellar spacing (λ_a) is used here (**Fig. 5.17**) to avoid the effect caused by the coarsening of the lamella tips (dash-line circles in **Fig. 5.6** and **Fig. 5.9**). The grain size and SDAS decreased as the lamellar spacing increases, and the decrease in Al-1.2Fe-0.7Mn-*x*Mg appears to be more severe when lamellar spacing increases compared with Al-2Si-1.2Fe-0.7Mn-*y*Mg. Unfortunately, the colony sizes of Fe-IMCs were not measured as 2D observation cannot represent the actual colony size in 3D observation due to the continuous complex morphology.

5.4 Discussion

5.4.1 Effect of Mg content on Solidification Sequence

As there are some disagreement between thermodynamic calculations and the experimental observation for both Al-1.2Fe-0.7Mn-*x*Mg and Al-2Si-1.2Fe-0.7Mn-*y*Mg alloys, the solidification sequence was summarised by analysing the microstructure and phase diagram calculations conducted with Pandat^{TM}.

5.4.1.1 Al_6(Fe,Mn)

For the Al-1.2Fe-0.7Mn-*x*Mg alloy, the predominant Al_6(Fe,Mn) (**Fig. 5.6**) suggests that Al_6(Fe,Mn), is the preferred phase in non-equilibrium solidification (TP-1 condition) compared with the equilibrium phase $Al_{13}Fe_4$ (**Fig. 5.1a**). As $Al_{13}Fe_4$ was not observed in the microstructure regardless of the casting condition, $Al_{13}Fe_4$ did not nucleate. Once $Al_{13}Fe_4$ is supressed, Al_6(Fe,Mn) appears to be the preferred phase with Pandat^{TM}, which suggests that the metastable Al_6(Fe,Mn) is highly likely to replace $Al_{13}Fe_4$ and form in Al-1.2Fe-0.7Mn-*x*Mg alloy in non-equilibrium conditions. The difficulty in nucleation for $Al_{13}Fe_4$ may also be the reason for the suppression of primary Al_6(Fe,Mn) (**Fig. 5.6**) at hypo-eutectic alloy composition (**Fig. 5.1a)**. When the cooling rate decreases (≤ 0.8K/s), the rod-like primary Al_6(Fe,Mn), showing parallelogrammatic morphology in 2D, nucleated with CA (**Fig 5.8a**) and CF conditions (**Fig. 5.8d**). This suggests that the nucleation of primary Al_6(Fe,Mn) can be facilitated at lower cooling rate (≤ 0.8K/s). Due to the relatively lower nucleation barrier, α-Al nucleated firstly during TP-1 casting leading to increase in solute concentration in the remaining liquid during α-Al growth. Consequently, as the solute concentration increases in remaining liquid, the driving force for diffusion of solute atoms to the nucleation embryo should be increased, and eventually the critical radius of Al_6(Fe,Mn) nucleus can be achieved. Then the Al_6(Fe,Mn) nucleus can start free growth. Al_6(Fe,Mn)/α-Al eutectic form at the primary Al_6(Fe,Mn) grain boundaries or between α-Al dendrite arms. Given above, the non-equilibrium solidification sequence is summarised as:

when the $x \geq 3.2$wt.%

$L \rightarrow Al_6$(Fe,Mn) (reaction (R) 5.1)

$L_1/L \rightarrow \alpha\text{-Al} + Al_6(Fe,Mn)$ (R5.2)

when the x <3.2wt.%

$L \rightarrow \alpha\text{-Al}$ (R5.3)

$L_1 \rightarrow \alpha\text{-Al} + Al_6(Fe,Mn)$ (R5.4)

where the primary reaction R5.1 is dependent on the cooling rate (≤0.8K/s), and the critical x is semi-empirical value based on microstructural observation of Al-1.2Fe-0.7Mn-xMg alloys (**Fig. 5.8**). It appears that the increasing Mg content can increase the volume fraction of $Al_6(Fe,Mn)$ (**Fig. 5.2a**) even though Mg atoms do not participate in the $Al_6(Fe,Mn)$ compound. This correlation of Mg content and $Al_6(Fe,Mn)$ volume fraction is likely caused by the immiscibility between Mg and Fe (Liu *et al.*, 2011). The formation reaction R5.1 is given in another form:

$L = L_{Al} + L_{Mg} + L_{Fe} + L_{Mn} \rightleftharpoons Al_6(Fe,Mn)$ (R5.5)

where L_i (i=Al, Mg, Fe and Mn) represent liquid atoms. The non-ideal Fe-Mg interaction in liquid solute might eject Fe atoms out of the liquid which facilitated the reaction R5.5 to the right side. As the Mg content increases, more Fe atoms were ejected from the liquid since the solubility of Mg in Al (18.9wt.% at 450°C) (Murray, 1982) is much higher than that of Fe in Al (0.8wt.%) (Phillips, 1959).

5.4.1.2 α-AlFeMnSi

For Al-2Si-1.2Fe-0.7Mn-yMg alloy, α-AlFeMnSi was observed as the predominant Fe-IMC phase as Mg content varies. In TP-1 casting, the primary α-AlFeMnSi was not observed with Mg addition, although calculated phase diagram suggested that α-AlFeMnSi is expected to form in Al-2Si-1.2Fe-0.7Mn-xMg system. Similarly to the suppression of primary $Al_6(Fe,Mn)$ phase in Al-1.2Fe-0.7Mn-xMg alloy, the nucleation of primary α-AlFeMnSi in Al-2Si-1.2Fe-0.7Mn-yMg was supressed in non-equilibrium solidification (TP-1 condition). This phenomenon was discussed in Section 4.4.2. Due to the insufficient solute diffusion the critical radius of primary α-AlFeMnSi nucleation embryo cannot be reached during the TP-1 cooling. Similar to $Al_6(Fe,Mn)$/α-Al eutectic, the nucleation of α-AlFeMnSi can finally occur when there is enough undercooling as the solute is concentrated from the growth of α-Al.

Combining the microstructure analysis and CALPHAD approach prediction, the solidification sequence can be suggested to be:

$L \rightarrow \alpha\text{-AlFeMnSi} + L_1$ (R5.6)

$L_1/L \rightarrow \alpha\text{-Al} + \alpha\text{-AlFeMnSi} + L_2$, (R5.7)

when $y < 2.20$wt.%

$L_2 \rightarrow \beta\text{-AlFeSi} + \alpha\text{-Al} + L_2'$ (R6.8)

$L_2' \rightarrow \pi\text{-AlMgFeSi} + \alpha\text{-Al}$; (R6.9)

when 2.20wt.% $\leq y <$ 4.65%wt.%

$L_2 \rightarrow Mg_2Si + \alpha\text{-Al} + L_2'$; (R5.10)

when $y \geq$ 4.65%wt.%

$L_2 \rightarrow Mg_2Si + \alpha\text{-Al} + L_2'$ (R5.11)

$L_2' \rightarrow Mg_2Si + \alpha\text{-Al} + Al_6(Fe,Mn)$ (R5.12)

where the appearance of reaction R5.6 is dependent on the cooling rate (≤0.8K/s). The Mg only participates into the formation of Mg_2Si and π-AlFeMgSi phase after the formation of α-AlFeMnSi, therefore the Mg content in remaining liquid after α-Al is considered additive as it increases. The immiscibility of Fe-Mg and the residual Fe and Mn concentration variation are very likely to be the main reasons leading to the increase in the formation temperature range and morphology evolution of α-AlFeMnSi/α-Al eutectics when Mg content in Al-2Si-1.2Fe-0.7Mn-*y*Mg alloy changes.

Thus, during TP-1 cooling the primary Fe-IMCs in Al-1.2Fe-0.7Mn-*x*Mg and Al-2Si-1.2Fe-0.7Mn-*y*Mg alloys were suppressed due to the insufficient diffusion driving force at 3.5K/s cooling rate. Meanwhile increased Mg lead to a higher Fe-IMC volume fraction as Mg dissolution in Al rejects more Fe atoms from the liquid.

5.4.2 Effect of Mg Addition on Microstructure of α-Al

The microstructure of α-Al matrix can be a determining factor for the solidification behaviour including morphology and distribution of intermetallic compounds especially in hypo-eutectic alloys, since in hypo-eutectic alloys' secondary Fe-IMCs only forms between the primary α-Al dendrite arms which then affect the morphology and distribution of secondary Fe-IMCs (Taylor, 2012; Caceres *et al.*, 1999; Samuel and Samuel, 1995). Grain size is reduced with Mg addition. The effect of superheat on grain size reduction is negligible in the current investigation as the casting superheat is higher than 40K and the difference is no greater than 20K. It is very important to address the enhanced nucleation by Mg addition as dispersed Mg oxides are ideal substrates for heterogeneous nucleation of α-Al (Li, Wang and Fan, 2012). However, the current experimental observation does not show significant α-Al refinement by Mg addition presumably due to the insufficient wetting and severe agglomeration of Mg oxides particles. Thus the grain size reduction is believed mainly caused by growth restriction.

Although α-Al grain size by itself was reported to have limited influence on the morphology of Fe-IMCs (Samuel and Samuel, 1995), it is used in this study to reflect the influence of elemental segregation which is defined as the constitutional-supercooling parameter (P) (Tarshis, Walker and Rutter, 1971), at the growth front of α-Al and Fe-IMCs. Solutes are widely acknowledged for their outstanding contribution to growth restriction (Easton and Stjohn, 1999; Johnsson, 1995; Spittle and Sadli, 1995). The grain size reduction observed as Mg content increases agrees with the grain size prediction parameter $P=\sum mC_0(k-1)/k$ (Kearns and Cooper, 1997; Johnsson, 1995; Tarshis, Walker and Rutter, 1971). The **Fig. 5.17** shows that the α-Al and Fe-IMC in both Al-1.2Fe-0.7Mn-*x*Mg and Al-2Si-1.2Fe-0.7Mn-*y*Mg alloys effectively show a linear relationship with increase of Mg content. The constitutional-supercooling parameter, which has a close relationship with α-Al grain size as solute content increases, might have an indirect relationship with Fe-IMC eutectic lamellar spacing. This to some extent supports the idea of solute segregation restricting the growth of Fe-IMCs causing growth restriction at the growth front. Assuming that the constitutional supercooling is a dominant factor for the growth of anisotropic Fe-IMCs, Hunt (Hunt, 1984), Rappaz and Thevoz (Rappaz and Thevoz, 1987), and Chai and Backrued (Chai, Bäackerud and Arnberg, 1995) developed an equation of the form,

$$V = \frac{AD_i \Delta T^2}{\Gamma m_i (1-k) C_i} \tag{5.2}$$

where A is a constant and V is the growth rate. Thus, as the Mg content increases, the solute concentrations (C_i, i = Fe, Mn and Si) will consequently decrease during the solidification of Fe-IMCs. This equation is not an additive function for multicomponent systems, but it should give a qualitative idea about the effect of solute concentration on the growth of multicomponent phases.

The SDAS can be affected by many coarsening mechanisms, such as competitive growth, coalescence (Li, Brody and Kazimirov, 2004; Flemings, 1974), which consequently lead to SDAS increase (**Fig. 5.5**). Therefore, the measurement for average SDAS was performed at the initial point of dendrite arms (λ_2) so that inaccuracies caused by coarsening can be reduced. Generally, the primary α-Al dendrite has a direct influence on Fe-IMCs (Samuel and Samuel, 1995) that larger dendrite arm spacing tends to cause finer Fe-IMC morphology. At a constant cooling rate (3.5K/s), Mg appears to be an effective at reducing SDAS (**Fig. 5.15**), which is very likely to be one of the factors causing the Fe-IMCs' morphology evolution with increased Mg content. More importantly, the equilibrium phase diagram (**Fig. 5.2**) suggests that the volume fraction of α-Al did not change significantly at varied Mg contents in both Al-1.2Fe-0.7Mn-*x*Mg and in Al-2Si-1.2Fe-0.7Mn-*y*Mg alloys. Thus, as Mg content either become solid solution in α-Al or rejected to remaining liquid melt during solidification, the Mg content in remaining liquid at the inter-dendritic regions can be additive as Mg content increases. Also, as the current alloys show a Fe-IMC/α-Al and primary α-Al mixed microstructure with various Mg addition, the amount of Fe and in remained the liquid at the α-Al inter-dendritic regions was considered at a similar level when Mg content varies. Thus, a reduction of Fe and Mn at the α-Al inter-dendritic regions can be encouraged as Mg content increases.

5.4.3 Effect of Mg Addition on Eutectic

5.4.3.1 Morphology of Eutectics

The effect of solute elements on Fe-IMCs is commonly reflected on three aspects: morphology evolution by changing SDAS (Caceres *et al.*, 1999; Samuel and Samuel, 1995), formation of new Mg containing Fe-IMC phases (Samuel *et al.*, 1998; Samuel and Samuel, 1997) and solute segregation at the growth front of Fe-IMCs (Shabestari, Keshavarz and Hejazi, 2009; Shabestari *et al.*, 2002; Samuel *et al.*, 1999; Samuel *et al.*, 1998). In current investigation, the Mg did not participate in the formation of Al_6(Fe,Mn) and α-AlFeMnSi in Al-1.2Fe-0.7Mn-*x*Mg and Al-2Si-1.2Fe-0.7Mn-*y*Mg alloys, respectively. Thus, the morphology modification Al_6(Fe,Mn) and α-AlFeMnSi was considered to be the result of segregated Mg content in the remaining liquid after the solidification primary α-Al and the solute segregation at the growth front of Fe-IMCs. Due to the complex 3D morphology of Al_6(Fe,Mn) and α-AlFeMnSi (see **Fig. 5.7** and **Fig. 5.10**), it is hard to determine the boundary of individual Fe-IMC particles. Subsequently, it is challenging to conclude the correlation of SDAS, α-Al grain size as a function of Fe-IMCs particle size.

The eutectic lamellar morphology evolution of Fe-IMCs is significant with Mg. Firstly, the needle-to-lamella morphology transition of Al_6(Fe,Mn) has been revealed by 3D observation (**Fig. 5.7**). As the Mg content increases the preferred growth orientation (indicated with solid arrow in **Fig. 5.7c** and **Fig. 5.8a**) of Al_6(Fe,Mn) is suppressed, and then the growth towards less preferred orientations (the dash-line arrows indicated orientations in **Fig. 5.7c** and **Fig. 5.7d**) is facilitated. As a consequence, the interconnected lamellar morphology became more significant when Mg content increased. This phenomenon is believed to be the result of Mg content piling up at the interface because the more significant Mg segregation at the preferred growth orientation (higher growth velocity) compared with less preferred orientations (lower growth velocity). As the Mg segregation became severe during growth (**Fig. 5.18**), Fe and Mn become relatively lower causing a constitutional undercooling zone at the growth front to restrict the growth of Fe-IMC. As a result of this solute segregation (or Mg enrichment) at the growth interface, an Mg rich layer forms at the Fe-IMC/α-Al interface (**Fig. 5.13**). It is considered to form during solidification due to the considerable size (length > 300μm and 5μm < thickness <

20μm), and there is little time available for solid-state transformation. Secondly, the α-AlFeMnSi changes from a dot-lamella mixed morphology to a branched lamellar morphology. It may be explained with the same mechanism: the solute profile changing on the preferable branches facilitates the development of less preferred orientations, which consequently leads to this interconnected morphology.

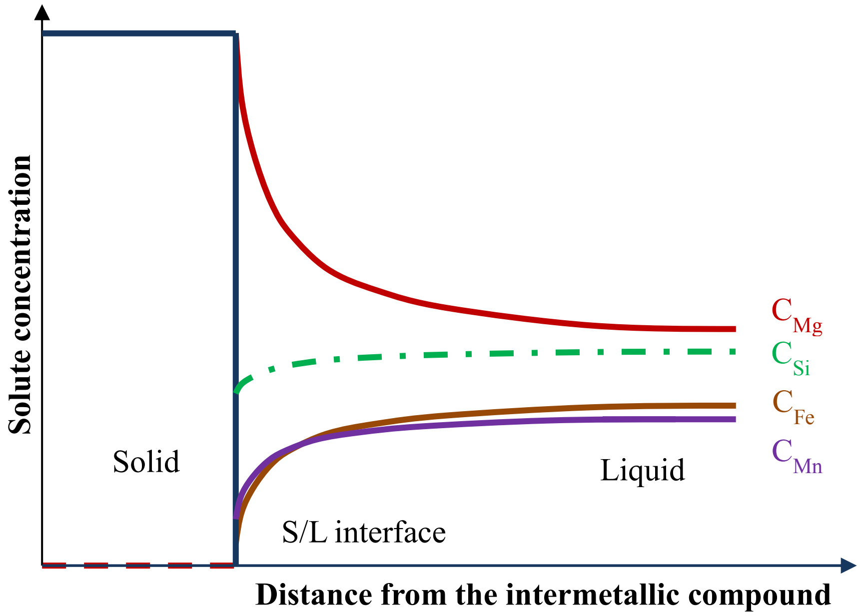

Figure 5.18 Schematic illustration of the solute concentration profile at the growth front of Fe-IMC particle. The equilibrium boundary layer was suggested in **Chapter 4** according to the interface solute piling-up description by Kurz and Fisher (Kurz and Fisher, 1986).

5.4.3.2 Eutectic Lamellar Spacing

Lamellar spacing in eutectic structure is widely used as a common parameter for regular eutectic (Elliott, 2013; Hunt and Jackson, 1966), and in quantifying solidification behaviour of irregular eutectics (Gündüz *et al.*, 2004; Magnin and Kurz, 1987). $Al_6(Fe,Mn)$ and α-AlFeMnSi, as faceted phases, are expected to be irregular eutectic as the faceted phase tend to grow only along well-define planes and/or directions (Dantzig and Rappaz, 2009; Magnin and Kurz, 1987). Both $Al_6(Fe,Mn)$ and α-AlFeMnSi exhibit coarsened morphology at the tips of the lamellae (see **Fig. 5.6** and **Fig. 5.9**) without any contribution from Mg. This is a result of the enrichment of solute elements (Mg, Fe and Mn) at the growth interface as well as S/L interface during the growth of faceted irregular eutectic (Hunt and Jackson, 1966). Relatively more rapid consumption of Al atoms than solute atoms forces Fe-IMC to form thick lamellar is also an important factor that causes the coarsening. In order to fit the undercooling criteria for non-isothermal irregular growth (Hunt and Jackson, 1966), the growth of the lamellar branches next to preferred lamellar branches were restricted to maintain the lamellar spacing (λ_a) during growth. This results in incomplete growth of some lamellar branches and coarsening, especially at the tip of the lamellae preferred orientations. The difference between maximum lamellar spacing λ_M and minimum lamellar spacing λ_a is an outcome of incomplete growth and coarsening. Consequently, using λ_a is more representative of the actual lamellar spacing in a relatively more isothermal liquid.

The eutectic lamellar spacing is often described with growth rate related function or undercooling related function (Magnin and Trivedi, 1991; Magnin and Kurz, 1987; Hunt and Jackson, 1966) given as:

$$\lambda^2 V = K_2/K_1, \qquad \lambda = \lambda_e \tag{5.3a}$$

and

$$\Delta T = K_1 \lambda V + K_2/\lambda \tag{5.3b}$$

For branched lamellar eutectic, Liu suggests that the revised Jackson/Hunt model provides the best fit for the measurement (Liu and Shang, 1992); and the parameters for eutectic solidification is given (Liu, 1992),

$$K_1 = \frac{m_\alpha + m_\beta}{m_\alpha m_\beta} * \frac{P(1+\varepsilon)^2 C_0}{\varepsilon D_L \pi^3} \tag{5.4}$$

$$K_2 = 2(1+\varepsilon)\Gamma^\alpha sin\theta_\alpha\left(\frac{m_\beta}{m_\alpha + m_\beta}\right) \tag{5.5}$$

where V is the growth rate, K_1 is alloy dependent constant and K_2 is curvature dependent constant. This addressed the effect of chemical composition on the growth of eutectic, which is often neglected by assuming very low cooling rate and perfect eutectic composition. Current experiment with various Mg content shows an increasing linear relationship between Mg composition and eutectic Fe-IMC's lamellar spacing of eutectic Fe-IMCs (**Fig. 5.16)** while the cooling rate was constant (3.5K/s). It suggests that Mg composition has influence on ΔT and/or the constants (K_1 and K_2). As established, the increasing Mg content can lead to more significant local solute segregation, which means the solute concentration of Fe or Mn C_0 at the growth front was reduced at higher Mg contents. Since the other parameters are inherent properties of the system and significant change on ε was not observed, K_1 of Fe-IMC/α-Al eutectic decreased and K_2 remained the same. As the heat extraction rate and temperature gradient in TP-1 mould are the same, the parameter V is considered to be stable. Thus, the eutectic lamellar spacing of Fe-IMC/α-Al increases with a higher Mg content in current alloys. In order to gain the value of for Al-1.2Fe-0.7Mn-*x*Mg and Al-2Si-1.2Fe-0.7Mn-*y*Mg alloys, the growth rate or heat extraction has to be measured in further work.

Given that, the morphology modification by Mg is caused by severe Mg segregation at the growth front of facet Fe-IMCs especially at the preferred growth orientation and the eutectic lamellar spacing increase is caused by the same mechanism.

5.4 Summary

In this chapter, effect of Mg on the Fe-IMCs in Al-1.2Fe-0.7Mn-*x*Mg and Al-2Si-1.2Fe-0.7Mn-*y*Mg alloys has been described in detail. Phase diagram calculation by Pandat^{TM} shows that in Al-1.2Fe-0.7Mn-*x*Mg alloys the volume fraction of $Al_6(Fe,Mn)$ can increase from 4.8vol.% to 5.8vol.% as the Mg content increases to 6.0wt.%; and in Al-2Si-1.2Fe-0.7Mn-*y*Mg alloys the volume fraction of α-AlFeMnSi only increases from 3.1vol.% to 3.2vol.% when Mg content increased to 5.4wt.%. Although Mg does not participate in the formation of either $Al_6(Fe,Mn)$ or α-AlFeMnSi directly, Mg tend to reject Fe atoms from the Al to form more Fe-IMCs due to the Fe-Mg interaction and better miscibility between Mg and Al compared with Fe and Al. $Al_6(Fe,Mn)$, as a metastable phase before $Al_{13}Fe_4$, is the predominant Fe-IMC phase in Al-1.2Fe-0.7Mn-*x*Mg alloys, showing a consistent structure with $Al_6(Fe_{0.5}Mn_{0.5})$ which has a orthorhombic lattice structure with lattice parameters of a=7.4986nm, b=6.495nm, c=8.837nm and γ=107.7°. α-AlFeMnSi, as the predominant Fe-IMC phase in Al-2Si-1.2Fe-0.7Mn-*y*Mg alloy, shows a consistent structure with body-centred cubic lattice structure with lattice parameter of a=1.256nm, $Al_{19}Fe_4MnSi_2$.

Mg content changes the morphology of Fe-IMCs significantly, especially $Al_6(Fe,Mn)$ which changed from a needle shape to interconnected lamellar morphology when Mg composition increased. An Mg-rich layer with thickness of 5-20nm was commonly observed on the Fe-IMC/α-Al interface in the alloys with Mg addition. Cooling rate is very important to the solidification of Al-1.2Fe-0.7Mn-*x*Mg and Al-2Si-1.2Fe-0.7Mn-*y*Mg alloys as they reach completely eutectic microstructure with cooling rate ≥3.5K/s. In full eutectic microstructure, the increase of Mg content can increase eutectic lamellar spacing considerably. In Al-1.2Fe-0.7Mn-*x*Mg alloys the eutectic lamellar spacing increased from 1.3±0.3μm to 2.9±0.8μm as Mg content rise to 6.0wt.%. In Al-2Si-1.2Fe-0.7Mn-*y*Mg the eutectic lamellar spacing increased from 1. ±0.3μm to 3.3±0.8μm at the Mg content rise to 5.4wt.%. Due to the strong anisotropy of Fe-IMC crystals, the solute segregation Mg segregation on preferred growth orientation is more severe causing greater growth restriction on this orientation. Thus, the relative growth velocity on less preferred orientations becomes more significant. Considering Mg is insoluble to Fe-IMCs, the growth restriction can be more significant than other soluble elements. In addition, concentration of Fe and/or Si in Fe-IMCs (Al_6(Fe,Mn) and α-Al_{12}(Fe,Mn)$_3$) can be reduced with increased Mg content and/or increased cooling rate due to the interactions between Mg, Fe and Mn atoms.

Chapter 6 Role of TiB_2 Particles on the Solidification of Fe-rich Intermetallic Compounds

Enhancing the nucleation of Fe-IMC and refining its morphology provide significant benefit through reducing their detrimental effect on the mechanical property of Al alloys, particularly secondary Al alloys. Considering the significant difficulty in nucleation of Fe-IMCs explained in previous chapters and the lack of effective nucleation catalyst, developing a grain refiner for Fe-IMCs becomes very important. The concept of composition templating for enhancing heterogeneous nucleation will be introduced in this part of the research. This chapter is dedicated to understanding the nucleation behaviour of α-AlFeMnSi in Al-5Mg-2Si-1.2Fe-0.7Mn alloy with the addition of surface modified TiB_2 particles through a novel Al-Ti-B(Fe) master alloy.

The experimental plan was to produce a novel master alloy Al-Ti-B(Fe) for nucleation enhancement of α-AlFeMnSi and to study the effect of this master alloy using slow cooling and water quench experiments. The TiB_2 particles for heterogeneous nucleation should be surface modified during the preparation of novel master alloy Al-Ti-B(Fe) (described in section 3.1). Slow cooling experiment (described in section 3.2.2) was carried out by simply adding the Al-Ti-B(Fe) master alloy to the alloy melt and furnace cooling the melt in the electric resistance furnace until it fully solidified. Water quench experiment (described in section 3.2.5) used quartz tube to draw the liquid melt heated with induction furnace and quenched the quartz tube along with drawing the melt in a water tank.

6.1 Al-Ti-B(Fe) Master Alloy

In order to have uncontaminated and wetted surface on the TiB_2 particles, the boride particles were synthesized in-situ at high temperature in a melts of Al-Ti and Al-B master alloys molten in an electric resistance furnace and then cast into thin rods (described in details in **Chapter 3**). The microstructure of the Al-Ti-B(Fe) master alloy and the in-situ synthesized TiB_2 was characterized and will be presented in following sections.

6.1.1 Microstructure

Micrographs shown in **Fig. 6.1** were taken from the vertical cross section of the thin plate sample so that the effect of gravity segregation can be avoided. The **Fig. 6.1a** shows that after holding for 8 hours at 900°C TiB_2 particles (light grey particles) is the dominant phase in the microstructure, although there was some AlB_2 (or $(Al,Ti)B_2$) (dark grey particles) observed due to the excess boron in the Al-Ti-B(Fe) alloy. TiB_2 particles tend to locate near the grain boundary forming a continuous "ring cluster"; except for these agglomerations where TiB_2 particles were most often observed evenly distributed in the microstructure. AlB_2 particles were normally observed in the form of clusters surrounded by TiB_2 particle rings, although there are a few AlB_2 found in the matrix by itself. The 2D morphology of in-situ synthesized TiB_2 particles shown in **Fig. 6.1b** and **Fig. 6.1c** indicates a faceted morphology of the boride with particle size less than 10μm in diameter and less than 4μm in thickness. Meanwhile, **Fig. 6.1b** shows the TiB_2 particles grow with the steps on their {0001} basal planes.

It is very difficult to distinguish among the TiB_2 (a=0.303nm, c=0.323nm (Johnsson and Eriksson, 1998), AlB_2 (a=0.301nm, c=0.325nm (Hofmann and Jäniche, 1936)) and $(Al,Ti)B_2$ whose lattice parameter is dependent on Ti/B ratio (Fjellstedt, Jarfors and Svendsen, 1999), due to their almost identical lattice parameters and the crystal symmetry (hexagonal). The $(Al,Ti)B_2$, as a transition phase of the peritectic reaction from AlB_2 to TiB_2, requires high-resolution chemical analysis equipment (TEM/EDS) for its identification. In present investigation, the TiB_2 in the microstructure is readily distinguished from AlB_2 by the chemical composition obtained using SEM/EDS (**Fig. 6.1e** and **Fig. 6.1f**). Sometimes a minor amount of Ti was detected on the boundary of these AlB_2 particles, which suggests that the nominal AlB_2 are possibly $(Al,Ti)B_2$ phase. In present study, the minor lattice parameter difference among AlB_2, $(Al,Ti)B_2$ and TiB_2 should not affect the outcome of the experiment. The phase identification was carried out with XRD on the particle powder extracted from the master alloy by dissolving Al matrix using a 15 vol.% HCl aqueous solution. As shown in **Fig. 6.2**, the presence of Al and TiB_2 is confirmed using the crystal information of FCC Al, hexagonal TiB_2, respectively. Arguably, low intensity of tetragonal Al_3Ti crystal was also detected, indicating a limited amount of free Ti can exist in boron rich side of stoichiometric TiB_2 (Cornish, 1975). Due to the almost identical crystal structures of AlB_2 and TiB_2, it is hard to confirm the existence of AlB_2 by XRD as the diffraction peaks almost fully overlap.

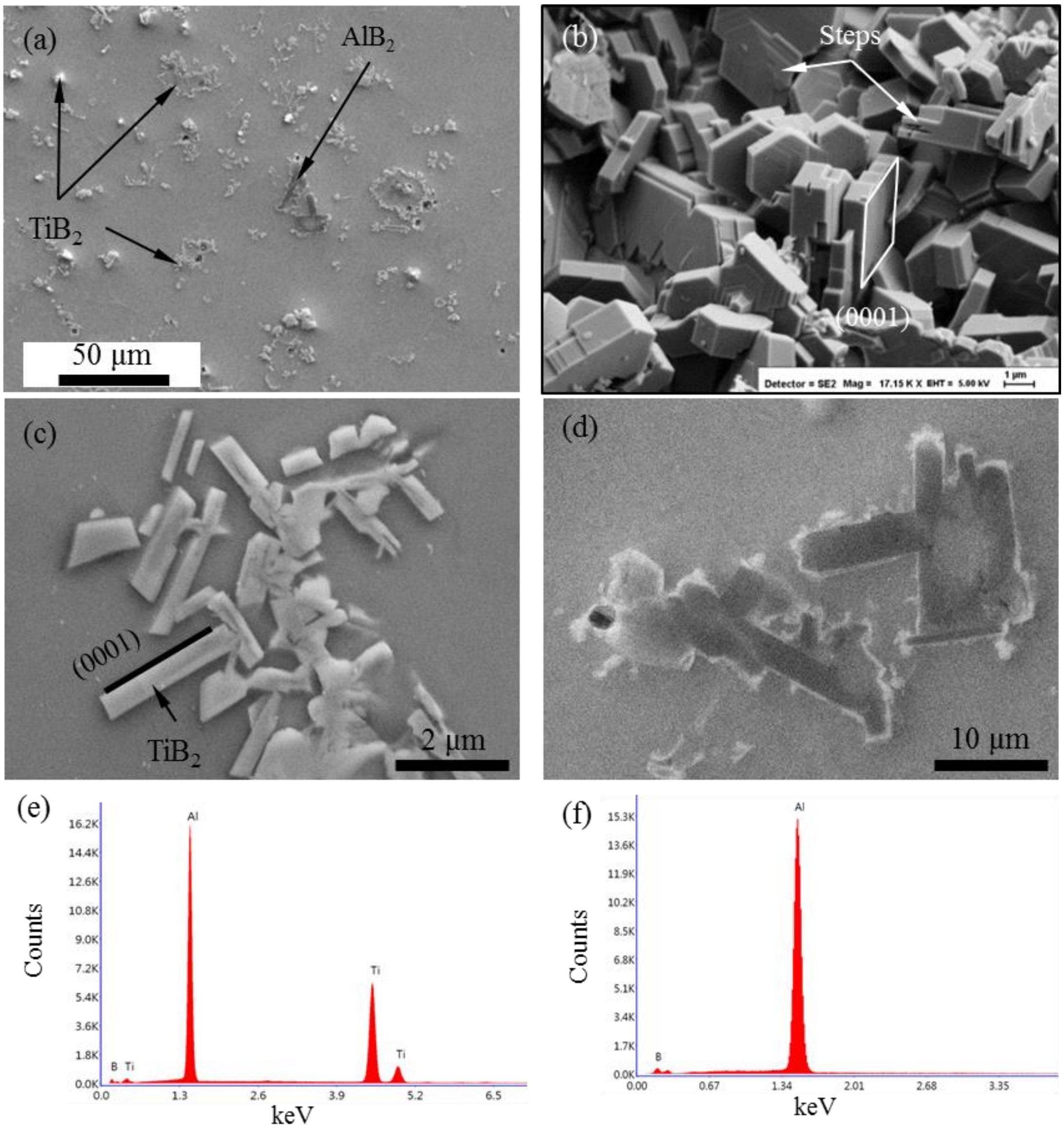

Figure 6.1 SEM micrographs showing (a) the microstructure of Al-Ti-B(Fe) master alloy, (b) the morphology of synthetic TiB_2 (or AlB_2) particles in 3D, (c) TiB_2 particles in 2D and AlB_2 (or $(Al,Ti)B_2$) particles in 2D; SEM/EDS result showing the chemical composition of (d) the faceted TiB_2 particles and (f) AlB_2 (or $(Al,Ti)B_2$) particles (gun voltage: 20kV). The TiB_2 and AlB_2 (or $(Al,Ti)B_2$) particles are marked with black arrows. Growth steps were indicated with white arrows. (0001) plane of TiB_2 (or AlB_2) was indicated in (b) and (c).

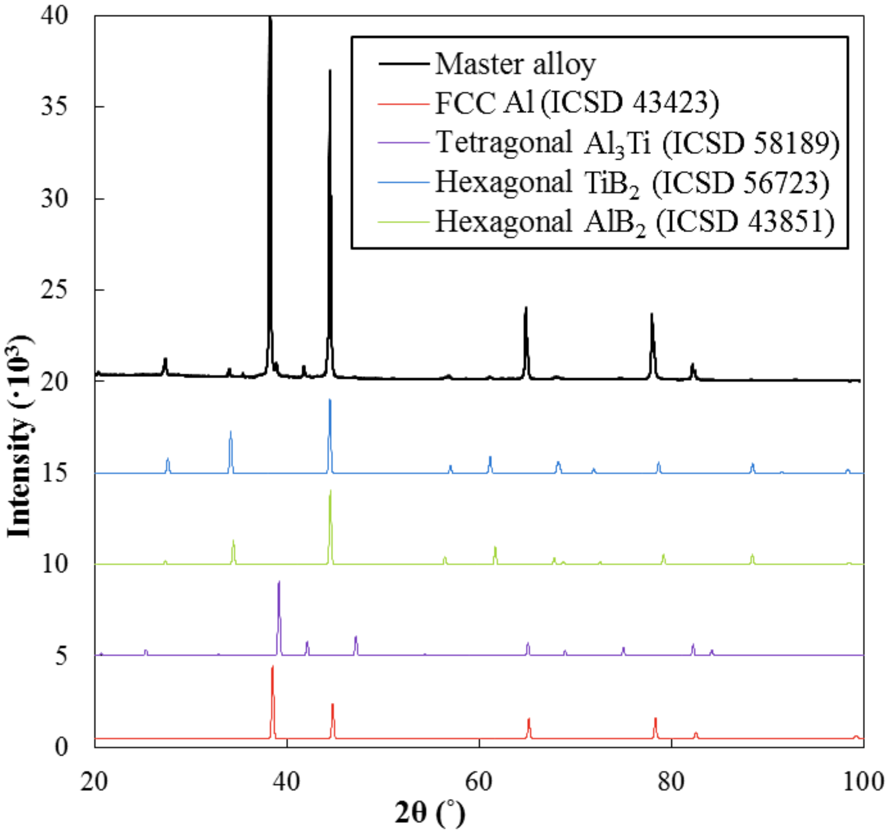

Figure 6.2 XRD line profile of Al-Ti-B(Fe) master alloy compared with the standard crystal information of relevant phase from Inorganic Crystal Structure Database of National Chemical Database Chemical (ICSD of CDS) using intensity (a.u.) for Y-axial.

6.1.2 Fe Adsorption on $(Al,Ti)B_2$ Particle

The aim of designing this master alloy was to provide substrates modified with element adsorption layer on its surface to reduce the surface energy for heterogeneous nucleation (Fan, 2013). The Al-Ti-B(Fe) master alloy was held at 900˚C for 8 hours during preparation, where Fe is expected to be fully dissolved in the melt. Fe atoms distributed homogeneously in the alloy melt, given its considerable diffusivity in liquid Al (2.2×10^{-9} m^2/s (Du *et al.*, 2003)). Under the equilibrium state the maximum solubility of Fe in solid Al is 0.052wt.% (Edgar, 1949), which means Al-Fe phase should be thermodynamically stable in Al-Ti-B(Fe) master alloy that has Fe content of 0.5wt.%. The prepared master alloy was characterized with TEM to verify the adsorption behaviour of Fe or any other solute elements on substrate particles (TiB_2). As shown in **Fig. 6.3**, the observation suggests that there is segregation of a monolayer of atoms on the surface of the duplex (Al,Ti)B_2 particle on the {10-10} planes of AlB_2 substrate. Crystallographic indexing using SAED pattern confirms a crystal structure of TiB_2 or AlB_2. Due to the close crystal structure between AlB_2, (Al,Ti)B_2 and TiB_2, the lattice image cannot distinguish them. The observed area shown in **Fig. 6.3** was identified to be AlB_2 by HR-EDS (**Fig. 6.4**). STEM observation (**Fig. 6.3**) suggested a Zig-Zag atom arrangement of adsorption layer along the interface on (10-10) plane of the entire particle. The atoms on this layers appeared to be aligned with the atoms in AlB_2 particle on (10-10) towards [0001] direction (horizontal direction).

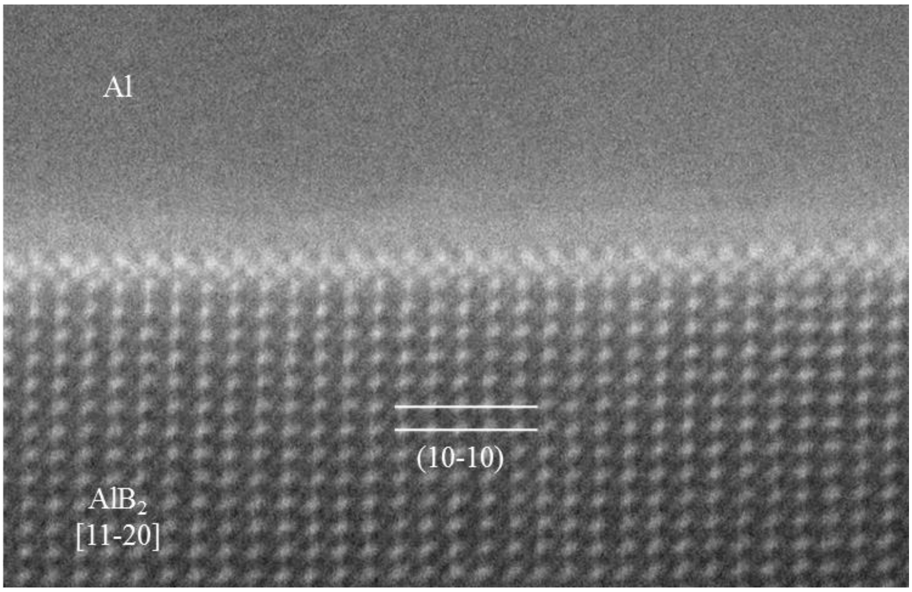

Figure 6.3 STEM HAADF image showing the atom arrangement at the AlB_2 particle boundary. It indicates that atom arrangement on the interface layer is slightly disagreed with the atom on (10-10) plane of AlB_2. The planer spacing of the interface layer is about 0.7 times of the spacing on {10-10} plane of AlB_2. The atom distance along horizontal direction is almost the same to the spacing of {0001} planes of AlB_2 (courtesy of Dr. Y. Wang).

In order to identify the adsorption layers on the surface of AlB_2 particle, chemical composition mapping was carried out in the area across the Al/AlB_2 interface with high resolution EDS (**Fig. 6.4)**. Firstly, the HAADF image on zone axis of substrate particle suggests that the atom columns on the interface with Al matrix (**Fig. 6.4c**) are brighter than that in the AlB_2 substrate, indicating the existence of heavier atoms. Secondly, Ti columns were detected at the bottom part of the image of the same boride particle from inside of the particle to the interface (**Fig. 6.4d**), which suggests a structure of $(Al,Ti)B_2$. Most importantly, as shown in **Fig. 6.4b**, Fe enrichment is clearly shown on the interface area of the AlB_2 particle, which is correspondent to the bright atom layer in **Fig. 6.4a**.

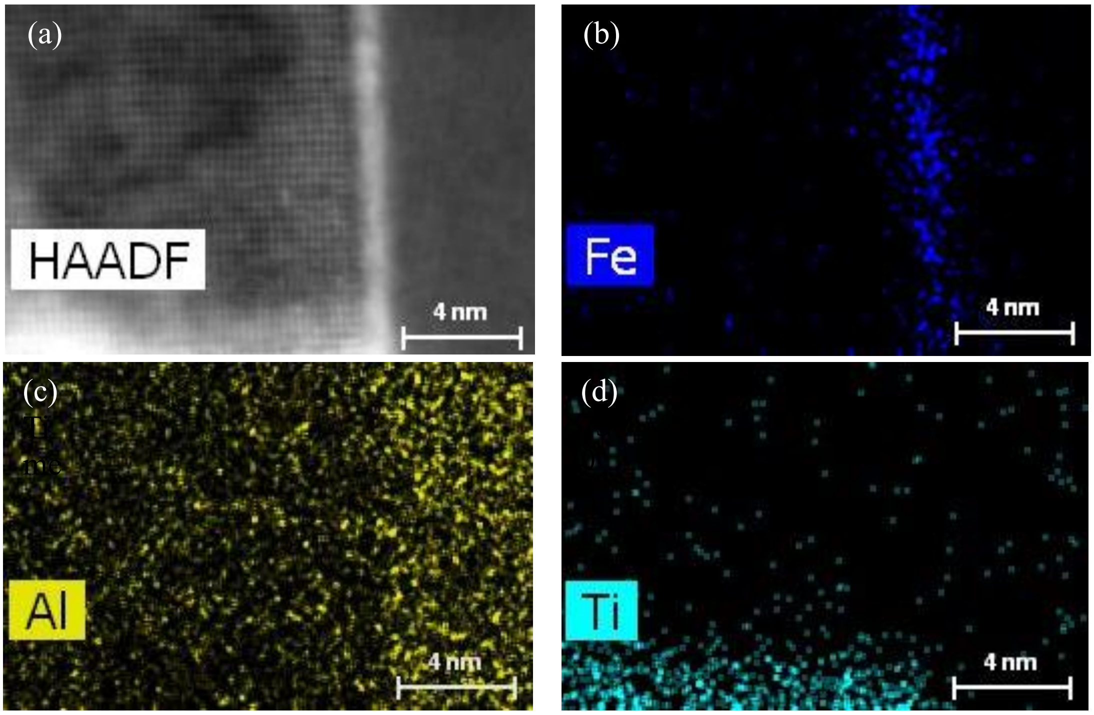

Figure 6.4 STEM micrographs showing (a) HADDF image of the Al/ $(Al,Ti)B_2$ interface area, (b) the Fe distribution across Al/ $(Al,Ti)B_2$ interface by HR-EDS mapping, (c) the Al distribution across $Al/(Al,Ti)B_2$ interface by HR-EDS mapping and (d) the Ti distribution across $Al/(Al,Ti)B_2$ interface by HR-EDS mapping (courtesy of Dr. Y. Wang). Element distribution maps are correspondent to the HADDF image.

6.2 Refinement of α-AlFeMnSi phase

6.2.1 Microstructure through Slow Cooling

In the present study, a low cooling rate was achieved in CF condition with and without electromagnetic (EM) field provided by induction furnace. In the CF process without EM field the sedimentation of compact Fe-containing particles were inevitable. The morphology of the primary α-AlFeMnSi in CF samples of Al-5Mg-2Si-1.2Fe-0.7Mn alloy with and without Al-Ti-B(Fe) addition are shown in **Fig. 6.5**. The primary α-AlFeMnSi particles were much smaller in size, larger in number density; they have similar polyhedral morphology when the Al-Ti-B(Fe) master alloy

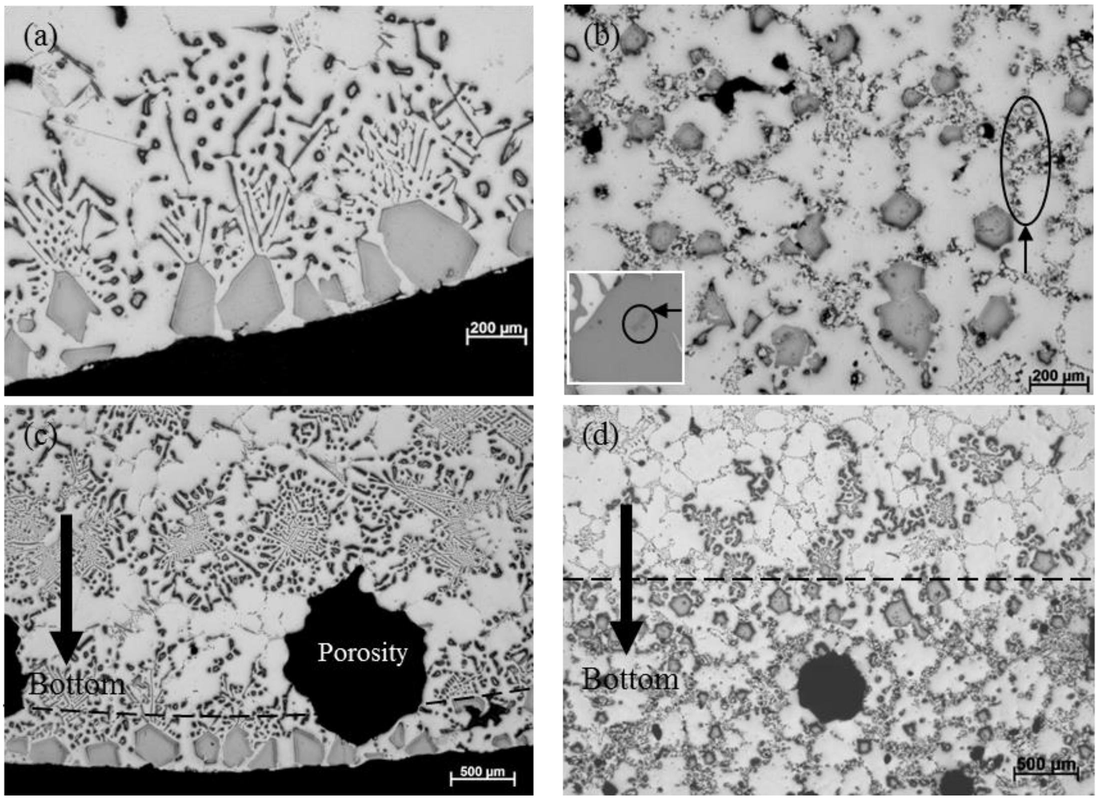

Figure 6.5 Optical micrographs showing primary $Al_{12}(Fe,Mn)_3Si$ in Al-5Mg-2Si-1.2Fe-0.7Mn alloy (a) and (c) without and (b) and (d) with Al-Ti-B(Fe) addition (nominally 1000 ppm synthetic TiB_2) under the same container (graphite crucible) and the same cooling condition (CF). Solid arrow (thin) indicate that TiB_2 particle clusters (dark dots). Dash line in (c) and (d) refers to the gravitational segregation line for α-AlFeMnSi particles of each sample.

was introduced compared to that without Al-Ti-B(Fe) addition under the same casting condition (graphite crucible and cooling in furnace). The primary particles distribute at more than 2μm and less than 0.5μm from the bottom of crucible surface in the alloy with (**Fig. 6.5d**) and without Al-Ti-B(Fe) (**Fig. 6.5c**) addition respectively. This proved that the primary α-AlFeMnSi experienced a more severe gravitational settling effect to the bottom of the crucible when there was no Al-Ti-B(Fe) addition. When there is no Al-Ti-B(Fe), eutectic α-AlFeMnSi was often seen to develop from the primary α-AlFeMnSi, whilst the growth of eutectic α-AlFeMnSi on primary particle was significantly supressed when Al-Ti-B(Fe) was added to the alloy. On the other hand, TiB_2 particles were found within the primary α-AlFeMnSi in Al matrix and mostly along the grain boundaries (**Fig. 6.5b**); TiB_2 particles also suffered from the gravitational settling as they agglomerated at the bottom part of the crucible (**Fig. 6.5d**).

6.2.2 Microstructure through Water Quench

In order to investigate the solidification process of α-AlFeMnSi at primary α-AlFeMnSi formation temperature range, water quench experiment using a quartz tube was performed using the Al-5Mg-2Si-1.2Fe-0.7Mn alloy with and without Al-Ti-B(Fe) addition. The water quench temperature (660˚C, 650˚C, 640˚C and 630˚C) was carefully selected to be within the primary α-AlFeMnSi formation temperature range (670.4 – 620.5˚C) according to equilibrium phase diagram (**Fig. 4.1**). The melt was stirred and cooled to the selected quenching temperatures in controlled magnetic field powered with an induction furnace before water quenched in quartz tubes. As describe in Section 3.2.5 that the characterization of the resultant alloy was conducted at longitudinal section of the quenched cylinder samples (6mm in diameter) that was about 4 to 5cm from the top side of the sample. The microstructures of the quartz tube water quench (TQ) sample at different quenching temperatures (660˚C, 650˚C, 640˚C and 630˚C) are shown in **Fig. 6.6**. The Primary α-AlFeMnSi particles, with a compact polyhedral morphology, were retained in the liquid melt due to magnetic stirring powered by induction furnace, instead of settling quickly due to the gravity. Porosity is observed at the centre of the quenched sample (**Fig. 6.6d**), next to TiB_2 clusters (**Fig. 6.6f**) and alongside α-AlFeMnSi particles (**Fig. 6.6c** and **6.6h**). Cracks are often seen to penetrate primary α-AlFeMnSi particles (**Fig. 6.6e** and **6.6h**)

6.2.3 Sedimentation

Gravity segregation is a common phenomenon when a second phase, such as inclusions, in-situ immiscible substances and primary phases in liquid metal, has a different density than the melt (Yang, Yang and Ji, 2015; Mondolfo, 2013; Mondolfo, 2013; Zhang *et al.*, 2012; Shabestari, Keshavarz and Hejazi, 2009; Cao, Saunders and Campbell, 2004; Murty, Kori and Chakraborty, 2002; Murty *et al.*, 1999; Jones and Pearson, 1976). After more than 6 hours of CF process, TiB_2 ($4.52 g/cm^3$) and primary α-AlFeMnSi ($3.71 g/cm^3$), which exhibits compact and faceted morphology

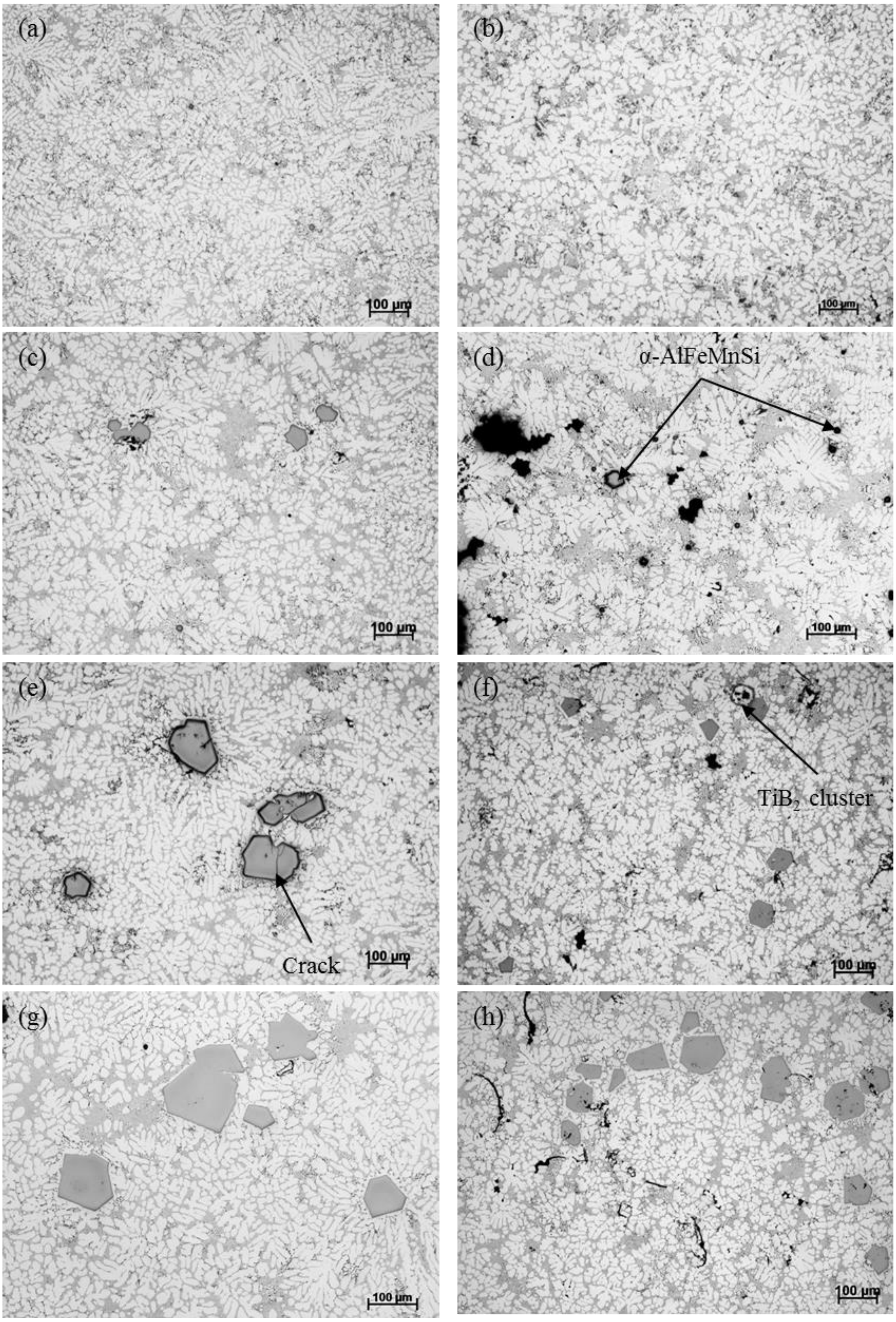

Figure 6.6 Optical micrographs showing the microstructure of Al-5Mg-2Si-1.2Fe-0.7Mn alloy without Al-Ti-B(Fe) addition quenched from (a) 660˚C, (c) 650˚C, (e) 640˚C and (g) 630˚C, and with 2wt.% Al-Ti-B(Fe) addition quenched from (b) 660˚C, (d) 650˚C, (f) 640˚C and (h) 630˚C.

tend to settle towards the bottom of the crucible since the density of liquid Al is (2.38g/cm^3) lower than those of the two phases. Thus, these two kinds of particles were observed in the bottom of the crucible (**Fig. 6.5c** and **Fig. 6.5d**). With Al-Ti-B(Fe) addition, the refined primary α-AlFeMnSi particles, shows lower amount of segregation due to gravity; they locate at the same vertical level with TiB_2 sediment, whilst the upper areas of the CF sample where not much TiB_2 did not contain refined primary α-AlFeMnSi particle. This negative effect from gravity segregation can be reduced by magnetic stirring of the melt during electromagnetic induction heating. As shown in **Fig 5.6**, the particle distribution in the liquid melt in quartz tube water quench experiment is uniform due to the magnetic field provided by induction furnace during heating.

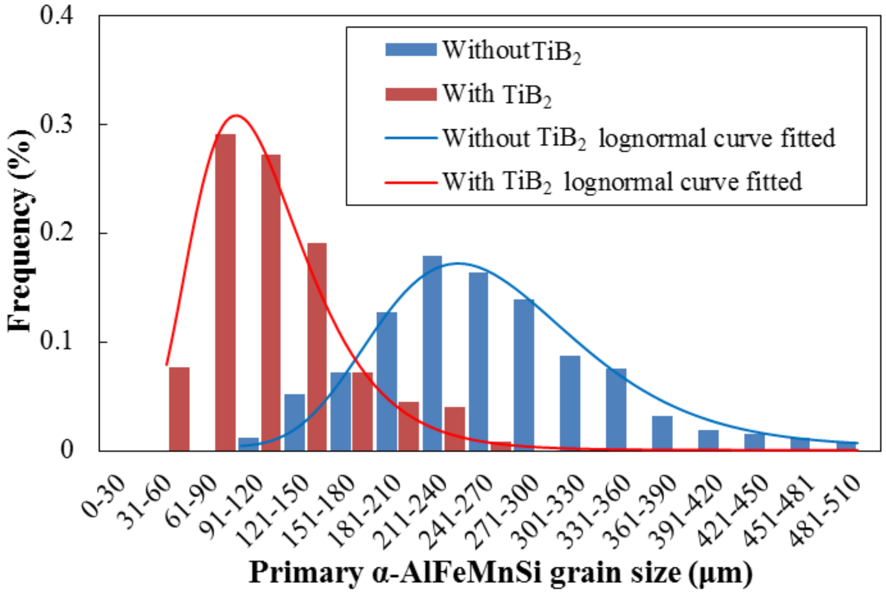

Figure 6.7 Primary α-AlFeMnSi size distribution in furnace cooled Al-5Mg-2Si-1.2Fe-0.7Mn alloy with (blue) and without Al-Ti-B(Fe) addition (red). The distributions are fitted by lognormal functions as suggested by solid curves. The entire solidified sample was examined. The mean primary α-AlFeMnSi particle sizes with and without Al-Ti-B(Fe) addition are 110.9±45.5μm and 251.3±75.3μm, respectively. The primary α-AlFeMnSi number density was 0.05±0.004/mm^2 without Al-Ti-B(Fe) addition, and the primary α-AlFeMnSi number density was 1.09±0.02/mm^2 with Al-Ti-B(Fe) addition.

6.2.4 Volume Fraction, Particle Density and Size Distribution of Primary α-AlFeMnSi

The measured size distribution of the primary α-AlFeMnSi particles in Al-5Mg-2Si-1.2Fe-0.7Mn alloy solidified with CF condition is presented in **Fig. 6.7.** The distributions of primary α-AlFeMnSi with and without the Al-Ti-B(Fe) addition are fitted with a lognormal function. Considering the primary particles are affected by gravity segregation, the whole longitudinal transverse section of CF sample was examined for a comprehensive assessment of particle density. The density of primary α-AlFeMnSi in the entire sample is 0.05±0.004/mm^2 when no Al-Ti-B(Fe) is added (reference alloy); with the addition of 2wt.% Al-Ti-B(Fe), the particle density increased dramatically by 20 times to 1.09±0.02/mm^2 of that in reference alloy. The average particle sizes of the primary α-AlFeMnSi in the CF sample with and without Al-Ti-B(Fe) addition are 110.9±45.5μm and 251.3±75.3μm, respectively.

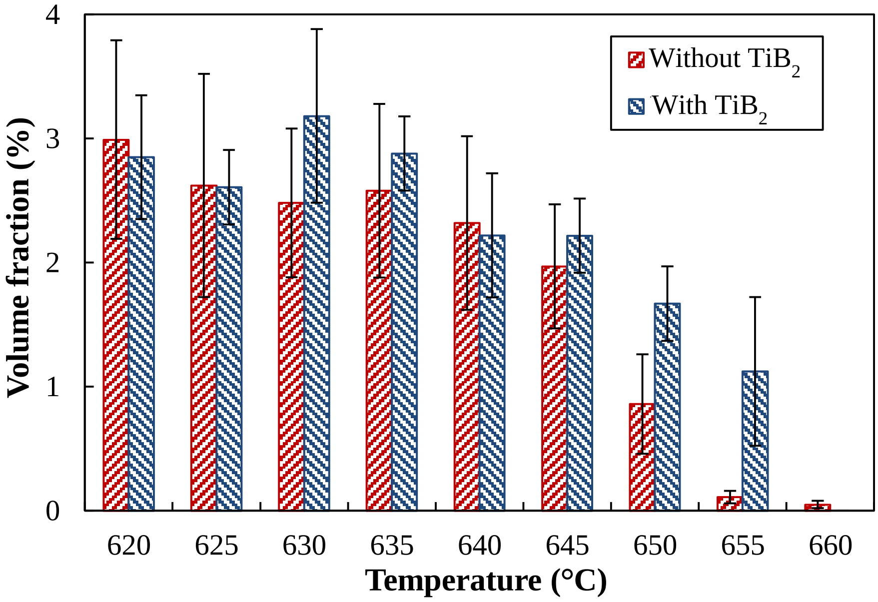

Figure 6.8 Volume fraction of primary α-AlFeMnSi with and without TiB_2 addition using Al-Ti-B(Fe) as a function of temperature in transverse section of Al-5Mg-2Si-1.2Fe-0.7Mn alloy by quartz tube water quench. Quantification was performed on at least 10 frames of 3.81mm^2 of the microstructure for each data point using AxioVision software produced by Zeiss.

Volume fraction of the primary α-AlFeMnSi with nominally 2wt.% Al-Ti-B(Fe) addition is determined from the quartz tube water quench samples with the melt being cooled to 660˚C, 650˚C, 640˚C, 630˚C and 620˚C in a magnetic field before water quenched in quartz tubes. As shown in **Fig. 6.8**, the volume fraction of primary α-AlFeMnSi increase with the decreased quenching temperatures before stabilizing at the final value. When there is no TiB_2 addition (reference sample), it increased rapidly from 0.05±0.03vol.% at 660˚C to 2.3±0.7vol.% at 640˚C and followed by a small increase to 2.9±1.1vol.% until 620˚C; when there is 2wt.% Al-Ti-B(Fe) master alloy (1500ppm TiB_2) addition, the volume fraction increased to 1.1±0.6vol.% at 655˚C, followed by a considerable increase to 3.2±0.7vol.% at 630˚C before a small decrease to 3.0±0.5vol.% at 620˚C. In reference sample the primary α-AlFeMnSi are less at high quenching temperature (from 650˚C to 645˚C) compared with TiB_2 added sample, their volume fractions was similar at 2.9±0.9vol% and 3.0±0.8vol% when quenching from 625˚C and 620˚C, respectively. The overall volume fraction of primary α-AlFeMnSi was stabilized at around 2.9±0.6vol.% when quench temperature decreased with and without addition of Al-Ti-B(Fe). The volume fraction of primary α-AlFeMnSi increased with time as temperature decreases in the furnace cooling stage; the volume fraction increase of primary α-AlFeMnSi stops as the growth of α-AlFeMnSi at water quench stage was severely restricted due to insufficient growth time, and the remaining of the solute atoms contributed to the growth of eutectic α-AlFeMnSi or other Fe-IMCs.

As shown in **Fig. 6.9**, when Al-Ti-B(Fe) is added, the average size of primary α-AlFeMnSi, is approximately half (61%) of the average particle size in the reference for all the selected quenching temperatures, except when quenching from 660˚C where the primary α-AlFeMnSi was not observed and quenching from 655˚C where primary α-AlFeMnSi particles with and without Al-Ti-B(Fe) are similar in size (14.4±5.1μm). Also, the size of α-AlFeMnSi in both alloys with and without Al-Ti-B(Fe) addition shows an increase trend as the quenching temperature decreases. In the presence of Al-Ti-B(Fe), the average size of primary α-AlFeMnSi particle increase gradually from 12.5±2.0μm at 655˚C to 73.6±20.1μm at 620˚C, and reaches its peak (within error margin due to small sample volume). Meanwhile, in the reference alloy, the average particle size increased considerably and continuously from 16.3±3.1µm at 655˚C to 127.0±26.1µm at 620˚C and outreach its peak 127.3±36.2µm at 630˚C.

Additionally, as shown in **Fig. 6.9**, the number density of primary α-AlFeMnSi particles was approximately 3.5 times larger when there is Al-Ti-B(Fe); it reached 5.2±1.2/mm^2 when quenched from 655˚C where the particle density was approximately 25 times higher compared with the alloy without Al-Ti-B(Fe) addition (about 0.2±0.1/mm^2). Further, the particle density reached 9.6/mm^2 when quenched from 640˚C after the sharp increase when quench from 655˚C, and then stabilized in the range of 9.2/mm^2 to 11.0/mm^2 as the quenching temperature decreases. When there is no Al-Ti-B(Fe) addition, its number density increased considerably and gradually from 0.05/mm^2 at 660˚C to 3.6±1.6/mm^2 at 640˚C before stabilising between 3.2/mm^2 and 3.9/mm^2 as quenching temperature decreased. The density increase of primary α-AlFeMnSi particle was approximately 2 times by the Al-Ti-B(Fe) addition in Al-5Mg-2Si-1.2Fe-0.7Mn alloy.

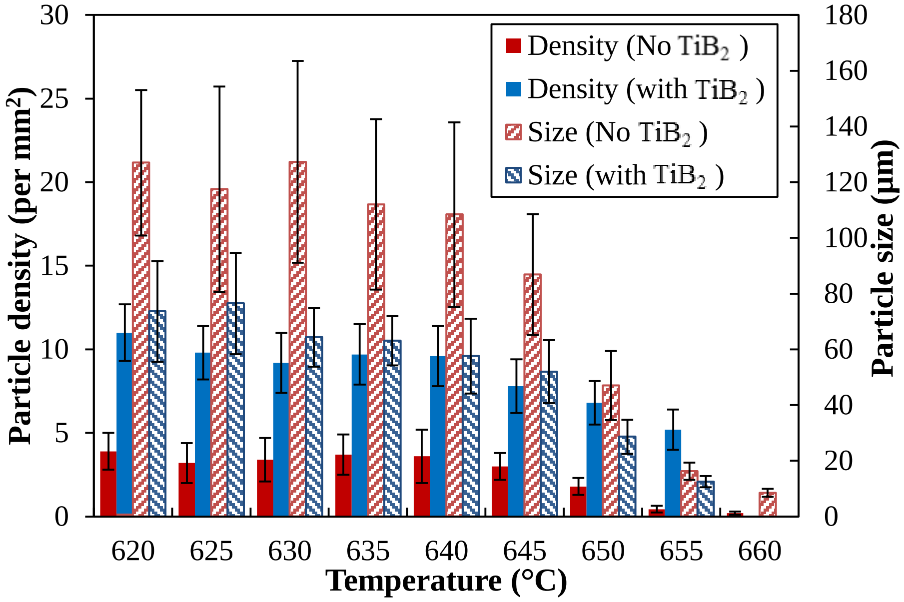

Figure 6.9 Comparisons of the number density and average particle size of primary α-AlFeMnSi in Al-5Mg-2Si-1.2Fe-0.7Mn as a function of temperature, showing the effect of Al-Ti-B(Fe) addition on particle size and number density. More than 1300 α-AlFeMnSi particles were included for this quantification analysis.

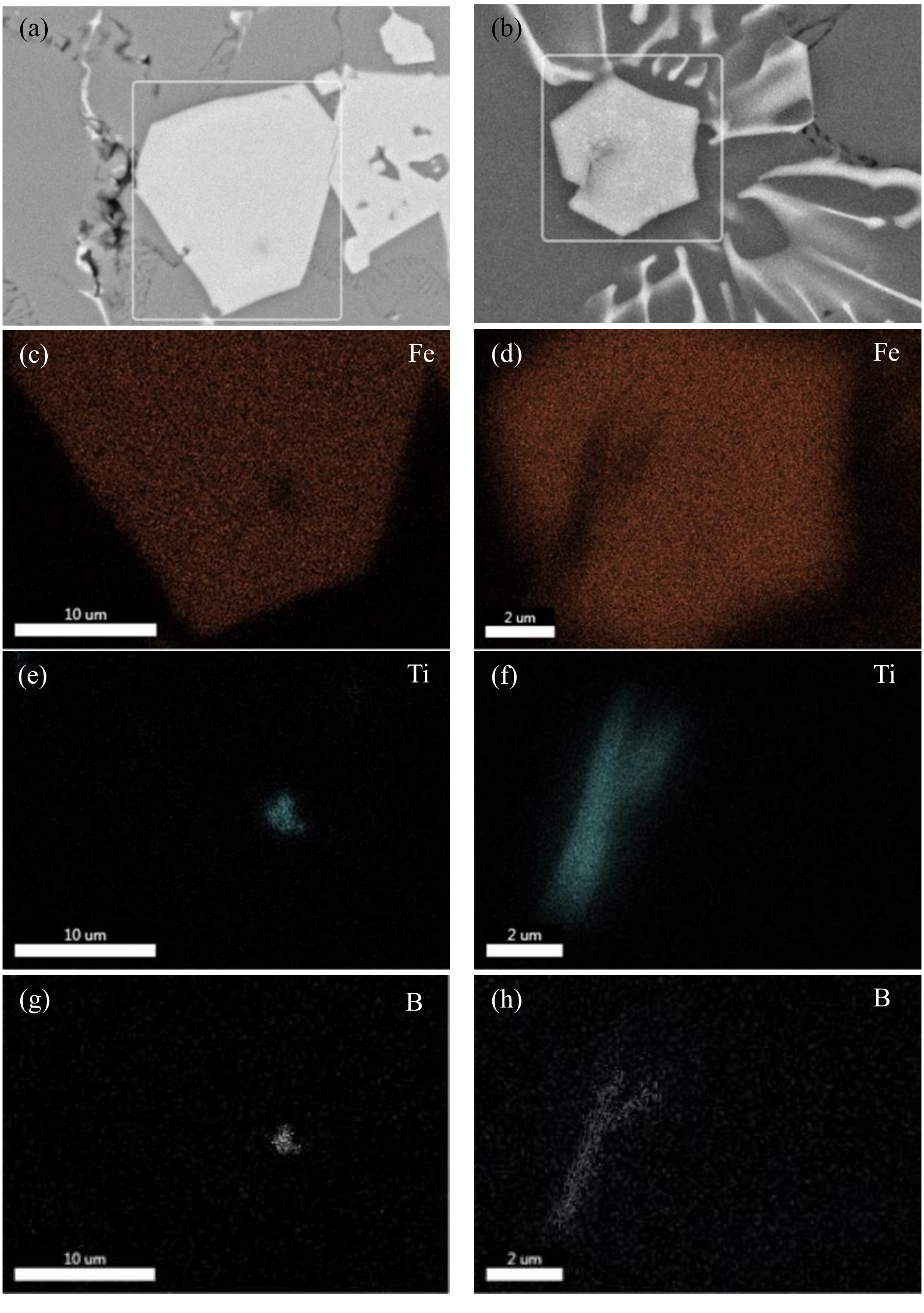

Figure 6.10 SEM micrographs showing (a) and (b) morphology of primary α-AlFeMnSi in quartz tube 650˚C water quenched sample of Al-5Mg-2Si-1.2Fe-0.7Mn alloy with Al-Ti-B(Fe) addition; SEM/EDS analysis corresponding to (a) and (b) showing the elemental distribution of (c) and (d) Fe, (e) and (f) Ti and (g) and (h) B, respectively.

6.3 Nucleation of Fe-IMCs on TiB_2 particles

6.3.1 TiB_2 Particles inside α-AlFeMnSi Phase

The physical contact between nucleation substrate and nucleation phase is an essential factor for heterogeneous nucleation (Fan, 2013; Turnbull, 1953). Similar to the coexistence of primary α-AlFeMnSi with oxides films and cracks in alloys with no Al-Ti-B(Fe) addition, TiB_2 particles or clusters were commonly observed to have physical contact with the α-AlFeMnSi phase when Al-Ti-B(Fe) master alloy was introduced to the alloy. As shown in **Fig. 6.10**, Ti and B, located at the centre of the primary α-AlFeMnSi particle, were confirmed with SEM/EDS mapping. The SEM/EDS suggests these TiB_2 containing particles are α-AlFeMnSi. The stoichiometry of the α-AlFeMnSi particle is determined as $Al_{12}(Fe,Mn)_3Si$ based on SEM/EDS analysis.

EBSD analysis was also carried out to confirm the crystal structure of the particles included in the primary α-AlFeMnSi particle. As shown in **Fig. 6.11,** there are multiple TiB_2 particles embedded in the primary α-AlFeMnSi grain; also few TiB_2 particles were observed at both the interface between α-Al and α-AlFeMnSi and α-Al grain boundaries. As shown in **Fig. 6.11c**, eutectic branches of α-AlFeMnSi developed from primary α-AlFeMnSi particle exhibit coherent orientation with primary particle given the same colour in Inverse Pole Figure (IPF).

6.3.2 Orientation Relationships (ORs) between TiB_2 and Fe-IMCs

Specific orientation relationships between nucleation substrate and nucleation phase is an essential factor for a heterogeneous nucleation event (Fan, 2013; Bramfitt, 1970). TEM examination investigated the orientation relationship between TiB_2 particles and Fe-IMCs in both Al-Ti-B(Fe) master alloy and Al-5Mg-2Si-1.2Fe-0.7Mn alloy. **Fig. 6.12a** is a bright field TEM micrograph showing a faceted particle and its adjacent Fe-IMC particle in Al-Ti-B(Fe) master alloy. TEM/EDS revealed that the chemical composition of the faceted particle has a stoichiometry of TiB_2 and its neighbouring particle has the stoichiometry of $Al_{13}Fe_4$. Further, TEM observation (**Fig. 6.12)** shows lattice image (**Fig. 6.12b**) where the incident beam is parallel to the [020] direction of $Al_{13}Fe_4$ (top-left part) and the [10-10] direction of adjacent

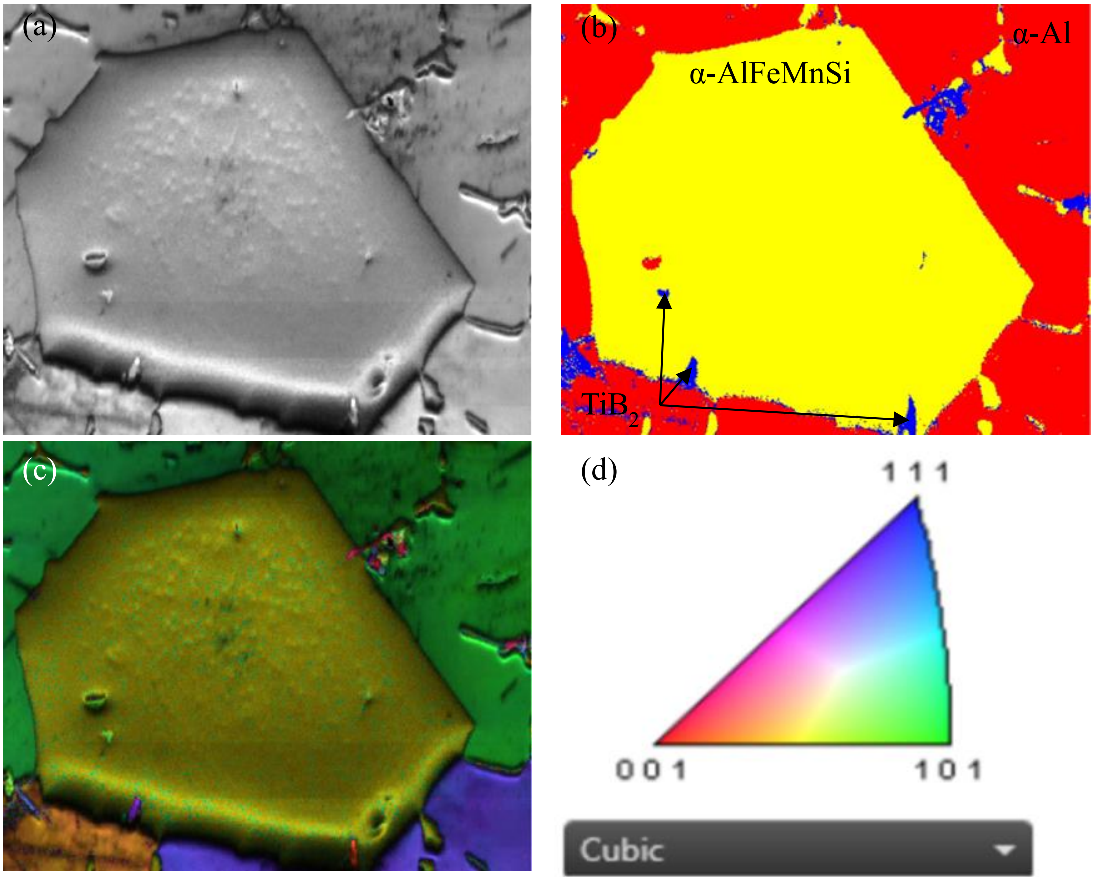

Figure 6.11 EBSD analysis showing (a) the morphology of primary α-AlFeMnSi particle, (b) phase distribution image and (c) Inverse Pole Figure (IPF) of the frame area; (d) orientation index table under cubic crystal system corresponding with (c). Positions of α-Al and α-AlFeMnSi are marked in (b) as red and yellow, respectively. Location of TiB_2 particles is indicated with arrows and shown blue in (b). The Al, TiB_2 and α-AlFeMnSi were indexed with Al (ICSD 43423), TiB_2 (ICSD 56723) and $Al_4MnSi_{0.74}$ (ICSD 59362), respectively.

TiB_2 (bottom-right part), the SAED of $Al_{13}Fe_4$ (**Fig. 6.12c**) on the orientation of [020] and the SAED of TiB_2 (**Fig. 6.12d**) on the direction of [10-10]. Particularly, **Fig. 6.12e** gives a schematic illustration of the orientation relationship:

$$(001)[020]\ Al_{13}Fe_4\ //\ (11\text{-}20)[10\text{-}10]\ TiB_2$$

with a tilt angle of 5.4° between the directions of (001)[100] $Al_{13}Fe_4$ and (11-20)[0001]TiB_2. As shown in **Fig. 6.13**, one atom layer on (001) plane of $Al_{13}Fe_4$ and one atom layer on (11-20) plane of TiB_2 overlapped to demonstrate atomic matching at the interface. It suggests a 5.4° tilt angle in lattice matching, as illustrated in **Fig. 6.13b**. Also, it shows atomic misfits for three pairs of orientations on the (001) $Al_{13}Fe_4$ and (11-20) TiB_2 interface (**Fig. 6.13a**):

OR1: (001)[020] $Al_{13}Fe_4$ // (11-20)[10-10] TiB_2, f_1= 1.6%;

OR2: (001)[100] $Al_{13}Fe_4$ // (11-20)[0001] TiB_2, f_2 = 8.8%;

OR3: (001)[120] $Al_{13}Fe_4$ ∠6.05˚ (11-20)[10-11] TiB_2, f_3 = 4.2%.

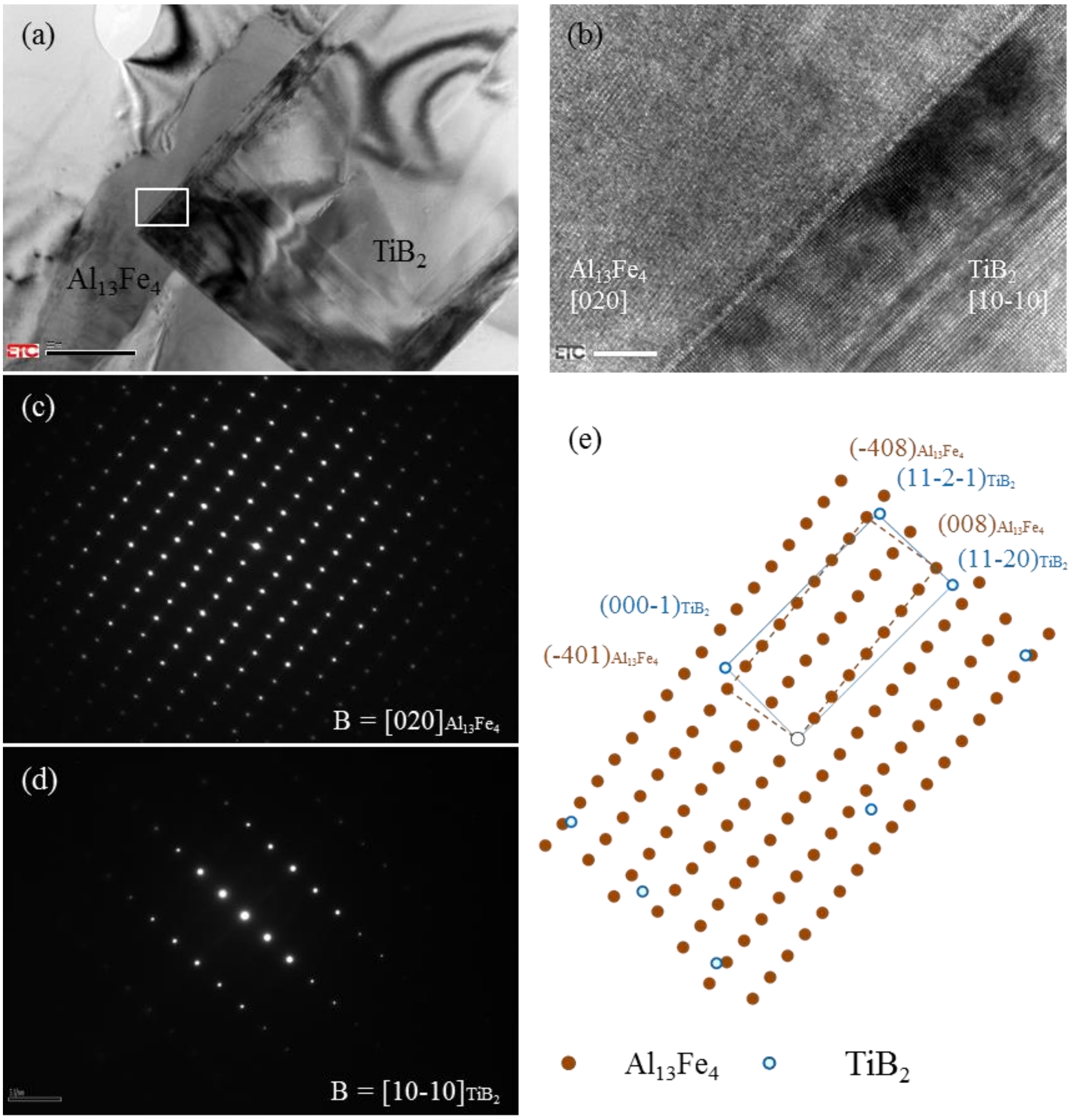

Figure 6.12 Transmission Electron Microscopy showing (a) the bright field image of local area of $Al_{13}Fe_4$ and it adjacent TiB_2 particle; (b) high resolution image of the interface (white rectangle in (a)) of $Al_{13}Fe_4$ (top-left) and TiB_2 particles (bot-right) when incident electron beam is parallel to both [10-10] of TiB_2 and [020] of $Al_{13}Fe_4$; (c) the SAED pattern of $Al_{13}Fe_4$ on the zone axis of [020]; (d) the SAED pattern of TiB_2 on the zone axis of [10-10]; and (e) a schematic illustration of SAED patterns that suggest an orientation relationship of (001)[020] $Al_{13}Fe_4$ // (11-20)[10-10] TiB_2 with a tilt angle of 5.4˚.

The crystallographic observation of TiB_2 particle in Al-5Mg-2Si-1.2Fe-0.7Mn alloy was conducted on CF sample in which there is a higher number density for both α-AlFeMnSi and TiB_2 particles. **Fig. 6.14a** is a bright field TEM micrograph showing faceted particles either embedded in the α-AlFeMnSi particle or at the α-AlFeMnSi/α-Al interface. TEM/EDS analysis suggested that the stoichiometry of faceted particle and its containing particle are TiB_2 and $Al_{12}(Fe,Mn)_3Si$, respectively. An example of crystallographic relation between the TiB_2 and α-AlFeMnSi is

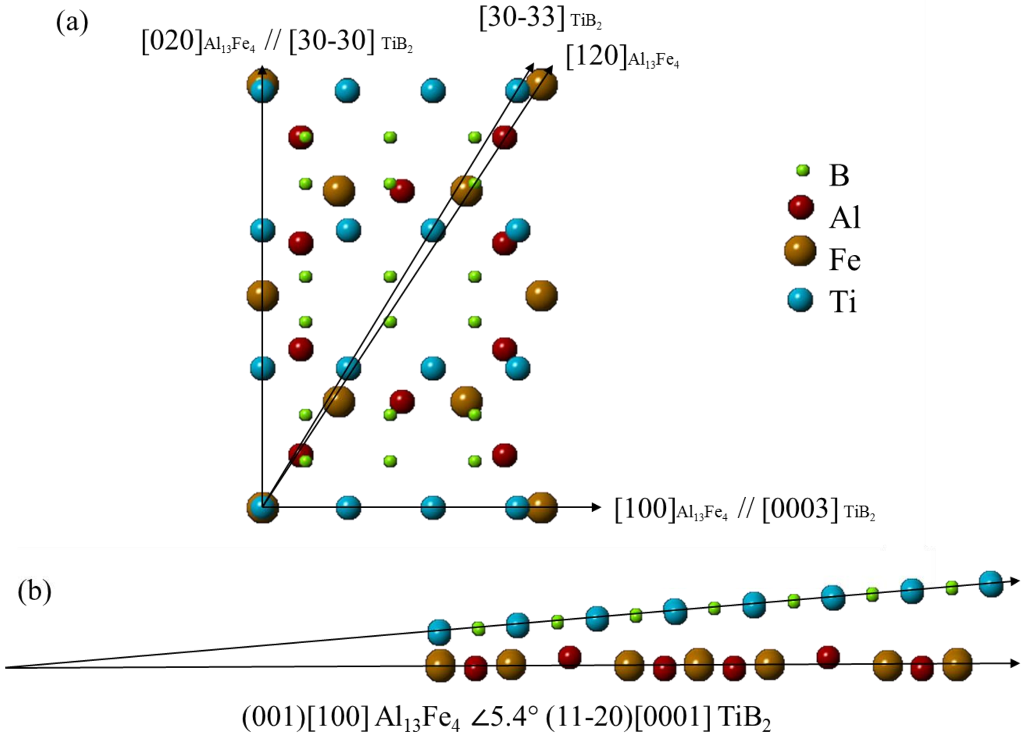

Figure 6.13 A schematic illustration for the nucleation of $Al_{13}Fe_4$ on (11-20) surface of TiB2 particle showing (a) atomic matching on (001) plane of $Al_{13}Fe_4$ and (11-20) plane of TiB_2 which has three orientation relationships indicated: [020] $Al_{13}Fe_4$// [10-10] TiB_2, [120] $Al_{13}Fe_4$// [10-11] TiB_2 and [100] $Al_{13}Fe_4$// [0001] TiB_2 with the lattice misfit of 1.6%, 4.2% and 8.8%, respectively; (b) an angle of 5.4° between the directions of (001)[100] $Al_{13}Fe_4$ and (11-20)[0001] TiB_2 viewing from [020] $Al_{13}Fe_4$ in (a). The boron, aluminium, iron and titanium atoms are marked as green, red, brown and blue spheres, respectively. The atom reconstruction was performed on Crystal Maker.

revealed by further TEM investigation showing that high resolution lattice image of TiB_2/α-AlFeMnSi interface area (**Fig. 6.14b**) where the incident beam is parallel to the [111] direction of α-AlFeMnSi (left) and [10-10] direction of TiB_2 (right), the SAED of α-AlFeMnSi on the orientation of [111] (**Fig. 6.14c**) and the SAED of TiB_2

on the orientation of [10-10] (**Fig. 6.14d**). For this TiB_2 and α-AlFeMnSi couple, **Fig. 6.13e** gives its schematic illustration of the orientation relationship:

(0-11) [111] α-AlFeMnSi // (0001)[10-10] TiB_2

with a twist angle 4.5˚ between the direction of (0-11) [111] α-AlFeMnSi // (0001)[10-10] TiB_2. The overlapped atomic arrangement on (0-11) plane of α-AlFeMnSi and (0001) plane of TiB_2 is twisted and shown in **Fig 6.15** to demonstrate the nucleation interface at atomic level. Only one layer of Fe atoms on (0-11) plane of α-AlFeMnSi and one player of Ti atoms on (0001) plane of TiB_2 were taken into the reconstruction in **Fig. 6.15a** as the effect from the second layer can be ignored; the nucleation interface of the multiplied basal plane of TiB_2 crystal cells and one atom layer on (0-11) plane of α-AlFeMnSi is shown in 3D in **Fig. 6.15b**. As indicated in **Fig. 6.15a** the TiB_2 atom arrangement on its (0001) plane was twisted 4.5˚ clockwise and matched with (0-11) plane of α-AlFeMnSi, showing calculated atomic misfits using atom spacing on two pairs of orientations:

OR1: (0-11)[100] α-AlFeMnSi // (0001)[-2110] TiB_2, $f_1 = -2.5\%$;

OR2: (0-11)[111] α-AlFeMnSi ∠4.5 (0001)[10-10] TiB_2, $f_2 = 3.02\%$.

6.4 Discussion

6.4.1 Formation of TiB_2 particle

There are two main methods to produce in-situ TiB_2, salts reaction (K_2TiF_6 + KBF_4) and master alloys reaction (Al-Ti + Al-B) (Emamy, Mahta and Rasizadeh, 2006; Han, Liu and Bian, 2002; Tee, Lu and Lai, 1999; Davies, Kellie and Wood, 1992). In this work, the latter was employed using the chemical composition on the boron rich side of stoichiometric TiB_2 (i.e. with a Ti/B weight ratio < 2.2) to prevent the adsorption replace each other to form $(Al,Ti)B_2$. However, Maxwell and Zupanic reported that of free Ti atom to TiB_2. Regardless of the production method, there is debate that, although TiB_2 is a thermodynamically stable phase, whether AlB_2 and TiB_2 exist as two separate phases or as a continuous solid solution, $(Al,Ti)B_2$, when there is excess B (Fjellstedt, Jarfors and Svendsen, 1999; Zupanič, Spaić and Križman, 1998a;

Arnberg, Backerud and Klang, 1982; Cornish, 1975; Maxwell and Hellawell, 1975b; Backerud, 1971). Cornish and Backerud have identified that Al or Ti atoms can the

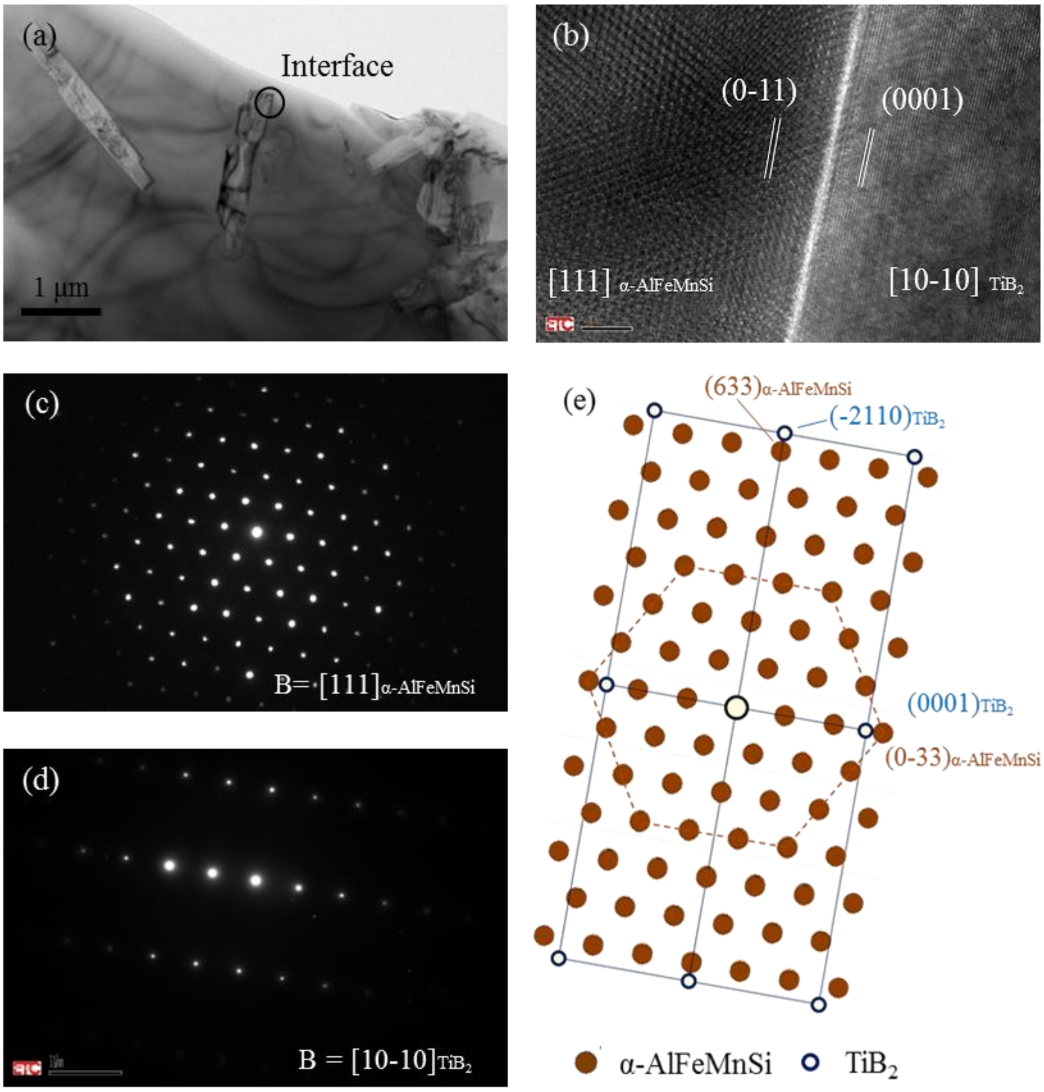

Figure 6.14 Transmission Electron Microscopy showing (a) the bright field image of faceted TiB_2 particles and a nucleated primary α-AlFeMnSi particle, (b) the high resolution image of the interface (indicated in (a)) of TiB_2 (right) and α-AlFeMnSi (left) particle s when the incident beam is parallel to both [10-10] of TiB2 and [111] of α-AlFeMnSi, (c) the SAED pattern of TiB_2 particle on the zone axis of [10-10] and (d) the SAED pattern of α-AlFeMnSi particle on the zone axis of [111]; (e) a schematic illustration of SAED patterns that suggest an orientation relationship of (0-11)[111] α-AlFeMnSi // (0001)[10-10] TiB_2. The experimental results shows that there is a 4.5° twist between (0001)[10-10] of TiB_2 and (01-1)[111] of α-AlFeMnSi. The stoichiometry is suggested to be $Al_{12}(Fe,Mn)_3Si$ by TEM/EDS.

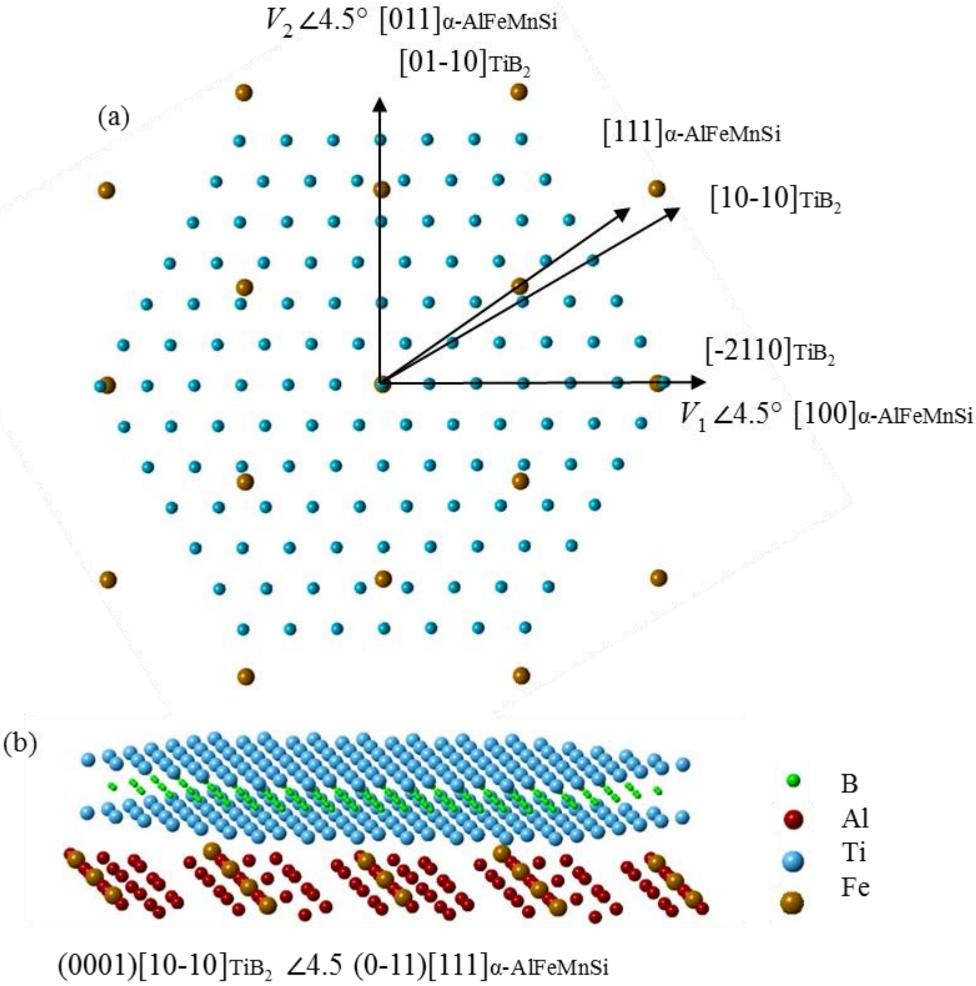

Figure 6.15 A schematic illustration for the nucleation of α-AlFeMnSi on (0001) surface of TiB2 particle showing (a) atomic matching on 4.5˚ clockwise twisted (0-11) plane of α-AlFeMnSi and (0001) plane of TiB_2 which has two orientation relationships indicated: *Vector 1 (V_1)* α-AlFeMnSi // [-2110] TiB_2, [111] α-AlFeMnSi // [10-10] TiB_2 with the lattice misfit of -2.50% and 3.02%, respectively; (b) 3D atomic matching (corresponding to (a)) of the interface of the basal plane multiplied TiB_2 crystal cells and one atom layer on (0-11) of α-AlFeMnSi. The boron, aluminium, iron and titanium atoms are marked as green, red, brown and blue spheres, respectively. The atom reconstruction was performed on Crystal Maker.

large particles and particles heat treated for a long-time tend to be close to AlB_2 and TiB_2 (Zupanič, Spaić and Križman, 1998a). Additionally, an update by Fan and co-workers suggest that alloying elements addition promotes thermodynamic stability of TiB_2 in Al-Ti-B-“X” system by affecting their activity coefficients (Fan, Yang and Zhang, 2005) , which is also adopted here to increase the stability of reaction product of current Al-Ti-B(Fe) master alloy. The potential reaction of this method should be:

$$AlB_2 + Al_3Ti \xrightleftharpoons{900^{\circ}C} TiB_2 + 4Al,\ \Delta G = -184.3\ \text{kJ/mol} \tag{R6.1}$$

or

$$Ti + AlB_2 \xrightleftharpoons{900^{\circ}C} TiB_2 + Al,\ \Delta G = -290.8\ \text{kJ/mol} \tag{R6.2}$$

The free energy calculation is based on PanAl2013 database using a temperature of 1173K. As shown in **Fig. 6.2**, the main peaks have confirmed predominant presence of TiB_2 or $(Al,Ti)B_2$, small amount of AlB_2 and a minor amount of Al_3Ti after 8 hours of reaction time. As suggested in **Fig. 6.4d**, the $(Al,Ti)B_2$ duplex particle has much higher Ti concentration on TiB_2 side, which tends to suggest that the $(Al,Ti)B_2$ duplex particle comprised of AlB_2 and TiB_2, instead of a continuous solid solution. However, it is difficult to eliminate the possibility that there is an insignificant amount of Ti replacing Al on the AlB_2 side of duplex particle. According to Zupanic (Zupanič, Spaić and Križman, 1998a), AlB_2 and TiB_2 should be the dominant stoichiometry of the borides, the existence of $(Al,Ti)B_2$ particles (**Fig. 6.4**) strongly indicates that there is no sufficient amount of free Ti to feed the reaction $Ti + B \leftrightarrow TiB_2$. Therefore, it is believed that, in the Al-Ti-B(Fe) master alloy, there is insufficient free Ti to form the 2D compound Al_3Ti on (0001) plane of TiB_2 particle (Fan *et al.*, 2015), which potentially allows the adsorption of other elements on TiB_2 surface. The quantification of product particles of the reactions is not conducted due to the difficulties in distinguishing TiB_2 and $(Al,Ti)B_2$.

6.4.2 Nucleation Potency of Modified TiB_2 for Primary α-AlFeMnSi

6.4.2.1 Comparison of Potential Nucleation Substrate

The interfacial energy at substrate/liquid (SuLi) interface plays a critical role during heterogeneous nucleation. However, a simple description of interfacial energy change and contact angle change is not enough to evaluate the nucleation potency of the specific substrate (Porter, Easterling and Sherif, 2009; Cao and Campbell, 2003; Bramfitt, 1970; Johnson Jr and Dettre, 1964). It has been commonly accepted that lattice mismatching at interface of substrate and nucleated solid can be used to evaluate the nucleation potency of the specific substrate: the higher the lattice mismatch, the lower the potency for heterogeneous nucleation. As shown in **Table**

6.1, the lattice parameters of substrate and nucleated crystals at 600˚C were calculated using the corresponding thermal expansion coefficients (Martienssen and Warlimont, 2006). For the present study, there are a few particles in alloy melt which could act as nucleation substrate for α-AlFeMnSi, such as MgAl$_2$O$_4$, MgO, γ-Al$_2$O$_3$ and TiB$_2$. **Table 6.1** gives the calculated lattice misfit values with the close-packed planes of α-AlFeMnSi and the substrates being parallel each other. It is obvious that the lattice misfit between the close-packed plane of the Fe-containing phases and

Table 6.1 Comparison of the lattice misfits between close-packed planes of potential substrate particles and α-AlFeMnSi.

Interface N/S	Crystal structure, Lattice parameter (nm)	OR: $(hkl)[uvw]_N$ // $(h'k'l')[u'v'w']_S$	Spacing $[uvw]$ (nm)	Spacing $[u'v'w']$ (nm)	*f* (%)
α-AlFeMnSi/ MgAl2O4	S: FCC, a=0.808(Martienssen and Warlimont, 2006)	(110)[111] // (100)[110]	1.088	2×0.571	-5.08
α-AlFeMnSi/ MgO	S: FCC, a=0.42(Martienssen and Warlimont, 2006)	(110)[111] // (001)[110];	1.088	4×0.298	-9.49
α-AlFeMnSi/ γ-Al$_2$O$_3$	S: FCC, a=0.792(Martienssen and Warlimont, 2006)	(110)[111] // (100)[110]	1.088	2×0.560	-0.30
α-AlFeMnSi/ TiB$_2$	S: HCP, a=0.302, c=0.322(Johnsson and Eriksson, 1998)	(110)[111] // (0001)[10-10]	1.088	2×0.523	3.85

* The “N” refers to Nucleation phase; the “S” stands for substrate.

** α-AlFeMnSi has a Body Centre Cubic (BCC) crystal structure with a lattice parameter of 1.256nm (Cooper, 1967).

TiB_2 is relatively small compared with the cases of MgO and $MgAl_2O_4$. Thus, TiB_2 is a potent substrate for the nucleation of primary α-AlFeMnSi in Al-Mg-Si-Fe-Mn system. γ-Al_2O_3 has an even smaller misfit with α-AlFeMnSi, but the nucleation might be severely restricted due to the highly agglomerated distribution γ-Al_2O_3.

In addition, considering the nearly identical crystal structure of TiB_2 (HCP, a=0.3028, c=0.3228 (Johnsson and Eriksson, 1998)), (Al,Ti)B_2 and AlB_2 (HCP, a=0.3010nm, c=0.3245nm (Hofmann and Jäniche, 1936)), the potencies in terms of lattice mismatching for potential nucleation on these particles in the master alloy are considered essentially the same.

6.4.2.2 Atom Arrangement of Nucleation Interface

Misfit, commonly used to evaluate the nucleation potency, indicates the perfectness of the lattice matching, but it doesn't necessarily consider the atomic matching at the interface. For complex crystal system, such as intermetallic compounds which sometime has pseudo-symmetry (Hwang, Doty and Kaufman, 2008; Black, 1955), lattice structure parameters are not enough to represent the real situation of atom arrangement at nucleation interface (Cooper, 1967; Black, 1955). The edge-to-edge matching model proposed by Zhang and Kelly (Zhang and Kelly, 2005a) and the epitaxial nucleation model proposed by Fan (Fan, 2013) consider the role of the atom arrangement during the nucleation event. Atomic matching of $Al_{13}Fe_4$ and TiB_2 interface on three directions is illustrated in **Fig. 6.13**, showing small misfits of 1.6%, 4.2% and 8.8% on all three directions, which are (001)[020] $Al_{13}Fe_4$ // (11-20)[10-10] TiB_2, (001)[120] $Al_{13}Fe_4$ // (11-20)[10-11] TiB_2 and (001)[100] $Al_{13}Fe_4$ // (11-20)[0001] TiB_2. This strongly suggests a good nucleation potency of TiB_2 for $Al_{13}Fe_4$. For the nucleation of α-AlFeMnSi on the {0001} surface of TiB_2 particle, as shown in **Fig. 6.15**, atomic matching on three directions have been indicated suggesting two small misfits of -2.5% and 3.0% on the directions of (0-11)[111] α-AlFeMnSi // (0001)[10-10] TiB_2 and (0-11)[100] α-AlFeMnSi // (000)[-2110] TiB_2. However, as shown in **Table 6.2**, misfits calculated with lattice parameters and crystal structures disagrees with the misfit calculation based on the atom arrangement on the nucleation interfaces. It appears that, on the orientation matches confirmed with TEM, the atomic misfit tends to be smaller compared with the lattice misfit. This suggests that the structure templating plays a crucial role at accommodating through twist in the lattice when the lattice misfit (**Table 6.2**) is large, which consequently leads to a significant misfit decrease between the substrate and nucleating phase. Thus, the heterogeneous nucleation of $Al_{13}Fe_4$ on TiB_2 and α-AlFeMnSi on TiB_2 can be significantly facilitated by the lattice twisting.

6.4.2.3 Adsorption of Fe on TiB_2

In nucleation behaviour investigation, the elemental segregation is an essential consideration. The Fe enrichment on the surface of $(Al,Ti)B_2$ particle, as shown in **Fig. 6.4b,** clearly suggests Fe segregation on the $(Al,Ti)B_2$/α-Al interface. Similar segregation behaviours were observed in many systems (Yu *et al.*, 2012; Jiang and Carter, 2005; Belton, 1976; Gibbs, 1906). According to application of Gibbs adsorption rule in liquid metal system (Belton, 1976; Gibbs, 1906), metallic solute atoms in the alloy melt is very like to segregate to the L/N interface if this segregation leads to a reduction of surface energy. According the equilibrium binary Al-Fe phase diagram, the $Al_{13}Fe_4$ is stable when Fe concentration is higher than 0.052wt.% which is surpassed by Fe content (0.5wt.%) in current Al-Ti-B(Fe) master alloy. Similar to the Ti adsorption on TiB_2 particles (Fan *et al.*, 2015), when the master alloy was added to the alloy, this Fe segregation layer should still be relatively stable because of the 1.2wt.% Fe content in the alloy. Therefore, the adsorption of Fe at liquid/solid interface should be thermodynamically preferred as it

Table 6.2 Comparisons of lattice mismatching and atomic mismatching on the nucleation interface of Fe-IMCs and TiB_2 substrates.

Interface: (001) $Al_{13}Fe_4$ // (11-20) TiB_2			**Interface: (0-11) α-Fe // (0001) TiB_2**		
Orientations matches	**Lattice misfit(%)**	**Atomic misfit(%)**	**Orientations matches**	**Lattice misfit(%)**	**Atomic misfit(%)**
[020]//[10-10]	-1.6	1.6	[100]//[-2110]	1.91	-2.5
[100]//[0001]	-24.7	8.8	[111]//[10-10]	6.6	3.0
[120]//[10-11]	-17.6	4.2	-	-	-
* α-AlFeMnSi is denoted as α-Fe. ** The lattice parameters of TiB_2, $Al1_3Fe_4$ and α-AlFeMnSi are collected from (Johnsson and Eriksson, 1998), (Black, 1955) and (Cooper, 1967), respectively.					

reduces the interfacial energy. As shown in **Fig. 6.3**, the plane spacing of the adsorption atomic layer to AlB_2 surface was different from the plane spacing on (10-10) of AlB_2 or $(Al,Ti)B_2$. Considering the HRTEM results, the Fe-rich atomic layer potentially have $Al_{13}Fe_4$ atom arrangement. Thus, due to the well-matched Fe-rich atom layer the nucleation potency of the TiB_2 is presumably changed, which is likely to be the factor that facilitates the nucleation of primary α-AlFeMnSi during CF and quartz tube water quench (TQ) experiment.

6.4.2.4 Composition Templating

The composition templating is a crucial parameter for heterogeneous nucleation potency other than structure templating (between Nucleation phase and substrate). TiB_2 were often added to Fe-containing Al alloys, and some claimed that these additions influence the nucleation of Fe-IMCs. However, no refinement comparable to the refinement achieved in present research has been reported (Khalifa *et al.*, 2005; Allen *et al.*, 1999). As shown in the experimental result in **Fig. 6.14** crystallographic orientation relationship observed between TiB_2 and α-AlFeMnSi suggests that modified TiB_2 (**Fig. 6.3**) particles act as a nucleation substrate for primary α-AlFeMnSi. This suggests that the Fe adsorption likely reduced the interfacial energy between TiB_2 and α-AlFeMnSi and that between TiB_2 and liquid Al. This creates a more favourable condition for engulfing TiB_2 particle into the growing α-AlFeMnSi after the nucleation. The observed twist angle of 4.5˚ between [111] and [10-10] direction on the (0-11) α-AlFeMnSi // (0001) TiB_2 planes, suggested that there was a relatively large lattice misfit between Fe modified TiB_2 and α-AlFeMnSi according to epitaxial nucleation mechanism (Men and Fan, 2014; Fan, 2013). For the heterogeneous nucleation on the substrates with a relatively large misfit, the first layer of the solid accommodates the majority of the lattice misfit through the formation of an edge dislocation network; and the second layer of the solid can twists a specific angle relative to the first layer along the normal of the substrate through the formation of screw dislocations to minimise the lattice distortion caused by dislocation network in the first layer (Men and Fan, 2014). Due to the complexity of α-AlFeMnSi lattice cell, the lattice misfit which is slightly different from the atomic mismatching on the (0-11)[111] α-AlFeMnSi $\angle 4.5$ (0001)[10-10] TiB_2 is 4.9%, which is relatively large in terms of heterogeneous nucleation. This is in good agreement with Molecular Dynamics (MD) simulation of heterogeneous nucleation, which showed that a twist of 4-5° is required for heterogeneous nucleation with a lattice misfit of 5% (Men and Fan, 2014); it should be noted that this crystallographic analysis of lattice misfit does not take any consideration of the Fe segregation on the TiB_2 surface, which is expected to modify the lattice misfit in practical cases.

6.4.3 Efficiency of Nucleation Substrate

Nucleation efficiency, as another critical factor for a nucleation event, is used to describe the fraction of the particles participating in grain initiation out of the total number of available particles during the entire solidification process (Fan *et al.*, 2015; Fan, 2013; Li, Wang and Fan, 2012; Quested and Greer, 2004; Greer *et al.*, 2000). It evaluates the potent substrate number density, size, size distribution and cooling rate (Li, Wang and Fan, 2012; Men, Jiang and Fan, 2010; Easton and StJohn, 2001; Greer *et al.*, 2000). For instance, the oxides in Al or Mg alloys are often in the form of both films and agglomerate, which leads to very low nucleation efficiency (Li, Wang and Fan, 2012).

6.4.3.1 Comparison of Nucleation Substrates

When Al-Ti-B(Fe) is added to the system, TiB_2 is not the only particles and also Al_3Ti, AlB_2, $(Al,Ti)B_2$ and $Al_{13}Fe_4$, are introduced to the Al alloy melt. The nucleation potency of a substrate includes structure templating (misfit) and composition templating (element adsorption) (Fan, 2013). For the relatively structural potent oxide particles (small Nucleus/Substrate lattice misfit), microstructure observation (**Fig. 6.1** and **Fig. 6.6**) and XRD analysis (**Fig. 6.2**) suggest that there is limited amount of oxides films that are present next to cracks and agglomerates on the grain boundaries in the Al-Ti-B(Fe) and Al-5Mg-2Si-1.2Fe-0.7Mn alloys; this indicates an poor nucleation efficiency of these oxides as these structural potent particles rarely participated in the nucleation of α-AlFeMnSi. Thus, despite the considerable structural potency for α-AlFeMnSi, the oxides' contribution to facilitating nucleation of α-AlFeMnSi is ruled out of consideration. As shown in **Fig. 6.1**, TiB_2 evenly distributed in the microstructure due to the constant stirring and rapid cooling, whereas AlB_2 mainly exist in agglomerates. Fe modified TiB_2 is the principle factor that contribute to the nucleation enhancement shown in **Fig. 6.5**. Due to poor composition templating, oxides were hardly observed to nucleate α-AlFeMnSi.

As discussed previously, the Al_3Ti has been mostly consumed during the master alloy preparation by $2Ti + B \rightleftharpoons TiB_2$; therefore the effect of Al_3Ti to the refinement can be ignored. Some reports show that $Al_{13}Fe_4$ can be the seed for the nucleation for other Fe-IMCs (Khalifa, Samuel and Gruzleski, 2003; Kuijpers *et al.*, 2003; Hsu *et al.*, 2001), such as, β-AlFeSi, α_h-AlFeSi and α-AlFeMnSi when there is Mn content. Given the considerable refinement of primary α-AlFeMnSi by Al-Ti-B(Fe) addition, the Fe adsorption layer on borides is highly likely to have the structure of $Al_{13}Fe_4$, and the nucleation of α-AlFeMnSi can be facilitated with the presence of this adsorption layer.

6.4.3.2 Involvement of Multiple TiB_2 during Growth

As established previously, Fe modified TiB_2 has a good nucleation potency including good structure templating and composition templating for α-AlFeMnSi. The modified TiB_2 particle was considered to have relatively good nucleation efficiency as they were fully wetted and uniformly distributed compared with other potential substrates. Additionally, the coexistence of TiB_2 and primary α-AlFeMnSi (**Fig. 6.10, 5.11, 5.12a** and **5.14a**) strongly suggests a nucleation relationship between TiB_2 and primary α-AlFeMnSi. The orientation relationship (**Fig. 6.14**) and good atomic matching (**Fig. 6.15**) on the TiB2/α-AlFeMnSi interface further confirms that the potent TiB_2 was active during nucleation of α-AlFeMnSi under slow cooling rate (<3.5K/s).

Meanwhile, it is very important to address the embedding of multiple TiB_2 particles in one primary α-AlFeMnSi particle. Generally, one substrate should be enough for the nucleation of one particle, unless there is fragmentation which does not need a nucleation substrate. As shown in **Fig. 6.6f**, **5.6h**, **5.11b** and **5.14**, there are multiple TiB_2 particles embedded in one primary α-AlFeMnSi. It is a common phenomenon for composite alloys where the composite particles ejected into the inter-dendritic regions, which show the microstructure of multiple particles embedded in dendritic grain. However, as established in **Chapter 4**, α-AlFeMnSi as a faceted particle show a strong anisotropy on some specific orientations, such as <111> (**Fig. 4.4** and **Fig.**

4.5); which is highly likely to lead to the capture of solid particles during the growth. Especially, when there is TiB_2 cluster neighbouring the substrate TiB_2 particle, the TiB_2 agglomerates forms within the primary α-AlFeMnSi particle. Therefore, the TiB_2 clusters neighbouring the substrate TiB_2 and the growth mechanism of faceted primary α-AlFeMnSi result in the excess TiB_2 particles trapped within the primary α-AlFeMnSi.

6.4.4 Nucleation Behaviour of α-AlFeMnSi by Inoculation of Modified TiB_2

6.4.4.1 Undercooling

Undercooling is one of the common factors that characterise the substrates' nucleation ability. The maximum undercooling can be significantly decreased when there is a potent nucleation substrate; and it can be further reduced if the potent substrate has good nucleation efficiency (Men and Fan, 2011; Men, Jiang and Fan, 2010; Quested and Greer, 2004; Greer *et al.*, 2000; Becker and Döring, 1935). As shown in **Fig. 6.8** and **5.9**, large amount primary α-AlFeMnSi was first observed in sample quenched from 655˚C with Al-Ti-B(Fe) addition, whereas good amount (0.9% in volume fraction) of primary α-AlFeMnSi only starts to be observed in 650˚C quenched sample in reference alloy. The **Fig. 6.9** shows that the number density increase of primary α-AlFeMnSi is a continuous process after the first nucleation event, indicating a continuous nucleation event. It suggests that the nucleation commence at around 650˚C for α-AlFeMnSi in reference alloy and 655˚C for the alloy with Al-Ti-B(Fe) addition. In other words, the nucleation undercooling for primary α-AlFeMnSi was reduced by the Al-Ti-B(Fe) inoculation changing from 20-15K to 15-10K at 0.15K/s cooling rate suggesting approximately 5K reduction in undercooling for the solidification of primary α-AlFeMnSi. **Fig. 6.9** shows that the number density increase significantly slows at 650˚C and 645˚C in the alloys with and without Al-Ti-B(Fe) addition, respectively. This phenomenon is considered to be a result of solute concentration reduction during the continuous solidification of primary α-AlFeMnSi leading the phase diagram drifting to the Al-rich side. Therefore, the undercooling required to activate more nucleation site cannot be met as liquid temperature decreases. Additionally, the solute diffusion in the induction furnace experiment (0.15K/s) is considered less efficient compared with cooling in furnace experiment (0.02K/s), and the solute consumption during the solidification of primary α-AlFeMnSi should be lower at a higher cooling rate at the sample temperature. Thus, higher cooling rate can provide a larger undercooling when liquid temperature was the same, which leads to activation of many more nucleation site for primary α-AlFeMnSi. As a result the number density of primary α-AlFeMnSi in the alloy with Al-Ti-B(Fe) addition at 0.15K/s (**Fig. 6.9**) was 9.2/mm^2 with is higher than 1.09±0.02/mm^2 when cooling rate was 0.02K/s (**Fig. 6.7**).

6.4.4.2 Kinetics

The experimental observation (**Fig. 6.5**, **Fig. 6.6** and **Fig. 6.7**) of primary α-AlFeMnSi show that with Al-Ti-B(Fe) addition the average size can be reduced to less than half of that obtained in the reference and the number density can be increased considerably. When cooling in furnace at a cooling rate of 0.02K/s (**Fig. 6.7**), the number density of primary α-AlFeMnSi increased 20 times by Al-Ti-B(Fe) addition, however the number density of primary α-AlFeMnSi only increased by 2 times when cooling in induction furnace at a cooling rate of 0.15K/s (**Fig. 6.9**). This refinement effect is apparently not as significant as the effect of Al-5Ti-1B grain refiner for Al alloys. It is neither comparable to the grain refinement effect of well dispersed oxide particles in both Al- and Mg- alloys (Li, Wang and Fan, 2012; Men, Jiang and Fan, 2010; Greer *et al.*, 2000). For such a complex nucleation substrate, α-AlFeMnSi, and sophisticated nucleation grain refiner, Al-Ti-B(Fe), there are a few possible factors leading to this ineffective refinement result. Firstly, as the adsorption of liquid atoms on solid surface is a slow and kinetic dependent process (Cantor, 2003; Kim and Cantor, 1994; Gibbs, 1906), 8 hours of reaction and holding time at 900°C may not allow sufficient time for both formation of TiB_2 and Fe adsorption on TiB_2 surface, which leads to a poor potency to not fully modified TiB_2 or AlB_2 particles. Secondly, the relatively large formation free energy barrier means that the primary α-AlFeMnSi needs either relatively larger undercooling or relatively larger substrate even when the substrate is potent. Thus, the formation of a stable nucleation embryo of α-AlFeMnSi may be difficult due to the complex diffusion process and solute interaction at the local area during the formation of a stable nucleation embryo for α-AlFeMnSi. Therefore, with CF condition (0.02K/s) where there is a longer diffusion time for solute atoms compared with that of 0.15K/s, the nucleation embryo is more likely to become stable and start free growth. Thus, it is suggested that the enhanced nucleation of primary α-AlFeMnSi with modified TiB_2 addition are significantly facilitated due to the interfacial energy reduction and the diffusion and interactions of solute elements played a critical role at the nucleation of primary α-AlFeMnSi on the potent substrate.

6.5 Summary

In this chapter, the effect of Fe modified TiB_2 and $(Al,Ti)B_2$ particle in the novel Al-Ti-B(Fe) grain refiner for Fe-IMCs on the nucleation behaviours of primary α-AlFeMnSi in Al-5Mg-2Si-1.2Fe-0.7Mn alloy was described. Fe adsorption was observed with HR-TEM on the surface of $(Al,Ti)B_2$ particle in this novel grain refiner, which exists as zigzag fashion on the prismatic plane surface of the boride particle. With the addition of 2wt.% Al-Ti-B(Fe), under a cooling rate of 0.02K/s the average primary α-AlFeMnSi particle size reduced by 57.3% from 251.3±75.3μm to 110.9±45.5μm and the primary α-AlFeMnSi particle density increased by 20 times from 0.05±0.004/mm^2 to 1.09±0.02/mm^2 in the entire sample. Meanwhile, with a cooling rate of 0.15K/s the Al-Ti-B(Fe) addition reduced the average primary α-AlFeMnSi particle size by 40.0% from 127.3±36.2μm to 76.5±18.9μm and increase primary α-AlFeMnSi particle density by approximately 3 times from 2.5/mm^2 to 10.2/mm^2. At a cooling rate of 0.15K/s, the formation temperature of large fraction of primary α-AlFeMnSi particle increased from 650˚C to 655˚C by Al-Ti-B(Fe) addition, suggesting a nucleation undercooling decrease by 5K from 20K to 15K by Al-Ti-B(Fe) addition. In these nucleation enhanced Fe-IMC particles, TiB_2 particles are often found within or alongside of Fe-IMC particles with SEM and TEM. Some orientation relationships between TiB_2 and Fe-IMCs were found to be:

$$(001)[020]\ Al_{13}Fe_4\ //\ (11\text{-}20)[10\text{-}10]\ TiB_2,\ f_1 = 1.6\%;$$
$$(001)[120]\ Al_{13}Fe_4\ \angle 6.05^\circ\ (11\text{-}20)[10\text{-}11]\ TiB_2,\ f_2 = 4.2\%;$$

and

$$(0\text{-}11)[100]\ \alpha\text{-}AlFeMnSi\ //\ (0001)[\text{-}2110]\ TiB_2,\ f_1 = \text{-}2.5\%;$$
$$(0\text{-}11)[111]\ \alpha\text{-}AlFeMnSi\ \angle 4.5^\circ\ (0001)[10\text{-}10]\ TiB_2,\ f_2 = 3.0\%.$$

The misfit was calculated with atomic mismatching instead of lattice mismatching based on the crystal structure of α-AlFeMnSi and TiB_2. The structure templating of $Al_{13}Fe_4$ by the (11-20) TiB_2 plane and α-AlFeMnSi by the TiB_2 (0001) leads to the twist of 6.1° and 4.5° of α-AlFeMnSi, respectively. The segregation of Fe on TiB_2 surface provides composition templating and hence enhances the heterogeneous nucleation of the α-AlFeMnSi phase resulted in a considerable refinement of α-AlFeMnSi under controlled solidification.

Chapter 7 Conclusions

1. Using conventional castings, the predominant primary and eutectic Fe-IMC in Al-5Mg-2Si-1.2Fe-0.7Mn alloy are identified as α-AlFeMnSi, which has a BCC crystal structure and a lattice parameter of a=1.256nm. The nucleation of primary α-AlFeMnSi prefers to occur at a cooling rate ≤0.8K/s independent of casting temperature. Otherwise, eutectic α-AlFeMnSi will be the dominant Fe-IMC.

2. The formation of eutectic α-AlFeMnSi is dependent on the primary α-AlFeMnSi. When primary α-AlFeMnSi forms, the eutectic α-AlFeMnSi/α-Al is found to nucleate on primary α-AlFeMnSi initiated with eutectic α-AlFeMnSi branches nucleate on primary α-AlFeMnSi. When primary α-AlFeMnSi does not form, the α-Al nucleates first and then α-AlFeMnSi eutectic nucleates as the critical undercooling and solute concentration for its nucleation are satisfied, which eventually leads to a non-primary α-AlFeMnSi microstructure.

3. The volume fraction of primary α-AlFeMnSi and eutectic α-AlFeMnSi are effectively manipulated with vary casting temperatures. In Al-5Mg-2Si-1.2Fe-0.7Mn alloy, lower casting temperatures result in a significant increase in volume fraction of primary α-AlFeMnSi from 0.2±0.1vol.% when casting at 680˚C to 3.6±0.5vol.% at 630˚C in TP-1 casting. As a consequence of solute atom consumption by the formation of primary α-AlFeMnSi, the volume fraction of eutectic α-AlFeMnSi decreases from 6.3±0.3vol.% to 3.4±0.3% as the casting temperature decrease from 680˚C to 630˚C. Meanwhile the overall volume fraction of α-AlFeMnSi remained constant.

4. The size and composition of Fe-IMCs is significantly affected by cooling rate. In Al-5Mg-2Si-1.2Fe-0.7Mn alloy with a casting superheat (e.g. 20K), the size of primary α-AlFeMnSi increases gradually from 24.5±3.1μm to 251.3±75.3μm as the cooling rate decreases from 870K/s to 0.02K/s. At the meantime, the size of α-AlFeMnSi eutectic increases gradually from 102.0±12.1μm to 623.3±157μm. The Fe and Mn concentration in α-AlFeMnSi appears to be reduced by increased

cooling rate. The is due to the relatively insufficient solute supply when solute concentration is low (e.g. 1.2wt.% Fe and 0.7wt.% Mn)

5. Primary α-AlFeMnSi phase grows with a star-like morphology in the early stage in 2D and then faceted growth starting at the "star-tips" until the faceted planes are connected. <111> directions of the primary α-AlFeMnSi crystal are the preferred growth orientations, resulting in rhombic dodecahedral morphology in 3D when the growth is completed. For this phase the four- and five-sided polyhedral morphology in also observed 2D.

6. The Mg content significantly influences the morphology of α-Al in both Al-1.2Fe-0.7Mn-*x*Mg (T3) and Al-2Si-1.2Fe-0.7Mn-*y*Mg (Q4) alloys. The grain size of α-Al decreased from 1336±209μm to 513±80μm as Mg content increased from 0.004wt.% to 6.04wt.%) in T3 alloy and from 1233±238μm to 945±68μm as Mg content increased from 0.04wt.% 5.41wt.% in Q4 alloy. Meanwhile, the secondary arm spacing decreased gradually from 41.9±6.6μm to 24.2±5.0μm as Mg content increases from 0.004wt.% to 6.04wt.%) in T3 alloy and from 32.1±4.6μm to 19.3±2.3μm as Mg content increases from 0.04wt.% 5.41wt.% in Q4 alloy.

7. The Mg content can significantly alter the morphology of Fe-IMCs, especially Al_6(Fe,Mn) in Al-1.2Fe-0.7Mn-*x*Mg alloy. The increasing Mg content additively changes Al_6(Fe,Mn) from a needle-like morphology to a lamellar morphology. As the consequence of the Mg segregation at the Al_6(Fe,Mn)/liquid interface, an Mg-rich enrichment region forms in at the Al_6(Fe,Mn)/α-Al interface with thickness of 5-20nm. This morphology change is caused by severe solute segregation of Mg at the preferred growth direction compared with perpendicular direction.

8. The addition of Mg content increased the Fe-IMC eutectic lamellar spacing in Al-1.2Fe-0.7Mn-*x*Mg alloys the eutectic lamellar spacing increased from 1.3±0.3μm to 2.9±0.8μm as Mg content increased to 6.0wt.%. In Al-2Si-1.2Fe-0.7Mn-*y*Mg, the eutectic lamellar spacing increased from 1.4±0.3μm to 3.3±0.8μm at the Mg content increased to 5.4wt.%. This is because non-ideal

Fe-Mg interaction when Mg is added to the alloy and the difference in diffusion efficiency of various elements.

9. Fe segregation on TiB_2 surface has been deliberately achieved by in-situ reaction of Al-Ti-B(Fe) master alloy at high temperature. HR-TEM reveals that the Fe adsorption on in-situ $(Al,Ti,)B_2$ particle in this master alloy is in a zigzag fashion on the prismatic plane surface of the boride particle. Such adsorption on the nucleation catalyst surface facilitates the composition templating to enhance the heterogeneous nucleation process of Fe-IMCs.

10. The surface modified TiB_2 particles is an effective nucleation catalyst for α-AlFeMnSi under controlled solidification. With the addition of 2wt.% Al-Ti-B(Fe) (nominally 1500ppm TiB_2), average particle size of the primary α-AlFeMnSi is reduced by 57.3% from 251.3±75.3μm to 110.9±45.5μm under a cooling rate of 0.02K/s. At the same time, particle's number density of the primary α-AlFeMnSi is increased by 20 times from $0.05 \pm 0.004/mm^2$ to $1.09 \pm 0.02/mm^2$ in the entire sample.

11. The surface modified TiB_2 appears to be relatively moderate on the grain refinement of primary α-AlFeMnSi at a higher cooling rate (0.15K/s). With the addition of 2wt.% Al-Ti-B(Fe) master alloy, at a cooling rate of 0.15K/s the primary α-AlFeMnSi particle size reduced by 40% from 127.3±36.3μm to 76.5±18.2μm and the primary α-AlFeMnSi particle number density can be increased by approximately 4 times from $2.5/mm^2$ to $10.2/mm^2$. Meanwhile, in this specific Al-5Mg-2Si-1.2Fe-0.7Mn alloy, nucleation undercooling decreases by 5˚C from 20˚C to 15˚C by Al-Ti-B(Fe) addition.

12. TiB_2 particles are frequently found within Fe-IMCs particle in Al-Ti-B(Fe) master alloy. Specific orientation relationships between the TiB_2 and the Fe-IMCs:
    (001)[020] $Al_{13}Fe_4$ // (11-20)[10-10] TiB_2, $f_1 = 1.6\%$;
    (001)[120] $Al_{13}Fe_4$ ∠6.05˚ (11-20)[10-11] TiB_2, $f_2 = 4.2\%$;

13. TiB_2 particles are frequently found within refined Fe-IMCs particle in Al-5Mg-2Si-1.2Fe-0.7Mn alloy with Al-Ti-B(Fe) master alloy. Specific orientation relationships between the TiB_2 and the Fe-IMCs:

    (0-11)[100] α-AlFeMnSi // (0001)[-2110] TiB_2, f_1 = -2.5%;
    (0-11)[111] α-AlFeMnSi ∠4.5° (0001)[10-10] TiB_2, f_2 = 3.02%.

14. This research offers new understandings on the nucleation and growth of Fe-IMCs and grain refinement approaches for α-AlFeMnSi for optimising the morphology of Fe-IMCs in Fe-containing Al alloys. By implementing these approaches, the optimised Fe-IMC morphology in microstructure secondary Al alloys is able to offer a promising the mechanical performance.

Chapter 8 Suggestions for Further Work

In the thesis, the nucleation and growth behaviour of both α-AlFeMnSi and Al_6(Fe,Mn) with and without additional Al-Ti-B(Fe) have been discussed in order to further the understanding on the solidification behaviour of these Fe-IMCs. The effect of cooling rate on the nucleation of primary α-AlFeMnSi and Al_6(Fe,Mn) was investigated. The results show that the nucleation of both primary α-AlFeMnSi and Al_6(Fe,Mn) requires large undercooling and slow cooling rate compared with pure liquid or solid solution and the nucleation of eutectic α-AlFeMnSi and Al_6(Fe,Mn) tend to initiate from the corresponding primary Fe-IMC particles. Additionally, the formation of compact primary α-AlFeMnSi can significantly reduce the volume fraction of coarse eutectic α-AlFeMnSi. The deep-etching technique developed in home successfully reveal 3D morphology of Fe-IMCs, which significantly facilitate the understanding on the anisotropic growth mechanism of Fe-IMCs. Mg is introduced to the Al_6(Fe,Mn) and α-AlFeMnSi containing alloys for the understanding of solute on the solidification behaviours of Fe-IMCs. The result shows that Mg content can cause growth restriction on Fe-IMC's, especially on their preferred growth directions. A novel Al-Ti-B(Fe) grain refiner for enhancing the homogeneous nucleation of Fe-IMCs is developed. Fe segregation layer was revealed by HRTEM on surface of $(Al,Ti)B_2$ in the grain refiner. The results show that in controlled solidification primary the Al-Ti-B(Fe) addition can significantly refines the primary α-AlFeMnSi. The refinement mechanism has been discussed in detail to provide further understanding of the structure templating and composition templating for the heterogeneous nucleation.

The critical cooling rate for the nucleation of primary α-AlFeMnSi in the alloys different Fe composition: The formation of compact primary α-AlFeMnSi can reduce the volume fraction of eutectic α-AlFeMnSi with a coarse Chinese-script morphology. The further investigation of these parameters can be beneficial to optimising the microstructure of Fe-containing secondary Al alloys. Further study on the effect cooling rate on the nucleation of Fe-IMCs is constructive for understanding the nucleation kinetics for Fe-IMCs.

Identification of crystal growth orientation for both eutectic α-AlFeMnSi and Al_6(Fe,Mn): Unlike the irregular eutectics, the growth Fe-IMC eutectics appears be initiate from primary Fe-IMCs. A study can provide further understanding on the crystals with great growth anisotropy, such as Fe-IMCs.

High resolution TEM observation on the TiB_2/α-AlFeMnSi interface for the adsorption layer: the adsorption layer was observed in Al-Ti-B(Fe) grain refiner, however the direct evidence is locking for the adsorption layer on the nucleating substrate. The structure of this adsorption has to be understood in order to gain a better understanding on composition templating for heterogeneous nucleation.

Grain refinement of Al-Ti-B(Fe) grain refiner for other Fe-IMCs: currently, the grain refinement was only been achieved on primary α-AlFeMnSi in during controlled solidification. Achieving grain refinement of various Fe-IMCs can be very important for further understanding on heterogeneous nucleation as well as any potential applications.

Optimising the effectiveness of the Al-Ti-B(Fe) grain refiner: the study on the grain refinement effectiveness has been preliminary. It is very important to be able to add minor amount of inclusion particles and achieve good grain refinement. This is crucial for any potential industrial application.

Mechanical property evaluation of secondary Al alloys with Al-Ti-B(Fe) grain refiner addition: present study mainly focus on theoretical study on the solidification behaviour of Fe-IMCs. The mechanical property improvement by Al-Ti-B(Fe) grain refine addition should be investigated in order to make the grain refiner reliable for the applications using secondary Al alloys.

References

Abedi, K. and Emamy, M. (2010) 'The effect of Fe, Mn and Sr on the microstructure and tensile properties of A356–10% SiC composite', *Materials Science and Engineering: A*, 527(16), pp. 3733-3740.

Adam, C.M.L. and Hogan, L. (1972) 'The aluminum-iron eutectic system', *Journal of the Australian Institute of Metals*, 17(2), pp. 81-90.

Alexander, D. and Greer, A. (2004) 'Nucleation of the Al6 (Fe, Mn)-to-α-Al–(Fe, Mn)–Si transformation in 3XXX aluminium alloys. I. Roll-bonded diffusion couples', *Philosophical Magazine,* 84(28), pp. 3051-3070.

Alexander, D. and Greer, A. (2002) 'Solid-state intermetallic compound phase tranformations in 3XXX aluminium alloys', *Acta Materialia,* 50(10), pp. 2571-2583.

Allen, C., O'reilly, K., Cantor, B. and Evans, P. (1998) 'Intermetallic compound phase selection in 1XXX Al alloys', *Progress in Materials Science*, 43(2), pp. 89-170.

Allen, C., O'Reilly, K., Evans, P. and Cantor, B. (1999) 'The effect of vanadium and grain refiner additions on the nucleation of secondary phases in 1xxx Al alloys', *Acta materialia*, 47(17), pp. 4387-4403.

Aluminium Association (1987) 'Standard Test Procedure for Aluminium Alloy Grain Refiners: TP-1', *The Aluminium Association, Washington DC*.

Arnberg, L., Backerud, L. and Klang, H. (1982) '1: Production and properties of master alloys of Al–Ti–B type and their ability to grain refine aluminium', *Metals Technology*, 9(1), pp. 1-6.

Backerud, L. (1971) 'On the Grain Refining Mechanism in Al-Ti-B Alloys', *Jernkontorets Ann.*, 155(8), pp. 422-424.

Backerud, L., Chai, G. and Tamminen, J. (1990) 'Solidification characteristics of aluminum alloys. Vol. 2. Foundry alloys', *American Foundrymen's Society, Inc., 1990,* pp. 266.

Baker, J.C. and Cahn, J.W. (1971) 'Thermodynamics of solidification', *The Selected Works of John W.Cahn,* pp. 249-251.

Barlock, J.G. and Mondolfo, L.F. (1975) 'Structure of Some Aluminum-Iron-Magnesium- Manganese-Silicon Alloys', *Zeitschrift fur Metallkunde,* 66(10), pp. 605-611.

Becker, R. and Döring, W. (1935) 'Kinetische behandlung der keimbildung in übersättigten dämpfen', *Annalen der Physik*, 416(8), pp. 719-752.

Belton, G. (1976) 'Langmuir adsorption, the gibbs adsorption isotherm, and interracial kinetics in liquid metal systems', *Metallurgical Transactions B,* 7(1), pp. 35-42.

Black, P. (1955) 'The structure of FeAl3. I', *Acta Crystallographica,* 8(1), pp. 43-48.

Bramfitt, B.L. (1970) 'The effect of carbide and nitride additions on the heterogeneous nucleation behavior of liquid iron', *Metallurgical and Materials Transactions B,* 1(7), pp. 1987-1995.

Bravais, A. (1866) *Etudes cristallographiques.* Gauthier-Villars.

Bunn, A., Schumacher, P., Kearns, M., Boothroyd, C. and Greer, A. (1999) 'Grain refinement by Al–Ti–B alloys in aluminium melts: a study of the mechanisms of poisoning by zirconium', *Materials science and technology,* 15(10), pp. 1115-1123.

Bykov, T. and Zeng, X.C. (2002) 'Heterogeneous nucleation on mesoscopic wettable particles: A hybrid thermodynamic/density-functional theory', *The Journal of chemical physics,* 117(4), pp. 1851-1868.

Caceres, C., Davidson, C., Griffiths, J. and Wang, Q. (1999) 'The effect of Mg on the microstructure and mechanical behavior of Al-Si-Mg casting alloys', *Metallurgical and materials transactions A,* 30(10), pp. 2611-2618.

Callister, W.D. and Rethwisch, D.G. (2011) 'Materials Science and Engineering SI Version,-8/E.'.

Cantor, B. (2003) 'Heterogeneous nucleation and adsorption', *Philosophical Transactions of the Royal Society of London A: Mathematical, Physical and Engineering Sciences,* 361(1804), pp. 409-417.

Cao, X. and Campbell, J. (2004) 'The solidification characteristics of Fe-rich intermetallic compounds in Al-11.5 Si-0.4 Mg cast alloys', *Metallurgical and Materials Transactions A,* 35(5), pp. 1425-1435.

Cao, X. and Campbell, J. (2003) 'The nucleation of Fe-rich phases on oxide films in Al-11.5 Si-0.4 Mg cast alloys', *Metallurgical and Materials Transactions A,* 34(7), pp. 1409-1420.

Cao, X. and Campbell, J. (2000) 'Precipitation of primary intermetallic compounds in liquid Al 11.5 Si 0.4 Mg alloy', *International Journal of Cast Metals Research,* 13(3), pp. 175-184.

Cao, X., Saunders, N. and Campbell, J. (2004) 'Effect of iron and manganese contents on convection-free precipitation and sedimentation of primary α-Al (FeMn) Si phase in liquid Al-11.5 Si-0.4 Mg alloy', *Journal of Materials Science,* 39(7), pp. 2303-2314.

Carpenter, G. and Le Page, Y. (1993) 'Revised cell data for the β-FeSiAl phase in aluminum alloys', *Scripta metallurgica et materialia,* 28(6), pp. 733-736.

Cerri, E. and Evangelista, E. (1999) *Metallography of Aluminium alloys.* Brussels, Belgium: European Aluminium Association.

Chai, G., Bäackerud, L. and Arnberg, L. (1995) 'Relation between grain size and coherency parameters in aluminium alloys', *Materials Science and Technology,* 11(11), pp. 1099-1103.

Chanyathunyaroj, K., Patakham, U., Kou, S. and Limmaneevichitr, C. (2017) 'Microstructural evolution of Fe-rich intermetallic compounds in scandium modified Al-7Si-0.3 Mg alloys', *Journal of Alloys and Compounds,* 692, pp. 865-875.

Chen, S.L., Daniel, S., Zhang, F., Chang, Y.A., Yan, X.Y., Xie, F.Y., Schmid-Fetzer, R. and Oates, W.A., 2002. 'The PANDAT software package and its applications', *Calphad*, *26*(2), pp.175-188.

Chernov, A. (1974) 'Stability of faceted shapes', *Journal of Crystal Growth,* 24, pp. 11-31.

Cooper, M. (1967) 'The crystal structure of the ternary alloy α (AlFeSi)', *Acta Crystallographica,* 23(6), pp. 1106-1107.

Cooper, M. and Robinson, K. (1966) 'The crystal structure of the ternary alloy α (AlMnSi)', *Acta Crystallographica,* 20(5), pp. 614-617.

Cornish, A. (1975) 'The influence of boron on the mechanism of grain refinement in dilute aluminium-titanium alloys', *Metal Science,* 9(1), pp. 477-484.

Couture, A. (1981) 'Iron in aluminum casting alloys-a literature survey', *International cast metals journal,* 6(4), pp. 9-17.

Crepeau, P. (1995) 'Effect of Iron in Al-Si Casting Alloys: A Critical Review (95-110)', *Transactions of the American Foundrymen's Society,* 103, pp. 361-366.

Dantzig, J.A. and Rappaz, M. (2009) *Solidification.* EPFL press.

Davies, P., Kellie, J.L.F. and Wood, J.V., 1992. Development of cast aluminium metal matrix composites. In *Key Engineering Materials* (Vol. 77, pp. 357-362). Trans Tech Publications.

Davignon, G., Verlinden, B., Delaey, L. and Serneels, A. (1996) 'An isothermal section at 550 C in the Al-rich corner of the Al-Fe-Mn-Si system', *Metallurgical and Materials Transactions A,* 27(11), pp. 3357-3361.

de Moraes, H.L., de Oliveira, J.R., Espinosa, D.C.R. and Tenório, J.A.S. (2006) 'Removal of iron from molten recycled aluminum through intermediate phase filtration', *Materials Transactions,* 47(7), pp. 1731-1736.

Diepers, H., Beckermann, C. and Steinbach, I. (1999) 'Simulation of convection and ripening in a binary alloy mush using the phase-field method', *Acta Materialia,* 47(13), pp. 3663-3678.

Dinnis, C.M., Taylor, J.A. and Dahle, A.K. (2005) 'As-cast morphology of iron-intermetallic compounds in Al–Si foundry alloys', *Scripta Materialia,* 53(8), pp. 955-958.

Dinnis, C., Taylor, J. and Dahle, A. (2006) 'Interactions between iron, manganese, and the Al-Si eutectic in hypoeutectic Al-Si alloys', *Metallurgical and Materials Transactions A,* 37(11), pp. 3283-3291.

Dinsdale, A. (1991) 'SGTE data for pure elements', *Calphad,* 15(4), pp. 317-425.

Dobrzański, L., Borek, W. and Maniara, R. (2006) 'Influence of the crystallization condition on Al-Si-Cu casting alloys structure', *Journal of Achievements in Materials and Manufacturing Engineering,* 18(1-2), pp. 211-214.

Donnadieu, P., Lapasset, G. and Sanders, T. (1994) 'Manganese-induced ordering in the α-(Al-Mn-Fe-Si) approximant phase', *Philosophical Magazine Lletters,* 70(5), pp. 319-326.

Donnay, J.H. and Harker, D. (1937) 'A new law of crystal morphology extending the law of Bravais', *Am.Mineral,* 22(5), pp. 446-467.

Double, D. and Hellawell, A. (1995) 'The nucleation and growth of graphite—The modification of cast iron', *Acta Metallurgica et Materialia,* 43(6), pp. 2435-2442.

Du, Y., Chang, Y., Huang, B., Gong, W., Jin, Z., Xu, H., Yuan, Z., Liu, Y., He, Y. and Xie, F. (2003) 'Diffusion coefficients of some solutes in fcc and liquid Al: critical evaluation and correlation', *Materials Science and Engineering: A,* 363(1), pp. 140-151.

Du, Y., Jin, Z., Huang, B., Gong, W., Xu, H., Yuan, Z., Schuster, J.C., Weitzer, F. and Krendelsberger, N. (2004) 'A thermodynamic description of the Al-Mn-Si system over the entire composition and temperature ranges', *Metallurgical and Materials Transactions A,* 35(5), pp. 1613-1628.

Du, Y., Schuster, J.C., Liu, Z.K., Hu, R., Nash, P., Sun, W., Zhang, W., Wang, J., Zhang, L., Tang, C. and Zhu, Z., 2008. 'A thermodynamic description of the Al–Fe–Si system over the whole composition and temperature ranges via a hybrid approach of CALPHAD and key experiments', *Intermetallics, 16*(4), pp.554-570.

Dutta, B. and Rettenmayr, M. (2002) 'Microsegregation and its effects on quantity and morphology of secondary phases during solidification of Al-Fe-Si alloys', *Materials Science and Technology,* 18(12), pp. 1428-1434.

Dutta, B. and Rettenmayr, M. (2000) 'Effect of cooling rate on the solidification behaviour of Al–Fe–Si alloys', *Materials Science and Engineering: A*, 283(1), pp. 218-224.

Easton, M. and StJohn, D. (2008) 'Improved prediction of the grain size of aluminum alloys that includes the effect of cooling rate', *Materials Science and Engineering: A,* 486(1), pp. 8-13.

Easton, M. and StJohn, D. (2001) 'A model of grain refinement incorporating alloy constitution and potency of heterogeneous nucleant particles', *Acta Materialia,* 49(10), pp. 1867-1878.

Easton, M. and StJohn, D. (2005) 'An analysis of the relationship between grain size, solute content, and the potency and number density of nucleant particles', *Metallurgical and Materials Transactions A,* 36(7), pp. 1911-1920.

Easton, M. and Stjohn, D. (1999) 'Grain refinement of aluminum alloys: Part I. the nucleant and solute paradigms—a review of the literature', *Metallurgical and Materials Transactions A*, 30(6), pp. 1613-1623.

Easton, M. and StJohn, D. (1999) 'Grain refinement of aluminum alloys: Part II. Confirmation of, and a mechanism for, the solute paradigm', *Metallurgical and Materials Transactions A,* 30(6), pp. 1625-1633.

EDAX (2017) *DigiView EBSD Camera*. Available at: http://www.edax.com/Products/EBSD/DigiView-EBSD-Camera.aspx 2017).

Edgar, J. (1949) 'Solubility of iron in solid aluminum', *Transaction of the American Institute of Mining and Metallurgical Engineers*, 180, pp. 225-229.

Elliott, R. (2013) *Eutectic solidification processing: crystalline and glassy alloys.* Elsevier.

Emamy, M., Mahta, M. and Rasizadeh, J. (2006) 'Formation of TiB_2 particles during dissolution of $TiAl_3$ in Al–TiB_2 metal matrix composite using an in situ technique', *Composites Science and Technology*, 66(7), pp. 1063-1066.

Fan, T., Yang, G. and Zhang, D. (2005) 'Thermodynamic effect of alloying addition on in-situ reinforced TiB_2/Al composites', *Metallurgical and Materials Transactions A,* 36(1), pp. 225-233.

Fan, Z., Wang, Y., Zhang, Y., Qin, T., Zhou, X., Thompson, G., Pennycook, T. and Hashimoto, T. (2015) 'Grain refining mechanism in the Al/Al–Ti–B system', *Acta Materialia*, 84, pp. 292-304.

Fan, Z. (2013) 'An epitaxial model for heterogeneous nucleation on potent substrates', *Metallurgical and Materials Transactions A,* 44(3), pp. 1409-1418.

Fatahalla, N., Hafiz, M. and Abdulkhalek, M. (1999) 'Effect of microstructure on the mechanical properties and fracture of commercial hypoeutectic Al-Si alloy modified with Na, Sb and Sr', *Journal of Materials Science,* 34(14), pp. 3555-3564.

Ferdian, D., Josse, C., Nguyen, P., Gey, N., Ratel-Ramond, N., De Parseval, P., Thebault, Y., Malard, B., Lacaze, J. and Salvo, L. (2015) 'Chinese Script vs Plate-Like Precipitation of Beta-Al9Fe2Si2 Phase in an Al-6.5Si-1Fe Alloy', *Metallurgical and Materials Transactions A,* 46(7), pp. 2814-2818.

Fick, A. (1855) 'Ueber diffusion', *Annalen der Physik,* 170(1), pp. 59-86.

Fisher, D. and Kurz, W. (1980) 'A theory of branching limited growth of irregular eutectics', *Acta Metallurgica,* 28(6), pp. 777-794.

Fjellstedt, J., Jarfors, A.E. and Svendsen, L. (1999) 'Experimental analysis of the intermediary phases AlB_2, AlB_{12} and TiB_2 in the Al–B and Al–Ti–B systems', *Journal of Alloys and Compounds,* 283(1), pp. 192-197.

Flemings, M.C. (1974) *Solidification processing.* Wiley Online Library.

Foss, S., Olsen, A., Simensen, C. and Taftø, J. (2003) 'Determination of the crystal structure of the π-AlFeMgSi phase using symmetry-and site-sensitive electron microscope techniques', *Acta Crystallographica Section B: Structural Science,* 59(1), pp. 36-42.

Gao, T., Wu, Y., Li, C. and Liu, X. (2013) 'Morphologies and growth mechanisms of α-Al (FeMn) Si in Al–Si–Fe–Mn alloy', *Materials Letters,* 110, pp. 191-194.

Ghosh, G., 2008. 'Aluminium–iron–silicon', *Iron Systems, Part 1* (pp. 184-266). Springer Berlin Heidelberg.

Gibbs, J.W. (1906) *The scientific papers of J. Willard Gibbs.* Longmans, Green and Company.

Goodhew, P.J., Humphreys, J. and Beanland, R. (2000) *Electron microscopy and analysis.* CRC Press.

Green, J.A. (2007) *Aluminum recycling and processing for energy conservation and sustainability.* ASM International.

Greer, A. (2003) 'Grain refinement of alloys by inoculation of melts', *Philosophical transactions of the Royal Society of London A: Mathematical, Physical and Engineering Sciences,* 361(1804), pp. 479-495.

Greer, A., Bunn, A., Tronche, A., Evans, P. and Bristow, D. (2000) 'Modelling of inoculation of metallic melts: application to grain refinement of aluminium by Al–Ti–B', *Acta materialia,* 48(11), pp. 2823-2835.

Gündüz, M., Kaya, H., Çadırlı, E. and Özmen, A. (2004) 'Interflake spacings and undercoolings in Al–Si irregular eutectic alloy', *Materials Science and Engineering: A,* 369(1), pp. 215-229.

Gustafsson, G., Thorvaldsson, T. and Dunlop, G. (1986) 'The influence of Fe and Cr on the microstructure of cast Al-Si-Mg alloys', *Metallurgical Transactions A,* 17(1), pp. 45-52.

Ha, H. and Hunt, J. (2000) 'A numerical and experimental study of the rate of transformation in three directionally grown peritectic systems', *Metallurgical and Materials Transactions A,* 31(1), pp. 29-34.

Haitani, T., Tamura, Y., Motegi, T., Kono, N. and Tamehiro, H., 2003. Solubility of iron in pure magnesium and cast structure of Mg-Fe alloy. In *Materials science forum* (Vol. 419, pp. 697-702). Trans Tech Publications.

Han, Q. and Viswanathan, S. (2003) 'Analysis of the mechanism of die soldering in aluminum die casting', *Metallurgical and Materials Transactions A,* 34(1), pp. 139-146.

Han, Y., Liu, X. and Bian, X. (2002) 'In situ TiB_2 particulate reinforced near eutectic Al–Si alloy composites', *Composites Part A: Applied Science and Manufacturing,* 33(3), pp. 439-444.

Ho, C. and Cantor, B. (1992) 'Effect of ge on the heterogeneous nucleation of cd solidification by al', *Philosophical Magazine A,* 66(1), pp. 141-149.

Hofmann, W. and Jäniche, W. (1936) 'Die Struktur von Aluminiumborid AlB2', *Zeitschrift für Physikalische Chemie,* 31(1), pp. 214-222.

Hsu, C., O’reilly, K., Cantor, B. and Hamerton, R. (2001) 'Non-equilibrium reactions in 6xxx series Al alloys', *Materials Science and Engineering: A,* 304, pp. 119-124.

Hughes, I. and Jones, H. (1976) 'Coupled eutectic growth in Al-Fe alloys', *Journal of Materials Science,* 11(10), pp. 1781-1793.

Hunt, J. (1984) 'Steady state columnar and equiaxed growth of dendrites and eutectic', *Materials Science and Engineering,* 65(1), pp. 75-83.

Hunt, J. and Jackson, K. (1966) 'Binary eutectic solidification', *Transactions of the Metallurgical Society of AIME,* 236(6), p. 843.

Hwang, J., Doty, H. and Kaufman, M. (2008) 'Crystallographic studies on the iron-containing intermetallic compound phases in the 319-type aluminium casting alloys', *Philosophical Magazine,* 88(4), pp. 607-619.

Ji, S., Watson, D., Fan, Z. and White, M. (2012) 'Development of a super ductile diecast Al–Mg–Si alloy', *Materials Science and Engineering: A,* 556, pp. 824-833.

Ji, S., Wang, Y., Watson, D. and Fan, Z. (2013a) 'Microstructural evolution and solidification behavior of Al-Mg-Si alloy in high-pressure die casting', *Metallurgical and Materials Transactions A,* 44(7), pp. 3185-3197.

Ji, S., Yang, W., Gao, F., Watson, D. and Fan, Z. (2013b) 'Effect of iron on the microstructure and mechanical property of Al–Mg–Si–Mn and Al–Mg–Si diecast alloys', *Materials Science and Engineering: A,* 564, pp. 130-139.

Jiang, D. and Carter, E.A. (2005) 'Carbon atom adsorption on and diffusion into Fe (110) and Fe (100) from first principles', *Physical Review B,* 71(4), pp. 045402.

Joenoes, A. and Gruzleski, J. (1991) 'Magnesium effects on the microstructure of unmodified and modified Al-Si alloys', *Cast Metals,* 4(2), pp. 62-71.

Johnson Jr, R.E. and Dettre, R.H. (1964) 'Contact angle hysteresis. III. Study of an idealized heterogeneous surface', *The Journal of Physical Chemistry,* 68(7), pp. 1744-1750.

Johnsson, M. and Eriksson, L. (1998) 'Thermal expansion of Al and TiB2 in the temperature range 300 to 900 K and calculated lattice fit at the melting temperature for Al', *Zeitschrift für Metallkunde,* 89(7), pp. 478-480.

Johnsson, M. (1995) 'Grain refinement of aluminium studied by use of a thermal analytical technique', *Thermochimica Acta,* 256(1), pp. 107-121.

Jones, G.P. and Pearson, J. (1976) 'Factors affecting the grain-refinement of aluminum using titanium and boron additives', *Metallurgical Transactions B,* 7(2), pp. 223-234.

Jones, H. (1969) 'Observations on a structural transition in aluminium alloys hardened by rapid solidification', *Materials Science and Engineering,* 5(1), pp. 1-18.

Jones, H. and Kurz, W. (1981) 'Relation of interphase spacing and growth temperature to growth velocity in Fe-C and Fe-Fe3C eutectic alloys', *Zeitschrift fur Metallkunde,* 72(11), pp. 792-797.

Kamyabi-Gol, A. and Sheikh-Amiri, M. (2010) 'Spheroidizing kinetics and optimization of heat treatment parameters in CK60 steel using Taguchi robust design', *Journal of Iron and Steel Research, International,* 17(4), pp. 45-52.

Kaye, A. and Street, A. (2016) *Die Casting Metallurgy: Butterworths Monographs in Materials.* Elsevier.

Kearns, M. and Cooper, P. (1997) 'Effects of solutes on grain refinement of selected wrought aluminium alloys', *Materials Science and Technology,* 13(8), pp. 650-654.

Kelton, K. and Greer, A.L. (2010) *Nucleation in Condensed Matter: Applications in Materials and Biology.* Elsevier.

Khalifa, W., Samuel, F. and Gruzleski, J. (2003) 'Iron intermetallic compound phases in the Al corner of the Al-Si-Fe system', *Metallurgical and Materials Transactions A,* 34(3), pp. 807-825.

Khalifa, W., Samuel, F., Gruzleski, J., Doty, H. and Valtierra, S. (2005) 'Nucleation of Fe-intermetallic compound phases in the Al-Si-Fe alloys', *Metallurgical and Materials Transactions A,* 36(4), pp. 1017-1032.

Kim, D. and Cantor, B. (1994) 'Structure and decomposition behaviour of rapidly solidified Al-Fe alloys', *Journal of Materials Science,* 29(11), pp. 2884-2892.

Kim, H.Y., Park, T.Y., Han, S.W. and Lee, H.M. (2006) 'Effects of Mn on the crystal structure of α-Al (Mn, Fe) Si particles in A356 alloys', *Journal of Crystal Growth,* 291(1), pp. 207-211.

Kim, W. and Cantor, B. (1994) 'An adsorption model of the heterogeneous nucleation of solidification', *Acta Metallurgica et Materialia,* 42(9), pp. 3115-3127.

Kotadia, H. (2010). *Solidification behaviour of Al-Sn-Cu immiscible alloys and Al-Si cast alloys processed under intensive shearing*, Unpublished PhD dissertation. Brunel University London.

Kral, M. (2005) 'A crystallographic identification of intermetallic compound phases in Al–Si alloys', *Materials Letters,* 59(18), pp. 2271-2276.

Kral, M., McIntyre, H. and Smillie, M.J. (2004) 'Identification of intermetallic compound phases in a eutectic Al–Si casting alloy using electron backscatter diffraction pattern analysis', *Scripta Materialia,* 51(3), pp. 215-219.

Kuijpers, N., Kool, W., Koenis, P., Nilsen, K., Todd, I. and Van der Zwaag, S. (2002) 'Assessment of different techniques for quantification of α-Al (FeMn) Si and β-AlFeSi intermetallic compounds in AA 6xxx alloys', *Materials Characterization,* 49(5), pp. 409-420.

Kuijpers, N., Vermolen, F., Vuik, C., Koenis, P., Nilsen, K. and Van Der Zwaag, S. (2005) 'The dependence of the β-AlFeSi to α-Al (FeMn) Si transformation kinetics in Al–Mg–Si alloys on the alloying elements', *Materials Science and Engineering: A,* 394(1), pp. 9-19.

Kuijpers, N.C., Vermolen, F.J., Vuik, K. and van der Zwaag, S. (2003) 'A model of the β-AlFeSi to α-Al (FeMn) Si transformation in Al-Mg-Si alloys', *Materials Transactions,* 44(7), pp. 1448-1456.

Kuni, F., Shchekin, A., Rusanov, A. and Widom, B. (1996) 'Role of surface forces in heterogeneous nucleation on wettable nuclei', *Advances in Colloid and Interface Science,* 65, pp. 71-124.

Kurz, W. and Fisher, D. (1986) 'Fundamentals of solidification', *Trans Tech Publications, Switzerland.*

Kvackaj, T. and Bidulsky, R. (2011) *Aluminium Alloys: Theory and Applications.* InTech.

Lacaze, J., Eleno, L. and Sundman, B. (2010) 'Thermodynamic assessment of the aluminum corner of the Al-Fe-Mn-Si system', *Metallurgical and Materials Transactions A*, 41(9), pp. 2208-2215.

Lai, Z. and Li, C. (1993) 'The disorder-order transformation of C-Al (Mn, Fe) Si phase', *Scripta Metallurgica et Materialia,* 29(7), pp. 895-900.

Langsrud, Y. (1990) 'Silicon in Commercial Aluminium Alloys-What Becomes of it during DC-Casting?', *Key Engineering Materials.* Trans Tech Publ, 95-116.

Li, B., Brody, H. and Kazimirov, A. (2004) 'Real-time observation of dendrite coarsening in Sn-13% Bi alloy by synchrotron microradiography', *Physical Review E,* 70(6), pp. 062602.

Li, C., Liu, X. and Wu, Y. (2008) 'Refinement and modification performance of Al–P master alloy on primary Mg 2 Si in Al–Mg–Si alloys', *Journal of Alloys and Compounds,* 465(1), pp. 145-150.

Li, H., Wang, Y. and Fan, Z. (2012) 'Mechanisms of enhanced heterogeneous nucleation during solidification in binary Al–Mg alloys', *Acta Materialia,* 60(4), pp. 1528-1537.

Liu, J. and Shang, B. (1992) 'Theory and experiments on irregular eutectic growth: investigation on Al-Si eutectic growth', *Journal of Materials Science,* 27(8), pp. 2067-2074.

Liu, K., Cao, X. and Chen, X. (2014) 'Tensile properties of Al-Cu 206 cast alloys with various iron contents', *Metallurgical and Materials Transactions A,* 45(5), pp. 2498-2507.

Liu, L., Xiao, L., Feng, J., Li, L., Esmaeili, S. and Zhou, Y. (2011) 'Bonding of immiscible Mg and Fe via a nanoscale Fe_2Al_5 transition layer', *Scripta Materialia,* 65(11), pp. 982-985.

Liu, P. and Dunlop, G. (1986) 'Constituent Phases Formed During Solidification of Al-Fe-Si Alloys', *Proceedings of Aluminum Alloys Their Physical and Mechanical Properties,* 1, pp. 3-16.

Liu, Y., Huang, G., Sun, Y., Zhang, L., Huang, Z., Wang, J. and Liu, C. (2016) 'Effect of Mn and Fe on the formation of Fe-and Mn-rich intermetallic compounds in Al–5Mg–Mn alloys solidified under near-rapid cooling', *Materials,* 9(2), pp. 88.

Liu, Z. and Chang, Y.A. (1999) 'Thermodynamic assessment of the Al-Fe-Si system', *Metallurgical and Materials Transactions A,* 30(4), pp. 1081-1095.

Lu, L. and Dahle, A. (2005) 'Fe-rich intermetallic compound phases and their role in casting defect formation in hypoeutectic Al− Si alloys', *Metallurgical and Materials Transactions A*, 36(13), pp. 819-835.

Lu, S. and Hellawell, A. (1995) 'Modification of Al-Si alloys: microstructure, thermal analysis, and mechanisms', *JOM Journal of the Minerals, Metals and Materials Society*, 47(2), pp. 38-40.

Maggs, S.J., 1996. *Intermetallic phase selection in dilute Al-Fe-Si alloys*, Doctoral dissertation. University of Leeds.

Magnin, P. and Kurz, W. (1987) 'An analytical model of irregular eutectic growth and its application to Fe-C', *Acta Metallurgica*, 35(5), pp. 1119-1128.

Magnin, P. and Trivedi, R. (1991) 'Eutectic growth: A modification of the Jackson and Hunt theory', *Acta Metallurgica et Materialia*, 39(4), pp. 453-467.

Makarov, S., Apelian, D. and Ludwig, R. (1998) 'Inclusion removal and detection in molten aluminum: mechanical, electromagnetic and acoustic techniques', *One Hundred Third Annual Meeting of the American Foundrymen's Society*, 727-735.

Martienssen, W. and Warlimont, H. (2006) *Springer handbook of condensed matter and materials data.* Springer Science & Business Media.

Maxwell, I. and Hellawell, A. (1975a) 'A simple model for grain refinement during solidification', *Acta Metallurgica*, 23(2), pp. 229-237.

Maxwell, I. and Hellawell, A. (1975b) 'An analysis of the peritectic reaction with particular reference to Al-Ti alloys', *Acta Metallurgica*, 23(8), pp. 901-909.

MelTech, *MeltTech Crucible Induction Furnace*. Available at: http://www.induction-furnaces.co.uk/New_furnaces.html 2017).

Men, H. and Fan, Z. (2014) 'Atomic ordering in liquid aluminium induced by substrates with misfits', *Computational Materials Science*, 85, pp. 1-7.

Men, H. and Fan, Z. (2011) 'Effects of solute content on grain refinement in an isothermal melt', *Acta Materialia*, 59(7), pp. 2704-2712.

Men, H., Jiang, B. and Fan, Z. (2010) 'Mechanisms of grain refinement by intensive shearing of AZ91 alloy melt', *Acta Materialia*, 58(19), pp. 6526-6534.

Miller, D., Lu, L. and Dahle, A. (2006) 'The role of oxides in the formation of primary iron intermetallic compounds in an Al-11.6 Si-0.37 Mg alloy', *Metallurgical and Materials Transactions B*, 37(6), pp. 873-878.

Minkoff, I. (1983) *The physical metallurgy of cast iron.* Wiley.

Mondolfo, L.F. (2013) *Aluminum alloys: structure and properties.* Elsevier.

Mordike, B. and Ebert, T. (2001) 'Magnesium: properties—applications—potential', *Materials Science and Engineering: A*, 302(1), pp. 37-45.

Mortensen, A. (1991) 'On the rate of dendrite arm coarsening', *Metallurgical Transactions A*, 22(2), pp. 569-574.

Munson, D. (1967) 'A clarification of the phases occurring in aluminium-rich aluminium-iron-silicon alloys, with particular reference to the ternary phase alpha-AlFeSi', *Journal of the Institute of Metals*, 95(7), pp. 217-219.

Murali, S., Raman, K. and Murthy, K. (1995) 'The formation of β-FeSiAl5 and Be□Fe phases in Al7Si0.3Mg alloy containing Be', *Materials Science and Engineering: A*, 190(1-2), pp. 165-172.

Murray, J.L. (1982) 'The Al− Mg (aluminum−magnesium) system', *Journal of Phase Equilibria*, 3(1), pp. 60-74.

Murray, J.L. and McAlister, A.J. (1984) 'The Al-Si (Aluminum-Silicon) system', *Bulletin of Alloy Phase Diagrams*, 5, pp. 74-84.

Murty, B., Kori, S. and Chakraborty, M. (2002) 'Grain refinement of aluminium and its alloys by heterogeneous nucleation and alloying', *International Materials Reviews*, 47(1), pp. 3-29.

Murty, B., Kori, S., Venkateswarlu, K., Bhat, R. and Chakraborty, M. (1999) 'Manufacture of Al–Ti–B master alloys by the reaction of complex halide salts with molten aluminium', *Journal of Materials Processing Technology*, 89, pp. 152-158.

Narayanan, L.A., Samuel, F. and Gruzleski, J. (1994) 'Crystallization behavior of iron-containing intermetallic compounds in 319 aluminum alloy', *Metallurgical and Materials Transactions A*, 25(8), pp. 1761-1773.

Nyahumwa, C., Green, N.R. and Campbell, J. (1998) 'The concept of the fatigue potential of cast alloys', *Journal of the Mechanical Behavior of Materials*, 9(4), pp. 227-236.

Orozco-González, P., Castro-Román, M., López-Rueda, J., Hernández-Rodríguez, A., Muñiz-Valdez, R., Luna-Álvarez, S. and Ortiz-Cuellar, C. (2011) 'Effect of iron addition on the crystal structure of the α-AlFeMnSi phase formed in the quaternary Al-Fe-Mn-Si system', *Revista de Metalurgia*, 47(6), pp. 453.

Oxford Instruments (2017) *FOUNDRY-MASTER Pro*. Available at: https://www.oxford-instruments.com/products/spectrometers/optical-emission-spectroscopy/foundry-master-pro.

Patakham, U. and Limmaneevichitr, C. (2014) 'Effects of iron on intermetallic compound formation in scandium modified Al–Si–Mg Alloys', *Journal of Alloys and Compounds*, 616, pp. 198-207.

Phillips, H.W.L. (1959) *Annotated equilibrium diagrams of some aluminium alloy systems*'. The Institute of Metals, London.

Phragmén, G. (1950) 'On the phases occurring in alloys of aluminium with copper, magnesium, manganese, iron, and silicon', *Journal of the Institute of Metals,* 77(6), pp. 489-551.

Porter, D.A., Easterling, K.E. and Sherif, M. (2009) *Phase Transformations in Metals and Alloys, (Revised Reprint).* CRC press.

Pryds, N. and Huang, X. (2000) 'The effect of cooling rate on the microstructures formed during solidification of ferritic steel', *Metallurgical and Materials Transactions A,* 31(12), pp. 3155-3166.

Puncreobutr, C., Phillion, A., Fife, J., Rockett, P., Horsfield, A. and Lee, P. (2014) 'In situ quantification of the nucleation and growth of Fe-rich intermetallic compounds during Al alloy solidification', *Acta Materialia,* 79, pp. 292-303.

Qian, M., Cao, P., Easton, M., McDonald, S. and StJohn, D. (2010) 'An analytical model for constitutional supercooling-driven grain formation and grain size prediction', *Acta Materialia,* 58(9), pp. 3262-3270.

Qian, M. (2007) 'Heterogeneous nucleation on potent spherical substrates during solidification', *Acta Materialia*, 55(3), pp. 943-953.

Que, Z.P., Zhou, Y.P., Wang, Y. and Fan, Z. (2017) 'Composition templating for heterogeneous nucleation of intermetallic compounds', *Proceedings of the 6th Decennial Conference on Solidification Processing,* pp. 158-161, Windsor, UK.

Quested, T. (2004) 'Understanding mechanisms of grain refinement of aluminium alloys by inoculation', *Materials Science and Technology,* 20(11), pp. 1357-1369.

Quested, T. and Greer, A. (2005) 'Grain refinement of Al alloys: Mechanisms determining as-cast grain size in directional solidification', *Acta Materialia,* 53(17), pp. 4643-4653.

Quested, T. and Greer, A. (2004) 'The effect of the size distribution of inoculant particles on as-cast grain size in aluminium alloys', *Acta Materialia,* 52(13), pp. 3859-3868.

Rana, R., Purohit, R. and Das, S. (2012) 'Reviews on the influences of alloying elements on the microstructure and mechanical properties of aluminum alloys and aluminum alloy composites', *International Journal of Scientific and Research Publications,* 2(6), pp. 1-7.

Rappaz, M. and Thevoz, P. (1987) 'Solute diffusion model for equiaxed dendritic growth', *Acta Metallurgica,* 35(7), pp. 1487-1497.

Redlich, O. and Kister, A. (1948) 'Algebraic representation of thermodynamic properties and the classification of solutions', *Industrial & Engineering Chemistry,* 40(2), pp. 345-348.

Rivlin, V. and Raynor, G. (1981) '4: Critical evaluation of constitution of aluminium-iran-silicon system', *International Metals Reviews*, 26(1), pp. 133-152.

Rømming, C., Hansen, V. and Gjønnes, J. (1994) 'Crystal structure of β-Al4. 5FeSi', *Acta Crystallographica Section B: Structural Science*, 50(3), pp. 307-312.

Salleh, M.S., Omar, M.Z. and Syarif, J. (2015) 'The effects of Mg addition on the microstructure and mechanical properties of thixoformed Al–5% Si–Cu alloys', *Journal of Alloys and Compounds,* 621, pp. 121-130.

Samuel, A. and Samuel, F. (1997) 'Modification of iron intermetallic compounds by magnesium and strontium in Al-Si alloys', *International Journal of Cast Metals Research,* 10(3), pp. 147-157.

Samuel, A. and Samuel, F. (1995) 'Effect of alloying elements and dendrite arm spacing on the microstructure and hardness of an Al-Si-Cu-Mg-Fe-Mn (380) aluminium die-casting alloy', *Journal of Materials Science,* 30(7), pp. 1698-1708.

Samuel, F., Pucella, G., Villeneuve, C., Samuel, A., Doty, H. and Valtierra, S. (1999) 'Microstructural observations on Fe-intermetallic compounds in unmodified and Sr-modified Al-Si-Cu (A380.1) die casting alloy', *International Journal of Cast Metals Research,* 12(3), pp. 197-210.

Samuel, F., Samuel, A., Ouellet, P. and Doty, H. (1998) 'Effect of Mg and Sr additions on the formation of intermetallic compounds in Al-6 wt pct Si-3.5 wt pct Cu-(0.45) to (0.8) wt pct Fe 319-type alloys', *Metallurgical and Materials Transactions A,* 29(12), pp. 2871-2884.

Schumacher, P. and Greer, A. (1997) 'On the reproducibility of heterogeneous nucleation in amorphous Al85Ni10Ce5 alloys', *Materials Science and Engineering: A*, 226, pp. 794-798.

Schumacher, P. and Greer, A. (1994) 'Heterogeneously nucleated α-Al in amorphous aluminium alloys', *Materials Science and Engineering: A,* 178(1-2), pp. 309-313.

Schumacher, P. and McKay, B. (2003) 'TEM investigation of heterogeneous nucleation mechanisms in Al–Si alloys', *Journal of Non-Crystalline Solids,* 317(1), pp. 123-128.

Scientific, H. (2012) *A guidebook to particle size analysis*. Horiba Instruments, Inc, pp. 1-29.

Sha, G., O’Reilly, K., Cantor, B., Worth, J. and Hamerton, R. (2001) 'Growth related metastable phase selection in a 6xxx series wrought Al alloy', *Materials Science and Engineering: A,* 304, pp. 612-616.

Shabestari, S., Keshavarz, M. and Hejazi, M. (2009) 'Effect of strontium on the kinetics of formation and segregation of intermetallic compounds in A380 aluminum alloy', *Journal of Alloys and Compounds,* 477(1), pp. 892-899.

Shabestari, S., Mahmudi, M., Emamy, M. and Campbell, J. (2002) 'Effect of Mn and Sr on intermetallic compounds in Fe-rich eutectic Al-Si alloy', *International Journal of Cast Metals Research,* 15(1), pp. 17-24.

Shabestari, S. and Malekan, M. (2005) 'Thermal analysis study of the effect of the cooling rate on the microstructure and solidification parameters of 319 aluminum alloy', *Canadian Metallurgical Quarterly,* 44(3), pp. 305-312.

Shabestari, S. and Shahri, F. (2004) 'Influence of modification, solidification conditions and heat treatment on the microstructure and mechanical properties of A356 aluminum alloy', *Journal of Materials Science,* 39(6), pp. 2023-2032.

Sivarupan, T., Caceres, C.H. and Taylor, J.A. (2013) 'Alloy composition and dendrite arm spacing in Al-Si-Cu-Mg-Fe Alloys', *Metallurgical and Materials Transactions A,* 44(9), pp. 4071-4080.

Skjerpe, P. (1988) 'Structure of Al_mFe', *Acta Crystallographica Section B: Structural Science,* 44(5), pp. 480-486.

Skjerpe, P. (1987) 'Intermetallic compound phases formed during DC-casting of an Al− 0.25 Wt Pct Fe− 0.13 Wt Pct Si alloy', *Metallurgical and Materials Transactions A,* 18(2), pp. 189-200.

Smallman, R.E. (1985) *Modern physical metallurgy.* Elsevier.

Spittle, J. and Sadli, S. (1995) 'Effect of alloy variables on grain refinement of binary aluminium alloys with Al–Ti–B', *Materials Science and Technology,* 11(6), pp. 533-537.

St John, D. and Hogan, L. (1987) 'A simple prediction of the rate of the peritectic transformation', *Acta Metallurgica,* 35(1), pp. 171-174.

Stefaniay, V., Griger, A. and Turmezey, T. (1987) 'Intermetallic compound phases in the aluminium-side corner of the AlFeSi-alloy system', *Journal of Materials Science,* 22(2), pp. 539-546.

StJohn, D., Qian, M., Easton, M. and Cao, P. (2011) 'The Interdependence Theory: The relationship between grain formation and nucleant selection', *Acta Materialia,* 59(12), pp. 4907-4921.

Sun, C. and Mondolfo, L. (1967) 'A clarification of phases occurring in aluminium-rich aluminium-iron-silicon alloys', *Journal of the Institute of Metals,* 95, pp. 384.

Sun, D., Kang, S. and Koo, H. (2000) 'Characteristics of morphology and crystal structure of α-phase in two Al-Mn-Mg alloys', *Materials Chemistry and Physics,* 63(1), pp. 37-43.

Sunagawa, I. (1999) 'Growth and morphology of crystals', *FORMA-TOKYO-,* 14(1/2), pp. 147-166.

Sunagawa, I. (1995) *Morphology of Crystals: Part A: Fundamentals Part B: Fine Particles, Minerals and Snow Part C: The Geometry of Crystal Growth by Jaap van Suchtelen.* Springer Science & Business Media.

Sunagawa, I. (1990) 'Growth and morphology of diamond crystals under stable and metastable contitions', *Journal of Crystal Growth,* 99(1-4), pp. 1156-1161.

Tang, S. and Sritharan, T. (1998) 'Morphology of β-AIFeSi intermetallic compound in AI-7Si alloy castings', *Materials Science and Technology,* 14(8), pp. 738-742.

Tarshis, L., Walker, J. and Rutter, J. (1971) 'Experiments on the solidification structure of alloy castings', *Metallurgical Transactions,* 2(9), pp. 2589-2597.

Tash, M., Samuel, F., Mucciardi, F. and Doty, H. (2007) 'Effect of metallurgical parameters on the hardness and microstructural characterization of as-cast and heat-treated 356 and 319 aluminum alloys', *Materials Science and Engineering: A,* 443(1), pp. 185-201.

Taylor, J.A. (2012) 'Iron-containing intermetallic compound phases in Al-Si based casting alloys', *Procedia Materials Science,* 1, pp. 19-33.

Tee, K., Lu, L. and Lai, M. (1999) 'In situ processing of Al–TiB_2 composite by the stir-casting technique', *Journal of Materials Processing Technology,* 89, pp. 513-519.

Terzi, S., Taylor, J., Cho, Y., Salvo, L., Suéry, M., Boller, E. and Dahle, A. (2010) 'In situ study of nucleation and growth of the irregular α-Al/β-Al 5 FeSi eutectic by 3-D synchrotron X-ray microtomography', *Acta Materialia,* 58(16), pp. 5370-5380.

Tiller, W.A., Jackson, K.A., Rutter, J.W. and Chalmers, B., 1953. 'The redistribution of solute atoms during the solidification of metals', *Acta Metallurgica*, 1(4), pp.428-437.

The University of Manchester (2016) ***Transmission Electron Microscopes***. Available at: http://www.materials.manchester.ac.uk/our-research/facilities/electron-microscopy/transmissionelectronmicroscopes/.

Williams, D.B. and Carter, C.B. (1996) 'The transmission electron microscope', *Transmission Electron Microscopy.* Springer, pp. 3-17.

Turnbull, D. (1953) 'Theory of catalysis of nucleation by surface patches', *Acta Metallurgica,* 1(1), pp. 8-14.

Turnbull, D. and Vonnegut, B. (1952) 'Nucleation catalysis.', *Industrial & Engineering Chemistry,* 44(6), pp. 1292-1298.

Underwood, E. (1969) 'Stereology, or the quantitative evaluation of microstructures', *Journal of Microscopy,* 89(2), pp. 161-180.

Vandersluis, E. and Ravindran, C. (2017) 'Comparison of Measurement Methods for Secondary Dendrite Arm Spacing', *Metallography, Microstructure, and Analysis,* 6(1), pp. 89-94.

Vander-Voort, G. (2015) *The World Beyond Brightfield Illumination.* Buehler TechNotes, Buehler.

Verma, A., Kumar, S., Grant, P. and O'Reilly, K. (2013) 'Influence of cooling rate on the Fe intermetallic compound formation in an AA6063 Al alloy', *Journal of Alloys and Compounds,* 555, pp. 274-282.

Volmer, M. and Weber, A. (1926) 'Keimbildung in übersättigten Gebilden', *Zeitschrift für Physikalische Chemie,* 119(3/4), pp. 277-301.

Walton, D. (1962) 'Nucleation of vapor deposits', *The Journal of chemical physics,* 37(10), pp. 2182-2188.

Wang, F., Eskin, D., Connolley, T. and Mi, J. (2016) 'Effect of ultrasonic melt treatment on the refinement of primary Al 3 Ti intermetallic compound in an Al–0.4 Ti alloy', *Journal of Crystal Growth,* 435, pp. 24-30.

Wang, L., Makhlouf, M. and Apelian, D. (1995) 'Aluminium die casting alloys: alloy composition, microstructure, and properties-performance relationships', *International Materials Reviews,* 40(6), pp. 221-238.

Wang, Q. and Davidson, C. (2001) 'Solidification and precipitation behaviour of Al-Si-Mg casting alloys', *Journal of Materials Science,* 36(3), pp. 739-750.

Warmuzek, M., Rabczak, K. and Sieniawski, J. (2005) 'The course of the peritectic transformation in the Al-rich Al–Fe–Mn–Si alloys', *Journal of Materials Processing Technology,* 162, pp. 422-428.

Watanabe, H., Ohori, K. and Takeuchi, Y. (1984) 'Phase change in 3004 base alloys at elevated temperatures', *Aluminium,* 60, p. 310.

Weidmann, E. and Guesnier, A. (2016) '*Metallographic preparation of aluminium and aluminium alloy',* Application Note, Struers ApS.

West, R. and Fredriksson, H. (1985) 'On the mechanism of facetted growth', *Journal of Materials Science*, 20(3), pp. 1061-1068.

Wood, J., Davies, P. and Kellie, J. (1993) 'Properties of reactively cast aluminium–TiB2 alloys', *Materials Science and Technology*, 9(10), pp. 833-840.

Yang, L., Birchenall, C., Pound, G. and Simnad, M. (1954) 'Some observations on heterogeneous nucleation of sodium crystals from atomic beams', *Acta Metallurgica*, 2(3), pp. 462-469.

Yang, W., Ji, S., Zhou, X., Stone, I., Scamans, G., Thompson, G.E. and Fan, Z. (2014) 'Heterogeneous nucleation of α-Al grain on primary α-AlFeMnSi intermetallic compound investigated using 3D SEM ultramicrotomy and HRTEM', *Metallurgical and Materials Transactions A*, 45(9), pp. 3971-3980.

Yang, W., Yang, X. and Ji, S. (2015) 'Melt superheating on the microstructure and mechanical properties of diecast Al-Mg-Si-Mn alloy', *Metals and Materials International*, 21(2), pp. 382.

Yoo, J.E., Shan, A., Moon, I.G. and Maeng, S.J. (1999) 'A study on composition and crystal structure of dispersoids in AlMgSi alloys', *Journal of Materials Science*, 34(11), pp. 2679-2683.

Young, K. and Kerkwood, D. (1975) 'The dendrite arm spacings of aluminum-copper alloys solidified under steady-state conditions', *Metallurgical Transactions A*, 6(1), pp. 197-205.

Young, R. and Clyne, T. (1981) 'An Al-Fe intermetallic compound phase formed during controlled solidification', *Scripta Metallurgica*, 15(11), pp. 1211-1216.

Yu, X., Wang, S., Li, Y., Wang, J. and Jiao, H. (2012) 'Single gold atom adsorption on the Fe3O4 (111) surface', *The Journal of Physical Chemistry C*, 116(19), pp. 10632-10638.

ZEISS Inc (2017) *ZEISS AxioCam ICc 3*. Available at: https://www.zeiss.com/microscopy/int/products/microscope-cameras/axiocam-ic.html.

Zhang, D. and Cantor, B. (1990) 'Effect of Ge on the heterogeneous nucleation of Pb solidification by Al', *Journal of Crystal Growth*, 104(3), pp. 583-592.

Zhang, J., Fan, Z., Wang, Y. and Zhou, B. (2000) 'Microstructural development of Al–15wt.% Mg 2 Si in situ composite with mischmetal addition', *Materials Science and Engineering: A*, 281(1), pp. 104-112.

Zhang, L., Gao, J., Damoah, L.N.W. and Robertson, D.G. (2012) 'Removal of iron from aluminum: a review', *Mineral Processing and Extractive Metallurgy Review*, 33(2), pp. 99-157.

Zhang, M. and Kelly, P. (2005a) 'Edge-to-edge matching and its applications: Part I. Application to the simple HCP/BCC system', *Acta Materialia*, 53(4), pp. 1073-1084.

Zhang, M. and Kelly, P. (2005b) 'Edge-to-edge matching and its applications: Part II. Application to Mg–Al, Mg–Y and Mg–Mn alloys', *Acta Materialia*, 53(4), pp. 1085-1096.

Zheng, J., Vincent, R. and Steeds, J. (2000) 'Crystal structure of an orthorhombic phase in β-(Al-Fe-Si) precipitates determined by convergent-beam electron diffraction', *Philosophical Magazine A*, 80(2), pp. 493-500.

Zhou, X., Zhu, X., Gao, T., Wu, Y. and Liu, X. (2016) 'Evolution of a novel Si-18Mn-16Ti-11P alloy in Al-Si melt and its influence on microstructure and properties of high-Si Al-Si alloy', *Results in Physics*, 6, pp. 737-745.

Zupanič, F., Spaić, S. and Križman, A. (1998a) 'Contribution to ternary system Al-Ti-B Part 1: Study of diborides present in the aluminium corner', *Materials Science and Technology*, 14(7), pp. 601-607.

Zupanič, F., Spaić, S. and Križman, A. (1998b) 'Contribution to ternary system Al–Ti–B Part 2–Study of alloys in Al–AlB2–TiB2 triangle', *Materials Science and Technology*, 14(12), pp. 1203-1212.